THE DEVELOPMENT OF A MICROFLUIDIC *IN VITRO* MODEL OF MICROVASCULAR COLLAPSE TO AID IN THE DEVELOPMENT OF A DIAGNOSIS FOR ACUTE COMPARTMENT SYNDROME

by

STEPHANIE MARIE HALLAM

A thesis submitted to the University of Birmingham for the degree of

DOCTOR OF PHILOSOPHY

Word Count: 38042

School of Chemical Engineering

College of Engineering and Physical Sciences

University of Birmingham

September 2024

I. Abstract

Trauma conditions affecting the microvasculature in humans such as Acute Compartment Syndrome (ACS) lack reliable and fast diagnosis methods. Advances in “Lab-on-a-chip” technology through the use of microfluidics have allowed for *in vitro* models of microvascular dysfunction and collapse to be created. Their design is complex, with variables such as biological compatibility, geometry, and the ability of the hydrodynamics to be experimentally measured at the microscale competing with the creation of a design that maintains physiological relevance.

Various microfluidic models of blood vessels and blood vessel networks were developed to investigate the effect of microvascular collapse on wall shear stress using soft lithography methods and PDMS. The flow within the models over a physiologically relevant range of applied upstream pressures 2000 to 4700 Pa was measured using Ghost Particle Velocimetry (GPV), an optical method. Changes in wall shear stress are known to affect cell behaviour which could be used in creating diagnostic criteria for conditions such as ACS. It was found that small changes in the geometric design, using models with channel widths of 200, 300 and 400 μm, could be used to mimic the resistance changes seen as the microvasculature collapses and mimic shear stress ranges seen *in vivo*, 1-9.5 Pa in the 200 μm model. Flows within the models had Reynolds numbers of 1-23 in the non-stenosed region and a maximum of 38 in the stenotic region at the highest pressure, 4700 Pa. Increased resistance to flow was observed when a stenosis, an area of decreased cross-sectional area, is incorporated into the design mimicking increased resistance in the channel during collapse, at the physiologically relevant pressures of 2000, 3200 and

4700 Pa. Using ANSYS Fluent, laminar steady-state Computational Fluid Dynamics (CFD) models were created to replicate the experiments and were validated using GPV data and via analytical solutions, supporting claims of increasing resistance, decreasing flow rate and detecting a peak range in wall shear stress.

Experimental models incorporating side branches following Murray's law, side branching with one branch at 45° from the main channel and even branching, where the main channel branches into two channels both at 45° to the main channel; were found to increase resistance further and display variation of shear stress in different locations within the device, with values of 0.1-3.5 Pa at Reynolds numbers of 0.3-1. These branched models also mimicked shear stress ranges seen *in vivo,* creating suitable models for studying cell behaviour under physiologically relevant conditions. Models with deformable side walls, controlled by fluid bladders (referred to as micropumps) on the sides of the channel, were created through modification of the initial 200 μm designs using a 25:1 ratio of PDMS base to curing agent. Additionally, the inclusion of micropumps into the device design allowed for dynamic studies of up to 100% deformation of the channel width at the point of maximum stenosis. These models highlighted how the channel cross-section affects the *in vitro* resistance increase and the resultant shear stress ranges, maintaining suitable shear stress values for the study of cell behaviour, 0.3-2.4 Pa at flows with Reynolds numbers of 0.02-0.06.

II. Acknowledgements

Firstly, I would like to thank the EPSRC for funding my research and giving me the opportunity to conduct this study through the PREMIERE Programme Grant and the University of Birmingham Doctoral Training Grant.

To my supervisors: Prof. Mark Simmons, Dr. Nina Kovalchuk, Dr. Zoe Schofield and Dr. Pranav Vasanthi Bathrinarayanan, I would like to thank you for your support, guidance and patience with me throughout this project. For answering all my questions at any time and diving through my many spreadsheets and documents to get to where my tangent started. I really appreciate your direction, ideas and the opportunities you have given to me. It has been an honour and a privilege to work in such a vastly talented and multidisciplinary team. Also thank you to Ryan Jones, for all your support both in the lab, clean room and emotionally.

To my family, without your ongoing encouragement of education and good moral values throughout my life this would not have been possible. Thank you for your love, support, for always being at the other end of the phone and never faltering belief that this was achievable for me. To my friends, of which there are too many to mention by name, thank you immensely for your support. From bringing me emergency support biscuits, ESBs, cooking me meals at busy periods, listening to my rants and encouraging words and advice. For every drink shared at the Goose and every train journey to see one another across the country. I couldn’t have done it without you.

Table of Contents

III. List of Figures

Chapter 2

Chapter 3

Chapter 4

Chapter 5

Chapter 6

Appendix

IV. List of Tables

V. List of Acronyms

ACS	*Acute Compartment Syndrome*
ATP	*Adenosine Triphosphate*
BEM	*Boundary Element Method*
CFD	*Computational Fluid Dynamics*
CGMD	*Coarse Grained Molecular Dynamics*
CT	*Computed Tomography Angiography*
CTA	*Computed Tomography Angiography*
DEM	*Discrete Element Method*
DMP	*Discrete Multiphysics*
DNA	*Deoxyribonucleic Acid*
DVT	*Deep Vein Thrombosis*
ELS	*Electrophoretic Light Scattering*
FEM	*Finite Element Method*
FFT	*Fast Fourier Transform*
FPS	*Frames Per Second*
FSI	*Fluid-Structure Interaction*
GPV	*Ghost Particle Velocimetry*
HDF	*Human Dermal Fibroblasts*
hiPSC	*Human Induced Pluripotent Stem Cells*
HPLC	*High Performance Liquid Chromatography*
HUVEC	*Human Umbilical Vein Endothelial Cells*
ICP	*Intracompartmental Pressure*
LB	*Lattice Boltzmann*
LEC	*Lymphatic Endothelial Cells*
LSM	*Lattice Spring Model*
MADLS	*Multiangle Dynamic Light Scattering*
MEMS	*Microelectromechanical Systems*
MRI	*Magnetic Resonance Imaging*
NHS	*National Health Service*
NO	*Nitric Oxide*
PBMC	*Peripheral Blood Mononuclear Cells*
PDMS	*Polydimethylsiloxane*
PIV	*Particle Image Velocimetry*

PTV	*Particle Tracking Velocimetry*
SIMPLE	*Semi-Implicit Method for Pressure-Linked Equations*
SPH	*Smooth Particle Hydrodynamics*
TEPEM	*Transversally Enriched Pipe Element Method*
TNF	*Tumour Necrosis Factor*

VI. List of Equations

3.10 Implicit Scheme For Steady Navier Stokes Equations
3.11 Implicit Scheme For Steady Navier Stokes Equations
3.12 Implicit Scheme For Steady Navier Stokes Equations
3.13 Intermediate Velocity Field
3.14 Velocity Correction
3.15 Pressure Correction
3.16 Underrelaxation
3.17 Underrelaxation
3.18 Underrelaxation
3.19 Underrelaxation
3.20 Divergence
3.21 Divergence

4.1 Volumetric Flow Rate
4.2 Pressure Resistance Flow Rate
4.3 Resistance In A Circular Cross-Section Channel
4.4 Resistance In A Rectangular Cross-Section Channel
4.5 Special Case Of The Bernoulli Equation
4.6 Resistance Modelling
4.7 Resistance Modelling
4.8 Resistance In The System
4.9 Flow Rate Dependence On Aspect Ratio In A Rectangular Channel

5.1 Murray's Law Diameters
5.2 Murray's Law Angles
5.3 Murray's Law Angles
5.1-5.6 Equations used in the derivation of Murray's Law
5.7 Fick's Law
5.8 Hydraulic Diameter
5.9 Hooper's Law
5.10 Form of Hagen Poiseuille
5.11 Constant for cylindrical channels
5.12 Resistance in a rectangular channel
5.13 Flow rate in a rectangular channel
5.14-5.19 Branching factors
5.20 Conservation of flow rate
5.21-5.22 Pressure loss at a bifurcation

6.1 Pressure force area

7.1 CFD Timestep
7.2 Forces in Smoothing Deformation
7.3 Courant Number
7.4 Courant Friedrichs Lewy condition

VII. List of Symbols

δ_z	*Longitudinal Characteristic Speckle Size*
L_{IR}	*Interrogation Area Size*
$f(\kappa\alpha)$	*Henry's Function*
d	*Diameter*
D	*Diffusion Coefficient*
E	*Elastic Constant/ Young's Modulus*
F	*Force*
G(t)	*Relaxation Function*
h	*Height*
k	*Spring Constant/ Boltzmann Constant/ Loss Coefficient*
L	*Length*
Nac	*Numerical Aperture*
P	*Pressure*
Q	*Flowrate*
R/r	*Radius*
T	*Tension*
t	*Time*
T	*Temperature*
u	*Velocity*
U_E	*Electrophoretic Mobility*
v	*Velocity*
x	*Extension*
α	*Aspect Ratio*
ε	*Dielectric Constant*
ζ	*Zeta Potential*
η	*Dynamic Viscosity*
λ	*Extension Ratio*
λ	*Wavelength Of Light*
μ	*Dynamic Viscosity*
ρ	*Density*
σ	*Stress*

Chapter 1: Introduction

Introduction

1.1 Motivation

Acute Compartment Syndrome, ACS, is an emergency trauma condition that causes the collapse of the microvasculature (the venules, capillaries, and arterioles) within the tissue and requires a fast diagnosis to prevent harm to the human patient. ACS is typically the result of a traumatic injury such as a gunshot wound or forceful traumatic event, where swelling causes the pressure in a muscular compartment to rise to a point where the blood flow is restricted, and the pressure cannot be released without high-risk surgical intervention (1). The current method of diagnosis is based on clinical signs and intracompartmental pressure (ICP) monitoring, where the pressure in the muscle compartment is measured using a pressure monitoring system (2). However, these methods are highly inaccurate – therefore, there is no best practice or clear consensus. The progression of ACS is rapid thus, a rapid diagnosis is needed to prevent the maximum damage to the patient (3).

To mitigate ACS, the pressure is released by a fasciotomy which is a deep incision into the muscle to relieve pressure. If this is not performed in a timely manner, e.g. due to misdiagnosis, cell necrosis (death) will occur due to lack of oxygen, which can lead to loss of limb or, in some cases, loss of life as well as expensive litigation for the National Health Service, NHS (1)(4). The converse is unnecessary harm and infection risk to the patient caused by the surgery if ACS is not present.

Since it is well known that collapse increases resistance in the microvasculature, the flow distribution will change and thus also the profile and ranges of values of wall shear stress in the network. It is important to understand the impact of these

parameters on the behaviour of the endothelial cells lining the blood vessel walls as this may provide a criterion for diagnosis (5). If tools were available that could examine these effects *in vitro*, the potential for the development of new diagnostic criteria for ACS could be explored via biological studies, for example, due to the detection of biomarkers released by the cells.

1.2 Scope

Given the above challenge, the research presented in this thesis is concerned with the development of *in vitro* and *in silico* models which may be used to develop a deeper understanding of the circulatory aspects and hydrodynamics that occur *in vivo* during ACS when there is microvascular collapse.

A soft lithography method using polydimethylsiloxane (PDMS) is applied to develop a range of *in vitro* microfluidic models incorporating different microvasculature features such as branches and constrictions (stenoses). The appropriateness and applicability of the devices to represent the microvasculature are assessed, through the determination of properties of PDMS walls (e.g. Young's modulus) and in the accuracy and repeatability of the fabrication methods used.

The flows through these devices are measured over a range of physiologically relevant conditions to determine their usefulness and applicability for biological studies. It should be noted that biological studies are beyond the scope of this thesis. A state-of-the-art method for flow measurement in microchannels, Ghost Particle Velocimetry (GPV) was used to develop the relationship between flow and

consequent changes in wall shear stress for pressure-driven flows under physiologically relevant conditions.

In silico laminar flow models of the microfluidic devices are developed using Computational Fluid Dynamics, CFD, using ANSYS Fluent. The CFD models are validated by experimental methods and were created to provide additional insight into the flows in regions where measurements were challenging or impossible due to geometrical constraints. These measurements coupled with GPV were used to determine changes in wall shear stress ranges in both stenotic and non-stenotic regions due to increasing stenosis in straight, branched, and deformable models.

1.3 Aims and Objectives

This thesis aims to develop *in vitro* microfluidic platforms that can be used to provide a better understanding of microvascular collapse, providing robust platforms for studying the resultant hydrodynamics and quantifying shear stress ranges to inform biological studies as a scope for a diagnosis for Acute Compartment Syndrome. Specific objectives of the research presented in this thesis are:

1. Conduct a comprehensive review of existing models of microvascular collapse, lab-on-a-chip and microfluidics and their methodologies, limitations, and applications (Chapter 2).
2. Identify key physiological and pathological factors contributing to microvascular collapse *in vivo* to inform the design of the *in vitro* and *in silico* models (Chapter 2).

3. Design and construct an experimentally measurable microfluidic device that simulates flow behaviour in the microvascular environment using PDMS (Chapter 4)
4. Investigate flow behaviour within the microfluidic devices using Ghost Particle Velocimetry in response to increasing stenosis and use this data to validate *in silico* models created using CFD (Chapter 4)
5. Investigate flow behaviour within the microfluidic devices using Ghost Particle Velocimetry in response to increasing stenosis within different branching geometries and use this data to validate *in silico* models created using CFD (Chapter 5)
6. Design and fabricate deformable microfluidic devices by altering PDMS properties and fabrication processes (Chapter 6)
7. Measure flow behaviour within the deformable microfluidic device using Ghost Particle Velocimetry in response to increasing deformation within straight and branched geometries and use this data to validate *in silico* models created using CFD (Chapter 6)
8. Propose future studies to further validate the model and explore additional applications (Chapter 7)

1.4 Thesis Structure

This thesis is comprised of seven chapters including Introduction, Literature Review, Materials and Methods, three results chapters and finally Conclusions and Future Work. The first results chapter is concerned with initially designing the PDMS

microfluidic device, the results of the accuracy of the fabrication method and determining the experimental limitations of GPV at the microscale for models with increasing fixed stenosis. The second results chapter investigates the effect of branching on the flow behaviour in long fixed stenosis models with three different types of branching geometry whilst increasing stenosis. The final results chapter investigates the creation of a deformable microfluidic model by varying PDMS composition and thus Young's modulus and how increasing deformation in the model affects flow behaviour as studied through GPV in straight and branched microfluidic devices.

1.5 Outputs from this Research

Journal papers

Vasanthi Bathrinarayanan, P., Hallam, S., Grover, L.M., Vigolo, D., Simmons, M.J.H. 2024. Microfluidics - a powerful tool to investigate microvascular dysfunction in trauma conditions: a review of the state-of-the-art, *Advanced Biology*, 202400037, https://doi.org/10.1002/adbi.202400037

Conference papers

Hallam, S.M., Vasanthi Bathrinrayanan, P., Schofield, Z., Kovalchuk, N.M., Simmons, M.J.H. 2024. Use of ghost particle velocimetry to determine the flows within *in vitro* models of microfluidic collapse, ChemEngDayUK 2024, Imperial College London, 25-26 April 2024, London, UK. (Poster)

Hallam, S.M., Vasanthi Bathrinrayanan, P., Schofield, Z., Kovalchuk, N.M., Simmons, M.J.H. 2024. A microfluidic model of microvascular collapse, Micro and Nanoflows 2023, University of Padua, 18-20 September 2023, Padua, Italy (Presentation)

Hallam, S.M.[1], Vasanthi Bathrinrayanan, P [1], Schütt M.[1], Kovalchuk, N.M[1], Schofield, Z.[2], Simmons, M.J.H.[1] 2023. The Development of an *In Vitro* Model of Microvascular Collapse using Microfluidics, 11th International Conference on Multiphase Flow, 2023, Kobe International Conference Centre, April 2-7 2023, Kobe, Japan. (Presentation)

Vasanthi Bathrinarayanan, P., Hallam, S., Anderton, C., George, N., Grover, L.M., Vigolo, D., Arrcucci, R., Matar, O., Simmons, M.J.H. 2022. Developing a Novel Deforming Vasculature-on-a-Chip Microfluidic Platform to Investigate Microvascular Dysfunction, Chem Eng Day U.K., 2022, University College London, April 7-8 2022, London, U.K. (Poster)

Chapter 2: Review of the Literature

Chapter 2: Review of the Literature[1]

Introduction

This chapter contains a review of the current literature necessary to underpin the research carried out in this study. The review is arranged around two major sections, (i) the current medical understanding and diagnostic methods for ACS, and how microvasculature changes are caused in trauma conditions and, (ii) how *in vitro* (microfluidic) models have been applied in aligned fields of study, the measurement techniques which have been used and how these can be supported by *in silico* models such as CFD. The review concludes with an explanation of the gaps in the current literature which motivate this study.

2.1 Medical Origins of Acute Compartment Syndrome, Diagnosis and Microvasculature

2.1.1 Cause and Pathophysiology

It is well known that ACS is typically the result of a traumatic injury, such as a gunshot wound or forceful traumatic event, that results in a fracture-making up 69% of cases (6)(7). Tibial diaphyseal (middle segment of the shin bone, Figure 2.1) fractures alone are responsible for 35% of cases with a further 23% of cases due to soft tissue injury, reported in the study by McQueen *et al.,* (2000) of 164 patients (1)(7)(8).

[1] Some of the concepts and content in this chapter are reported in Vasanthi Bathrinarayanan, P., Hallam, S., Grover, L.M., Vigolo, D., Simmons, M.J.H. 2024. *Advanced Biology*, 202400037, https://doi.org/10.1002/adbi.202400037

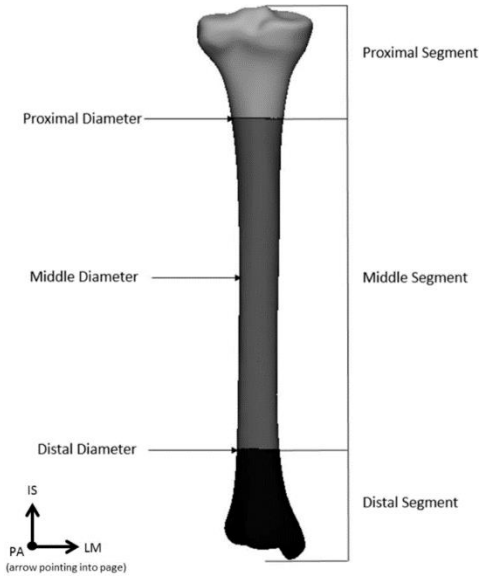

Figure 2.1: Tibia bone taken from Quintens et al. 2019 (9)

In some cases, the application of casts that restrict blood flow, lithotomy positioning, and the use of narcotics may also induce ACS (1)(10)(11). The physician must assess the patient's risk of developing ACS to aid with diagnosis, with cases being 10 times more common amongst males and having a higher prevalence in those under 35 (6)(7). ACS can fall outside of these criteria (12)(13), but being in this category should alert the physician of the relative incidence and risk.

Although there is no confirmed mechanism in which ACS occurs it is commonly agreed that ‘arteriovenous pressure gradient’ theory is the mechanism behind the condition (1)(14)(15)(16). The muscle is made up of compartments separated by connective tissue known as fascia as shown in Figure 2.2 (1). These compartments can be found in many areas of the body such as the leg (17), thigh (18), glutes (19), forearm (20), hands, and feet (1)(21)(22). The most common compartment for ACS is the anterior tibial compartment as shown in Figure 2.2 (23)(24).

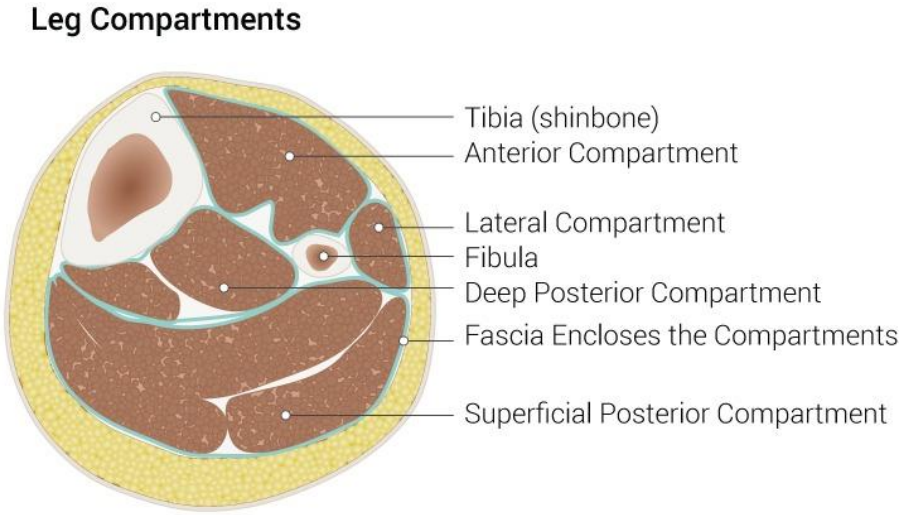

Figure 2.2: Leg compartments from Khan et al. 2024 (25)

The pressure rise in the compartment may be due to either an increase of fluid build-up inside the compartment, known as oedema, or a decrease in the compartment size. The fascia tissue is not elastic enough to allow for the expansion of the compartment therefore the compartmental pressure rises (24). The increased liquid volume in the compartment can come from oedema which can also be a result of medications and pregnancy (26)(27); or hematomas (28). Alternatively, the compartment size can be decreased, typically by tight casts and dressings or any circumferential dressing that restricts the compartment (1)(8)(23).

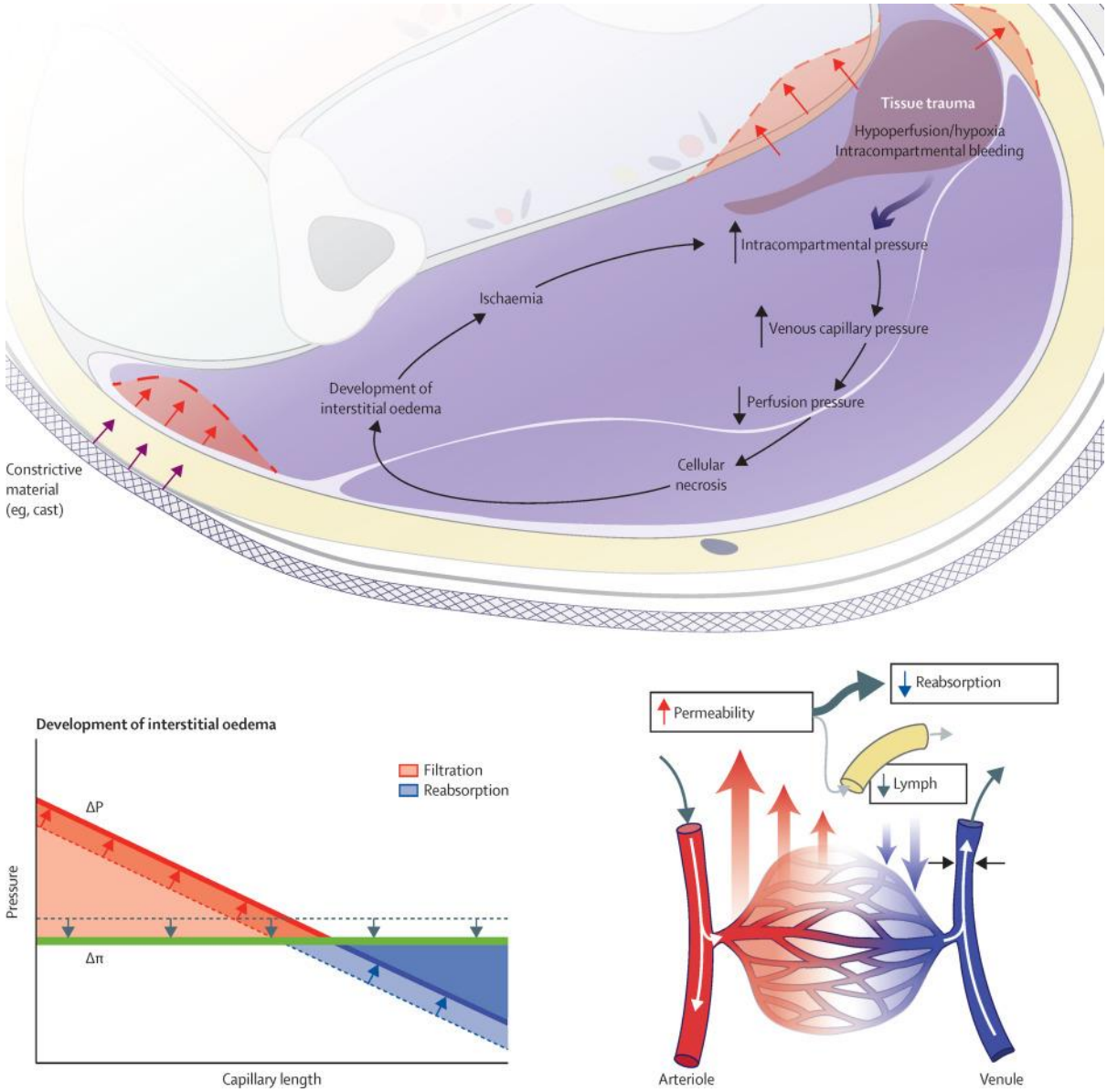

Figure 2.3: Taken from Von Keudell et al. (2012)(1)*. Figure 2.3 shows the cycle of pressure build-up in the compartment and the physiology of ACS.*[2]

[2] [a] Reprinted, The Lancet, Volume 386, Issue 10000, Arvind G von Keudell,Michael J Weaver,Paul T Appleton,Donald S Bae,George S M Dyer,Marilyn Heng,Jesse B Jupiter,Mark S Vrahas from Diagnosis and treatment of acute extremity compartment syndrome, P1299-1310., Copyright (2015), with permission from Elsevier Also Lancet special credit - "Reprinted from The Lancet, Vol 386. Issue 10000, Arvind G von Keudell,Michael J Weaver,Paul T Appleton,Donald S Bae,George S M Dyer,Marilyn Heng,Jesse B Jupiter,Mark S Vrahas from Diagnosis and treatment of acute extremity compartment syndrome P1299-1310 with permission from Elsevier."

The increased intra-compartmental pressure restricts the perfusion in the microvasculature and increases the pressure at the venule end, possibly resulting in their collapse as depicted in Figure 2.3 (1)(8). The permeability of the capillary bed increases, and net filtration increases, thus increasing the interstitial fluid pressure (1). The flow in the lymphatic (drainage) system and capillaries and smaller vessels decreases, decreasing flow in higher-order blood vessels and increasing the hydrostatic pressure (1,8). The onset of ischemia (reduced blood flow) may lead to hypoxemia, anoxia (the reduction of oxygen), and cell necrosis (cell death) (1). Hypoxemia reduces ATP (adenosine triphosphate) production and the sodium/potassium ATP channels close, resulting in the movement of chloride ions into the compartment. Due to osmosis water moves into the compartment leading to swelling and further necrosis, in a positive feedback loop (1). After 6-12 h cell necrosis is thought to be irreversible due to ischemia, despite a third of cases having cell necrosis 3-4 h after trauma highlighting how rapidly a diagnosis is needed (1)(23). This difference may be due to the variation in compartment size and location, and if the cause of ACS was a fracture, which was found in a 2021 study to not be present in 30% of cases (29)(30)(31).

As the time since injury increases, the risk of irreversible outcomes increases. Nerve damage caused by ACS in the leg may result in contractures, abnormal sensations, and foot drop (24)(1)(32). In the arm, muscle fibrosis, reduced motor ability and sensation in the hand, and clawing in response to damage to the median nerve may occur (1)(24)(33). Furthermore, if ACS is left undiagnosed, muscle death, extreme pain, and paralysis may occur, resulting in the need for amputation (34).

As the pressure is released reperfusion injuries can occur. After ischemia, the blood flow returns, rapidly producing free radicals. This, like the closure of the ATP channels, results in the mass movement of chloride ions into the cells. Mitochondrial phosphorylation is disrupted resulting in the cells' inability to maintain their membrane structure. At this stage, fatal complications such as multiple organ failure can occur if a fasciotomy is not performed (1)(35).

2.1.2 Diagnosis

ACS is very difficult to diagnose which is detrimental to both the clinician and patient, with some studies citing misdiagnosis rates as high as 45% (36). The main methods of assessment of ACS are to evaluate the five ‘Ps’; pain, pallor, paraesthesia, paralysis, and pulselessness (4)(37). The addition of poikilothermia, the inability to regulate body temperature, was also suggested by Tran *et al*., 2020 (6). However, this method of assessment is generally used with caution as the patients' assessment of these symptoms is subjective and the patient may present with a reduced/altered state of consciousness after a traumatic event (1)(38). This is especially important in response to ‘high-energy’ injuries in which painkillers or peripheral nerve blockers may be used (6), or when diagnosing children whose pain tolerance may be immeasurable/unquantifiable (8).

Additionally, the stages at which the symptoms present themselves may be too late to diagnose ACS without loss of motor function and thus may still result in legal challenges (4). The measure of pulselessness would already present a reduced blood flow and a decreased ATP (adenosine triphosphate) supply- used to provide

the cells with energy. Paralysis is a late symptom of ACS and is irreversible, regardless of whether the fasciotomy is performed (4).

In children, it is more common to assess using the 3 A's, anxiety, agitation, and increasing analgesic requirement (8). The accuracy of using clinical signs is debated due to this, therefore, alternative methods such as continuous ICP monitoring may be used. There is some debate around the critical values that should be used for the decision of a fasciotomy and the methods by which ICP monitoring can be done.

Slit catheters, side port needles, wick catheters, and arterial line transducers may be used to measure ICP; however, these present additional problems (1)(8)(32). It is easy for needles and catheters to become blocked by blood clotting which gives inaccurate compartment readings (4)(39). Near-infrared spectroscopy can also be used to measure relative levels of oxyhaemoglobin and deoxyhaemoglobin, perfusion, and compartment pressures (8). It is found that these diagnoses are as accurate as continuous ICP monitoring (1)(8)(40).

In some cases, a compartment pressure threshold of 30 mmHg was used to diagnose ACS, however, this had high levels of inaccuracy (41). Alternative thresholds for diagnosis have been suggested by McQueen and Court-Brown such as using the differential pressure between the interstitial and compartment pressure. In their 1996 study of 116 patients, using a differential pressure of 30 mmHg, there were no missed cases of ACS, significantly improving the diagnosis by 23% (42). Statistics for the number of cases of ACS are typically based on the number of fasciotomies performed, however, this may not necessarily represent the true ACS incidence due to the high misdiagnosis rates (43)(36).

Another influence on the success of diagnosis is the rate at which ACS proceeds. The time taken for ACS to cause irreversible damage is disputed but generally falls between 3-10 hours after injury (1)(8)(38). Furthermore, the speed at which the decision that fasciotomy is performed correlates to the success of the operation. A study of 626 patients by Mullett *et al.*, (2001), showed that the outcome is greater before 12 hours and poor after 24 hours (32). This influences the medical professional's decision and may be false, which leads to several expensive fiscal challenges (8)(44).

The combination of ICP monitoring and clinical signs should be used to diagnose ACS but the diagnosis has no gold standard. The use of biomarkers, biological compounds detectable in the blood, was recently suggested by Osborn *et al.,* 2020, in the early stages of ACS (43)(45).

2.1.3 Microvasculature

Microvascular networks are an integral part of the circulatory transport system in the human body, delivering oxygen and nutrients to the muscular system to allow for movement and to keep the body alive (46). Their damage or dysfunction influences muscle behaviour and can have devastating consequences such as hypoxia (a lack of oxygen) and the release of toxins to the surrounding tissue (46). The microvascular networks consist of venules, capillaries, and arterioles, although the oxygen and nutrient transfer occurs in the capillaries due to the single cell wall, reducing the distance for transport. Each vessel has defining characteristics, such as its wall thickness, composition, and diameter.

Depending on the type of blood vessel; artery, venule, vein, or capillary, the structure varies from 0.5-1 μm wall thickness of a capillary to the 1500 μm thickness of the arteries (47). To determine the mechanics of the blood vessel wall many factors should be considered. Initially, the blood vessel structure should be considered, particularly the elastin protein (stretchiness) and collagen protein (structural) content:

The highly elastic arteries have an inner diameter of 6-10 mm and a wall thickness of 1500 μm (48). This is due to their role in transporting high-pressure oxygenated blood away from the heart. The arteries are well studied due to their measurable size and importance in high-risk conditions such as thrombosis, atherosclerosis, myocardial infarction, and stroke. Blood pressure is measured from the arteries by taking the systolic and diastolic pressure, depending on the heart's filling and emptying process. A control blood pressure for a healthy individual is 120 mmHg (systolic) over 80 mmHg (diastolic) (49). The arterial wall has two layers, an internal and external wall which have different elastin and collagen compositions (48). The internal wall is 24.5% elastin and 37% collagen, whereas the outer wall is 2.5% elastin and 77.5% collagen (48). The cell composition of the wall is 33.5% smooth muscle cells. The wall shear stress within the artery can be estimated at 1-2 Pa (48). If there is an increase in the interstitial pressure, as seen in ACS or otherwise, the pressure within the artery is likely to be high enough to prevent collapse (50).

The arterioles, that connect the artery to the capillary have a smaller diameter and wall thickness, 1-6 mm and 125-800 μm, respectively. The outer wall consists of 2% elastin and 70% collagen- similar to the artery (48). Whereas the inner wall consists of 10% elastin and 7% collagen and overall 50% smooth muscle cells, higher than that of the artery. The mean pressure within the arterioles is 72 mmHg (48).

The capillary has the smallest diameter, 10 μm, which allows for the distance of one red blood cell within the inner lumen of the vessel. The wall thickness is also small at one endothelial cell thick, 0.5-1 μm (48). This allows for the shortest distance for mass transfer from the blood to the interstitial area and cells. The mean capillary pressure is 35-15 mmHg (47-20 mbar, 4700 Pa- 2000 Pa) which varies depending on the length and the resistance of the capillary in the network. The wall shear stress in the capillary ranges from 0.1-9.5 Pa (48). Further to this, the capillaries can be separated further into fenestrated, sinusoidal, and continuous depending on the pores in their endothelial linings as shown in Figure 2.4 (51).

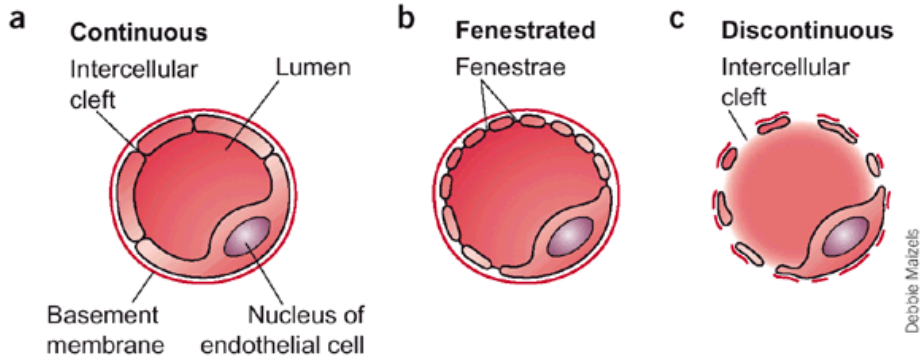

Figure 2.4: Capillary wall linings taken from Cleaver and Melton, 2003 (52)

Reproduced with permission from SpringerNature

The venule then connects the capillary to the vein and has a 1-6 mm diameter and a 40-500 μm wall thickness, again with an inner and outer layer (48). The outer layer is 64% collagen and the inner layer is 1.5% elastin and 12% collagen (48). The venules also have the highest smooth muscle cell percentage at 60.5%. The mean venule pressure is 20 mmHg (48).

The vein removes the deoxygenated blood away from the tissues towards the heart and accounts for approximately 80% of blood volume at any moment (50). It has a 6-15 mm lumen and throughout the veins are valves to maintain the direction of flow. The veins also have an inner and outer layer, the outer layer consists of 2% elastin and 70% collagen, and the inner layer consists of 10% elastin and 7% collagen. The mean vein pressure is 15 mmHg. The wall shear stress in the vein can be estimated at 0.1-0.6 Pa (48).

Microvascular Networks and Murray's Law

The capillary networks are complicated 3D structural networks of heavily branched vessels connected in the closed-circuit circulatory system. Many mechanisms have been considered and investigated into how blood flow networks become optimised; derived from fundamental transport equations such as the Navier-Stokes Equation, Murray's Law, the elastic tube theory, and shear-induced remodelling (53). Young estimated the branching required to get from the aorta to the capillary being 29 bifurcations at 1.26: 1 ratio of diameter of parent vessel to daughter vessel (54).

The branching of capillaries is an essential component of the microvasculature to ensure the delivery of nutrients and oxygen into tissues throughout the body. Such structures enable the delivery of nutrients and removal of waste materials at a suitable rate with minimal pressure losses. The glycocalyx, a layer of endothelial cells around the capillary circumference, is a key component over which the diffusion of these nutrients occurs (5).

In vivo, it is seen that capillaries branch in different manners such as side branching, and following Murray's law as well as rearrangements around obstructions (55)(56).

Murray's law is derived from the energy cost of pumping blood vs the energy cost of the blood lost due to friction and transfer (57). This results in a network with the minimum pressure losses whilst maintaining a shear stress suitable for mass transport across the endothelial layer. Murray's law assumes that the flow is steady state, which is the case in the capillaries at the small scale but is not applicable at higher order blood vessels such as the veins or arteries in which there is pulsatile flow. Murray's law is defined by Equations 2.1-2.3:

$$D_1^3 = D_2^3 + D_3^3 \tag{2.1}$$

Where (55):

$$\cos \alpha_1 = \frac{D_1^4 + D_2^4 - (D_1^3 - D_2^3)^{\frac{4}{3}}}{2D_1^2 D_2^2} \tag{2.2}$$

$$\cos \alpha_2 = \frac{D_2^4 + D_3^4 - (D_2^3 - D_3^3)^{\frac{4}{3}}}{2D_2^2 D_3^2} \tag{2.3}$$

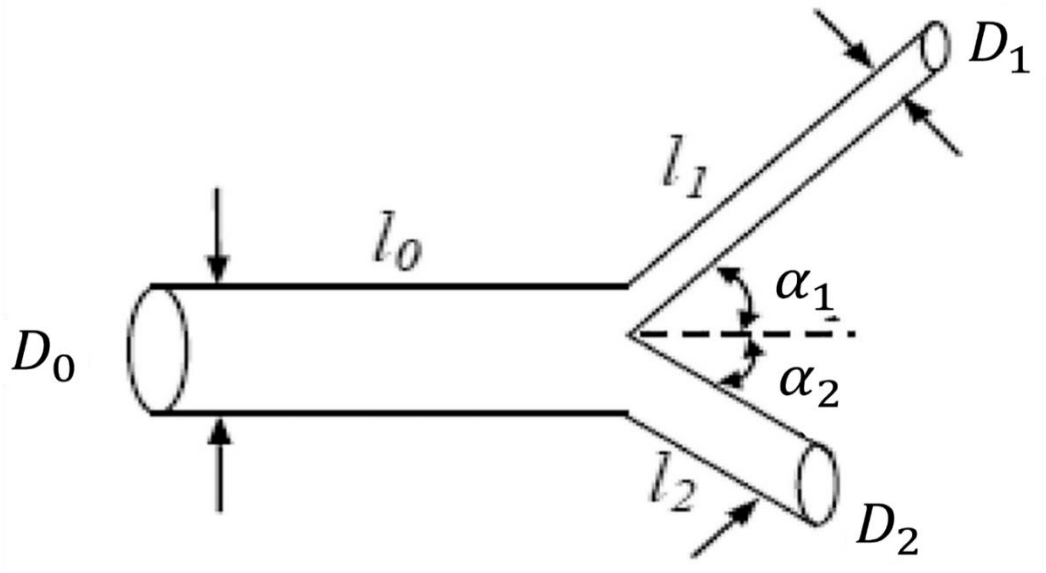

Figure 2.5 Representation of a branched vessel with labelling for Murray's Law adapted from Chen et al. 2020 (58)

In the capillaries, there are many important hydrodynamic phenomena, both the maintenance of a steady state flow at a constant pressure, consistent shear stress on the vessel walls, and a low enough velocity to facilitate the diffusion of molecules across the glycocalyx layer. This is affected by the blood pressure, resistance, and diffusion by the pressure and concentration gradients across the endothelial layer. Interestingly, the radius is of great importance here as the dependence of the flow is inversely proportional to the dependence of diffusion on the radius (54). Therefore, there is an optimum point at which the pressure is maintained and there is a maximum rate of diffusion. This needs to be done where there is a low enough flow rate for diffusion across the wall, but a fast enough pressure-driven flow rate to maintain a gradient of nutrients across the wall.

In vivo the competing phenomena of blood flow as pumped from the heart to transfer of nutrients needs to be kept homeostatic (in a state of balance), however, this will change when trauma conditions such as Acute Compartment Syndrome occur (35). The maintenance of the transfer of nutrients across the glycocalyx layer is essential, and in a state of low blood flow, this transfer becomes dysregulated, known as ischemia, which is seen in Acute Compartment Syndrome (35). When ischemia begins, the release of biomarkers changes, due to debated mechanisms, one of which being shear stress changes (59)(43). If microvascular dysfunction occurs, any flow change through branching may affect the downstream wall shear stress and thus change the range of biomarkers released.

Wall Shear Stress

The wall shear stress throughout the microvasculature changes based on many factors such as geometry, branching, pressure, and specific anatomical features. Although it is assumed that wall shear stress of the blood vessels can be calculated using Newton's Law of viscosity and the Hagen-Poiseuille Equation for pressure drop in a laminar flow, these values do not match the values for *in vivo* given in the literature for some vessels as shown in Figure 2.6 (60). These values are indicative, and each vessel has a large range quoted throughout the literature: 10-70 dyn/cm^2 for arteries, 1-6 dyn/cm^2 for veins, and 1-95 dyn/cm^2 for capillaries (60)(61).

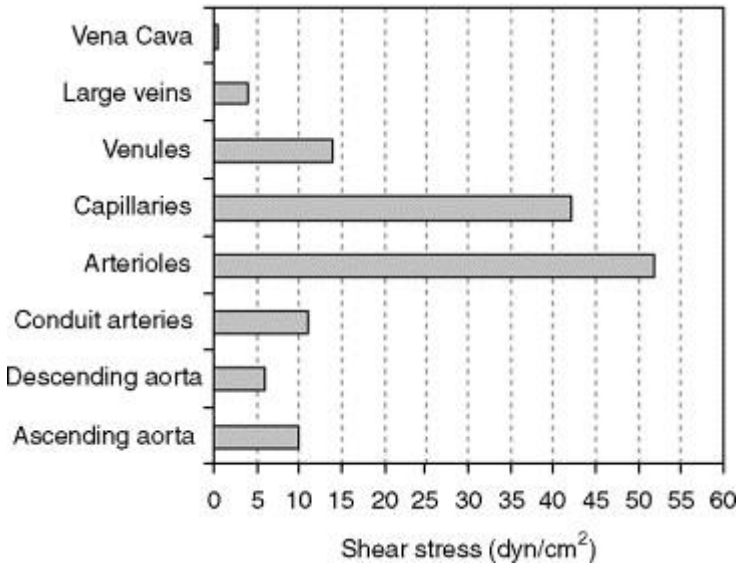

Figure 2.6: Shear stress values for blood vessels (60) *(1 dyn/cm^2 =0.1 Pa)*[3]

[3] Reprinted from International journal of cardiology, 113, 1, Theodore G. Papaioannou,Emmanouil N. Karatzis,Manolis Vavuranakis,John P. Lekakis,Christodoulos Stefanadis Assessment of vascular wall shear stress and implications for atherosclerotic disease, 7, Copyright (2006), with permission from Elsevier [credit - "Reprinted from The Lancet, Vol. number, Author(s), Title of article, Pages No., Copyright (2006), with permission from Elsevier."

In arteries, this could be due to changes in the vessel's geometry such as vasodilation and constriction controlled by biomarkers, such as nitric oxide and prostacyclin, released by the endothelium (62). During vasodilation, the smooth muscle cells relax and further smooth out decreasing resistance and reducing the shear stress. Additionally, venous flow is regulated by valves, which prevent backflow and maintain a pressure gradient along the vein. The valve opening and closing create small, localised pressure differentials which prevent shear stress from building up on the walls and reducing the velocity. Changes in wall shear stress combined with blood pressure on endothelial cells are known to change cell behaviour such as phenotype, and biomarker release perhaps leading to a criterion for diagnosis of microvascular dysfunction as suggested by Osborn *et al.*, 2014, (43) and Vasanthi *et al.*, 2024 (5).

2.2 *In Vitro* Microfluidics Models, Measurements and *In Silico* Modelling

2.2.1 Microtechnology and Lab-on-a-Chip

Microfluidics can be described as the study of flows that are lower in instantaneous volume, from 10^{-9} to 10^{-18} L of fluid (43). Microfluidics is a developing area that can be used to investigate a wide range of biological and non-biological topics including, but not limited to, model organ systems, immunoassays, DNA analysis, and chemical reaction rates (41)(42). As seen in Figure 2.7, lab-on-a-chip devices are at the microscale, which gives many advantages when designing devices for rapid diagnosis such as the reduced mass transfer distances, meaning that reactions occur

quickly, higher throughputs, the ability to quickly perform toxicity assays and reduced animal testing (44).

Figure 2.7: Lung-on-a-chip model from Wyss Institute for Biologically Inspired Engineering, Harvard (63) *Image redacted for copyright*

Lab-on-a-chip models have been used to investigate and model vascular dysfunction and a range of cardiovascular diseases utilising microfluidic systems thus allowing for measurement in 3D. Conditions affecting vascular function such as deep vein thrombosis, DVT (64), atherosclerosis (65), and localised drug delivery for tumours (66) have been investigated using these techniques. Additionally, cells can be integrated into these designs when created using a biocompatible scaffold or with the addition of a hydrogel network. Advances in lab-on-a-chip modelling, such as the integration of sensors and high geometric control are especially advantageous when creating models at this resolution.

Manufacture

Photolithography is the predominant mechanism for creating lab-on-a-chip models, allowing for intricate and high-resolution designs. Alternative methods to lithography can also be used in the fabrication of microfluidic devices but are less common such as microwire moulding and stereolithography (67). Microfluidic mould printing can be done by laserjet printers, inkjet/ solid ink printers, or 3D printers. Laserjet printers are limited in their resolution whereas 3D printers have a high particle size, limiting their accuracy (68). The benefits of these systems are outweighed by the cost, therefore,

lithographic techniques are used. Furthermore, methods such as microwire moulding, micro-milling, and direct laser plotting can be used, however, these methods have further limitations but can create different cross-sectional geometries (68). From the moulds created by photolithography- soft lithography is used to fill the mould with a polymer creating the channel. This is summarised in Figure 2.8.

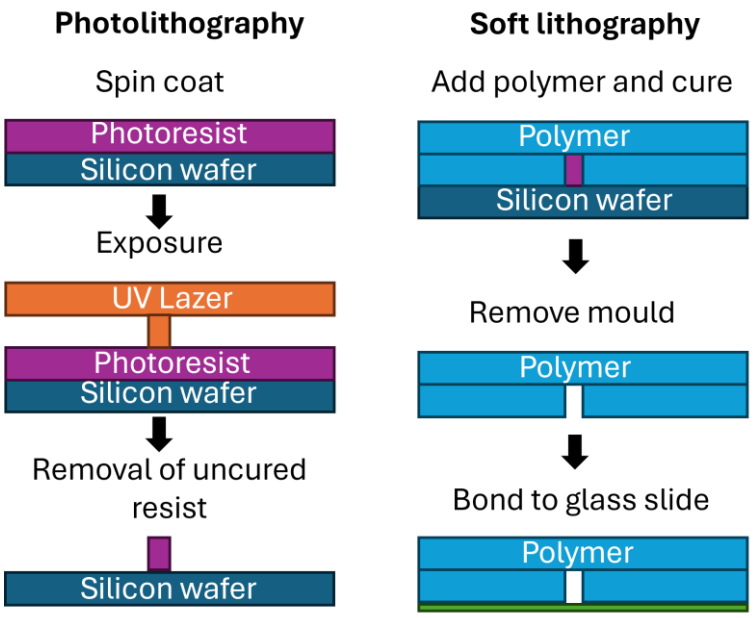

Figure 2.8: Photolithography and soft lithography process depicting the creation of a microfluidic channel

The predominant manufacturing material used in studies of microvasculature is PDMS, polydimethylsiloxane, which can be beneficial due to its advantageous properties although microfluidic devices can be fabricated by a range of different materials such as silicon, glass, paper, and any other polymer (69)(70). PDMS is commonly used due to its biocompatibility, transparency, and ability to manipulate hydrophobicity/ hydrophilicity (71).

PDMS is limited by large evaporation effects, the inability of molecules to attach to the hydrophobic walls (without treatment depending on molecular properties and environment), and incompatibility with non-polar organic solvents (69). PDMS can be beneficial due to its flexibility, with a variable Young's modulus depending on the base-to-curing agent ratio used in polymer production, curing time and temperature, and the ease of fabrication (69)(71)(72). The flexibility of PDMS provides the opportunity to model the deformation of the channel which is seen in microvascular collapse. PDMS is impermeable to water but is permeable to gases which creates controllable conditions suitable for cell culturing (71,73) and is optically transparent to wavelengths of 230-240 nm, which allows for confocal microscopy to be used for analysis (69,71). PDMS is permeable to gases due to the volume around the Si-O bonds (74). This can be both advantageous and disadvantageous depending on the desired usage. Barmaki *et al.*, 2018, created a model to simulate hypoxia, by taking advantage of the gas permeability of PDMS and varying its thickness to control oxygen concentration as well as using oxygen scavengers (48). Surface modification of PDMS can be used to overcome these properties.

Surface Modification

PDMS is hydrophobic with a low surface free energy of 0.02 Nm^{-1} (69), which is advantageous for some applications such as water retention, however, it prevents the connection of other materials (70). To overcome this hydrophobicity, the surface can be treated with oxygen plasma, hydrochloric acid, or coated (75). Furthermore, these treatment methods lead to the irreversible sealing of the microfluidic device and the ability to withstand pressures of up to 345 kPa (71). The sealing of microfluidic

devices can be assisted by polar organic solvents to allow for channel aligning using microscopy without loss of hydrophilicity (69).

2.2.2 Vascular Lab-on-a-Chip Models

Many models have been created to simulate the microvasculature (76)(64)(77)(78)(56), typically focusing on the endothelial linings and properties of the wall looking at angiogenesis, tumour growth, and the blood-brain barrier. A review of current vascular lab-on-a-chip models is summarised in Table 2.1, focusing on the model type, motivation, type of device, dimensions and investigations. It is commonly seen that models are generalised into ‘vessels’, ‘networks’ or are for higher-order vessels such as arteries.

The purpose of these models is to replicate the conditions of the vasculature to expose cell lines and investigate their response of releasing biomarkers, however, there is often less focus on the microfluidic device design when considering the haemodynamic environment than cell behaviour. Despite the impressive cell investigations that are achieved through lab-on-a-chip models there is a lack of experimental techniques used for the quantification of flow behaviour.

Table 2.1: Vascular lab-on-a-chip models

Vascular model	Disease	Device Type and size	Includes cell line	What they are looking at	CFD	Ref.
Blood vessel to tumour	Cancer	Microfluidic height of H=270 μm, L=7000 μm	x	Drug transport	Y Fluent	(66)
Microcapillary	x	H=150 μm,	Y HUVEC	Creation of blood networks	x	(79)
Vessel network	Hereditary haemorrhagic telangiectasia	x	Y hiPSCs	Biomarkers	x	(80)

Vascular model	Disease	Device Type and size	Includes cell line	What they are looking at	CFD	Ref.
'Blood vessel'	'Several vascular diseases'	x	Y hiPSCs	Biomarkers	x	(81)
'Vessel'	Plate aggregation and coagulation	height 200 μm, width 5 mm, length 50 mm	Y HUVECs	Biomarkers	x	(82)
'Organoid'	Hypoxia	2.6 mm in radius, 2 mm in height	Y HUVECs	Biomarkers	Y FEM	(83)
Microvascular network	Blood behaviour	10-75 μm	X	Flow, shear stress,	Y	(84)
Microvascular network	Transit time distribution, red blood cell movement	x	x	Transit time distributions	Y particle tracking	(85)
Vascular endothelium	Histamine-induced microvascular hyperpermeability	X Chamber	Y HMVECs HDFs	Permeability	x	(86)
Microvascular hepatic tumour	Cancer	3.5 cm	x	Particle count/ transport	x	(87)
Rat mesenchymal culture model	Angiogenesis	x	Rat mesenchymal cells	biomarkers	x	(88)
Parallel endothelialised vessels	Vasculogenesis Cyclic stretch, shear forces, ECM hydrogel stiffness	150-200 μm	HUVECs	Vascularisation	x	(89)
PDMS	Arteriovenous malformation	90 to 120 μm (h) 1500 μm (w)	HUVEC	Biomarkers	x	(90)
Flow chamber	Platelet activation	(h) 50 μm, (w) 3.0 mm, (l) 30 mm	HUVEC	Biomarkers	X	(82)
Body on a chip PDMS	Toxicology	X	HUVEC	Biomarkers	X	(79)
Stereolithography produced microfluidic device	Tumour-lymphatic microenvironment	x	Dermal LECs	Biomarkers	CFD, COMSOL	(91)
PDMS with pressurisation to make a 'heartbeat'	Beating heart on a chip	x	Cardiac cells on fibrin gel	Biomarkers	CFD-FEM	(92)
PDMS microfluidic device	Fibrosis	x	hiPSC-Ecs + primary human cardiac and lung fibroblasts	Biomarkers	x	(93)

2.3 Microtechnology Applications for Replication of ACS Pathophysiology

Throughout the literature, models are focused predominantly on higher-order blood vessels such as the arteries, arterioles, and veins, however, there is little focus on the capillary networks and flow behaviour during microvascular dysfunction. Previously, due to their size, replica *in vitro* models at the dimensions of the capillary were not created and animal models were used- however due to changes in cost, scientific development, and ethics; research is being driven away from animal models, and thus alternative microvascular models need creation (51). This could be due to many factors such as perceived biological importance, availability of *in vivo* data, and experimental modelling capabilities at the lower geometric scale, limiting resolution. However, this presents a gap in the literature for arguably the most important vessel in the circulatory system and also the most numerous blood vessels in the cardiovascular system in which the principle and ultimate role of metabolic transfer occurs (94). The creation of a simple, experimentally measurable, and scalable lab-on-a-chip model of the vasculature would aid in understanding the relative effects of scaling.

Furthermore, models of the microvasculature involving cell lines must be biocompatible which creates further limitations for their creation when not using PDMS. The geometry of these designs is seen to be either measured with the utmost importance or neglected depending on the application. In structures where specific hydrodynamic phenomena are being investigated, the geometry is tailored to meet this, such as through the addition of valves and pumps. This is done particularly well in Marsano *et al.*, (92), creating a beating heart on a chip, and in Schofield *et al.*,

(64), with the creation of flexible valves *in situ* mimicking that of valves in veins. However, in some models, hydrodynamics are ignored, which will make the model less replicable of the *in vivo* environment. To improve lab-on-a-chip models, the functionality of the microfluidic device should be designed with physiological relevance to the specific vasculature of interest.

Where particular variables of interest cannot be directly experimentally measured, such as that of shear stress, *in silico* models may be employed. These *in silico* models are good additions to the biological work and provide estimates of fluid behaviour, however, they are based on many approximations, and 'perfect' behaviour cannot be validated without some experimental measurements. Therefore, it is important when making a lab-on-a-chip model in combination with an *in-silico* model, particularly for the investigation of fluid behaviour, that all variables are quantified as depicted in Figure 2.9, which has not previously been done for capillary networks. This presents many challenges as the use of some materials and techniques may interrupt or prevent biological work or vice versa. The combination of these variables would allow for the creation of a successful *in vitro* model of microvascular collapse.

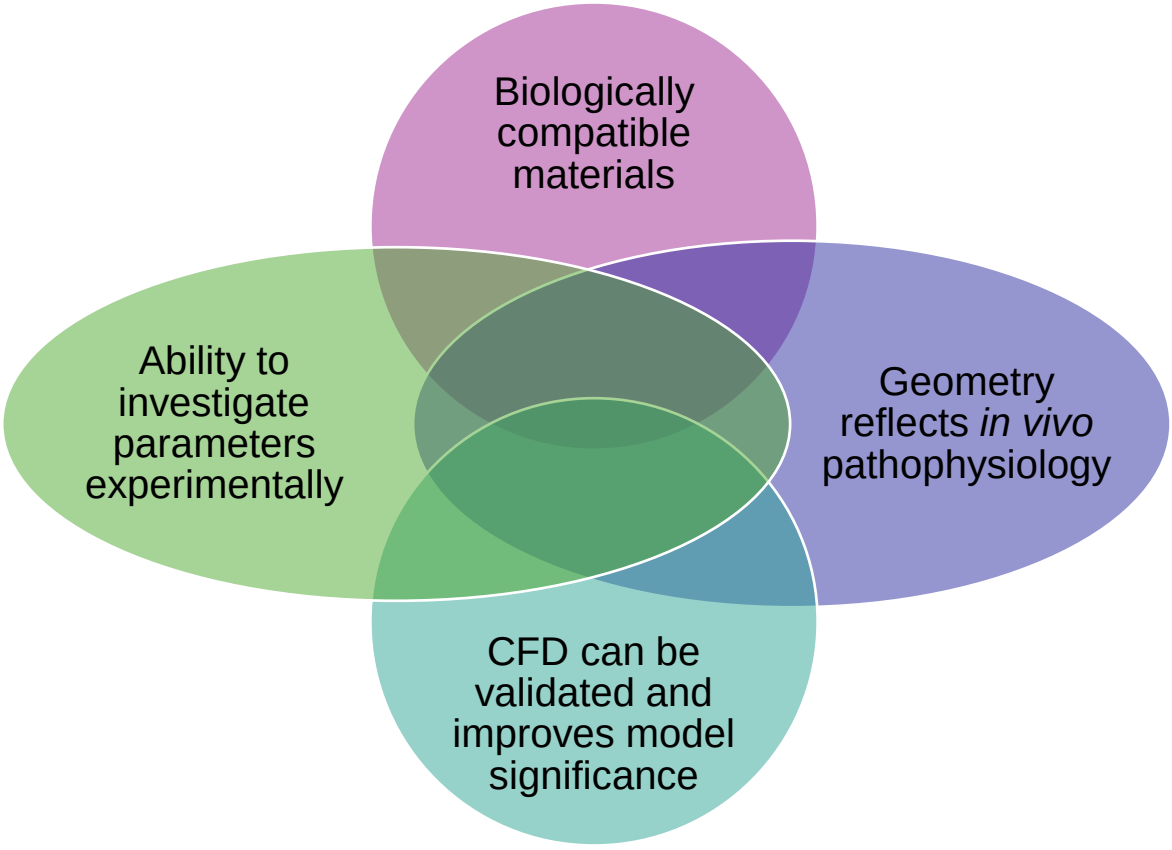

Figure 2.9: Important considerations for the model of microvascular collapse

Limitations

Blood vessel models are often scaled up from the *in vivo* diameter of a capillary, venule, or arteriole. The resolution of microfluidic devices is limited to the resolution of the production process machinery (5 nm to 5 μm) and may present variations in accuracy ranging from 100 nm to 3 μm (95). In designs where a mould technique is used, geometries are limited as no undercuts through the design are allowed, which limits the cross-section of the device to rectangles and trapeziums, etc., but prevents the creation of physiologically relevant circular cross-sections without further modification (96). In some cases, semi-circular cross-sectional channels can be

aligned but their alignment is difficult. Alternatively, microwire moulding may be used (97).

To develop models where expensive fabrication processes/ equipment are required the research area must have enough significance to warrant its investigation at a high cost. In high-incidence disease areas such as cancer, DVT, and atherosclerosis these models may be investigated thoroughly with many variations in design, however, for conditions with a lower incidence but extreme outcomes, such as Acute Compartment Syndrome these models are the first of their kind and the creation of complex circular geometries is inaccessible. The microtechnology used in their creation, particularly concerning the recreation of physiologically relevant conditions was not available in vascular healthcare applications before, and thus specific modifications should be drawn upon by reviewing a wider range of literature of lab-on-a-chip models, BioMEMS and microfluidic techniques.

To begin to build *in vitro- in vivo* and even *in silico* correlations to give scope for diagnosis, understanding and mimicking the pathophysiology of disease states becomes increasingly important when creating microfluidic *in vitro* models.

Geometric Design of Blood Flow Models

Geometric designs of microfluidic devices should be thoroughly considered to create a replicable environment and physiologically relevant hydrodynamics in the microfluidic device. Throughout the literature, many variations of geometric design are considered, with different channel diameters, cross-sections, lengths, and branchings, in addition to modifications of the internal surface with successful results. Duchamp *et al.*, 2019, used templating to create PDMS devices mimicking the microvasculature, followed by laser ablation to create pores for the seeding of

endothelial cells. The model was used to simulate tumour angiogenesis with success as shown in Figure 2.10 (50).

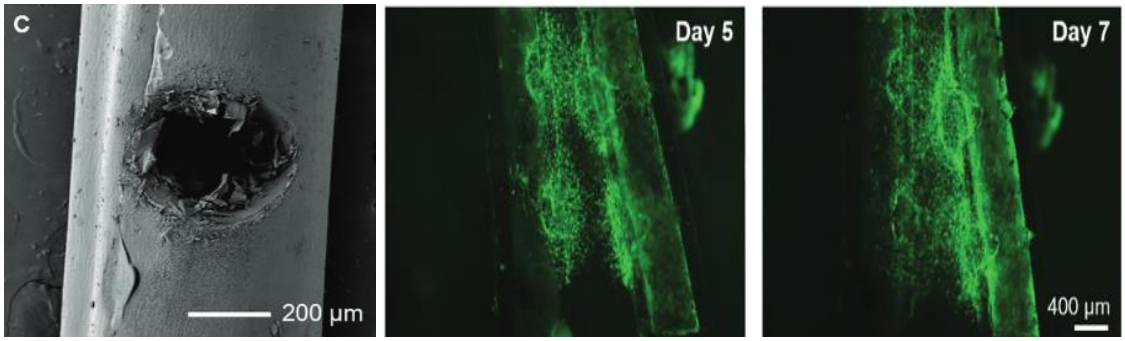

Figure 2.10: Laser-ablated PDMS microchannels used for the growth of cells simulating tumour angiogenesis with successful angiogenesis by day 7 from Duchamp et al. 2019 (56)*.*

Sivarapatna *et al.*, 2017, grew microvascular networks using PDMS and human-induced pluripotent stem cells, hiPSCs, and measured the effect of shear stress on the cells from 0.01-0.25 N/m^2. Immunofluorescence was used to analyse the phenotype and nitric oxide, NO, regulation with the results successfully mimicking *in vivo* NO production, rearrangement, and phenotypic changes (51).

Network and Branching Models

Another geometric factor often considered is the influence of flow in networks and branched models. This has been done in many ways with varying levels of success as summarised in Table 2.2.

Table 2.2: Network and branched models of microvasculature

Network model	Of	Branching	Findings	How	Ref.
Capillary network	Water capillary network	Murray's	Growth can be predicted using capillarity of	MATLAB	(98)

Network model	Of	Branching	Findings	How	Ref.
			max flowrate		
Capillary network of frogs	Frogs (Rana pipiens)	Measured	Path length 3.56 mm av +/- 1.6	Injection with microfil	(99)
Coronary microvasculature	Full vascular model of the heart	Determined by model	Created a model for in vitro in vivo correlations	Computational model	(100)
Cerebral blood circulation in capillary network	Blood network and influence of endothelial surface layer	Not considered	Model includes endothelial surface layer	Finite Element	(101)
Bifurcating microchannel	Blood flow	T junction	Haematocrit distribution depends on branching	Experimental, empirical, and CFD models	(102)
Branching network	Blood flow	Micronetwork T junctions	Varies based on branching	Empirical	(103)
Bifurcated Carotid artery	Blood flow	T junction	Low wall shear stress due to stenosis	Finite Element	(104)
Coronary microcirculation	Blood flow	Geometry collected via invasive coronary angiography	Defined coronary microvascular dysfunction	CFD-based fractional flow reserve	(105)
Microvessels	Blood flow	Simple vessel and sutured	Shear stress rate was underpredicted	Finite Volume ANSYS Fluent	(106)
Blood vessel	Blood flow	Bifurcation	There is energy loss at the bifurcation, the angle does not affect flow resistance	Finite volume Ansys Fluent	(107)
Artery branches	Blood flow	Murray’s law model and Invasive arterial studies	Variation of optimal exponent from Murray’s law model	Novel CFD model	(108)

The literature concludes that for most vascular models either straight ‘simple’ channels are used and T-junctions, often seen in microfluidics are predominant with some bifurcations followed by Murray’s law-specific branching. More developed models may use area-specific techniques such as fundus photography or coronary angiography, or in animal studies, such as in Plyley *et al.*, 1976, network geometries were taken from capillary networks of frogs through injecting the network with microfil (99). Li *et al.*, 2017, developed a PDMS and glass hydride microfluidic device to aid in the diagnosis of retinopathy. The researchers used fundus photography, the technique of photographing the retina of the eye, to mimic the shape of the microvascular network. This technique, limited to optometry, is a successful way of analysing the geometry of the microvascular network in the eye but is limited in its application. Endothelial cells and peripheral blood mononuclear cells, PBMC, were grown in the lab-on-a-chip model and the effect of tumour necrosis factor, TNF-a, on cell adhesion, was measured to create a correlation. At 10 ng/mL at 5 µL/min of TNF-a for 18 hours the number of adherent PBMCs was significantly higher than with no TNF-a or when applied at 10 µL/min which makes the device design such as branching and resultant shear stress able to replicate and help aid in the diagnosis of diabetic retinopathy (49).

Priyadarshani *et al.*, 2018, further developed the microvasculature networks by mimicking the geometry and branching of the microvasculature using a leaf following Murray's law (76)(45). Three orders of channel were formed, 600, 400, and 30 µm, and could be formed into microfluidic channels that remained open under pressure. The branching is likely to affect the flow direction, shear, and cell anchorage, therefore it must be included in the design of PDMS microvasculature models. In the

absence of *in vivo* data further models are created following Murray's law and bifurcations, and some networks consider the effect of the branching angle (107).

Deformation

Blood vessels are inherently flexible due to their outer wall structure as described in Section 2.1.3. The variable Young's modulus of PDMS can be manipulated to create a deformable wall system using micropumps to replicate microvascular collapse as is seen with ACS (109).

The Young's modulus of elastin was found to be 0.65 MPa and of collagen 550 MPa, however, it cannot be assumed that the Young's modulus of the blood vessel is determined using calculations from these compositions (54)(110). This is due to the arrangements of the collagen and elastin in each vessel which aligns differently giving the vessel different flexural properties. It is also dependent on the cyclic stress the blood vessel has endured. Measuring the Young's modulus of the vessel is difficult also as the stress on the vessel is dependent on the pressures surrounding the vessel walls (48).

The vessel walls however are known to be flexible/ deformable/ collapsible. It is seen in Acute Compartment Syndrome that there is venous-capillary collapse due to the increased interstitial pressure and decreased blood pressure explained in § 2.1.1. Furthermore, blood vessel walls are often modelled using Hooke's law, Equation 2.4, but at larger stresses, there is non-linearity in their mechanical response and the vessel is predicted to behave due to Fung's constitutive equation of hyperelasticity, Equation 2.5 (111).

$$F = -k \, . \, x \tag{2.4}$$

Where F is the force, k is the spring constant and x is the extension.

$$\sigma(t) = \int_0^t G(t-t') \frac{d\sigma^e[\lambda(t')]}{d\lambda} \frac{d\lambda(t')}{dt'} dt' \tag{2.5}$$

Where σ is the stress, σ^e, is the elastic response, λ is the extension ratio and $G(t)$ is a relaxation function (112).

The blood vessel has tension in the wall due to its elastic properties through elastin fibres which are typically modelled using a function of Hooke's' law at lower stress and strains, however, it is seen that for mammalian vessels, such as the vena cava, Hooke's' law is not obeyed and this disagreement is more likely for smaller order vessels such as capillaries (113). Burton 1950, suggests a Laplacian relationship between the tension, pressure, and radius of the capillary, Equation 2.6 (113).

$$\frac{dT}{dR} = \frac{E}{R_o} \tag{2.6}$$

Where *T* is the total tension, R_o is the unstretched radius, *R is* the radius and *E* is the elastic constant (113). There will also be tension due to the smooth muscle cells which can tense or relax depending on the state of vasodilation or constriction and interfacial tension from the fluid to the wall (113). The total critical tension, *Tc*, on the system can be back-calculated from the critical closing pressure, *Pc,* and closing radius.

$$Tc = PcRc \tag{2.7}$$

The shape of the cross-section of the capillary depends heavily on the pressure applied externally relative to the internal pressure known as the transmural pressure. When the internal pressure is low the tube cross-section relies on its wall structure to

maintain a circular cross-section which may only be achieved when the volume and transmural pressure are high, as before this we see an oval or collapsed/ deformed shape as the wall may not support itself as shown in Figure 2.11 (114).

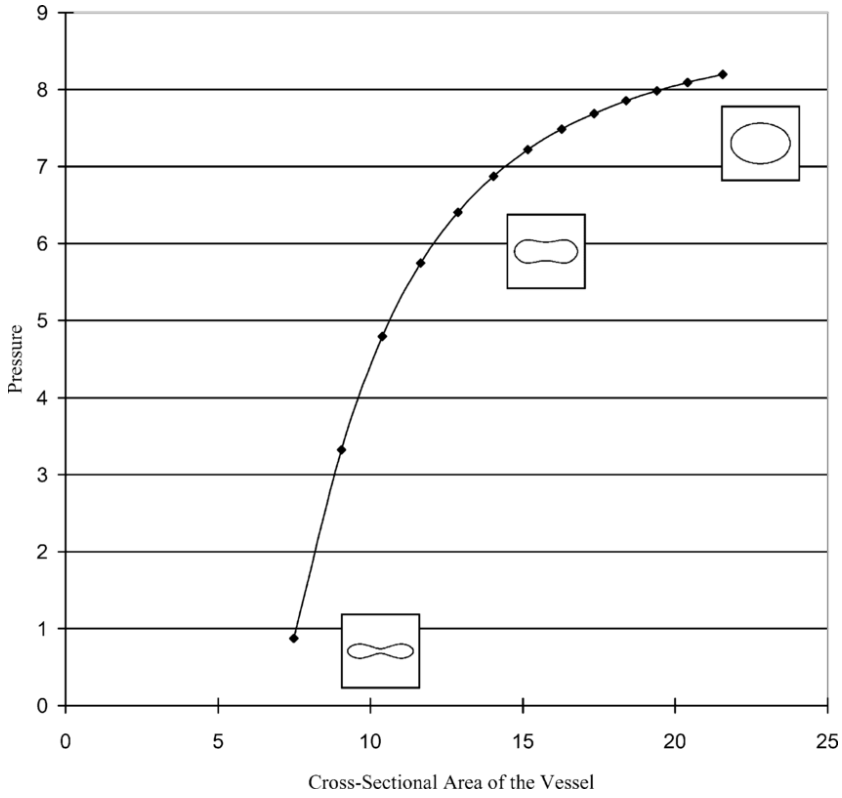

Figure 2.11: Pressure vs cross-sectional area for an elastic tube modelling a blood vessel taken from Chow, 2006 (50) [4] *https://pubmed.ncbi.nlm.nih.gov/16699834/*

When the cross-section has become circular there is a trade-off between the wall structure and the pressure difference across the wall before radial deformation can be seen. In veins, we have a low-pressure difference as interstitial pressure is estimated at 10 mmHg and venous pressure is 15 mmHg so with the same order of magnitude internal pressure increase, the vessel is likely to show a deformation,

[4] Use with permission from .W.Chow, A simple model for the two dimensional blood flow in the collapse of veins, Journal of Mathematical Biology, 52(6), 733-44, 2006, Springer Nature"

however, this may not be true for arteries due to their structural properties discussed in Section 2.1.3 (48).

Models of Deformation

Models of deformable tubing date back to the 1900s when large-scale rigs with sections of deformable tubing were studied. Holt, 1941, created an experimental setup to understand the venous flow, in which a section of deformable tubing was attached vertically to two rigid tubes, and the flow rate through the setup changed from 0-20 mL/s and ran at different inclinations from 0-90 degrees. The flow was measured using a plethysmograph. The results found that the inclusion of a collapsible tube does not affect the flow rate which is to be expected, due to the maintenance of continuity (115). With increasing flow rate the cross-section of the channel increased, as expected and corroborated by Katz, Chen, and Moreno in 1969, but stays constant under constant flow (114). It can thus be assumed that the transmural pressure is the presiding factor of deformation. Katz *et al.*, 1969, used the same setup to model fluid behaviour in deformable channels (114). They developed a model derived from the continuity equation and experimental data achieved using the same setup as Holt. The experiment was carried out at laminar Reynolds numbers and overall proposes a lumped parameter model for pressure and flow in a collapsible tube. Hysteresis was only found at higher flow rates and lower pressures due to oscillations due to elasticity and outlet pressure (114).

It is common for fluid behaviour in flexible/deformable/collapsible vessels to be studied in this manner, known as the Starling resistor, with a large set up of tubing encased in a pressure chamber and attached to rigid tubing at either end typically

with a gravity-driven flow and hydraulic pressure difference generated across the tubing (116). Using this set up valves can be closed before or after the channel to measure the resultant deformation of the channel. However, in this experiment the technique is unrepresentative of the vascular system due to its larger dimensions: 0.6 cm^2 cross-sectional area, 1.23 cm diameter, higher Reynolds numbers 100-1000; and less accurate flow and pressure control. Recent developments in microfluidics allow for microfluidic channels as thin as 50 μm to be constructed to create deformable channels with a more representative flow regime. Experimentally, Weibel *et al.* created a 'pump' style deformation using TWIST valves to overfill regions of channels in a PDMS network (117). The compartments can be pressurised and were used for the delivery of materials in sequence to the device. The ratio of base to curing agent was also altered to change the elastic properties of the PDMS creating an experimentally deformable model.

Furthermore, microfluidic flow and pressure control can be more accurately controlled using syringe pumps and pressure controllers. The study of the flow itself is not limited to mass over time, however, this can be seen as a useful checking tool but can be accurately measured within the deformed cross section using techniques such as micro-PIV, particle image velocimetry, and ghost particle velocimetry, GPV, also to give a spatial velocity distribution (118–120).

2.4 Deformation and Blood Flow Models

There are a few empirical and *in silico* models of deformation and blood flow as summarised in Table 2.3. Chow and Mal, 2006, created a model of 2D blood flow in the collapse of veins, derived from Navier Stokes, Poiseuille's law, and buckling of an

ellipse under the assumption of constant perimeter (50). Similarly, Ghazy *et al.*, 2018, investigated the collapse of blood vessels under high stresses with nonlinear deformable walls using the Fung-type isotropic constitutive equation for the deformation of an ellipse. The model showed that the non-linearity of the blood vessel walls affected the blood flow rates (121).

Table 2.3: Deformable blood flow models

Model	Dimension (1D/2D/3D)	Modelling	Finding	Ref.
Human leg- varicose veins under external pressure	2D	Finite element in ABAQUS	External pressure decreases transmural pressure	(122)
Collapse of veins	2D	Analytical model	Abides by Navier Stokes and continuity. Buckling shapes can be found analytically. Agrees with experimental	(50)
Collapse of blood vessels with non-linear wall material	3D	Analytical and numerical- Fung-type law applied	Buckling shape depends on the nonlinearity of the wall, blood flowrate increases with non-linearity	(121)
Blood flow under standing movement with arterial/ventricular contraction	1D	Empirical	Contractibility increases faster than peripheral resistance	(123)
Self-excited oscillation of blood vessels	2D	Finite difference, multi-block lattice Boltzmann method, momentum exchange coupling, FSI (Fluid-structure interaction)	Oscillation depends on distance, degree, and externally applied pressure	(124)
Blood flow in deformable models	3D	TEPEM and FSI (Transversally enriched pipe element method)	The addition of FSI and using TEPEM is comparable to the FEM model	(125)
Blood flow in the annulus porous region between	2D	Empirical	Relative effect of each parameter	(126)

deformable tubes				
Blood flow in compliant vessels	1D and 3D FSI	Coupled momentum method in Finite Element	Can be used to reduce computing time when estimating shear stress	(127)
Blood flow in elastic vessels	3D	Finite volume	Depends on flow velocity when using CFL condition	(128)

It is seen throughout the literature that the models are based on the Navier-Stokes Equation, the Poiseuille Equation, and continuity, often assuming Newtonian flow (129). The boundary conditions vary, some models use Dirichlet (125), Neumann, resistance, flow rate (130)(123), or pressure (124). The elasticity of the wall is often modelled using spring and dashpot models of Hooke's law (131)(132), or data on distensibility in some earlier models (133). However, almost all these models used computational techniques to model the flow, and this was not coupled with experimental data. Furthermore, blood flow is non-Newtonian- which means that the difference in phenomena due to viscosity needs to be accounted for.

Furthermore, there are many non-biological specific models of flow under collapsible tubings, such as in the Starling resistor and other analytical models, discussed thoroughly in Grotberg and Jensen, 2004 (134). The models use lumped parameter assumptions giving 'ideal' systems which are not the case in biological models due to wide ranges of variation and cell behaviour. This assumption was challenged and investigated through the creation of analytical models with non-linear wall properties by Ghazy *et al.*, 2018, which found that non-linear properties do affect blood flow rates (121). Often, throughout the creation of analytical models of collapse, behaviour is deemed to 'agree with experimental' however, the details of these experiments are absent from the literature or are compared to experimental work completed in a

different setting. For their validation against experimental, *in vivo* data should not be deemed as a direct comparison as there are many other factors, and smaller scale measurements and matching analytical parameters should be created with careful consideration of error. *In vivo* data is better, however, to validate *in silico* models, *in vitro* models provide quantifiable parameters with less variation. However, as most of this research was conducted before the wide accessibility and creation of microfluidic devices there is a gap in the literature for the validation of collapsible microfluidic models representing blood flow behaviour.

2.5 Models of Hydrodynamics in Microfluidics (*in silico*)

In microfluidics, flows of 10^{-9} to 10^{-18} L of fluid are used where the intermolecular distance between the fluid particles is greater than 0.3 nm and thus the fluid is defined as an incompressible continuum (43)(135).

Flows are assumed to abide by macroscopic flow behaviour at scales greater than 10 μm and are governed by continuity and the Navier Stokes equations (2.8, 2.9) below (135).

$$\partial_t \rho + \nabla.(\rho \boldsymbol{v}) = 0 \tag{2.8}$$

$$\rho\left(\frac{\partial \boldsymbol{u}}{\partial t} + \boldsymbol{u}.\nabla \mathrm{u}\right) = -\nabla \mathrm{p} + \nabla.[\mu(\nabla \mathbf{u} + (\nabla \mathbf{u})^{\mathrm{T}})] + \rho \boldsymbol{g} \tag{2.9}$$

Where ∂t is the time derivative, **u** is the velocity field.

Scaling laws can thus be applied to flow behaviour seen in non-microscopic flows. Initially, it is possible to scale the inertial to viscous forces on the fluid using the dimensionless Reynolds number, Equation 2.10.

$$Re = \frac{\rho v d}{\mu} \tag{2.10}$$

Where ρ is the density, v is the velocity, d is the diameter or hydraulic diameter and μ is the dynamic viscosity. In microfluidics, due to the small volumes of liquid and small geometries used, the Reynolds number is often of the order of unity (approaching the Stokes flow regime) and clearly falls into the laminar flow regime (Re < 2000).

In pressure-driven microfluidics, where the flow is laminar, in straight, circular cross-section pipes the flow is known to abide by the Hagen-Poiseuille equation (135).

$$\Delta P = \frac{8\mu L Q}{\pi r^4} \tag{2.11}$$

Starting from an elemental balance the equation for a velocity profile can be derived.

$$\frac{v}{v_{max}} = \left(1 - \frac{r^2}{R^2}\right) \tag{2.12}$$

By integrating this parabolic velocity profile, we can calculate the volumetric flow rate:

$$Q = 2\pi \int_0^R rv dr = \frac{\pi \Delta P}{8\mu L} R^4 \tag{2.13}$$

In rectangular microchannels, similar approaches can be used. Alternatively, the problem can be solved for steady-state, incompressible parallel flow in a square duct in 2D using Equation 2.14 (136)(135).

$$\frac{\partial^2 v}{\partial y^2} + \frac{\partial^2 v}{\partial z^2} = \frac{-\Delta P}{\mu L} \tag{2.14}$$

Using an Eigen function and Fourier series expansion:

$$Q = \frac{4\Delta P h^3 w}{2\mu L}\left(1 - \sum_{n=0}^{\infty} \frac{192}{(2n+1)^5 \pi^5} \frac{h}{w} \tanh\left(\frac{(2n+1)\pi w}{2h}\right)\right) \tag{2.15}$$

For all derivations, the boundary conditions were set to be no slip $v = o$ at $h = 0$ or $h = H$ and $v = 0$ at $w = 0$ and $w = W$. At the centre of the channel, the velocity is at its highest point, Vmax, which can be calculated as $\frac{1}{2}V_{max} = V_{av}$ for cylindrical channels, but changes based on cross sectional geometry and aspect ratio. The flow is incompressible, symmetric around the x-axis, fully developed, and at a steady state. Where n is a positive integer.

When:

$$\frac{h}{w} \ll 1 \tag{2.16}$$

The equation simplifies to:

$$v = \frac{\Delta P h^2}{2\mu L}\left(1 - \frac{w^2}{h^2}\right) \tag{2.17}$$

And thus:

$$Q = \frac{2\Delta P h^3}{3\mu L} \tag{2.18}$$

Alternatively, Equation 2.19 from Tanyeri et al., 2011, can be used for flow in a rectangular channel derived from the Navier Stokes equation with a no-slip condition of $u = 0$ at $w = -w/w$ and $z = 0\ h = 0$ (137).

$$Q = \frac{\Delta P h^4}{12\alpha\eta L}\left(1 - \sum_{n\ odd}^{\propto} \frac{192\alpha}{\pi n^5}\tanh\left(\frac{n\pi}{2\alpha}\right)\right) \tag{2.19}$$

Where α is the aspect ratio of the channel h/w. 3D modelling of microfluidic flow can be done empirically using Equation 2.16 following the work by Tanyeri *et al.*, 2011, as seen in Figure 2.12.

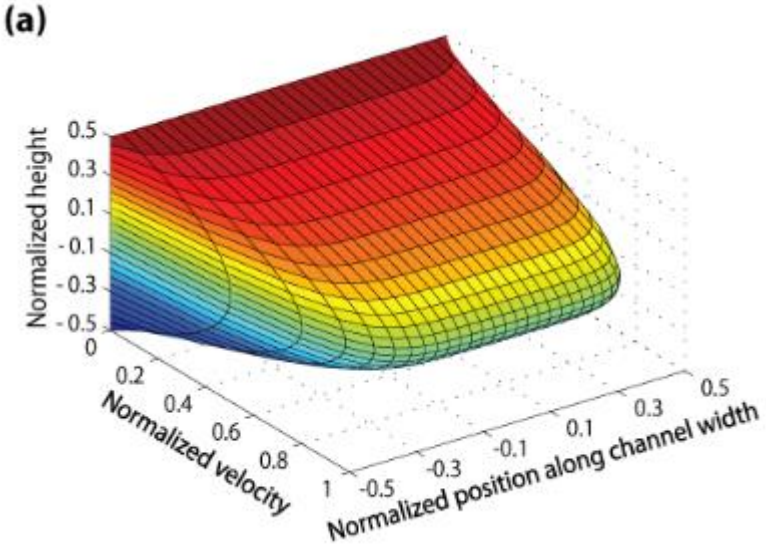

Figure 2.12: A 3D model of a velocity profile distribution from Tanyeri et al., 2011 (137)

2.5.1 Shear Stress

If the fluid is Newtonian, the wall shear stress may calculated using Newton's law of viscosity, Equation 2.20 (138). Where μ is the dynamic viscosity, dv is the change in velocity and dx is the displacement in the x direction as seen in Figure 2.13.

$$\tau_w = \mu \frac{dv}{dx} \tag{2.20}$$

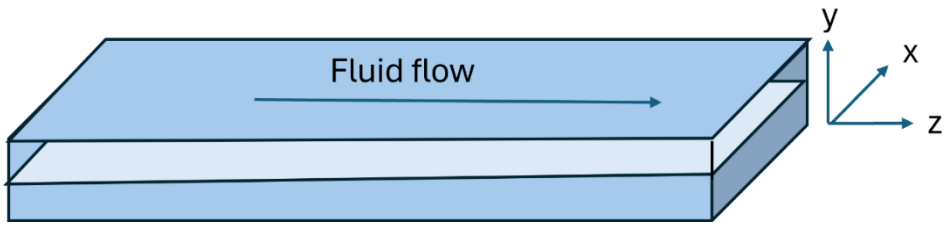

Figure 2.13: Depiction of microfluidic channel labelling axis and fluid flow direction, plane of measurement is light blue area

The values of velocity can be obtained using the aforementioned equations for velocity profiles in rectangular channels or through measurement techniques discussed in Section 2.6. Thus, the parameters that influence the wall shear stress are the fluid viscosity, velocity (determined by pressure in vascular systems), and geometric design. Determination of the value of velocity gradient $\frac{dv}{dx}$ close to the wall is challenging in measurements due to the high resolution needed imparted by the no-slip condition present at the channel wall. This is a feature of the research which later follows.

2.5.2 Numerical Models Including CFD

Throughout this literature review, computational models have been found with varying levels of *in vivo* parameters and employing many computational techniques as described in Table 2.4. which are employed when the complexity in the flow, geometry or fluid rheology precludes use of the simple analytical solutions to the governing Navier Stokes equations described in the above section.

Table 2.4: Modelling techniques and their capabilities (139)

Modelling Type	Uses
Discrete Element Method (DEM)	Motion of many small particles
Boundary Element Method (BEM)	Uses linear partial differentials Fluid mechanics and boundary conditions Used for linear homogenous media
Computational Fluid dynamics (CFD)	Used to model fluid flows and multiphase systems with boundary conditions Employs the Navier Stokes equation in both 2D and 3D
Lattice Boltzmann (LB)	Fluid simulation Navier Stokes Flow modelled as a lattice Fluids in porous media
Smooth Particle Hydrodynamics (SPH)	Continuum media Solid mechanics and fluid flows Mesh-free so employs complex boundary flows Can be hybridized Code for forces on particles
Finite Element Method (FEM)	Structural analysis Heat transfer, mass transfer, and fluid flow Solves partial differential equations
Coarse-grained Molecular Dynamics (CGMD)	The aggregation of molecules on the mesoscale

Impressive models have been produced in modelling blood flow. Alexiadis *et al.*, 2020, combined Discrete Multiphysics (DMP), Smooth Particle Hydrodynamics (SPH), the Lattice Spring Model (LSM), and the Discrete Element Method (DEM) to simulate blood flow as a Newtonian fluid (64,139,140). Ariane *et al.*, 2018, modelled flow and agglomeration in the vasculature using a discrete multi-hybrid system and Smooth Particle Hydrodynamics (140). SPH uses a spring and dashpot coding to model solid particles to model flexural and viscous behaviour. The technique was also used to model solid-liquid flows by Alexiadis, 2015, in combination with CFD and the DEM to measure particles in solution and interparticle interactions (139).

However, most computational models of blood flow within the literature use CFD. CFD encapsulates a wide range of modelling techniques that can be used to validate and develop experimental models of complex behaviour. CFD modelling can be used for a range of applications from models considering the flow as a Newtonian continuum, shear-thinning, or even as individual blood cells. In addition, CFD can be used with fluid-structure interaction (FSI) and the mesh can be carefully controlled for the extraction of variables, which is not seen in mesh-free techniques such as SPH.

In addition to the models discussed throughout the literature review, specific CFD models have been created to model wall shear stress in blood flow applications, as discussed in Table 2.5.

Table 2.5: Computational blood vessel models investigating wall shear stress

Model	Why	How	Dimensions	Comments	Ref.
Singular tube of blood vessel	Margination and adhesion of platelets due to shear	Dissipative particle dynamics DPD	20-micron inner diameter	Modelled blood flow as red blood cells and platelets	(102)
Coronary model	Myocardial perfusion	Multicomponent and fluid-structure interaction Set velocity profile SIMPLE No-slip on walls	Taken from a CT scan	Model as an incompressible, homogenous fluid under rigid walls	(141)
Network model	Distribution of wall shear stress in a microvascular network	3D computational model	Followed *in vivo* data diameters 6-24 micron	Red blood cells Calculated wall shear stress using second-order central differencing in the direction of the specified wall shear stress gradient	(142)
Wall shear stress variability in CFD-MRI coupled simulations of blood flow in	Aortic aneurysm affected by wall shear stress	CFD	Taken from MRI	Good to excellent correlation, small sample size, large ranges	(143)

Model	Why	How	Dimensions	Comments	Ref.
aortas					
Coronary artery CFD for quantification of pressure and wall shear stress	Atherosclerotic disease	3D CFD	CTA images with focal stenosis	Good agreement with patient data however *in vivo* data compared has lots of caveats	(144)
Modelling analysis of blood flow in renal bifurcated artery with stenosis	Renal artery stenosis	CFD finite element	2 mm x 4 mm	Compared to PIV data from the literature	(145)

The CFD model created by Hamidah and Hossain, 2024, although simplified, is a good predictor of many parameters that require investigation such as shear stress and pressure. Shear stress was found to be in the range of *in vivo* data. The model includes pulsatile flow and shear thinning rheology and is validated against experimental data (145). The model can be used as a development tool and although is specific to the renal artery can be used as a basis for the development of other models.

2.6 Measurement Techniques

A range of techniques may be used to perform measurements of the concentration of species or flow within microfluidic devices. Fluorescence may be used for spatial distribution concentration measurements; whilst outlet concentrations can be determined using high-performance liquid chromatography, HPLC, or gas phase chromatography (146). Immunostaining can be used to measure cell behaviour as well as live-dead assays.

Particle tracking techniques such as Particle Image Velocimetry, PIV, or microPIV can be used to measure flow distributions, flow rates, and calculate shear stresses within fluidic devices-with microPIV used for measurement in microfluidic devices. Some examples of flow analysis on the microscale are summarised in Table 2.6. Microparticle image velocimetry is a variation of the PIV technique used to measure velocity profiles in microchannels. It is a non-intrusive technique where the fluid is seeded with particles and the particle movement is measured using a high-speed camera up to 100 cm/s; detecting velocity vectors within the device and thus useful in measuring many fluid phenomena (147). It was detected by Bitsch *et al.*, 2003, using microPIV that there was a 3 μm boundary layer at the wall comprising 21% of the channel dimensions in a laminar flow model (148).

Although PIV and microPIV are the most commonly used techniques for measuring the velocity vectors of flow, recently *ghost particle velocimetry,* GPV, has become a cheaper and more accessible alternative for the assessment of flows in microfluidic devices (119). Riccomi *et al.*, 2018, compared the use of MicroPIV and GPV and found that for low Reynolds number values, GPV gave comparable measures to MicroPIV (50). Schofield *et al.*, 2020, developed a microfluidic model to represent deep vein thrombosis and successfully used GPV to measure vortexing and the accumulation of particles between symmetric and asymmetric valves whilst measuring the Young's modulus of the valve (64).

Table 2.6: Techniques used to analyse flow behaviour on the microscale

Device	Size	Purpose	Technique	CFD	Ref.
Microfluidic	D= 637 µm	Measure the effect of surface roughness on the walls	MicroPIV	Y Fluent	(147)
3D printed	D= 20 or 10 mm	Cardiovascular disease measures changes due to pulsatile flow	Time-resolved PIV	Y CFX	(149)
Rat mesenteric vessels	50-100 µm	Blood flow	Hybrid PIV and PTV	x	(150)
Square microchannel	100 µm	Blood flow and velocity profiles	Micro PIV	x	(151)
Microfluidic model	300 µm	Deep Vein thrombosis	Ghost particle velocimetry	x	(64)
Micro - capillary	28 µm x 360 µm	Boundary layer detection	MicroPIV	x	(148)
Parallel plates	400 mm with accurate measurements to 10 µm	Shear stress	MicroPIV	x	(152)
D shaped microchannel	10-30 µm	Velocity and shear stress	Fluorescent bead tracking	Y CFD	(153)
PDMS T junction	40.7 x 9.9 x 0.85 mm	Shear stress	Fluorescent bead tracking and MicroPIV	x	(118)

2.6.1 Ghost Particle Velocimetry

GPV is a technique developed by Buzzaccaro *et al.* in 2013 as an alternative to micro-PIV using easy access laboratory-based equipment, no laser but an optical microscope, and nano/microparticle solution (154). GPV uses a microparticle dispersion as the fluid- as in particle tracking velocimetry like PIV and micro PIV, but the speckle pattern created through light diffracted through the microparticle

dispersion acts as the tracer, not the particles directly. The speckle pattern is then analysed using the same autocorrelation algorithm as PIV (154). GPV is advantageous for many reasons such as reduced laboratory cost, no colloidal tracers to affect emulsion studies, and the ability to measure on the microscale without the use of a laser (154).

Brunazzi *et al.*, 2018, investigated variations on the setup parameters used in the GPV technique from Buzzaccaro *et al.*, 2013, such as the number of frames and the effects of nanoparticle concentration, and validated its accuracy compared to that of microPIV (119). Following this, GPV has also been used with success to measure flow field behaviour in droplets formed in T junction devices (155), and to investigate flow behaviour in microfluidic devices with valves (64).

For GPV the data extracted is the velocity magnitude and the flow rate is often supplied from the syringe pump measurement and not directly from GPV measurements, excluding in Schofield 2019, where the flow rate is calculated by multiplying the average velocity as measured by GPV by the cross-sectional area of the device (156). GPV is not currently known to have been used for shear stress measurements.

The diameter of the microparticles typically used are 200 nm as this should be less than the diffraction limit, 300 nm, (although the bulb used in these works was a Prior brightfield LDB103, which uses 450 nm, with a 400 nm to 750 nm range) as to not be measured as the tracer but the diffraction of the light (119). The speckle pattern is formed similarly to that of dynamic light scattering, measuring the change in the light

pattern caused by the movement of particles and their relative movement over time, Equation 2.21 (156).

$$\Delta x = v\Delta t \tag{2.21}$$

The images are split into grids with each box being an interrogation area and the movement between these areas over the timestep measured. This process is summarised in Figure 2.14.

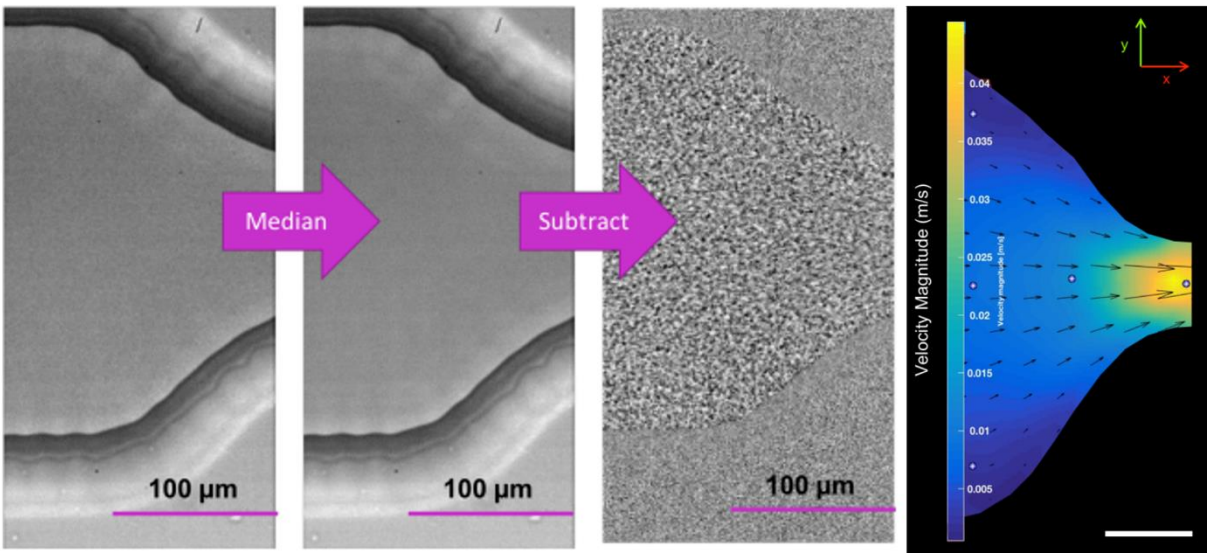

Figure 2.14: Raw image data collected from GPV, speckle pattern, vector maps collected from autocorrelation algorithm from Schofield, 2019 (156)

The pattern is then analysed by the autocorrelation function, Equation 2.22, to assess the movement of light with respect to time, where I_s is the scattered light intensity and t is the time (s) (156).

$$C_{(t')} \equiv \langle I_S(\mathrm{t}) \times I_S(\mathrm{t} + \mathrm{t}')\rangle = \lim_{T\to\infty} \frac{1}{2T} I_S(\mathrm{t}) I_S(\mathrm{t} + \mathrm{t}')\, dt \ \#(2.22)$$

For a clear speckle pattern, the microscope must be set up with Köhler illumination to give an even light distribution (119). The light source should also be inspected to

ensure an even light distribution. The aperture on the brightfield should be fully open whilst the aperture on the condenser lens is set to 15-30% (119). The speckle pattern can be determined via the Equation 2.23:

$$\delta_z \approx \frac{\lambda}{(NA_c)^2} \tag{2.23}$$

Where δ_z is the longitudinal speckle characteristic size, λ is the wavelength of light, and NA_c is the numerical aperture on the condenser lens. It is also important for the scale of GPV that the influence of flow is greater than that of Brownian motion (156). Up to 500 frames are taken to create a speckle pattern with the frame rate and shutter speed varied to reflect the flow rate used, as the frame rate should capture the particle whilst it is in the frame, and at higher velocities, the particle may have left the region of interest, the interrogation area (a defined region in the autocorrelation analysis) before the timestep (119). The shutter speed can be used to adjust clarity of the speckle pattern as it is the amount of time the shutter is open per frame and the light level.

For reliable GPV measurements, the frame rate and interrogation area must be synchronised (119). An approximation of this is Equation 2.24:

$$\Delta t = \frac{1L_{IR}}{4V} \tag{2.24}$$

Where Δt is the time step, L_{IR} the interrogation area size and V the average velocity (119). However, this is for a single pass of one velocity distribution therefore multiple passes and interrogation areas have been used to capture steeper velocity gradients.

Table 2.7: Advisory parameters for GPV analysis

Flowrate (μL/min)	Frame rate (fps)	Shutter speed
1	1000	1/5000 s
5	5000	1/6000 s
10	7000	1/12000 s
100 +	50000	1/50000 s
150 +	75000	1/75000 s

The accuracy of the speckle pattern may also change with fluid properties affecting the microparticles. Microparticle agglomerates can be reduced by making a solution containing 10% Tween, a surfactant added to remove steric interaction between particles due to the presence of impurities, such as salts, forming agglomerates (156). The agglomerates can be detected by the PIV autocorrelation algorithm creating vectors that slow down the flow.

2.7 Conclusions

This literature review has shown that there is limited possibility of fully comprehending the haemodynamics seen in microvascular collapse in capillary networks without first considering local and bulk hydrodynamics and their possible effects, which is an area that is often overlooked in vessel models, particularly that of lab-on-a-chip. As a reference, CFD models are often used to calculate shear stress ranges in microfluidic/lab-on-a-chip models, however, they are rarely validated using experimental techniques. This may be due to cost, time or a choice of biological or physical phenomena priority.

This review indicates the potential to use GPV in a novel study to characterise flow behaviour in microchannels to determine their potential as *in vitro* models of the microvasculature and microvascular collapse, specifically for the quantification of wall shear stress. The data from GPV could be combined with CFD data to quantify and verify local and bulk hydrodynamics before the model is used for biological investigation to aid in the development of new diagnostic methods for conditions such as ACS.

Chapter 3: Materials and Methods

3.1 Fabrication of mould for microfluidic devices

Photolithography was used to manufacture the mould for the microfluidic device. The process was conducted inside an ISO-8 level clean room with filtered UV light and air to prevent any imperfections caused by dust and prevent any UV curing of photosensitive materials. Any imperfections will decrease the accuracy of the channel dimensions and its ability to form many negative PDMS moulds reliably. The process is depicted in Figure 3.1

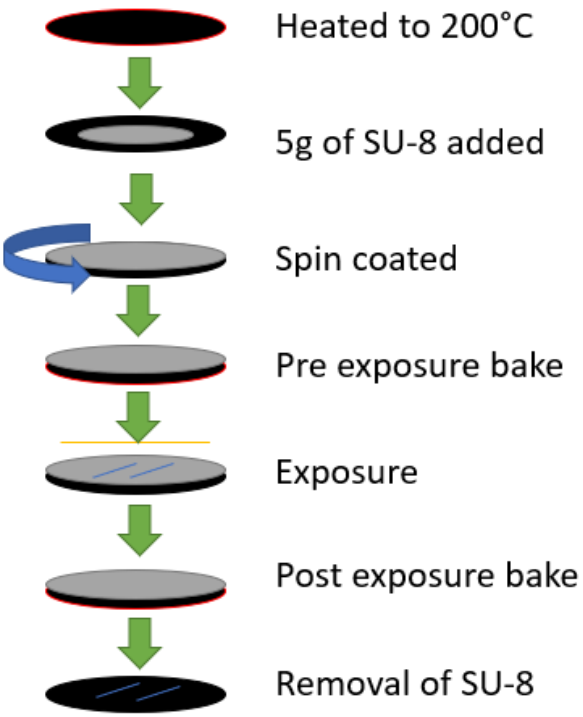

Figure 3.1: Production process of a positive resist wafer using photolithography and SU-8 on a silicon wafer

The substrate, a 4.5-inch silicon wafer from Si-Mat (Silicon Materials, Germany) was heated to 200°C using an Electronic Microsystems hot plate for 7 minutes to remove any organic contaminants that would prevent an even layer of SU-8 from forming.

To improve the reproducibility of SU-8 thickness, 5 g of SU-8 2075 photoresist (KayakuAM, USA) was spin-coated onto the wafer and the wafer was centralised on the spin coater using an alignment tool, (POLOS, Germany). It is possible to tune the height of the channel by altering the spin speeds as seen in Table 3.1. SU-8 is an epoxy-based viscous photoresist that is chemically and thermally stable and forms a solid structure when exposed to ultraviolet radiation with a wavelength of 350-400 nm via a crosslinking process (157). These properties along with its viscosity allow for the SU-8 to be cured vertically giving straight walls and thus greater accuracy when producing microfluidic moulds with rectangular cross-sections and a width (w) to height (h) aspect ratio where w>>h (157). Depending on the SU-8 viscosity, the maximum speed of the spin coating process varies as seen in Table 3.2 as with lower viscosities a higher rpm is needed to create the centrifugal force for a thinner layer of spreading.

Table 3.1: Maximum spin speeds for various SU-8 compositions the measured variation across the wafer is stated.

SU-8	**Spin speed (rpm) for 150 µm (146 µm +7/-8)**	**Spin speed (rpm) for 100 µm (131 +10/-12)**	**Spin speed (rpm) for 57 µm (+/- 8)**
Dilute 2075	-	-	1700
2075	1600	2100	-

There are 4 stages to the spin coating process, with two ramping stages to ensure a more even distribution of the photoresist before creating the thickness of the layer detailed in Table 3.2.

Table 3.2: Ramp settings used for spin coating of SU-8

SU-8 2075			
	End Spin Speed of ramp change (rpm)	**Spin acceleration (rpm/s)**	**Spin time (ss.s)**
Stage 1	100	300	10
Stage 2	750	100	20
Stage 3	Maximum value from Table 3.1	300	30
Stage 4	0	-300	30

The spin settings here depend on the type of SU-8 and desired height as with a greater viscosity there is more centrifugal force needed to spread the fluid. It was found that 1600 rpm is consistent in producing an average mould height of 146 µm (+/- 7/8) with SU-8 2075. The solvent within the SU-8, cyclopentanone, is rapidly evaporated during the spin coating process which leaves behind a thin film. The viscosity of the solution likely changes as the solvent evaporates during the spin-coating process (158).

The wafer coated with the photoresist is soft-baked at 65°C for 15 minutes, followed by increasing the temperature to 95°C for 45 minutes. The time at which the wafer is

hard-baked (higher temperature) depends on the desired thickness of the SU-8 layer (see Table 3.3) (157). The wafer is cooled to 60°C before it is placed in the Heidelberg Instruments Maskless Aligner μMLA (Germany); this step prevents SU-8 from cooling too quickly as it was found that rapid cooling caused cracking of the SU-8. The cracking of SU-8 reduces the adhesion to the silicon wafer surface upon crosslinking, rendering the mould unusable.

Table 3.3: Pre and post-exposure bake settings for SU-8 2075 during photolithography (157)

	Pre-exposure bake stage 1 65°C (mins)	**Pre-exposure bake stage 2 95°C (mins)**	**Post-exposure bake stage 1 65°C (mins)**	**Post-exposure bake stage 2 95°C (mins)**
100 μm SU-8 2075	7	45	5	15
50 μm SU-8 2075 dilute	6	20	1	5

The μMLA, maskless aligner, exposes the SU-8 using raster scan exposure with a 365 nm LED at 40 mm^2/min at a resolution of 1 μm (159). An AutoCAD design as shown in Section 3.4 is loaded onto the Heidelberg instruments maskless aligner (MLA) and after calibration is performed to find the correct UVA exposure dose and defocus, 600 mJ/cm^2 and -2 respectively for the 100 μm channels. The dose is the exposure energy which increases with increasing SU-8 viscosity and the defocus is an arbitrary value set on a scale of -10 to 10 which determines the focus distance between the focal point and the writehead and varies on photoresist thickness (157).

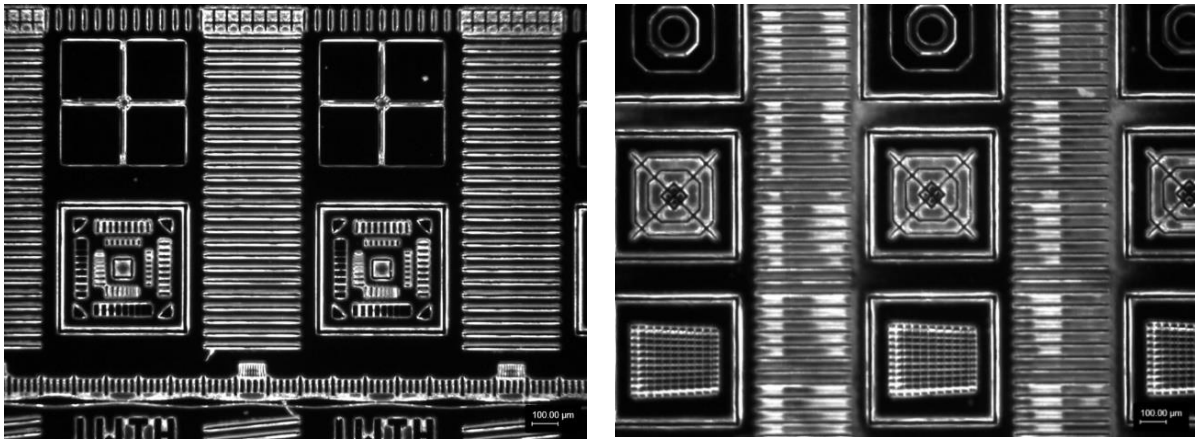

Figure 3.2: Calibration images from the Maskless Aligner showing the clarity and correct formation when using a dose and defocus of 600 nm -2 and 600 nm +6 at 60x zoom

The Heidelberg instruments MLA uses a spatial light modulator to project the AutoCAD design onto the wafer from the LED light source, curing the SU-8 in a two-step process. Initially, a strong acid is formed which catalyses a thermal cross-linking during post-exposure baking.

Once the SU-8 design has been cured the wafer is hard baked at 65°C for 5 minutes and then 95°C for 15 minutes on a completely flat and even hot plate known as the post-exposure bake (160). The wafer is then cooled to room temperature and SU-8 developer (KayakUM, USA) is used to remove the uncured SU-8 for 5-15 minutes depending on channel height (157). The wafer is rinsed in isopropanol alcohol (70%, Sigma, U.K.), dried using compressed air and fixed in a 0.1 x 0.1 m square petri dish (Sigma, U.K.) before removing from the clean room environment.

3.1.1 Modification of Process for 50 µm Geometry

To get thinner layers of SU-8 2075, the viscosity needs to be lowered. Therefore, to do this, cyclopentanone (Thermofisher, UK) was used as a diluting agent as it is the solvent used in the SU-8 photoresist formula (161). 11.6 mL of SU-8 2075 was combined with 0.828 mL of cyclopentanone and the solution mixed on a Stuart SRT6 roller mixer for 48 hrs to increase homogeneity. By adding this dilution step it was possible to reduce the viscosity.

The SU-8 was then loaded into the spin coater according to Section 3.1 and spin speeds were set to values from Table 3.2 to achieve a film thickness from 146 µm to 57 µm. The device mould was fabricated using the available photolithography process as its formation using the Heidelberg Instruments Maskless Aligner has greater control and resolution of 1 µm (159) than using the available Form 3 (FormLabs) 3D printing method at 25 µm (162)(119).

3.2 Production of PDMS Channel and Microfluidic Device

SYLGARD™ 184 Silicone Elastomer Base was combined with SYLGARD™ 184 Silicone Elastomer Curing Agent, Dow Corning, in a 10:1 ratio (w/w) of base: curing agent and mixed for 2 minutes. The mixture was then added directly onto the wafer ensuring all the mask surface was covered before putting it into a vacuum chamber for 15 minutes to degas the PDMS removing any bubbles that would change the device structure. After degassing the wafer and the mixture were placed into the oven for 1.5 h at 70 ºC to allow the flexible elastomer polydimethylsiloxane, PDMS to cure. The recommended settings for PDMS curing vary depending on the application of the

device from 48 h at 25 ºC to 10 minutes at 150 ºC (163). 1.5 h at 70 ºC was chosen as the structure was maintained and there was no sticky residue to allow for rapid manufacture.

After cooling, the PDMS channels were cut out using a No. 11 scalpel (SwannMorton, U.K.). Channels are left imprinted into the PDMS. Inlets and outlets can be punched into the device using a biopsy punch (KAI) with an internal diameter of 1.5 mm.

To produce the final closed system which is a microfluidic device, the PDMS layer was adhered to a 25 x 75 mm ISO 8037/1 glass slide (Avantor, U.S.A). A Henniker Plasma HPT-100 oxygen plasma chamber was used to expose the surface of the PDMS and glass slide with a 50% intensity, 15 sccm (standard cubic centimeters per minute) flow and 20 s of exposure to plasma. The device was placed onto a hot plate under a weight for 20 minutes at 95 ºC, then 40 minutes at 70 ºC to seal the bond. Various settings have been used when joining PDMS to glass using oxygen plasma, with exposure times ranging from 20-60 s (164)(165)(166)(167). The oxygen plasma process has previously been modified by increasing the exposure to increase the burst pressure (168)(169) or peel strength (169) however, these settings were for test pressures 185-610 kPa significantly greater than the 4.7 kPa needed to mimic blood flow in the capillary (168)(170)(171). From experimental data collected by Jiang *et al.*, 2002, the chemical properties of the PDMS surface mostly change rapidly in the first 20 seconds and then stabilise (172). As the maximum pressure the PDMS to glass bond would need to withstand was 4700 Pa, 20 s of exposure time was tested and the PDMS and glass slide adhered successfully. The oxygen plasma process removes silicone from the surface and replaces it with oxygen radicals, activating the surface, increasing hydrophobicity and allowing the PDMS and glass to form a bond

(173). To prevent any contaminants entering the device before use 500 µm internal diameter Polytetrafluoroethylene, PTFE tubing (Cole Parmer, U.K.) was attached to the inlet and outlet holes of the microfluidic device.

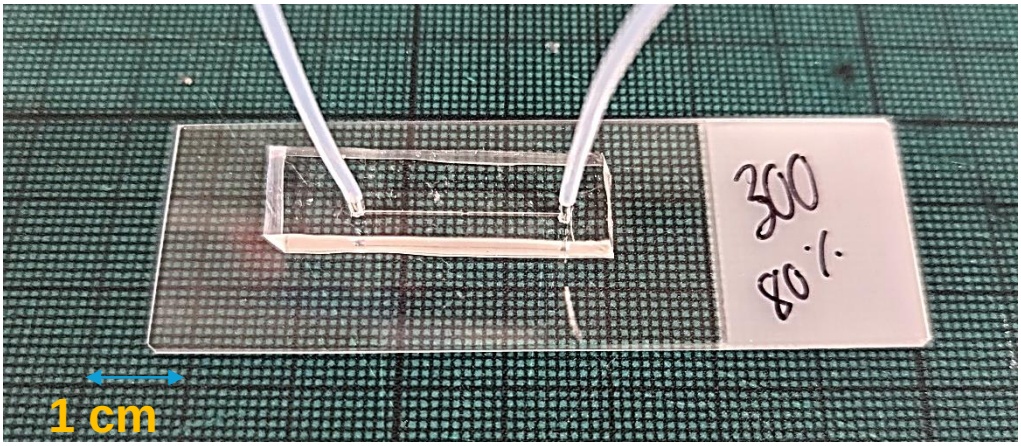

Figure 3.3: A microfluidic device formed using soft lithography with tubing secured in the inlet and outlet holes

Devices were produced using a 10:1 ratio of PDMS to maintain structure, however many ratios of PDMS were tested and used where specified for different purposes such as varying elastic properties as discussed in Chapter 6 to allow for the study of deformable walls (174)(175). Both fixed stenosis and deformable wall models were created to look at the effect of dynamic stenosis as replicable to ACS pathophysiology.

3.3 Tensile Testing of PDMS Compositions

PDMS samples underwent tensile testing to allow for the comparison of elastic properties and inform the design of channels with a deformable wall for mimicking ACS pathophysiology. Samples were prepared with SYLGARD 184 PDMS, (DOW, USA) using ratios of base to curing agent 10:1, 15:1, 20:1, 25:1 by weight. This was

done to vary the Young's modulus of the channel walls to replicate *in vivo* elastic behaviour and create a channel capable of deforming across the channel width. The PDMS is prepared according to Section 3.2. The PDMS is then cut using a specific ISO 37 dumbbell cutter.

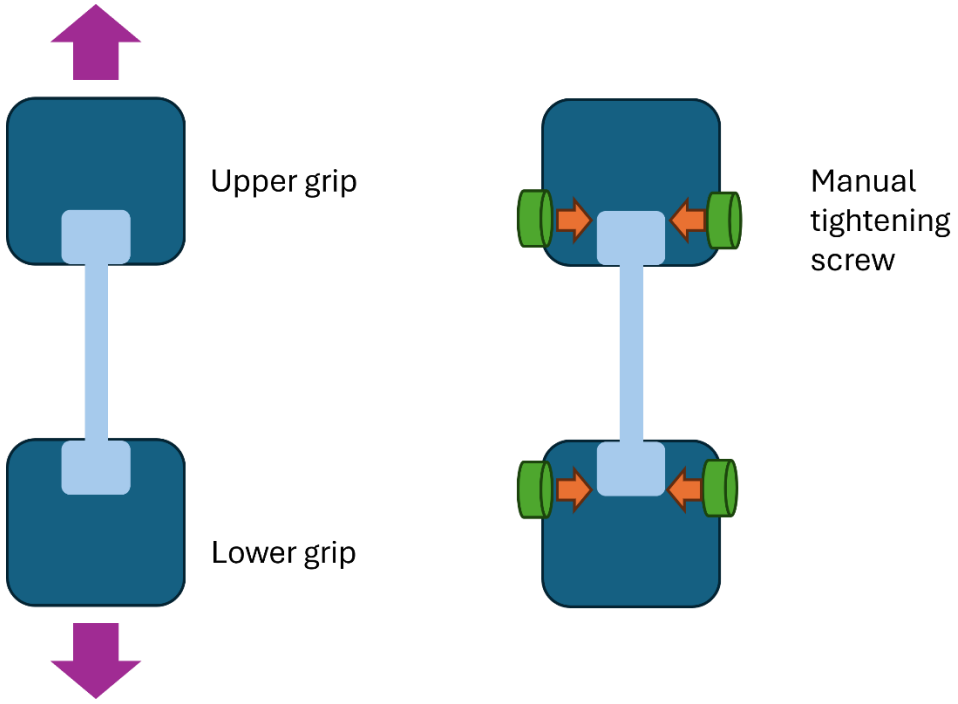

Figure 3.4: The set-up of the grips for the Zwick Roell tensile testing measurements

The width and the thickness of the middle of the dumbbell are measured using callipers, (Mitutoyo, U.K.). The samples were tested on the Zwick Roell Z030 Universal Tester and secured in the 8354 10 kN grips according to Figure 3.4 (ZwickRoell, Germany). The top portion of the dumbbell was secured in the centre of the upper grip vertically and the bottom portion of the dumbbell was secured vertically centred in the lower grip using manual hand-tightened screws. The sample is then pulled from 0 force at 10 mm/min until failure and the elongation and stress are recorded. The data is then extracted and the Young's moduli can be calculated using Equation 3.1 (176):

$$E = \frac{\sigma}{\varepsilon} \tag{3.1}$$

Where E is the Young's modulus, σ is the tensile stress and ε is the tensile strain.

3.4 Geometries

All geometries were created using AUTODESK and fabricated using the soft lithography process in Section 3.2.

3.4.1 Straight Channel

A simple straight channel geometry was used as a reference point for comparison with 1-D analytical solutions of the Navier Stokes equations in laminar flow for local and bulk values of velocity and pressure. In this way, the accuracy and repeatability of the experimental results and errors can be rigorously assessed. The straight channel model was also created to assess the hydrodynamic resistance in the experimental equipment as a function of channel cross-sectional area and contributed to enabling the determination of the ideal channel dimensions for a stable predictable flow rate within the experimental set-up.

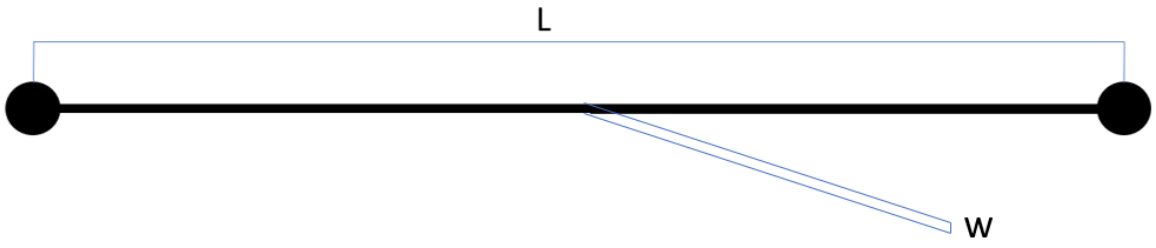

Figure 3.5: A straight channel geometry showing channel length, L, and width, w, observed from above

Table 3.4: Dimensions of the straight channel model

Dimensions		H (μm)		
		150	100	50
W (μm)	400		X	
	300	X		
	200			X

3.4.2 Fixed Short Stenosis

The ‘short’ stenosis model is a variant of the straight channel model in which a section of the wall is curved inwards using a three-point arc to create a stenosis, with the arc maximum creating the maximum stenosis as in Table 3.5. The width of the channel in the stenosis/stenotic region is decreased by 20, 40, and 60% of its original value respectively. This model was created to examine how the wall shear stress changes in both the non-stenotic and stenotic regions due to changes in flow rate and velocity profile within the channel in response to the increase in hydrodynamic resistance caused by the stenosis (177). This is the simplest form of microvascular collapse.

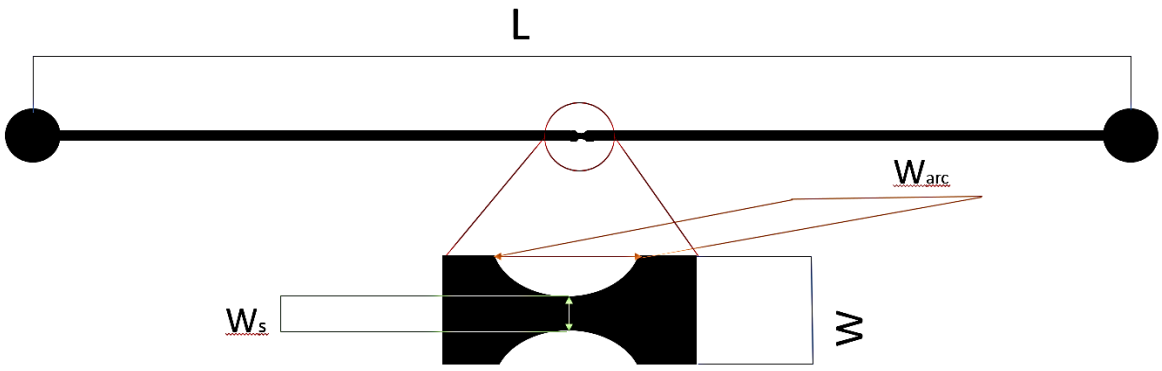

Figure 3.6: A short stenosis model

Table 3.5: Dimensions for the short stenosis model

Dimensions		**Minimum channel width at point of arc, Ws, (μm)**			
		Percentage of stenosis (%)			
		0	20	40	60
W (μm)	400	400	320	240	160
	300	300	240	180	120
	200	200	160	120	80

3.4.3 Long Stenosis

Long stenosis models were created to increase the comparative amount of resistance created by the stenosis region thus better mimicking the collapse of the blood vessel. This also allowed a greater change that could be measured significantly using the lower limits of GPV.

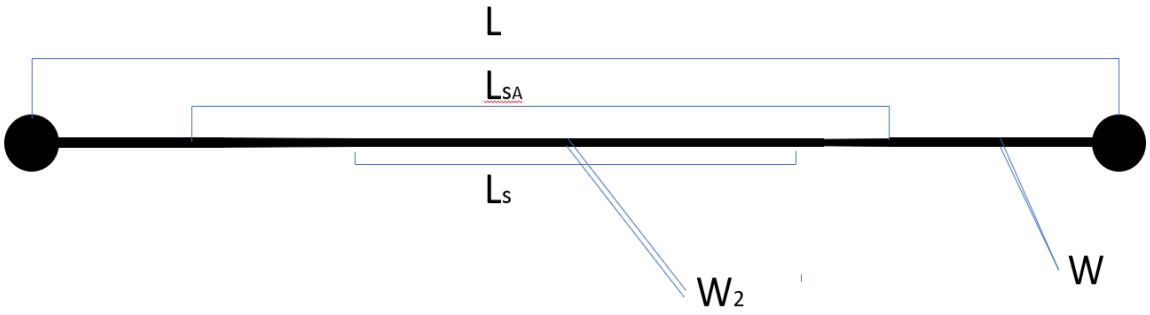

Figure 3.7: A long stenosis device

Table 3.6: Dimensions of the long stenosis device

Dimensions					
Width (µm)	200	Length of stenosis (L_S) (mm)			20
		Length of device (mm)			45
		Length of slope into stenosis (L_{SA}-L_S) (µm)			250
		Minimum channel width at point of arc, W_2, (µm)			
		Percentage of stenosis (%)			
		0	20	40	60
		200	160	120	80

3.4.4 Short Deformable Wall

The device has two fluid bladders with a deformable thin PDMS wall between the bladder and main channel that are pressurised through the pumping of fluid into the bladder, referred to as a ‘micropump’, with no output stream, thus pressurising the micropumps and causing them to inflate, as shown in Figure 3.8. The air can diffuse through the PDMS and the pumps are filled with ink to show any leakages (109). A

deformable model was created to mimic the capillary system further by seeing the measure of deformation on the walls in response to pressure on either side externally, created by the flow. This device design works similarly to the pneumatically activated micropump designs by Chiou *et al.*, 2015 (178). The fixed model in Section 3.4.2 can also be used to compare these measurements. The deformable wall can be used to mimic microvascular collapse in the *in vitro* model by compressing the channel at various geometries. This can be applied to the design using the method discussed in Section 3.2. The model was created to see the effect of deformation on the flow rate and shear stress profiles with feedback from internal pressure in a material with a closer Young's modulus to that of a capillary.

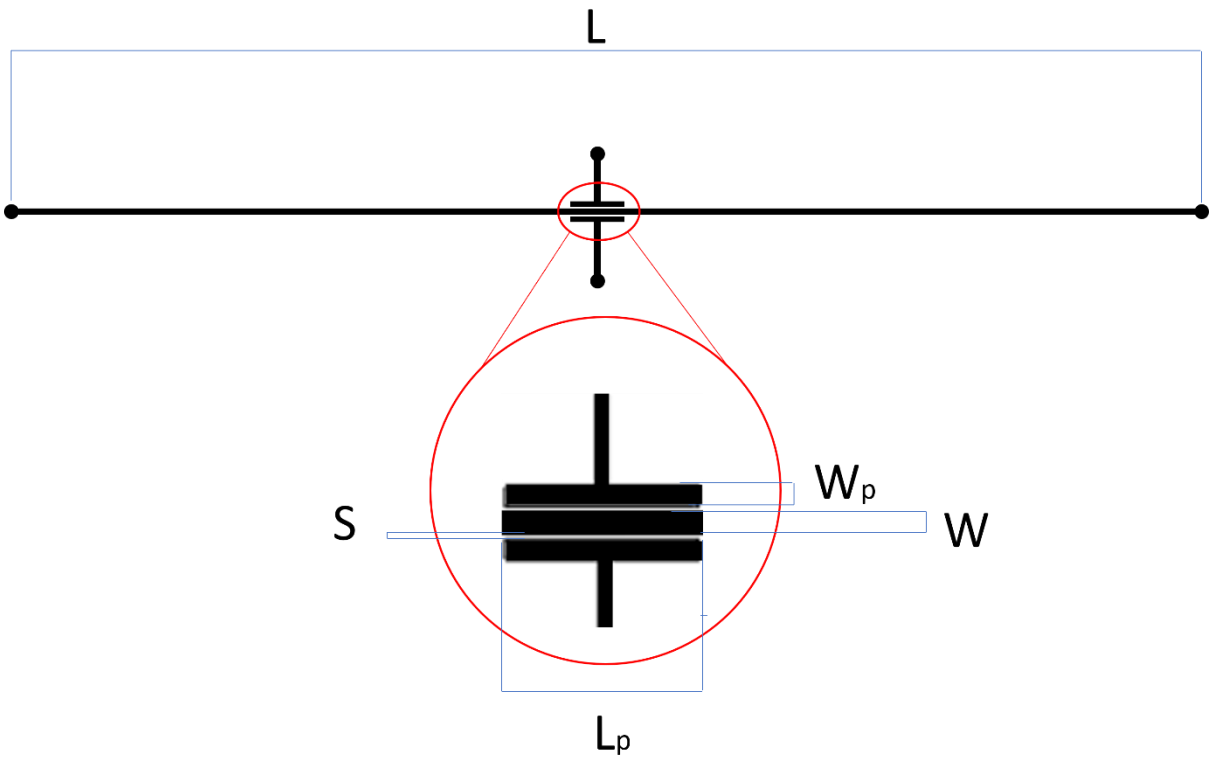

Figure 3.8: AutoCAD design of short deformable wall device

Table 3.7: Dimensions for short deformable wall model

Dimensions	
Length (mm)	20
Widths (µm)	200
Micropump length (µm)	700
Micropump width (µm)	150
Micropump separation from channel (µm)	65

3.4.5 Long Deformable Wall

The long deformable wall model has the same length as the fixed long stenosis model but is deformed using a set of micropumps in series with a 70 µm gap between each pump. This distance is the maximum found where PDMS will form a layer in the mould that maintains its structure during fabrication and testing without tearing. A series of micropumps was used as they maintained their structure better than a single large side pump which was prone to collapse. This model was created to better mimic the *in vivo* pathophysiology by having a deformable wall that responds to changes in internal and external pressure and allows for the deformation of the model (179). The model was created to see the effect of deformation on the flow rate and shear stress profiles with feedback from internal pressure. In addition, to investigate the model with a material with a closer Young's modulus to that of a capillary in a longer range creating more deformation. Additionally, by increasing the

elastic properties of the material it was possible to achieve more deformation across the width of the channel.

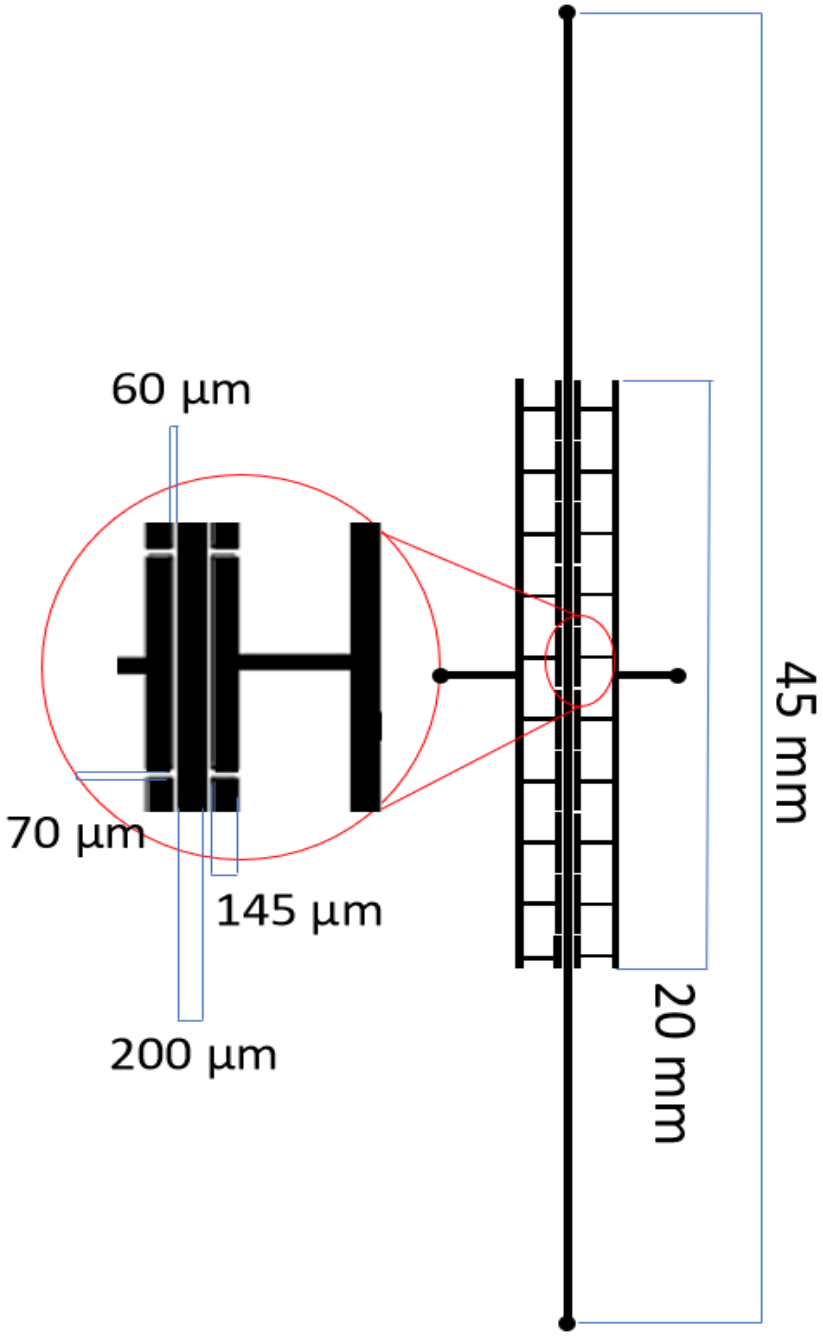

Figure 3.9: Long Deformable Wall model

.

Table 3.8: Dimensions for Long Deformable Wall Model

Dimensions	
Length (mm)	45
Widths (µm)	200
Micropump length (µm)	700
Micropump width (µm)	150
Micropump separation from channel (µm)	65
Number of micropumps	20

3.4.6 Murray's Law Branched Model

A branched model was created to see the effects of changes of resistance upstream on the effects downstream with branching (180). The stenosis must be placed close to the branching as the flow development length is short post-stenosis. The Murray's law model was created to more accurately represent the microfluidic network *in vivo* and see the result of flow rate change in the second-order channels in response to a stenosis upstream (181). There is some debate about the geometry of capillaries following Murray's Law, (182,183), therefore many branched designs were created and one following Murray's Law below and detailed in Table 3.9.

$$D_1^3 = D_2^3 + D_3^3 \tag{2.1}$$

$$\alpha = \frac{D_1^3}{D_2^3 + D_3^3} = 1 \tag{3.2}$$

The hydraulic diameter was used and an even height was set to back calculate each channel width. Where D is the channel width and the subscript refers to the vessel number.

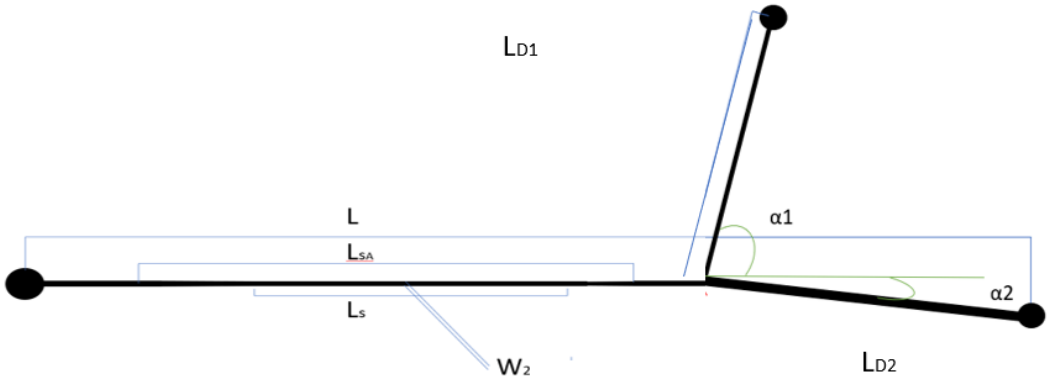

Figure 3.10: Device design of Murray's Law model

Table 3.9: Dimensions for Murray's Law model

Dimensions				
Length of main channel (mm)	30			
Length of daughter branch 1 L_{D1} (mm)	10			
Length of daughter branch 2 L_{D2} (mm)	10			
Length of stenosis L_s (mm)	20			
Width of main channel (µm)	200			
Width of daughter branch 1 (µm)	75			
Width of daughter branch 2 (µm)	100			
Angle 1 °	42			
Angle 2 °	33			
Minimum channel width at point of stenosis (µm)	% stenosis			
200	0	20	40	60
	200	160	120	80

3.4.7 Evenly Branched Model

As there is a range of branching in the microvasculature, including that when angiogenesis occurs a evenly-branched model was created (181). The even branch model was created to investigate the effect of stenosis on different geometries and the effect of flow rate on lower-order daughter vessels and when microvascular collapse may occur.

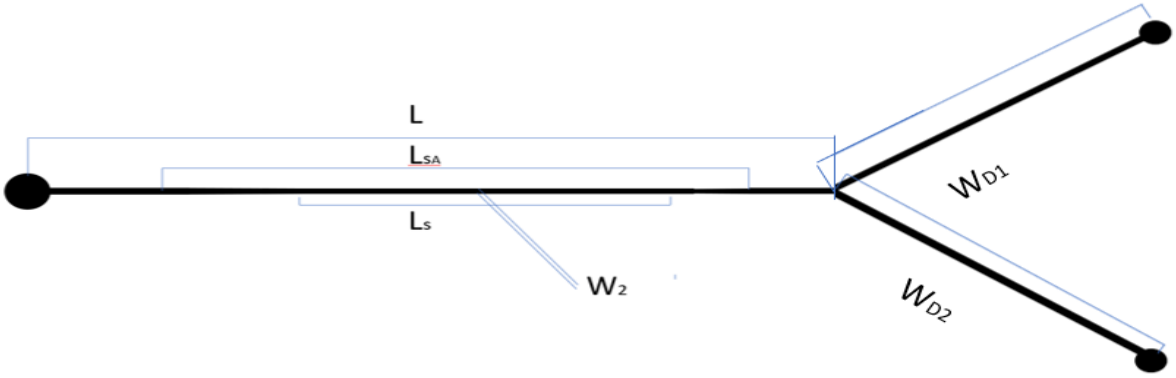

Figure 3.11: Evenly Branched Model

Table 3.10: Dimensions for evenly branched model

Dimensions				
Length of main channel (mm)	30			
Length of daughter branch 1 (mm)	10			
Length of daughter branch 2 (mm)	10			
Length of stenosis L_S (mm)	20			
Width of main channel (μm)	200			
Width of daughter branch 1 (μm)	200			
Width of daughter branch 2 (μm)	200			
Minimum width at point of maximum stenosis (μm)	% stenosis			
	0	20	40	60
200	200	160	120	80

3.4.8 Side Branch Model

The side branch model was created to investigate the effect of stenosis on different geometries and the effect of flow rate on lower-order daughter vessels and when microvascular collapse may occur.

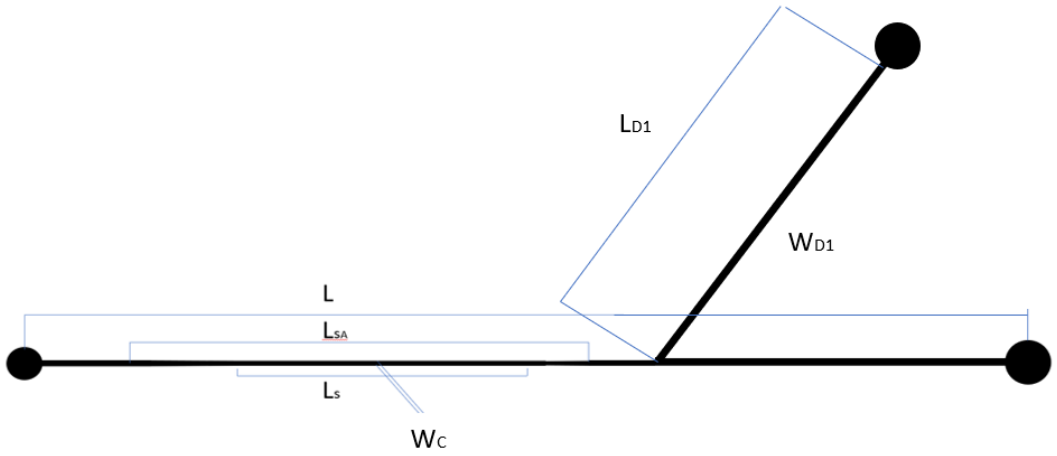

Figure 3.12: A side branch model design

Table 3.11: Dimensions for the side-branched model

Dimensions				
Length of main channel (mm)	30			
Length of daughter branch 1 (mm)	10			
Length of stenosis L_S	20			
Width of main channel W_C (μm)	200			
Width of daughter branch 1 W_{D1} (μm)	100			
Minimum width at point of maximum stenosis (μm)	% stenosis			
	0	20	40	60
200	200	160	120	60

3.4.9 Branched Deformable Model

A branched deformable model was created to investigate the effects of increasing resistance in a fixed height deformable model on the shear stress in lower-order down stream branches and to develop the most physiologically relevant model of microvascular collapse.

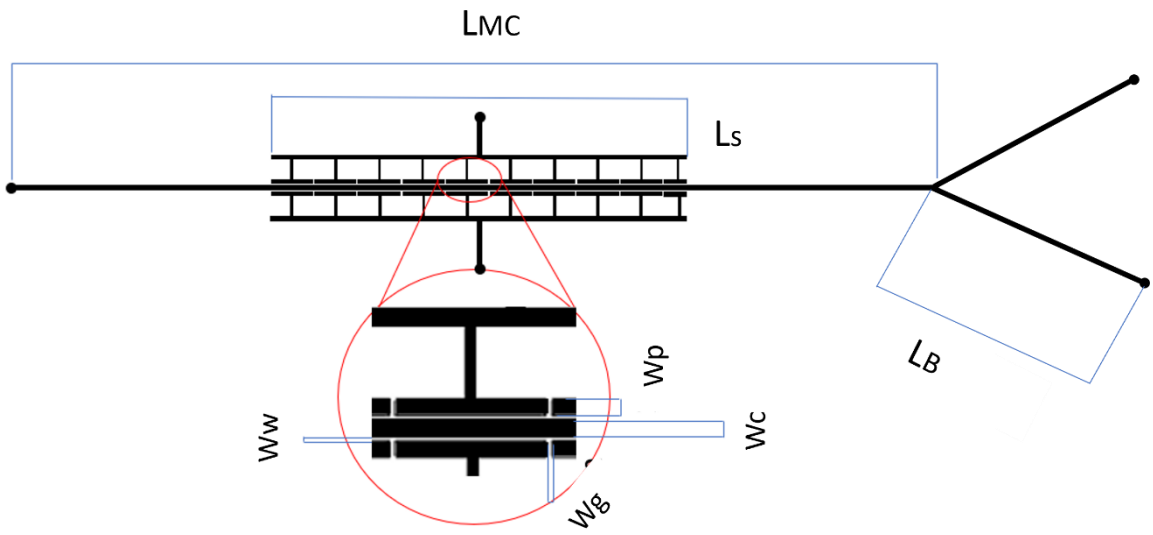

Figure 3.13: A deformable branched model design

Table 3.12: Dimensions for the deformable branched model

Dimensions	
Length of main channel (L_{MC}) (mm)	45
Length of daughter branch (L_B) (mm)	10
Widths (W_c) (µm)	200
Micropump length (µm)	700
Micropump width (W_p) (µm)	150
Micropump separation from channel (W_w) (µm)	60
Number of micropumps	20

3.5 Cross-Sectional Area

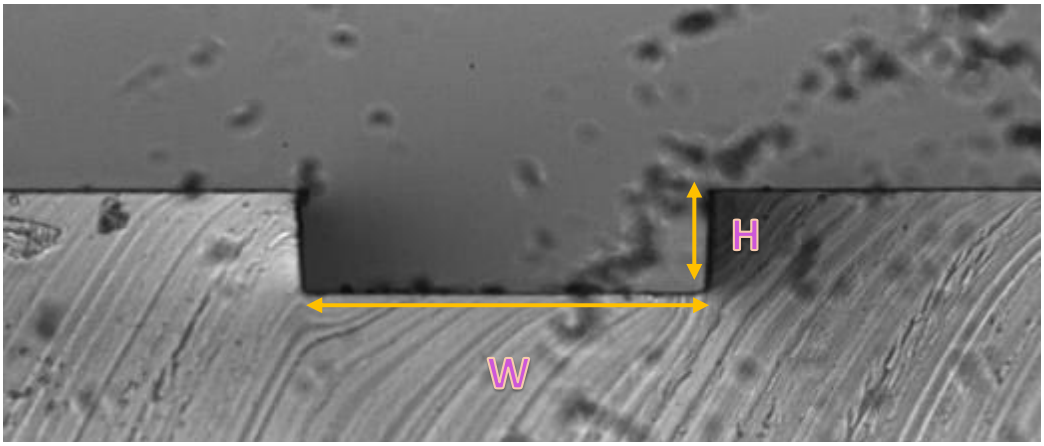

Figure 3.14: A microscope image of a cross-section of a microfluidic channel 20x zoom

The cross-sectional area of the fabricated channels in all cases is rectangular due to the manufacturing process discussed in Section 3.2. Fabrication of a cylindrical channel was attempted using 3D printing of a mould and alignment using the microscope, however, this had a minimum width of 500 µm and the two semi-circular cross sections could not be aligned and joined reliably and accurately. In all regions, the width is greater than the height. The cross-sectional area was measured by taking a slice across the microfluidic device and placing it sideways on the glass slide as seen in Figure 3.14. An image is then taken and by setting a global scale from a known microscope scale image in ImageJ software the distance can be measured.

3.6 Microfluidic Rig Design for Flow Measurements

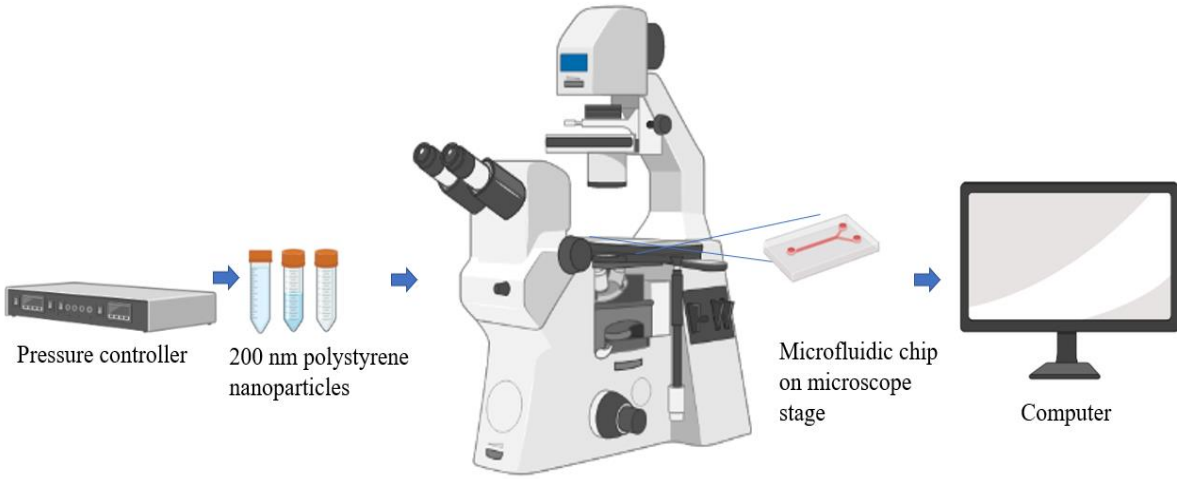

Figure 3.15 Ghost Particle Velocimetry set up created with Biorender.com

GPV was used for the measurement of flow within microfluidic devices (119). Ultra-pure deionised water was seeded with 0.02 % (v/v) of 200 nm microparticles based on polystyrene (10% solid, Sigma) and was supplied to the device using an Elveflow OB1 4 channel pressure controller at 2000, 3200 and 4700 Pa to replicate the minimum, average thigh and maximum vessel capillary pressure (119). A concentration of 0.02% (v/v) was used to ensure a suitable seeding density (119)(155). GPV uses as a flow tracer the speckle patterns produced by white light scattered by micro-particles. The flow of the micro-particle suspension was recorded using a high-speed camera (Photron NOVA s15) on PFV 4 software. The camera was connected to an inverted microscope (Nikon TI Eclipse) equipped with a 20x lens (Nikon, CFI Plan Fluor DLL) providing a spatial resolution of 1 µm/pixel with 500 frames recorded according to frame rates between 1000-75000 frames per second (fps) as discussed in the results chapters.

The microparticles must be kept in solution and stored in the fridge as they are pyrophoric (can combust when dry). The solution is then mixed using a whirlmixer™ on maximum intensity for 40 s to ensure an even distribution.

3.6.1 Microscope Set Up

The microparticle dispersion refracts the light to give the speckle pattern that is analysed in the autocorrelation algorithm (119). This means that initially, the microscope set-up should provide even light in the layer of measurement. The microscope was placed in Köhler illumination on the channel. The light was checked to ensure the brightfield illumination was giving an even distribution. All lenses were cleaned with lint-free wipes (Whatman, Sigma, U.K) to remove any dirt or imperfections before the measurements were taken as small deflections in light can cause anomalous measurements in GPV. The aperture was focused on 20% open to capture the specific plane of the channel with a 20 μm gap.

3.6.2 Camera Settings

A high-speed camera with a short timestep between frames was needed to accurately capture high flow rates in stenosed areas at high pressures. Additionally, a high resolution was needed to capture the vectors at the wall to measure the wall shear stress. A Photron Nova S-16 Fastcam was used to collect images the specifications are as follows (156,184–186):

Table 3.13: Maximum fps and resolution of varying Fastcam models

	Nova-S16	**SA3**	**SA5**
Max fps	1,100,000	60000	100000
Max resolution (px)	128 x 16	128 x 16	64 x 16

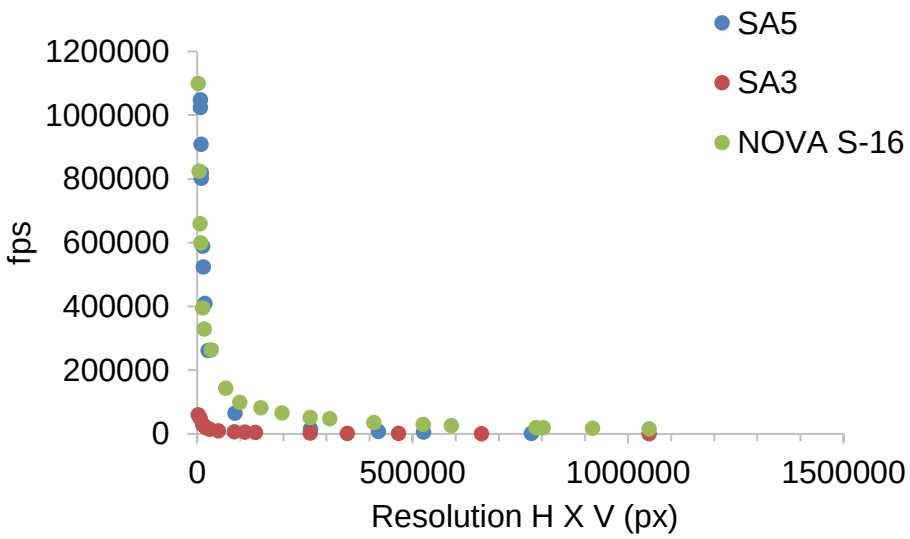

Figure 3.16: Varying Fastcam camera types and their resolution vs frames per second

The use of the Photron Nova S-16 allowed for greater resolution when collecting data from GPV measurements and allowed faster imaging than available from the SA3 used in Ricommi *et al.* (119). The set-up with Photron Nova 16 was capped at 75000 fps before banding was seen which prevented accurate GPV measurements.

3.6.3 Data Collection and Processing

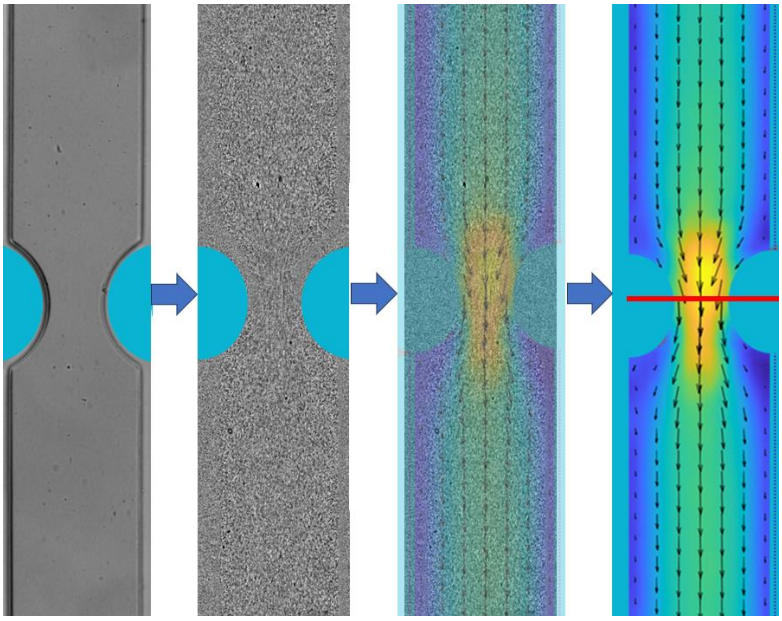

Figure 3.17: Data collection stages of GPV, raw images, speckle patterns from ImageJ, spatial velocity distributions and extraction from PIVLab

The frame rate of the camera was selected to capture the movement of vectors to each interrogation area based on the velocity. The interrogation area is the area where each speckle pattern is analysed over, per vector (119). The higher frame rates can be used to collect the higher velocities in stenosis or branches with a lower width than the main channel. Smaller interrogation zones or lower frame rates can also be used to capture lower flows such as those at the wall when determining shear rates. The interrogation area can also be increased to capture higher velocities.

Lower shutter speeds allowed in more light which allowed the speckle pattern to be captured more clearly. The experiment began once the flow was fully developed at steady state and it could be seen that the microparticles are moving in the channel.

The data was collected and the clarity of the speckle pattern was assessed as seen in Figure 3.18 to ensure clear speckles. Due to the flow being pressure-driven, the flow rates were unknown at this stage and thus a range of frame rates were tested. In the stenotic region, the interrogation area is limited by the width of the channel according to the settings in PIVlab, therefore smaller interrogation areas should be used with a higher frame rate, particularly for the measurement of shear stress.

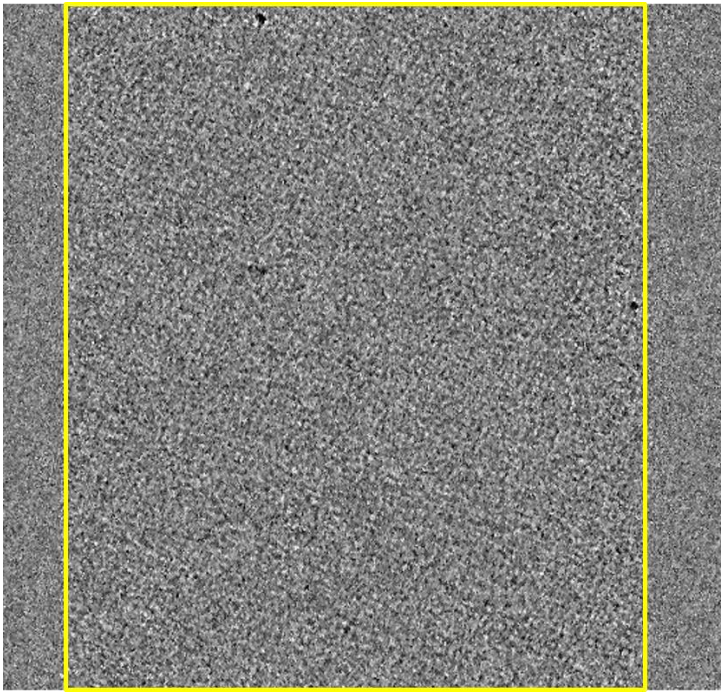

Figure 3.18: Flow in a 400 µm device recorded at 40000 fps

The GPV settings chosen were interrogation areas of 64, 32 and 16 px pass to increase vector resolution and signal-to-noise ratio, also improving the quality of measurements (187). These are more passes compared to the work by Riccomi *et al.*, and it was possible to capture higher velocity magnitudes at higher frame rates, 0.17 m/s was captured at 50000 fps as compared to 15000 fps in Riccomi *et al.* (119).

3.6.4 Fiji-ImageJ Processing

Fiji with ImageJ was used to process images collected from GPV (119). To enhance the speckle pattern from the raw image the static contribution is subtracted from each of the frames. The static contribution is obtained by using the median of all frames. By removing the static contribution, the speckle pattern remains in all the frames (119). To increase the efficiency of this process, a macro was created (see Appendix 1).

3.6.5 PIVLab Processing

The image sequence consisting of speckle patterns as seen in Figure 3.17 is imported pairwise into PIVLab - a MATLAB application (188). The images are imported pairwise to measure the movement in speckles between image pairs (187). The speckle pattern is a result of the light scattering due to the movement of the tracer particles. The particles will not be recorded as their size 200 nm, is smaller than the diffraction limit of white light (119). A mask is drawn around the speckle area and is applied to all frames. This removes surrounding areas outside the microfluidic device. The PIV settings are then chosen such as interrogation areas, 64, 32 and 16 px, the step between interrogation area overlaps was every 8 px, 50%, and the algorithm chosen, FFT window deformation. These values were selected to capture the higher velocity vectors in stenotic regions and lower velocity vectors at the wall for shear stress measurements. The analysis is then done using cross-correlation (188). After the analysis the image is calibrated using a microscope scale image of a known length and the time step is set to the difference between frames- altered by

the frame rate. The vectors are then plotted on a scatter plot and any anomalous vectors are removed. The temporal and spatial mean are then calculated to produce a velocity map. From this velocity map the vector values can be extracted, either from an area or by drawing a line on the image and extracting across the line as seen in Figure 3.17.

3.7 Characterisation of Microparticle Dispersion

The number of particles, particle size distribution and zeta potential of the microparticle dispersion were measured using a Zetasizer Ultra, MalvernPanalytical. The sample was inserted with a folded capillary cell cuvette, Malvern Panalytical. The Zetasizer uses Multi-Angle Dynamic Light Scattering (MADLS) to take multiple Dynamic Light Scattering (DLS) measurements from different angles to improve the accuracy of the particle size distribution (189)(190). A laser is shone through the cuvette and the light scattering is detected. The dynamic light scattering measures the rate of fluctuations in the intensity of light, light scattering, in response to Brownian motion. The Stokes-Einstein equation is then used to estimate the particles' hydraulic diameter (189)(190).

$$D_H = \frac{kT}{3\pi\eta D} \tag{3.3}$$

Where D_H is the hydraulic diameter of the particle, k is the Boltzmann constant, T is the temperature, η is the solvent viscosity and D is the diffusion coefficient.

The zeta potential is measured using Electrophoretic Light Scattering (ELS) in which an electric field is applied across the folded cuvette cell and the charged particles will move to oppositely charged electrodes. The velocity, known as electrophoretic

mobility, can be calculated using DLS theory and the Henry Equation, Equation 3.5 can be used to calculate the zeta potential (190)(191)(192)

$$U_E = \frac{2\varepsilon\zeta}{3\eta} f(\kappa\alpha) \tag{3.4}$$

Where U_E is the electrophoretic mobility, ε is the dielectric constant, ζ is the zeta potential, η, is the viscosity and $f(\kappa\alpha)$ is Henry's function.

3.8 Computational Fluid Dynamics

ANSYS Fluent™ was used to model laminar flow in the microfluidic device to identify flow development lengths and to allow for more complex models to be created. Fluent was chosen due to its ability to quickly solve multiple meshes in parallel, the cell is centred in each finite volume and its capability of using pressure coupling methods (193).

The geometries of the microfluidics models described in the previous section were created on AutoCAD Fusion 360 and imported into ANSYS workbench, see for example in Figure 3.19.

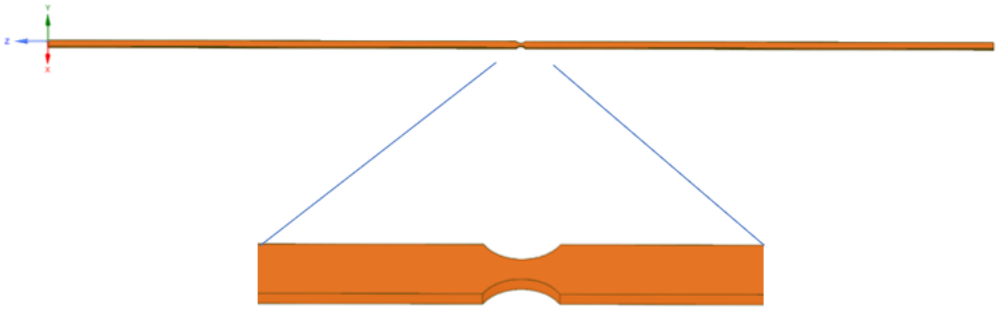

Figure 3.19: An example of a 200 µm short stenosis CAD design created in AUTODESK Fusion for use in CFD in a 200 µm x 50 µm x 20 mm channel

Within ANSYS workbench- the files are opened and regions; inlet, outlet, top and bottom walls and side walls, are labelled in ANSYS SpaceClaim. The height of the models is created by extruding the drawing to match the average measured height produced in the mould-making process.

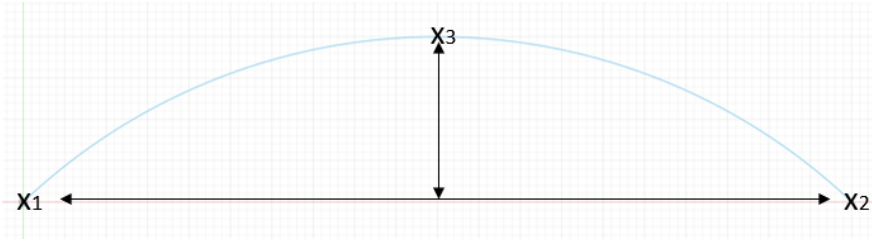

Figure 3.20: Arc geometry used in CFD design of models

The 3-point arc shape shown in Figure 3.20 is also used to allow for direct comparison between experimental and CFD models. The distance between x_1 and x_2 is specified then the height from the centre of the line x_1-x_2 to the peak of the arc x_3.

3.8.1 Mesh

The CFD mesh was created in Ansys Fluent™. A non-uniform mesh was created to maximise the accuracy of measurements at the side walls to accurately measure wall shear stress (194).

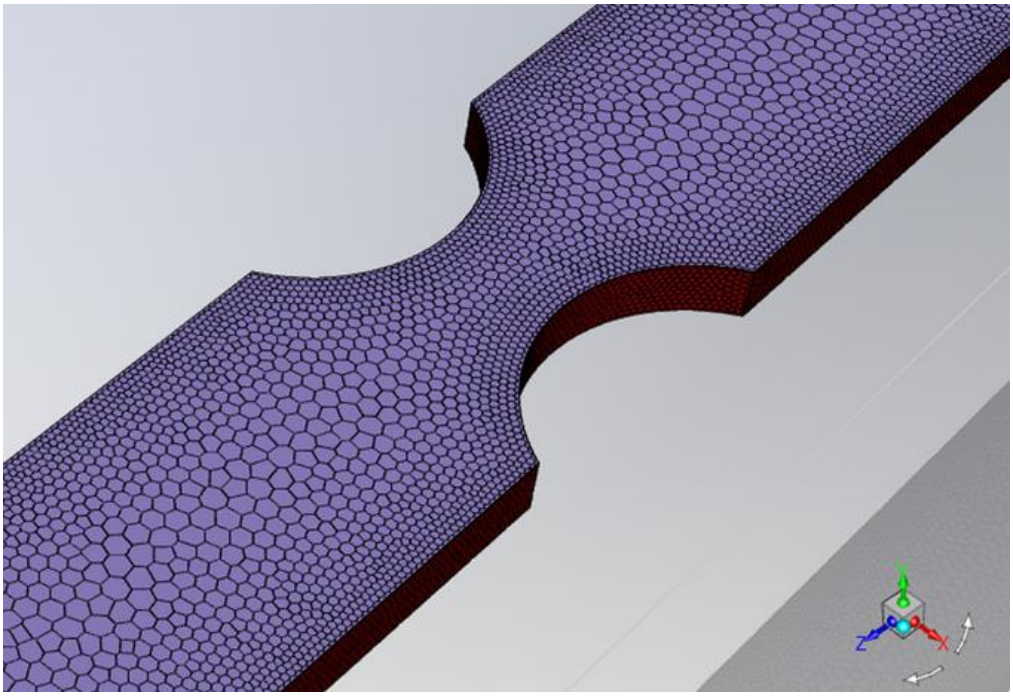

Figure 3.21: CFD mesh of 200 µm x 50 µm stenosed device created in ANSYS Fluent

The mesh was designed to have a growth rate of 1.16 on the top, bottom and side walls. There were 4 boundary layers applied with a transition ratio of 0.272, as default, and a growth rate of 1.16 to capture close to wall shear stress values around the curved geometry.

Each mesh design had the target mesh size and cell length varied and a mesh independent study was conducted. 8 cells per gap were applied to the side walls in meshes used for direct comparison with GPV to be able to extract across a more accurate central plane. A polyhedral mesh was used to reduce computational time (195)(196).

3.8.2 Boundary Conditions

A no-slip boundary condition was applied to each wall. The inlet boundary condition pressure value was set to be 4700/ 3200/ 2000 Pa and the outlet boundary condition was 0 Pa. These were selected to be definite variables from the experiment and the tubing was ignored due to variable resistance.

3.8.3 Solver

A laminar flow model was selected. The whole system was modelled as a fluid in the laminar regime. The simulation was run to 0.001 absolute convergence on x, y, z velocity as well as continuity. The Semi-Implicit Method For Pressure Linked Equations (SIMPLE) algorithm was used to solve the incompressible Navier Stokes Equations with no gravity, the velocity in the x direction and steady state (197).

$$0 = -\frac{\partial P}{\partial x} + \mu \frac{\partial^2 v_x}{\partial^2 z^2} \tag{3.5}$$

$$0 = -\frac{\partial P}{\partial z} \tag{3.6}$$

Conservation of mass:

$$\frac{\partial u_i}{\partial x_i} = 0 \tag{3.7}$$

Conservation of momentum:

$$\frac{\partial u_i}{\partial t} + \frac{\partial u_j u_i}{\partial x_j} = \frac{\partial}{\partial x_j}\left(\mu \frac{\partial u_i}{\partial x_j}\right) - \frac{1}{\rho}\frac{\partial u_i}{\partial x_i} \tag{3.8}$$

The SIMPLE algorithm: semi-implicit method for pressure linked equations:

Implicit Scheme for steady Navier Stokes Equations:

$$\nabla . \boldsymbol{u} = 0 \tag{3.9}$$

$$\nabla . (\boldsymbol{u} u_x) = -\frac{1}{\rho}\frac{\partial p}{\partial x} + v\nabla^2 u_x \tag{3.10}$$

$$\nabla . (\boldsymbol{u} u_y) = -\frac{1}{\rho}\frac{\partial p}{\partial y} + v\nabla^2 u_y \tag{3.11}$$

$$\nabla . (\boldsymbol{u} u_z) = -\frac{1}{\rho}\frac{\partial p}{\partial z} + v\nabla^2 u_z \tag{3.12}$$

Intermediate velocity field- based on estimated value for P:

$$a_P (u_i)_P^* = \sum_f a_f (u_i^* . n_i)_f - \frac{1}{\rho}\frac{\delta \rho^n}{\delta x_i} \tag{3.13}$$

Velocity and pressure correction – using continuity/ momentum equation:

$$u^{n+1} = u^* + u' \tag{3.14}$$

$$p^{n+1} = p^n + p' \tag{3.15}$$

Combining-underrelaxation:

$$a_P (u_i)_P^{n+1} = \sum_f a_f (u_i^{n+1} . n_i)_f - \frac{1}{\rho}\frac{\delta \rho^{n+1}}{\delta x_i} \tag{3.16}$$

$$a_P (u_i)_P^* = \sum_f a_f (u_i^* . n_i)_f - \frac{1}{\rho}\frac{\delta \rho^n}{\delta x_i} \tag{3.17}$$

$$a_P (u_i)_P' = \sum_f a_f [(u_i^{n+1} . u_i^*) . n_i]_f - \frac{1}{\rho}\frac{\delta \rho'}{\delta x_i} \tag{3.18}$$

$$(u_i)'_P = \overline{(u_\iota)}' - (\frac{1}{a_P}\frac{1}{\rho}\frac{\delta p'}{\delta x_i}) \#(2.19)$$

Divergence- check tolerance and iterate if not at tolerance:

$$\frac{\delta}{\delta x_i}(u_i)_P^{n+1} = 0 = \frac{\delta}{\delta x_i}(u_i)_P^* + \frac{\delta}{\delta x_i}(u_i)'_P \quad (3.20)$$

$$0 = \frac{\delta}{\delta x_i}(u_i)_P^* + \frac{\delta}{\delta x_i}\overline{(u_\iota)}' - \frac{\delta}{\delta x_i}\left(\frac{1}{a_P}\frac{1}{\rho}\frac{\delta p'}{\delta x_i}\right) \quad (3.21)$$

3.8.4 Mesh Independence

The mesh was ensured to be mesh independent, having output values of pressure and shear stress that do not change greater than 1% by reducing cell size, by running five mesh sizes: ‘finest’, ‘fine’, ‘medium’, ‘coarse’ and ‘coarsest’. Each of these categories were defined by varying the minimum and maximum cell size in the surface mesh, and the maximum cell length in the volume mesh.

Table 3.14: Computational Fluid Dynamics meshes and parameters for cell size

	Finest	**Fine**	**Medium**	**Coarse**	**Coarsest**
Minimum cell size (m)	1.00E-06	4.00E-06	6.00E-06	8.00E-06	1.60E-05
Maximum cell size (m)	1.00E-05	4.00E-05	6.00E-05	8.00E-05	1.60E-04
Maximum cell length (m)	0.000025	0.0001	0.00015	0.0002	0.0004

The velocity profile across three different planes was taken at 25%, 50% and 75% of the length of the channel at the centre of the height and across the width. The inlet

flow rate was also checked to be the same as the output to 3 significant figures and the area weighted average pressure on each of these planes was measured and the percentage change in the pressure less than 1% as well as the wall shear stress at h=2, w=0 and w=W to 3 significant figures.

3.8.5 Development Length

To measure the velocity change due to the effect of increased stenosis in the GPV set up it is important to know the development length before extracting data. A line was drawn down the length of the channel through the stenosis and the velocity was plotted as shown in Figure 3.22. When the velocity first stabilised the development length was found. This was used to design geometries and extract data excluding regions where the flow was not fully developed.

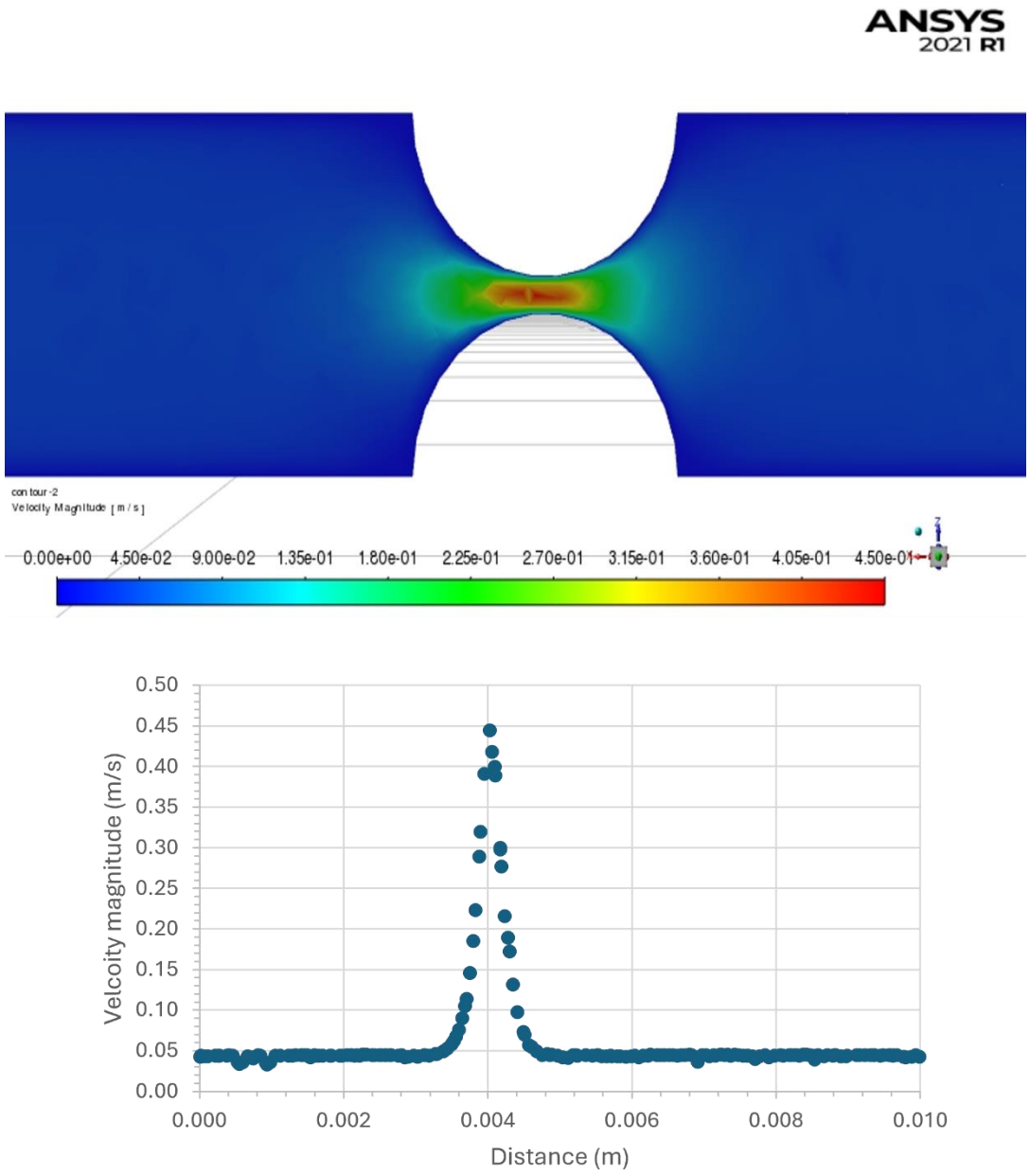

Figure 3.22: Velocity magnitude obtained from the CFD model with varying stenosis- the width at the base of each peak can be considered the length before flow normalises

Chapter 4 The Effect of Changing Geometry on Velocity Magnitude and Wall Shear Stress in an *In Vitro* Capillary Stenosis Model

4.1 Introduction

This chapter is concerned with the impact of changing the geometry of an *in vitro* model of a stenosed blood vessel (capillary) upon the flow rate, pressure drop, velocity distribution, and wall shear stress observed. The research presented in this chapter illustrates the trends and values of velocity change, shear stress and flow rate when resistance is increased, and the cross-sectional area of the stenosis is decreased. The sensitivity of these parameters in response to increasing stenosis and increased resistance were investigated both experimentally using GPV and numerically via CFD. The models were developed to quantify how shear stress behaviour changes as a response to increased stenosis and resistance; so that biological studies can be conducted into cell response under these conditions, perhaps, leading to a detectable level of change in biomarker response. It is expected there will be a peak of shear stress on the walls in all regions of the device, as the influence of increasing resistance becomes more significant (198). The consequences of these findings are discussed within the context of ACS.

4.1.2 Selection of Parameters

Within this chapter, a variety of pressures will be explored to mimic *in vivo* conditions, the upstream pressure of the microfluidic device was set to be constant at 2000, 3200 or 4700 Pa. 3200 Pa was chosen as this is the average pressure within the thigh muscle where 69% of ACS occurs (199) and the flow is generally not pulsatile in the capillaries (200). The pressure was selected to be a constant variable as in the body the pressure from the heart cannot be specifically altered by request.

4.1.3 Experimental Models

Microfluidic models with various cross-sectional areas were created according to § 3.2: with the measured cross-sectional dimensions (width × height) of 400 × 131 μm (+/- 5%), 300 × 145 μm (+/- 3%) and 200 × 57 μm (+/- 10%), with degrees of stenosis set to 0, 20, 40 and 60% of the overall width. These models were chosen to investigate different aspect ratios. A longer stenotic model was also created to measure the impact of increased resistance in the system, as detailed in materials and methods § 3.4, with dimensions of 200 x 58 μm (+/- 6%). CFD models matching these geometries were also created and used as specified in § 3.8.

Table 4.1: Accuracy of straight channel geometry fabrication using photolithography

Device width (μm)	**SU-8**	**Max spin speed (rpm)**	**Expected height (μm)** (157)	**Actual height (μm)**
400	2075	2100	100	124-138
300	2075	1600	150	142-150
200	Dilute 2075	1700	50	52-58

The accuracy of the photolithography process was assessed by measuring the variation in channel height across each wafer following the method described in § 3.5. With SU-8 2075 and spin speeds according to the manufacturer, the expected height can be compared to the actual height. For the 400 μm model there was a large range >10%, of variation in the fabrication, in the 300 μm model the photolithography process prepared moulds that were within the 10% accuracy range. For diluted SU-8 2075, the maximum measured height was over the expected height by over 10%.

Various parameters such as humidity and temperature will affect the viscosity of the SU-8 and thus may have influenced the spin coating process.

4.1.4 Measurements

The measurements were taken from the centre of the stenotic area and the top measurement was taken from 0.005 m along the channel. The location of the measurements was the same in the long stenosis model and in CFD models.

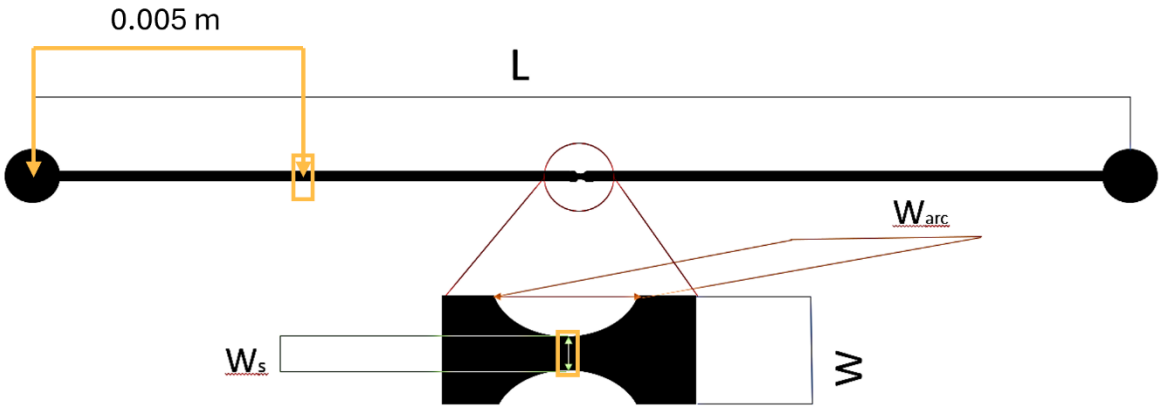

Figure 4.1: Short stenosis model depicting where the stenotic and main channel measurements were taken from with yellow boxes

4.1.5 Selection of Recording Speed

The recording speed was tested according to recommendations from Table 2.7 in Chapter 2, however, it was determined that the most suitable frame rates are as follows in Table 4.2.

Table 4.2: Frame rates used for capture of GPV measurements

	Recording frame rate			
Model (see §2.4)	**Main channel**	**Resolution**	**Stenosis**	**Resolution**
400	40000-50000	768 (w) x 496 (h) - 512 (w) x 512 (h)	75000	510 (w) x 336 (h)
300	40000-50000	768 (w) x 496 (h)- 512 (w) x 512 (h)	75000	510 (w) x 336 (h)
200	10000-20000	1024 (w) x 1024 - 768 (h)	20000	1024 (w) x 1024-768 (h)
Long stenosis	10000-20000	1024 (w) x 1024-768 (h)	20000	1024 (w) x 1024-768 (h)

4.2 Calculation of Variables

4.2.1 Analytical Resistance and Flow Rate

Conceptually, there are two competing factors controlling flow as discussed in § 2.5 (1)(8). According to continuity, for an incompressible (constant density) fluid (50):

$$A_1 v_1 = A_2 v_2 = Q \tag{4.1}$$

Where Q is the flow rate, A is the cross-sectional area and v is the mean average velocity.

Additionally, in pressure-driven flows, increasing the resistance, R, at constant pressure differential, ΔP, will decrease the flow rate, Q (201).

$$Q = \frac{\Delta P}{R} \tag{4.2}$$

To estimate the correct frame rate for GPV the analytical flow rate was calculated using Equation 4.2, where the resistance is calculated using Equations 4.3 and 4.4 for cylindrical (the tubing) and rectangular (the channel) pipes respectively (202):

$$R = \frac{128\mu L}{\pi d^4} \tag{4.3}$$

$$R = \frac{1}{1 - 0.63\left(\frac{h}{w}\right)} \frac{12\mu L}{h^3 w} \tag{4.4}$$

The resistance of the tubing, R_1+R_7, was calculated to be $5.22\ x\ 10^{11}\ Pa\ s\ m^{-3}$ for the total 80 cm of tubing used in the experimental set-up at 20°C.

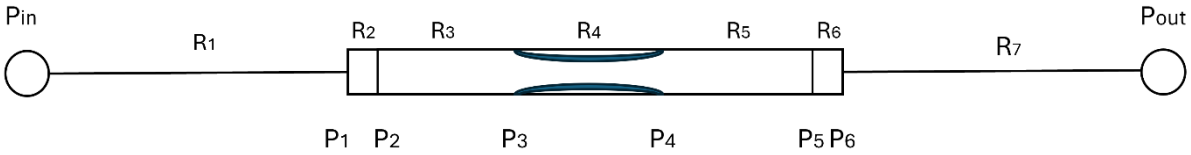

Figure 4.2: A diagram representing the microfluidic set-up with resistances

The inlet pressures here are the same input variables in the experiment and simulations, 2000, 3200 and 4700 Pa. The output pressure is 0 Pa (gauge). The resistance of the tubing R_1 + R_7 was discussed above. The head losses throughout microfluidic systems are difficult to estimate due to their size and are usually determined by CFD or experimentally and depend on the value of the Reynolds number (203). Although loss coefficients for turbulent flow are well-researched, in laminar systems these are determined experimentally (204). In microfluidic systems and particularly those mimicking the circulatory system these losses are important (205). Some research estimates the head loss due to fittings as 10%, other research uses loss coefficient methods (typically only agreeing with experiments for Re> 2300 (205)) or estimates head losses of 2 x 10^{-4} m from P_2-P_1 for microfluidic tubing to PDMS connections (205).

Here a head loss coefficient value of 0.3, k, was used in Equation 4.5 to calculate the pressure loss due to fittings, P_2-P_1 and P_6-P_5. This is a minor loss and due to the low velocity was deemed negligible <1% (206).

$$\frac{\Delta P}{\rho g} = k\frac{v^2}{2g} \tag{4.5}$$

Thus, the system becomes as follows, P_1=P_2 and P_5=P_6.

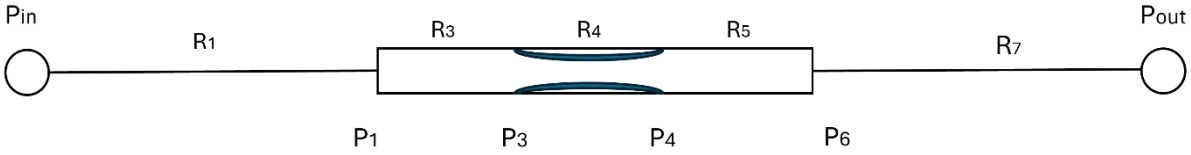

Figure 4.3: A diagram of the microfluidic set-up with simplified resistances

The flow rate in the system was approximated by estimating the resistance of the system as a whole combining the tubing resistance and the resistance of the microfluidic device as calculated by Equations 4.6 and 4.7 (135).

For straight channels:

$$R_{dev} = R_3 + R_4 + R_5 \tag{4.6}$$

and

$$R_{TOT} = R_1 + R_{dev} + R_7 \tag{4.7}$$

Then using Equation 4.8, the flow rate can be calculated throughout the system as resistance is summative.

$$Q = \frac{\Delta P}{R_{TOT}} \tag{4.8}$$

To find P_1 and P_6 the Hagen-Poiseuille Equation for laminar flow of Newtonian fluids in cylindrical pipes can be used as the tubing has a circular cross-section, the flow is laminar and incompressible (207).

$$\Delta P = \frac{128\mu LQ}{\pi d_0^4} \tag{2.11}$$

The pressure drop across the stenosis can be approximated using the head loss method as above for fittings, Equation 4.5, for gradual expansion and gradual reduction. For gradual expansion the ratio of diameter change at the higher diameter (main channel) to the lower diameter (stenosis) should be calculated and the k value found from graphs in literature such as in McFarland (206), and for a gradual reduction k = 0.04 (206).

For each geometry with 0% stenosis resistance was calculated using Equation 4.4 as shown in Table 4.3.

Table 4.3: Device resistance calculations for straight channel

Device (μm)	**Resistance without tubing (Pa s m^{-3})**
400	4.86×10^{11}
300	4.50×10^{11}
200	1.36×10^{13}

The resistance and flow rate of the geometries with stenosis could not be estimated without using CFD. To calculate the loss according to Equation 4.5, the velocity value in the contraction is needed. The velocity value cannot be determined without the

flow rate value and the flow rate value requires the resistance. Thus, only analytical values for straight channels are provided in Table 4.4 and Table 4.5.

Table 4.4: Analytical flow rate as calculated following the above method

Non-stenosed devices	Resistance with tubing (Pas/m^3)	Q at 2000 Pa (m^3/s)	Q at 3200 Pa (m^3/s)	Q at 4700 Pa (m^3/s)
200	1.42×10^{13}	1.41×10^{-10}	2.26×10^{-10}	3.32×10^{-10}
300	9.71×10^{11}	2.06×10^{-9}	3.29×10^{-9}	4.84×10^{-9}
400	1.01×10^{12}	1.98×10^{-9}	3.17×10^{-9}	4.66×10^{-9}

Table 4.5: Analytical mean average velocity magnitude as calculated following the above method

	Average velocity (m/s)		
Device	**2000 Pa**	**3200 Pa**	**4700 Pa**
200	0.014	0.022	0.032
300	0.046	0.073	0.108
400	0.039	0.063	0.093

4.2.2 Flow Rate from GPV Measurements

Firstly, the velocity profile is extracted from the GPV velocity magnitude spatial distribution map created following the method described in § 3.6.

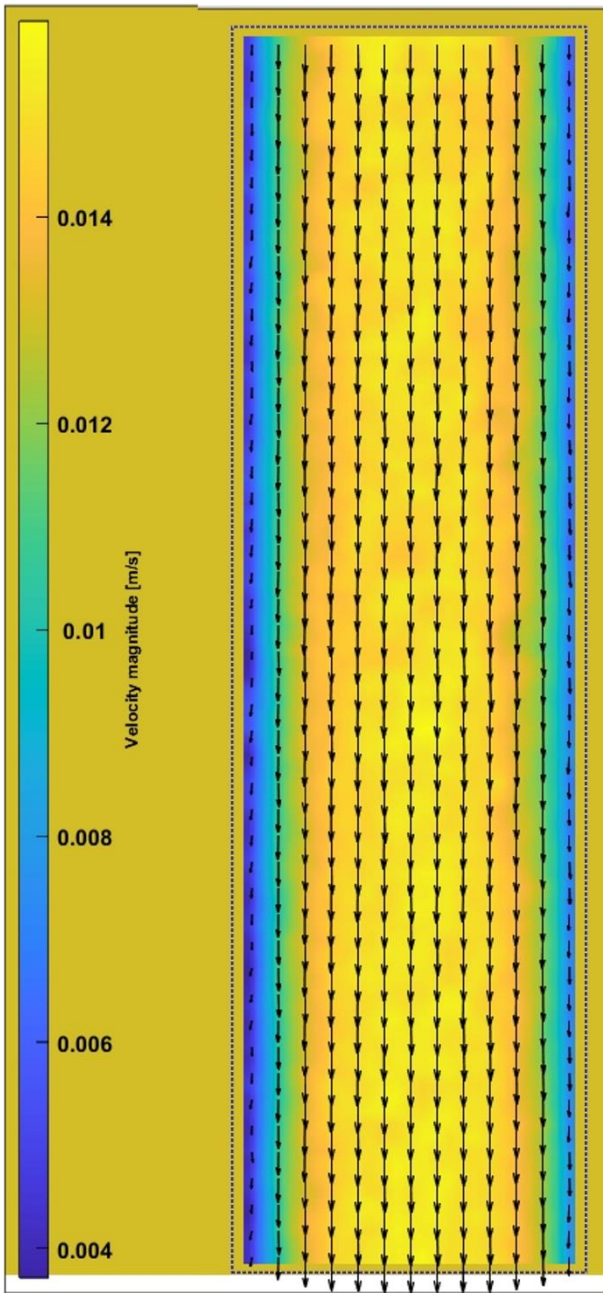

Figure 4.4: A spatial velocity distribution map as created using PIVLab of a 200 µm straight channel at 2000 Pa

The values for flow rate were calculated by taking the average velocity magnitude in the channel from the velocity profile taken at h=h/2 and multiplying it by the cross-sectional area as seen in Figure 3.14 and done in Schofield, 2019, for GPV

measurements. This method gives an estimate of the flow rate which can be over or under based on the aspect ratio (208).

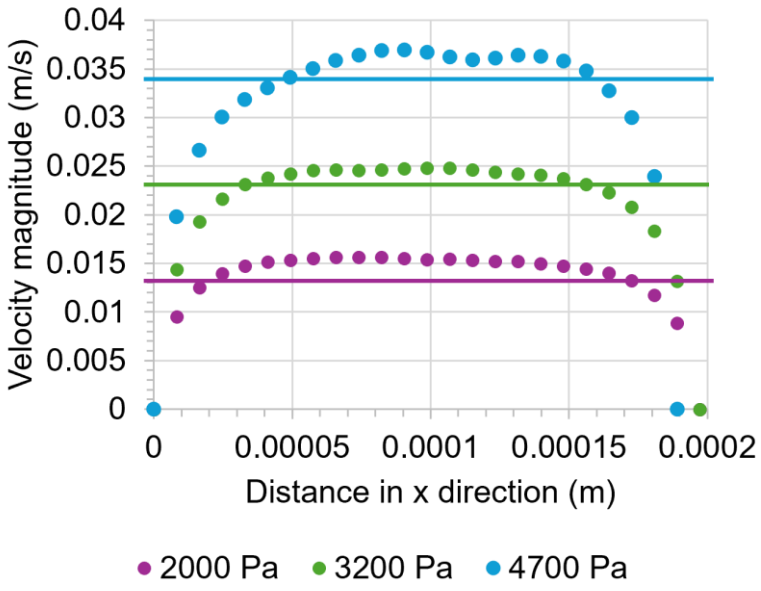

Figure 4.5: A velocity profile showing the average velocity shown by a line and velocity profiles at 2000 Pa, 3200 Pa and 4700 Pa in the 200 µm straight channel model

The GPV measurement of flow rate was calculated by measuring the mean average velocity from the range of planes depicted by the volume coloured in light blue in Figure 4.6 which the microscope measures controlled by the aperture, set to 20%. The mean average velocity is therefore the mean average velocity of the blue area, the maximum velocities in the central plane are underestimated by GPV, but in the whole height are overestimated. When this value is used as U_{av} in $Q = U_{av} . A_c$, this becomes an under/overestimate of the flow rate depending on the aspect ratio, if the plane is measured where w>>h. This work has been investigated by Tanyeri *et al.* (208).

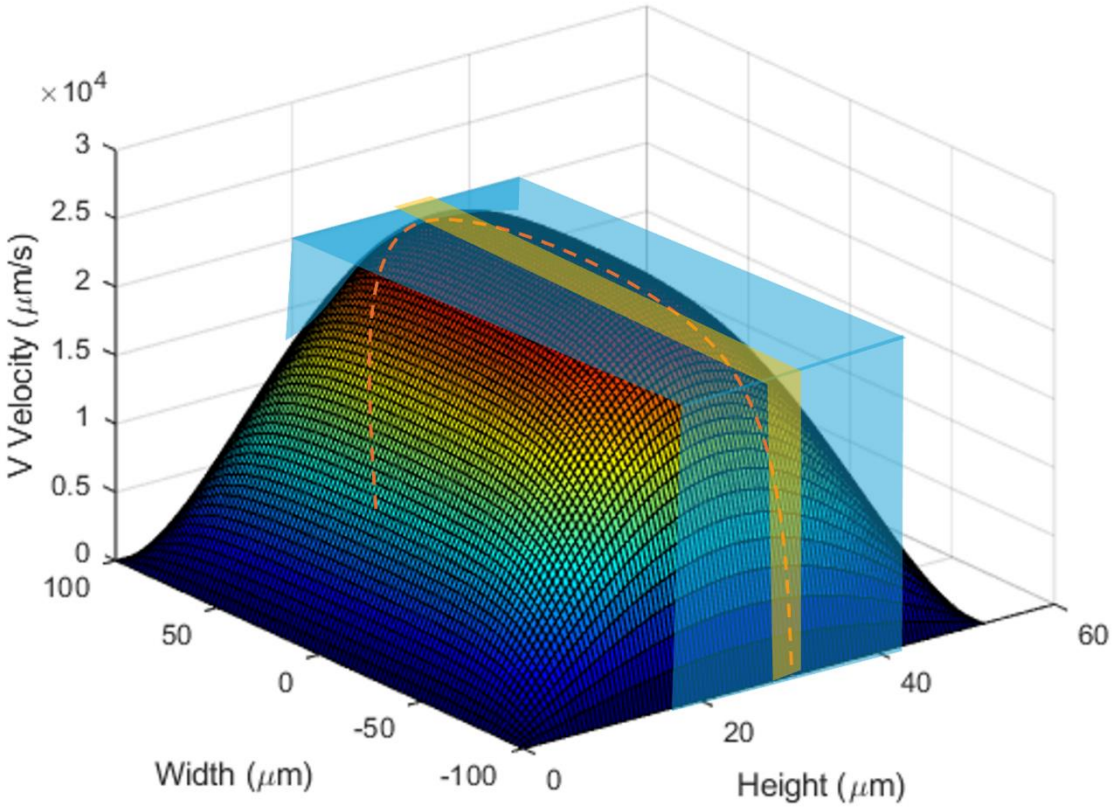

Figure 4.6: A 3D depiction of the velocity profile in a 200 x 57 μm channel with highlighted regions, the orange plane and line to show the central plane where CFD measurements are taken, representing the averaging determined by cell size see Appendix 2, and the blue section to show the region at which the GPV measurement was taken from. The 3D topography of the graph is created following Tanyeri's Equation 2.16 from § 2.5 with the matching parameters from the 200 x 57 μm microfluidic device dimensions.

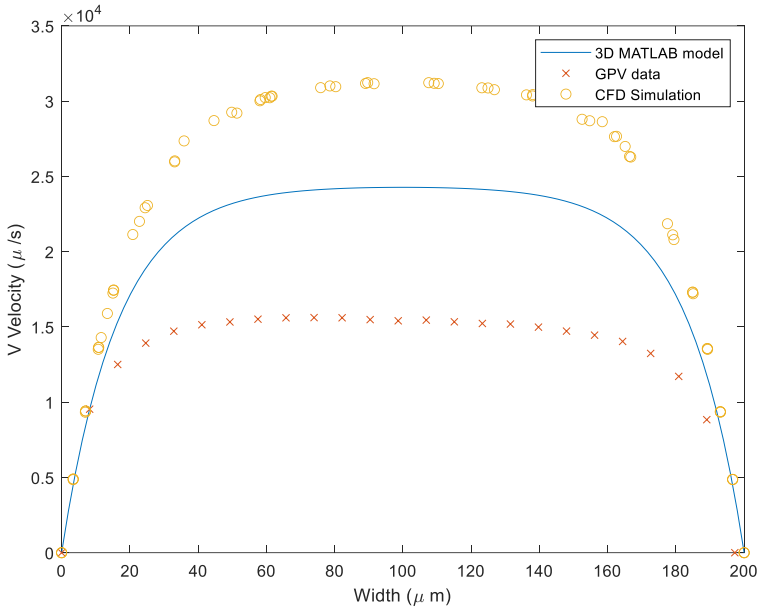

Figure 4.7: Extraction from 3D model comparing GPV, CFD and model data for a 200 x 57 µm channel at 2000 Pa

The mean velocity value was extracted from the GPV through calculating the mean average of the velocity magnitude vectors extracted. The cross-sectional area was calculated using a minimum of 8 measurements taken according to § 3.5 in the methods chapter and using the mean average value. Maximum and minimum measurements for flow rate were calculated using the maximum/minimum average velocity (average +/- standard deviation) multiplied by the maximum/ minimum cross-sectional areas (average +/- standard deviation) as summarised in Table 4.6.

Table 4.6: Estimation of maximum and minimum flow rate from GPV data

Flow rate estimation		**Height**	
		Minimum height (average - standard deviation) h_{min}	**Maximum height (average + standard deviation) h_{max}**
Velocity	Minimum velocity (average - standard deviation) v_{min}	$Q_{min} = v_{min} \cdot h_{min}$	$Q_{mid1} = v_{min} \cdot h_{max}$
	Maximum velocity (average + standard deviation) v_{max}	$Q_{mid2} = v_{max} \cdot h_{min}$	$Q_{max} = v_{max} \cdot h_{max}$

The values were calculated in this way as there was up to 10% variation of height across the channel moulds which, at these fine geometries, must be accounted for when comparing measurements. Not accounting for the fluctuations in geometry excludes the possibility at this small scale for direct comparison of values of flow rate when quantifying the effect of increased resistance.

4.2.3 GPV Flow Rate Compared to Analytical Flow Rate

Figure 4.8 shows the difference between the analytical flow rate as calculated following the method above, Equations 4.2-4.7, and the flow rate as calculated using GPV. For the 200 μm model, the GPV gave a very close value to the analytical value for all pressures tested. This, however, was not the case with the 300 or 400 μm models, which both gave larger estimates away from the analytical value, particularly that in 300 μm at 3200 Pa. This may be due to the smaller measurement region to channel height ratio, blue region in Figure 4.6, in the 300 and 400 μm models, as the heights of these channel were greater on average at 145 and 131 μm respectively. Additionally, this could be due to not enough resistance in the system to maintain a stable flow rate from the pressure controller in the larger channels.

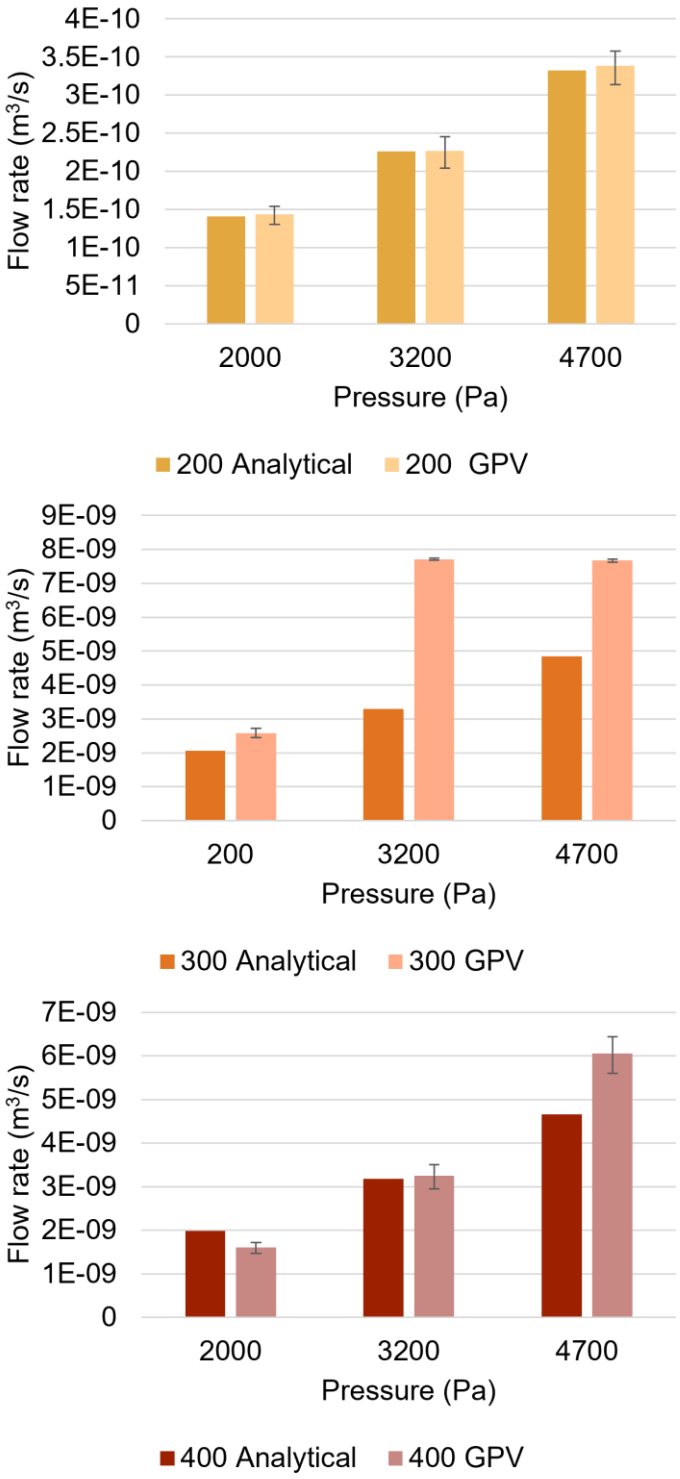

Figure 4.8: Analytical and GPV flow rates for each straight channel, 200, 300 and 400 µm at 2000 Pa, 3200 Pa, and 4700 Pa including the maximum and minimum GPV readings.

It is important to quantify the resistance in the system, as compared to the device, to measure the comparable effect of resistance caused by stenosis vs the tubing. Table 3.7 estimates the percentage of pressure drop on the tubing as a percentage of the total pressure drop across the system for all geometries.

Table 4.7: Percentage of pressure drop on tubing as a percentage of the total system pressure drop

Device (*μm)*	**2000 Pa**	**3200 Pa**	**4700 Pa**
200	2.39%	2.39%	2.39%
300	34.9%	34.9%	34.9%
400	33.6%	33.6%	33.6%

Table 4.7 shows the resistance of the tubing in the 200 μm model is of the lowest percentage, showing changes in the device should have a greater impact on the overall flow rate. Whereas in the 300 and 400 μm models, small geometric changes in the device may not impact the overall flow rate as significantly as there is a lower percentage of resistance on the device. There will also be greater variation in flow rate in the 400 and 300 μm models due to there being less resistance to maintain a stable flow.

4.2.4 Wall Shear Stress from GPV Measurements

The wall shear stress in different regions of the vessel is determined via Newton's law of viscosity as discussed in § 2.5.1 and requires measurement of the shear rate, $\frac{dv}{dx}$, in the vicinity of the wall as shown in Figure 4.9.

$$\tau_w = \mu \frac{dv}{dx} \tag{2.20}$$

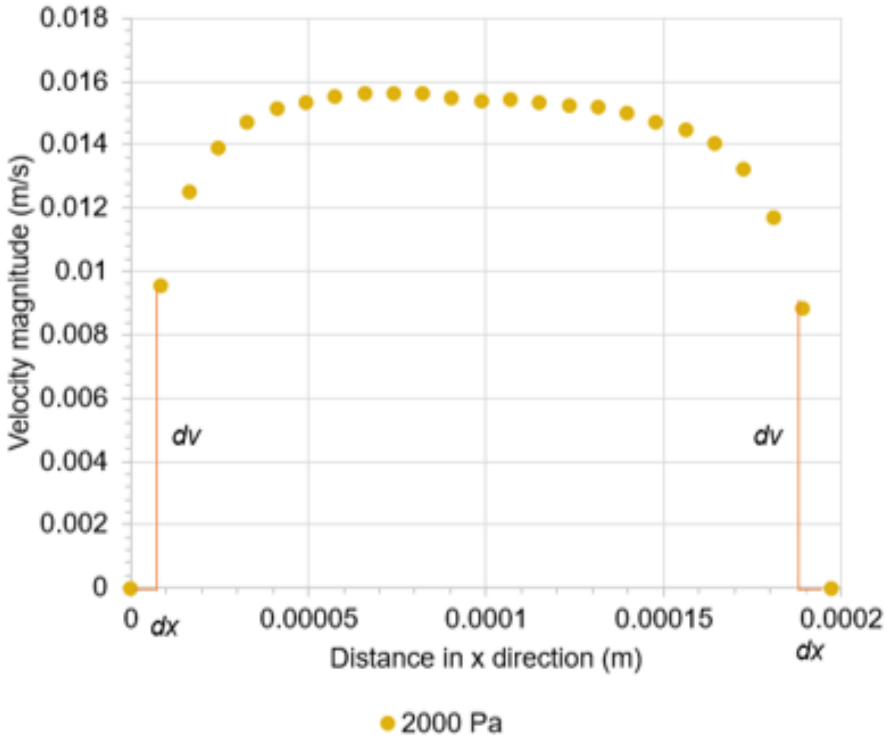

Figure 4.9: Velocity profile showing velocity vectors used in extracting wall shear stress for the 200 μm straight channel device at 2000 Pa

Figure 4.9 shows the velocity profile when extracted is parabolic, with deviation away from a quadratic fit due to the rectangular cross-section. Calculation of the shear stress near the wall is complicated by the resolution of the measurements and also the implication of no slip at the wall. The shear stress may vary depending on the region of the microfluidic device and therefore is important to quantify in different locations when creating stenotic models and when comparing to *in vivo* data.

The determination of shear stress from GPV is difficult due to the nature of GPV data analysis in PIVLab. The interrogation areas are calculated as depicted in Figure 4.10 when using an FFT window correlation algorithm- which leads to the final vector on across the line of measurement being calculated from an interrogation area which

overlaps with the excluded zone, as shown in Figure 4.10. This is true and characteristic of the PIV and GPV techniques (209). Previous works have corrected this error when taking shear stress measurements by zeroing the final half-pass vector calculated at the wall (210,211). This can be done as there is a zero velocity at the wall and as there is no slip in viscous incompressible laminar flows as is in the case in these experiments (212)(213).

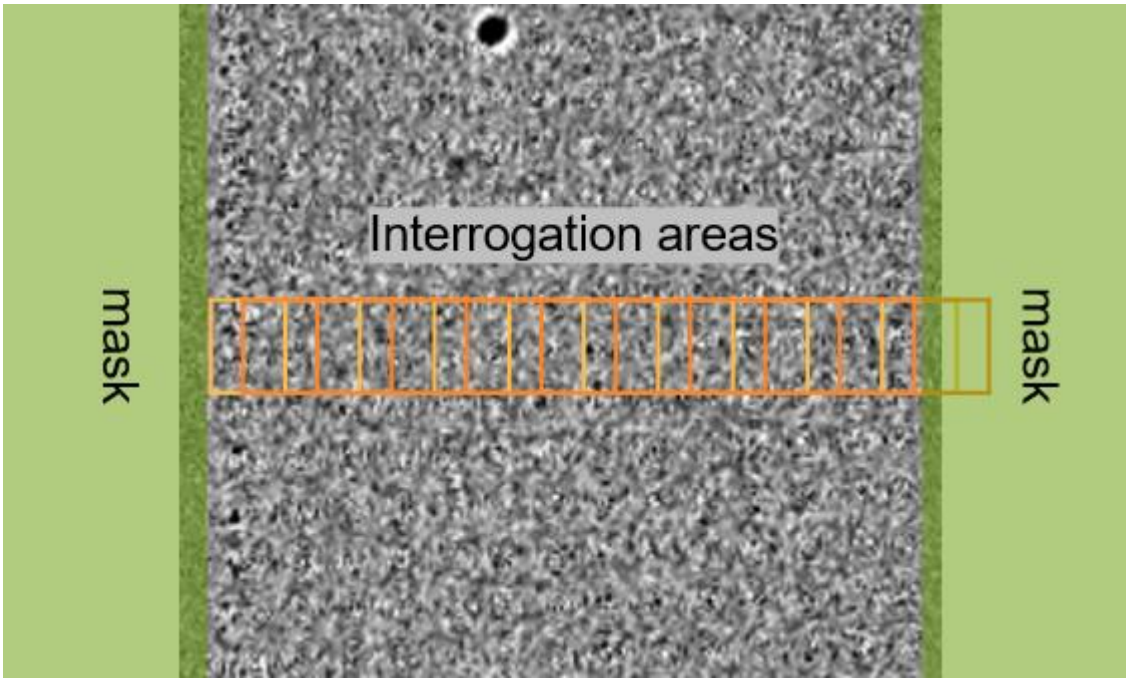

Figure 4.10: Illustration depicting the interrogation areas (yellow) and pass overlap (orange) across the stenosis when using an FFT window correlation algorithm each box is 8 px x 8 px on a 200 μm channel (not to scale)

The velocity gradient was calculated for both sides of the channel width, with the velocity extract being taken from the halfway height plane of the stenosis and averaged over 3 runs with the standard deviation plotted as detailed in Appendix 3.

4.2.5 Effect of Resolution

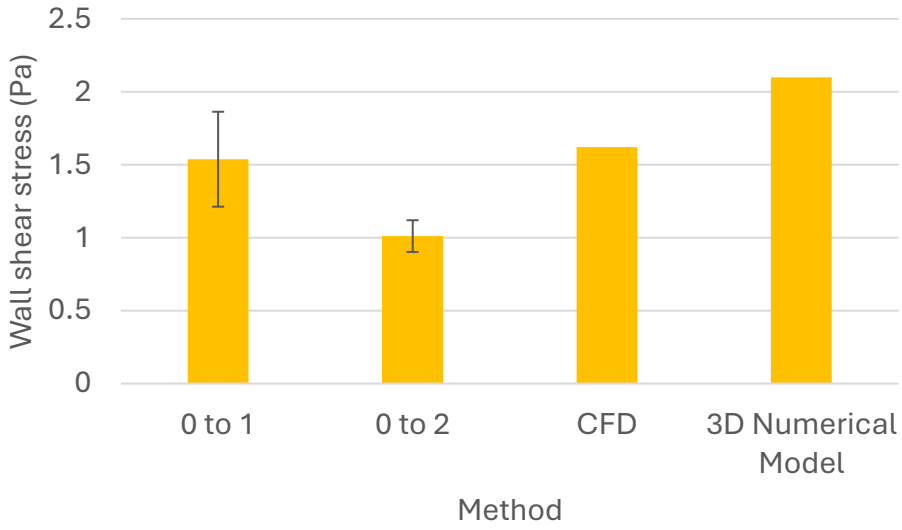

Figure 4.11: Different methods of calculating shear stress on the straight channel 200 μm model at 2000 Pa

To investigate the effect based on resolution, the shear stress as calculated from the first vectors starting at the wall, 0 and 1, in the velocity profile (as seen in Figure 4.9), $\tau_{0,1} = \mu \frac{dv_{0,1}}{dx_{0,1}}$, was compared to the value, $\tau_{0,2} = \mu \frac{dv_{0,2}}{dx_{0,2}}$. This was seen to be statistically different from the wall shear stress calculated using $\frac{dv_{0,1}}{dx_{0,1}}$. The shear stress value when calculated using $\frac{dv_{0,1}}{dx_{0,1}}$, had the largest standard deviation between the measurements from either side of the channel as detailed in Appendix 3. The $\tau_{0,1}$ value was used due to the agreement with CFD and most accurate measurement as it is closest to the wall. The value extracted from the 3D model as seen in Figure 4.6, created using Equation 2.16 from § 2.5, was greater than the 0 to 1 value and was not comparable.

Separated speckle pattern by mask

As seen by the parabolic velocity profile in Figure 4.9, there is a large range of velocity magnitudes that need to be captured using the same frame rate, with the fastest velocities being in the centre of the channel and lowest at the wall, where the shear stress is extracted.

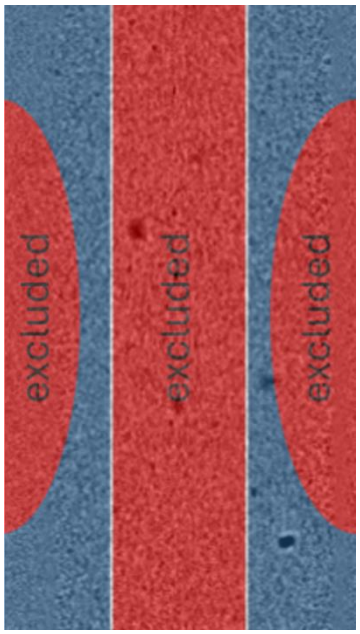

Figure 4.12: Alternative analysis PIV mask design in PIVLab covering GPV maximum velocity magnitude data at the stenosis

To reduce any error caused by the influence of the higher vectors from the centre of the channel in PIVLab, the centre section of the channel was excluded, and the algorithm ran on the outer portion of the channel as seen in blue in Figure 4.12. The value for wall shear stress was the same as the control method, $\frac{dv_{0,1}}{dx_{0,1}}$, however, was not statistically significant from the value calculated using $\frac{dv_{0,2}}{dx_{0,2}}$. This method was not used as it was the same as the control at the lower resolution method. The distance between each vector is determined by the interrogation area size and their overlap,

with a minimum of 8 px. Setting smaller interrogation areas caused the PIVLab software, used for analysis, to exceed its maximum memory limit and not perform the algorithm or analysis, limiting the resolution.

4.2.6 Determination of Wall Shear Stress from CFD Data

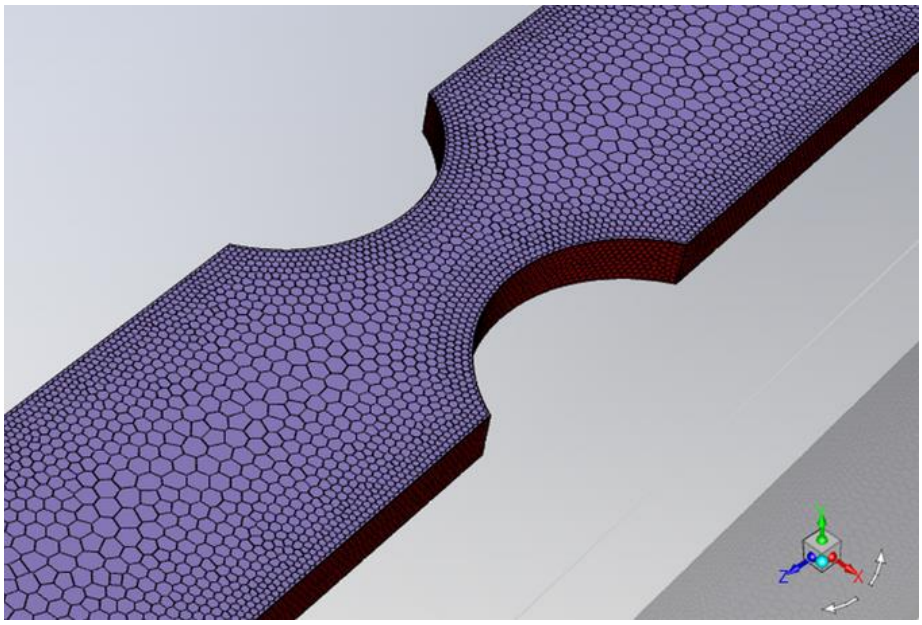

Figure 4.13: CFD mesh showing additional boundary layers to improve wall resolution

The wall shear stress value from CFD was calculated by extracting the shear stress at the refined mesh edge as described in §3.8. The mesh had boundary layers applied to improve the resolution and achieve more accurate wall shear stress values.

The CFD shear stress value is higher than that calculated from $\tau_{0,1=\mu} \frac{dv_{0,1}}{dx_{0,1}}$. The CFD samples from one central line at the maximum velocity profile give a higher average

of velocity vectors and thus wall shear stress than that of $\tau_{0,1} = \mu \frac{dv_{0,1}}{dx_{0,1}}$, because of this being reduced, due to including the influence of many planes as depicted in Figure 4.6. The CFD values provide estimates higher at the maximum velocities, but show closer velocity values at the walls. This could be due to the refined mesh, or due to the GPV sampling technique. The mesh independence of each model was investigated to determine the relative effect as seen in Table 4.8.

Table 4.8: Mesh independence data for the 200 μm straight channel model

	Finest	**Fine**	**Medium**	**Coarse**	**Coarsest**
Minimum cell size (m)	1.00×10^{-6}	4.00×10^{-6}	6.00×10^{-6}	8.00×10^{-6}	1.60×10^{-5}
Maximum cell size (m)	1.00×10^{-5}	4.00×10^{-5}	6.00×10^{-5}	8.00×10^{-5}	1.60×10^{-4}
Maximum cell length (m)	0.000025	0.0001	0.00015	0.0002	0.0004
Number of cells (For 200 non stenosed)	2327537	2275914	1376534	851856	598969

As maximum velocity is different between the CFD and GPV data, in order to validate between them, the flow rate from the CFD was compared to that calculated experimentally from the GPV to ensure the model is representative of the GPV, in addition to the wall shear stress and pressure as described in Chapter 3. Therefore, CFD should be used to calculate shear stress values.

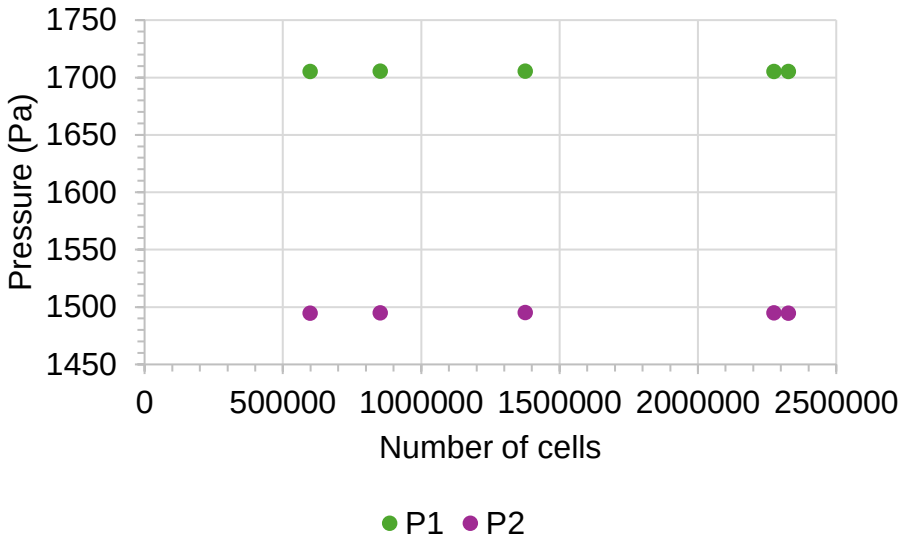

Figure 4.14: Number of cells vs pressure extracted across two planes P1, P2 for various mesh sizes in Table 3.13.

The coarsest mesh had the lowest run time, and the mesh was not made to have fewer cells as this would be likely to decrease the velocity when extracted from the centre plane as it would have calculated the area from a larger voxel not specifically capturing the velocity maximum as depicted in Figure 4.15.

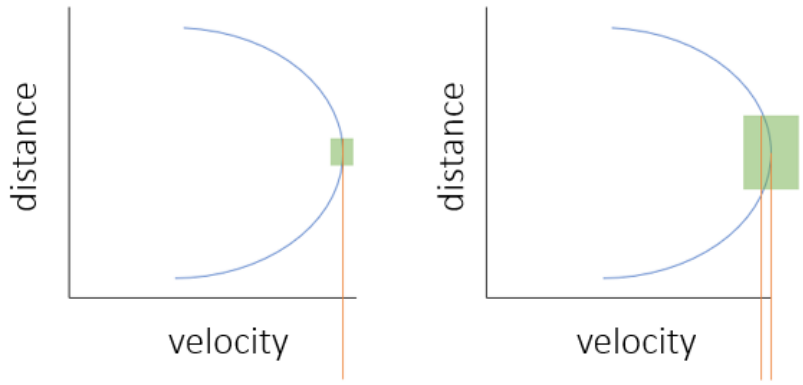

Figure 4.15: Area over which the finite volume would calculate velocity if cell size was increased

4.3 Error Quantification: Channel Aspect Ratio and Flow Rate Estimation

There are competing factors to be considered when estimating flow rate as the experimental flow rate is difficult to determine. The bucket test was found to give inappropriate estimations of flow rate due to many factors such as evaporation effects, capillarity and eventual clogging of the device over the timeframe needed to get accurate measurements, (30 minutes) when microparticle dispersions were used for all channels tested. The experimental flow rate is known to be an estimation as discussed previously and the CFD flow rate does not account for pressure losses in the tubing or fittings, however, these may be calculated if the flow rate and the resistances at this region are known.

Using the GPV and CFD values for flow rate and the resistance of the tubing the values for pressure loss in the tubing become 417, 849, and 1582 Pa at 2000, 3200, and 4700 Pa input pressures respectively for the 400 μm straight channel. The resistance in the system is summative so for example by adding the tubing and 400 μm device at 4700 Pa the flow rate was calculated using Equation 3.3, to be 3.25×10^{-9} m^3 /s. The total pressure drop in the tubing was calculated to be 824, 1319 and 1938 Pa for the 2000, 3200 and 4700 Pa pressures respectively. These values were inputted into the relevant CFD model and the output values are displayed in Figure 4.16.

The 200 μm model was also tested to cover the maximum and minimum geometries tested. The pressure drops used for the CFD model were 75, 120 and 175 Pa for 2000, 3200 and 4700 Pa respectively.

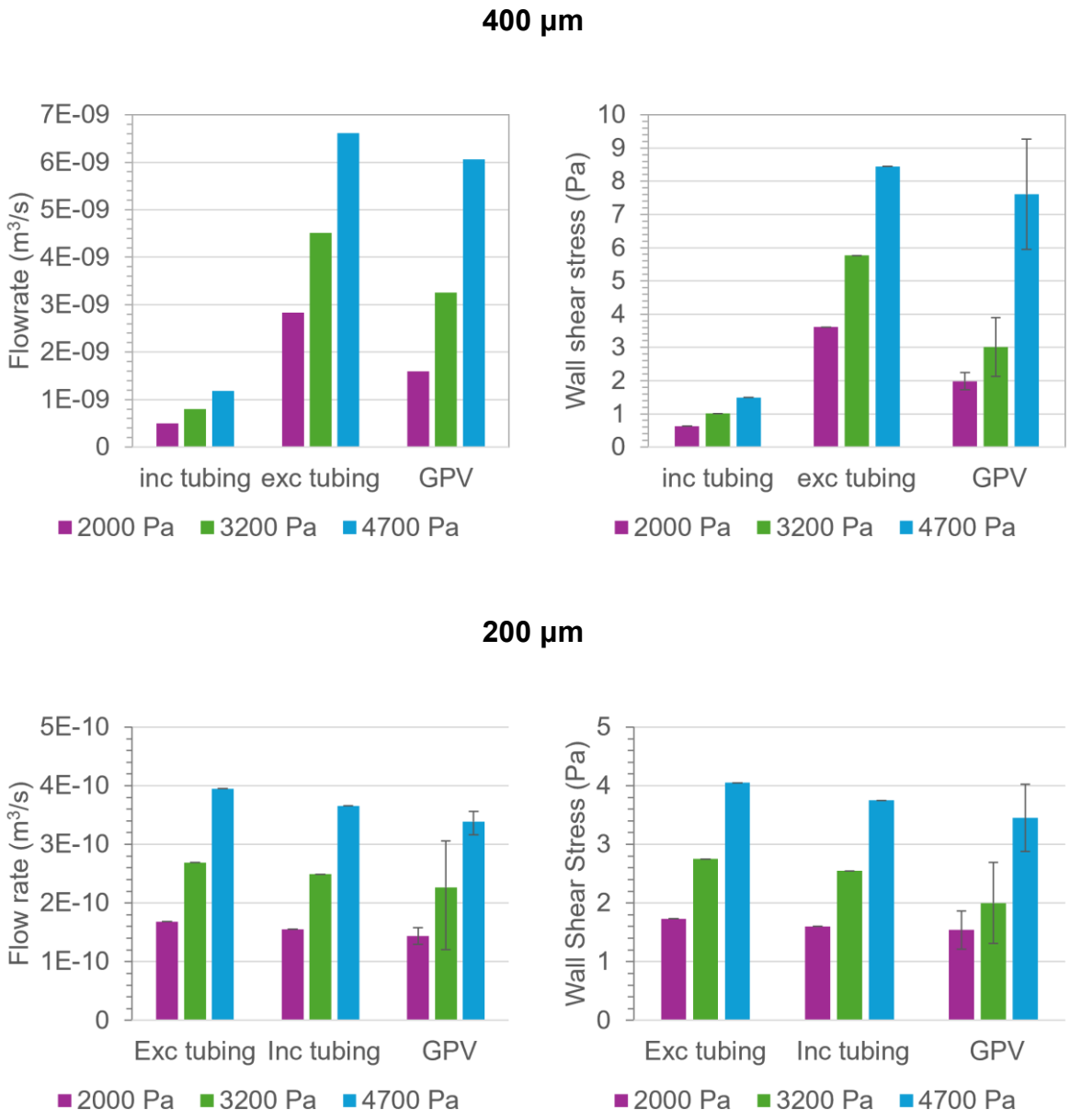

Figure 4.16: Flow rate and shear stress values extracted from CFD including tubing resistance, excluding tubing resistance and the GPV values at 2000, 3200 and 4700 Pa of the 400 and 200 µm model

Figure 4.16 shows for flow rate, for the 400 µm model it was found that excluding the pressure loss due to tubing gave a closer estimation of the flow rate found when measured using GPV. Excluding the tubing will give an overestimate as there will be losses in the tubing, and including the tubing gives a lower reading than is found with

GPV. For the 200 μm model both including and excluding the tubing models give good agreement with the CFD model for both wall shear stress and flow rate, likely as the pressure loss in the tubing is calculated to be 2.39%, which may be considered negligible.

Both including and excluding the pressure loss due to tubing in the 200 μm model give models that are within the range of GPV error making them both suitable for use and validated using GPV measurements. The excluded tubing model is used as these are definite values in the experiment that can be measured, as at the time of the experiment no commercially available pressure sensor could measure the pressure differential needed at these points and thus the true losses in the tubing could not be known. There was also better agreement with the exclusion of tubing models across both aspect ratios.

Tanyeri *et al.* proposed Equation 4.9, to estimate the flow rate in a microfluidic channel where α is the aspect ratio h/w (208).

$$Q \approx \frac{h^4 \Delta P}{12 \mu L \alpha}(1 - 0.63\alpha) \qquad (4.9)$$

However, when these values were calculated for the 400 μm channel it was found that the approximation gave higher results than expected, the CFD simulations agreed better with the data collected from GPV. Tanyeri's approximation is for a channel with a low aspect ratio, thus for the 400 μm design, there is a greater error and better models such as CFD should be used to better estimate the flow rate. The GPV flow rate was calculated using the method described in § 3.6, the approximation

values do not include the pressure loss in the tubing which for the 400 μm device will be substantial and thus why these values are overestimates.

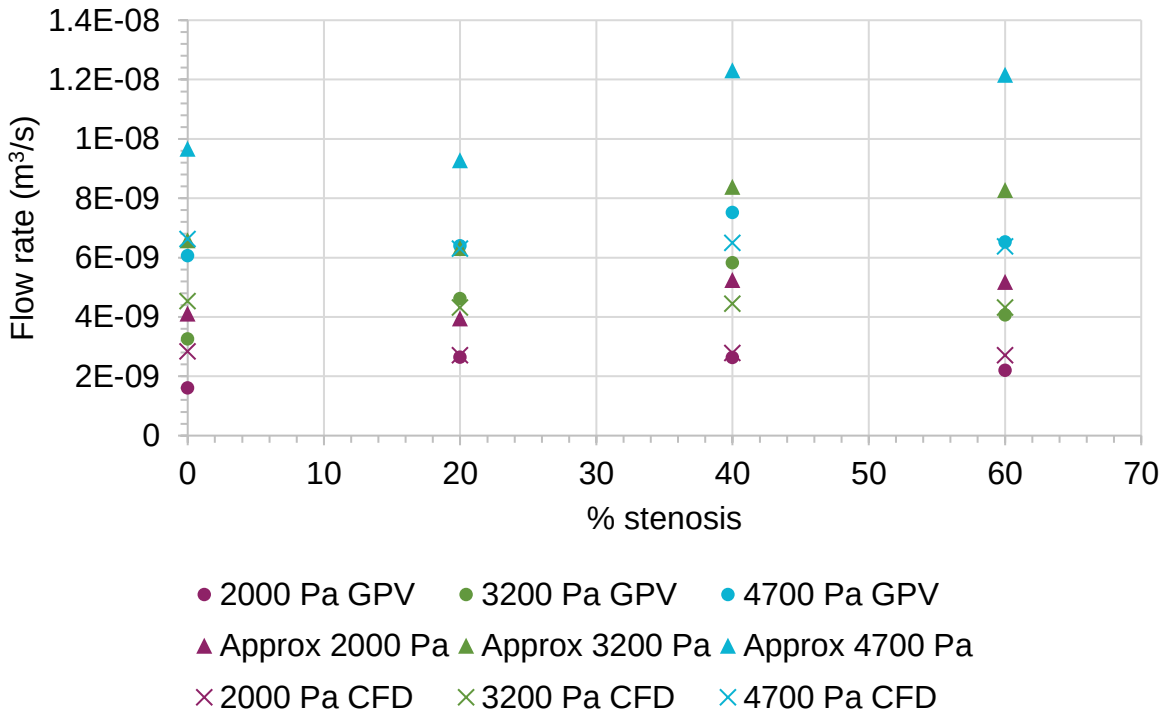

Figure 4.17: Flow rate calculations using the method described in § 4.2 from GPV, Tanyeri's approximation and CFD values based on a pressure input in the 400 μm *model*

Additionally, work by Hudson et al. (214) found that depending on the aspect ratio of the microfluidic channel there is a ratio of maximum velocity to average velocity which could be used to calculate a flow rate, the ratio being 1.8 for 4:1. The maximum to average velocity values were plotted against GPV values from the short stenotic models.

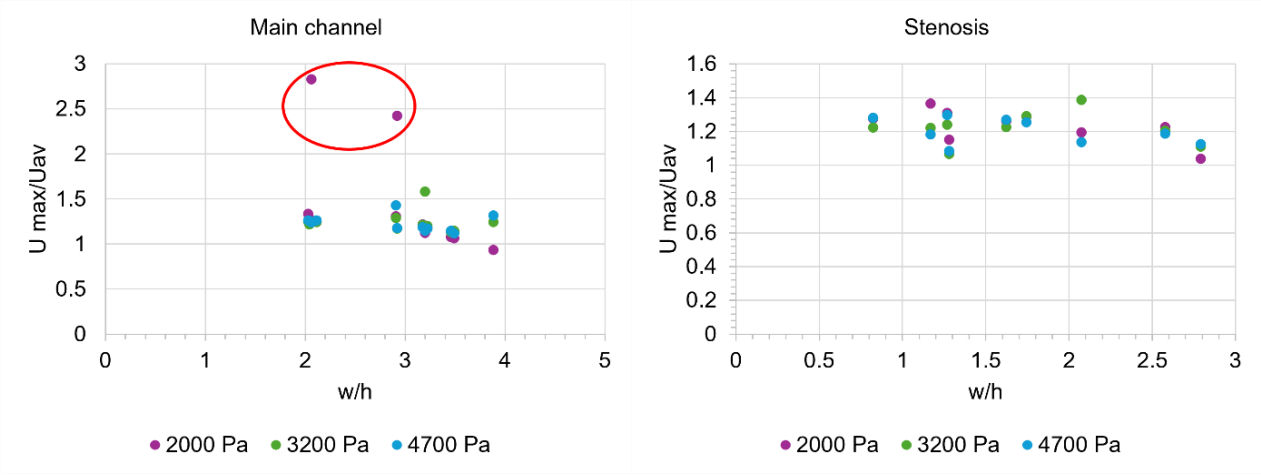

Figure 4.18: a b aspect ratios of the channels in the a) main channel and b) stenotic region and the relative maximum velocity to average velocity.

The experimental data shows that for the main channel the ratio of U max to U average falls at 1.3, however when removing the two data points for 2000 Pa at 60% stenosis for 300 and 400, circled, this value becomes 1.22 and for the stenotic region this value is 1.22. This quantifies how much the GPV technique overestimates. The maximum value we know is underestimated as it is taken from a range of planes. The average value is therefore overestimated due to the sampling method discussed in § 4.2.3.

Taking the maximum velocity measured from GPV, the average velocity and flow rate values were calculated, through dividing the maximum velocity by 1.8 following the aforementioned research by Hudson *et al* to give the average; and multiplying by the channel cross sectional area to calculate flow rate. These flow rate values were inputted into the 400 µm non-stenosed CFD model.

Table 4.9: Values for input into CFD simulation using a 1.8 ratio as suggested in work by Hudson et al. to 3 significant figures

Pressure (Pa)	Max velocity (m/s)	Av velocity (m/s)	Flow rate (m^3/s)
2000	0.0386	0.0215	1.08×10^{-7}
3200	0.0784	0.0436	2.20×10^{-7}
4700	0.143	0.0793	3.99×10^{-7}

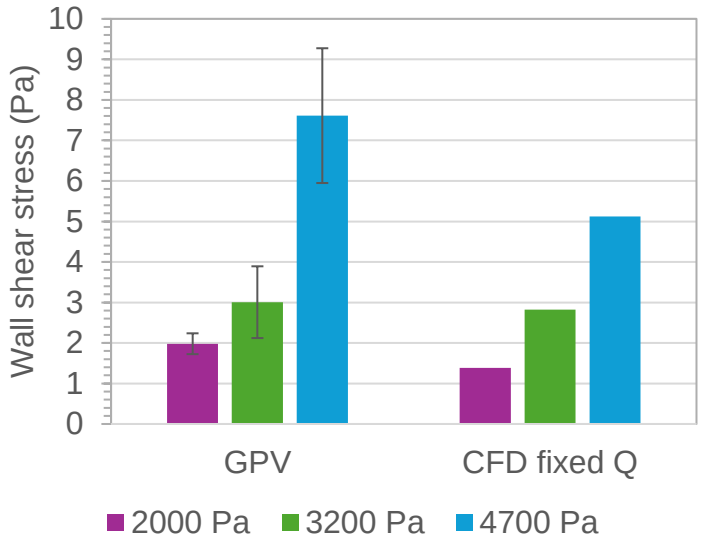

Figure 4.19: Wall shear stress values extracted from the CFD simulation where a fixed flow rate was applied, calculated using Hudson's 1.18 ratio of maximum to average velocity based on aspect ratio

The results show that for a fixed flow rate as calculated above in Table 4.9, the wall shear stress was underestimated by the CFD model as compared to the GPV. The wall shear stress as measured with GPV here is an overestimate as is known from the method of extraction and the bias introduced from the higher velocities in the channel centre. This is shown that for 4700 Pa the wall shear stress shows the largest difference. Additionally, the experimental flow is pressure-driven and not a

fixed flow rate. Therefore, to ensure there are no missed phenomena, particularly that of the effect on flow rate by increased resistance through devices, the fixed flow rate model was not used.

4.3.1 Flowrate in Different Aspect Ratios

Between each individual, there is biological variation, including the size of the blood vessel (215)(216)(217). Additionally, depending on the patient, there will be variations in lumen diameter such as cholesterol level, a build-up of fat on the wall and elasticity of the blood vessel wall due to health and age (218). This may influence ACS, as with a smaller lumen area there is a balance between pressure driving force and flow resistance, which will dictate fluid flow rate; in the absence of the latter, a higher velocity will be observed in the stenosis if a constant pressure driving force is maintained. However, depending on the degree of stenosis, an increase in flow resistance of the capillary may significantly decrease the bulk blood flow rate. If the patients' capillary resistance before experiencing trauma is already relatively high due to their health, microvascular collapse may occur faster, decreasing the time the clinician has available to decide whether to operate to relieve pressure. The resistance of the system increases in the time before microvascular collapse according to the pathophysiology of ACS as described in §2.1.1. As there is ultimately greater pressure externally to internally, and thus the lumen diameter is decreased, and the flow inside decreases until collapse occurs and blood flow stops (1). It is therefore important to test a range of pressures and cross-sectional areas to account for biological variance when creating a blood vessel model.

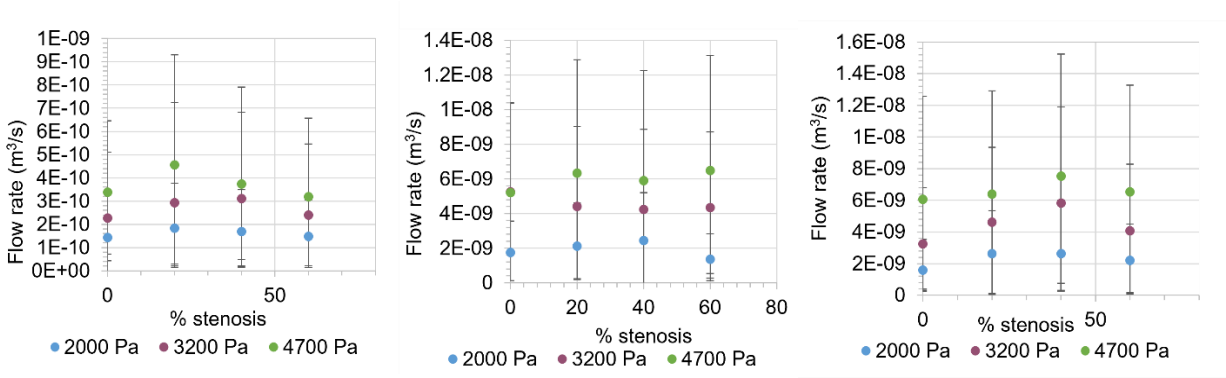

Figure 4.20 shows the flow rates in the 0, 20, 40 and 60% stenosis models from the (left to right) 200 µm, 300 µm and 400 µm devices.

Figure 4.20 shows in the 400 and 300 µm models the flow rate does not significantly decrease as stenosis increases. Although there is variation in the area throughout the device, there are large error bars which prevent direct comparison across devices with changing stenosis as discussed in § 4.2.2. There is no major change of resistance between the 300 and 400 µm models as the values of flow rate remain similar, 1.8 x 10^{-9} m^3/s to 8 x 10^{-9} m^3/s on average for each geometry respectively. This changes with the 200 µm model where the flow rate is an order of magnitude lower; from 1.3 x 10^{-10} m^3/s to 4.8 x 10^{-10} m^3/s. This is because of increasing resistance due to the geometry of each device as calculated in Table 4.4.

Compared to the analytical value of the tubing at 5.22 $\times$ 10^{11} Pa s m^{-3}, the resistance of the 300 and 400 µm models was not different enough to see small changes in flow rate imposed by the stenosis, therefore the decrease in flow rate was not seen. The 200 µm model was created with a greater resistance and this trend can be seen from the data shown in Figure 4.20c. At 200 µm the flow rate was 1.3 x 10^{-10} m^3/s to 4.8 x

10^{-10} m^3/s, and shows that there is increasing resistance by decreasing the geometry of the channel. Thus, to mimic microvascular collapse and ACS pathophysiology, it is important that the geometry has a higher resistance than the tubing, and the resistance across each model of that geometry increases through increasing the stenosis. Additionally, large ranges of variation of flow rate may be detectable in larger vessels such as the arteries/ veins.

In this model, the increase of resistance is quantified through flow rate decrease at constant pressure. *In vivo*, this could be done by measuring the blood flow through techniques such as near-infrared spectroscopy, NIRS or Doppler ultrasound and simultaneously measuring blood pressure (219).

4.3.2 Velocity magnitude changes with Decreasing Cross-Sectional Area

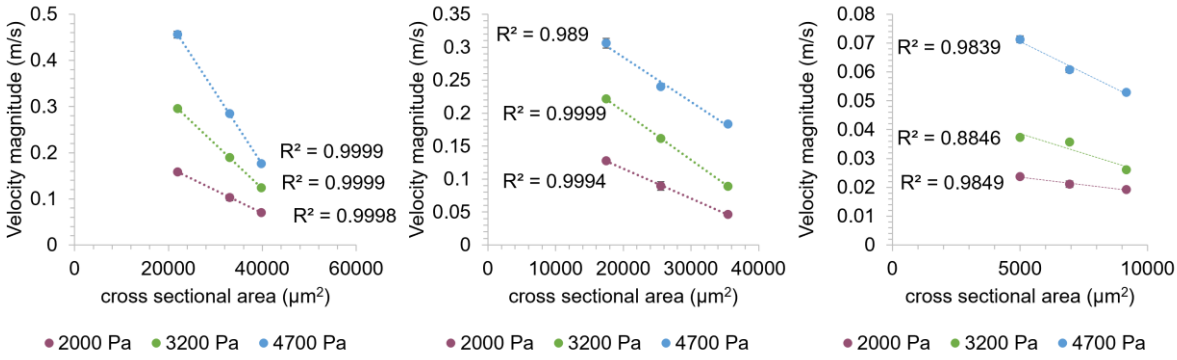

Figure 4.21 shows the velocity magnitudes in the 20, 40 and 60% stenosis models from the (left to right) 400 µm, 300 µm and 200 µm devices depending on their cross-sectional area

To account for changes seen in the cross-sectional area through each device- leading to the large error bars seen on flow rates in Figure 4.20, the average velocity

magnitude in the stenotic region compared to the cross-sectional area was plotted. This was done to examine the competing effects of coupling between cross-sectional area and maximum velocity if flow resistance changes are insignificant (constant flow rate, i.e. UA = constant) and increased flow resistance. Figures 4.21a and b show increasing the cross-sectional area in both 400 μm and 300 μm geometries leads to a decrease in velocity which is almost in inverse proportion. The R^2 values were > 0.999 for all pressures tested. This confirms that the continuity is observed when decreasing the cross-sectional area across devices and that given the data in Figure 4.21a, confirms the assumption that the flow rate was constant. For the 200 μm model; the average velocity for 2000, 3200 and 4700 Pa decreased less with increasing cross-sectional area than would be expected purely from as expected with continuity. This is due to the effect of increased resistance as discussed in §4.2.3.

These results show the importance of the change in flow rate and velocity magnitude over the short timeframe that ACS proceeds, from 3-10 h: both phenomena characterised by Equations 4.1 and 4.2 occur.

These changes are expected to occur sequentially as follows with increasing stenosis:

1) Stenosis increases, stenotic region mean velocity magnitude increases according to continuity, no detectable change in blood flow rate at the bulk/main channel level.
2) Stenosis further increases causing enough resistance to significantly decrease the mean velocity in the bulk/ main channel by decreasing the

flow rate, the stenosis mean velocity value will depend on the level of flow rate change due to resistance.

3) Stenosis increases and resistance is increased to the point where there is no flow, known as stopped-flow, defined as 0 m/s. *In vivo,* this would be synonymous with microvascular collapse and refers to when hypoxia, the lack of sufficient oxygen, begins due to the red blood cells being prevented from flowing to transfer oxygen (220)(221).

By investigating the trends and values of velocity change, shear stress and flow rate at which these three processes occur; it is possible that biological studies could be conducted into cell response under these conditions, perhaps, leading to a detectable level of change in biomarker response. Particularly, in response to shear stress changes as it is expected there will be a peak of shear stress as the influence of increasing resistance becomes more significant (198)(5).

4.4 Extraction and Validation of Shear Stress Data

The data for each model was collected following the decision tree in Figure 4.22.

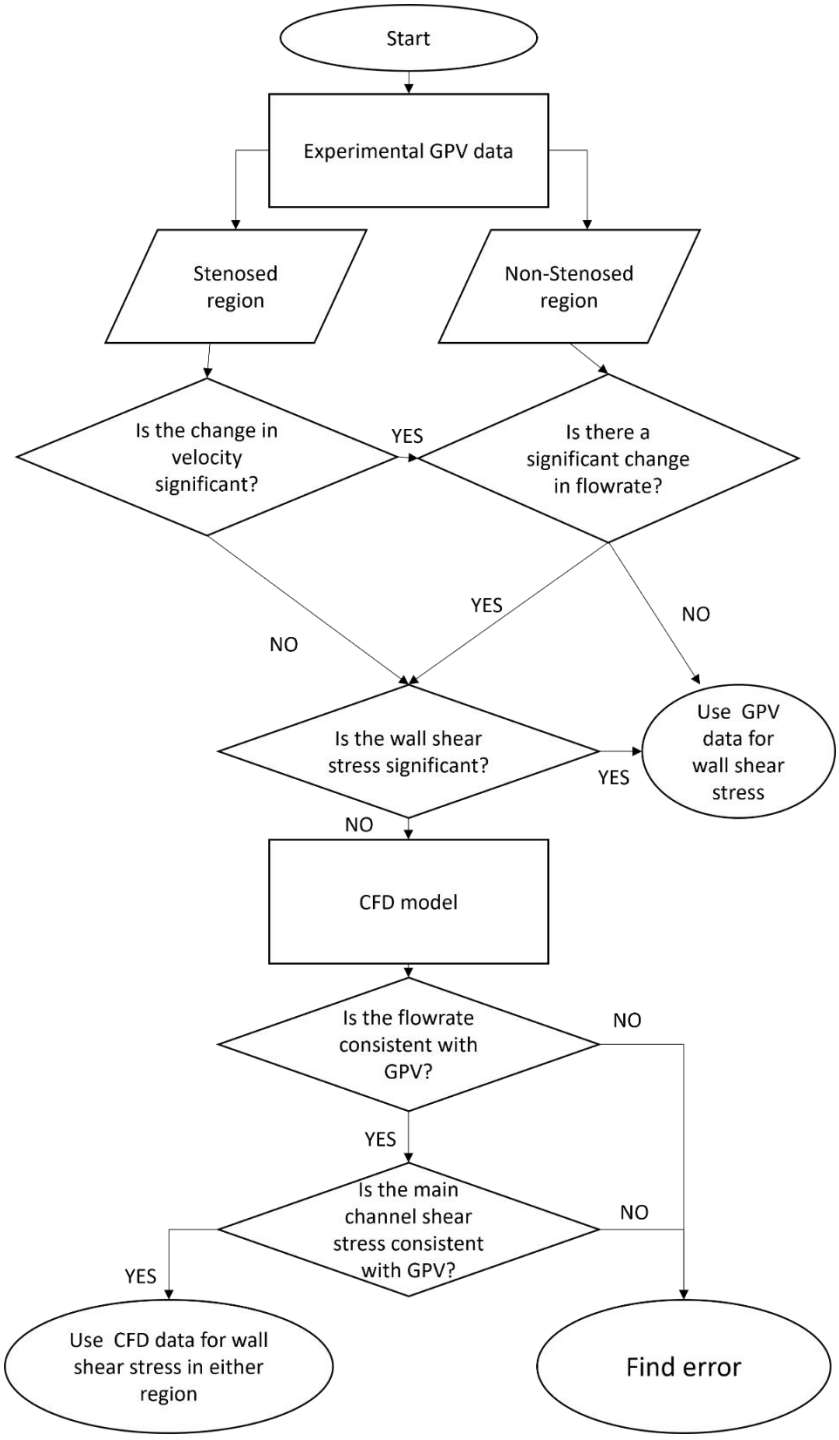

Figure 4.22: Decision tree depicting the selection and validation of shear stress measurements through CFD and GPV

Initially, experimental data was collected to investigate flow behaviour under each experimental condition. The velocity in the stenosed region is first considered as it

must be checked to increase in inverse proportion with cross-sectional area decrease, if the resistance is unchanged, following the method discussed above. This ensures that the fastest velocities are not only captured, validating the correct use of frame rate, but also giving the relative level of agreement and comparison between devices. The flow rates in the stenosed and non-stenosed regions are then checked for agreement to ensure the data is replicable and accurate and abides by continuity in the same device.

Next, the wall shear stress should be calculated and compared with increasing stenosis. Once a check for continuity is applied, other factors should be investigated such as fluctuations in geometry. If a valid reason for an unexpected velocity change, can be identified then the wall shear stress measurement is still valid, however, it should be noted that this applies to this set of specific variables and may deviate away from complete linearity.

If the wall shear stress measurements have large standard deviations and a trend cannot be identified the values can be checked against a CFD model. The CFD models are pressure-driven and the calculated flow rate should be checked to be in close agreement with the GPV detected flow rate (specifically as measured in the non-stenosed region to reduce any bias from steep velocity gradients) to validate the CFD model. The wall shear stress from the CFD model if in agreement with GPV can provide a more accurate and reproducible dataset as it is not limited by resolution if ensured to be mesh-independent. Finally, real-world variation can be quantified if reproducible data is obtained from experimental measurements that deviate away from the CFD model.

4.5 The effect of increasing the degree of stenosis on a 'short' stenosis 400 µm channel

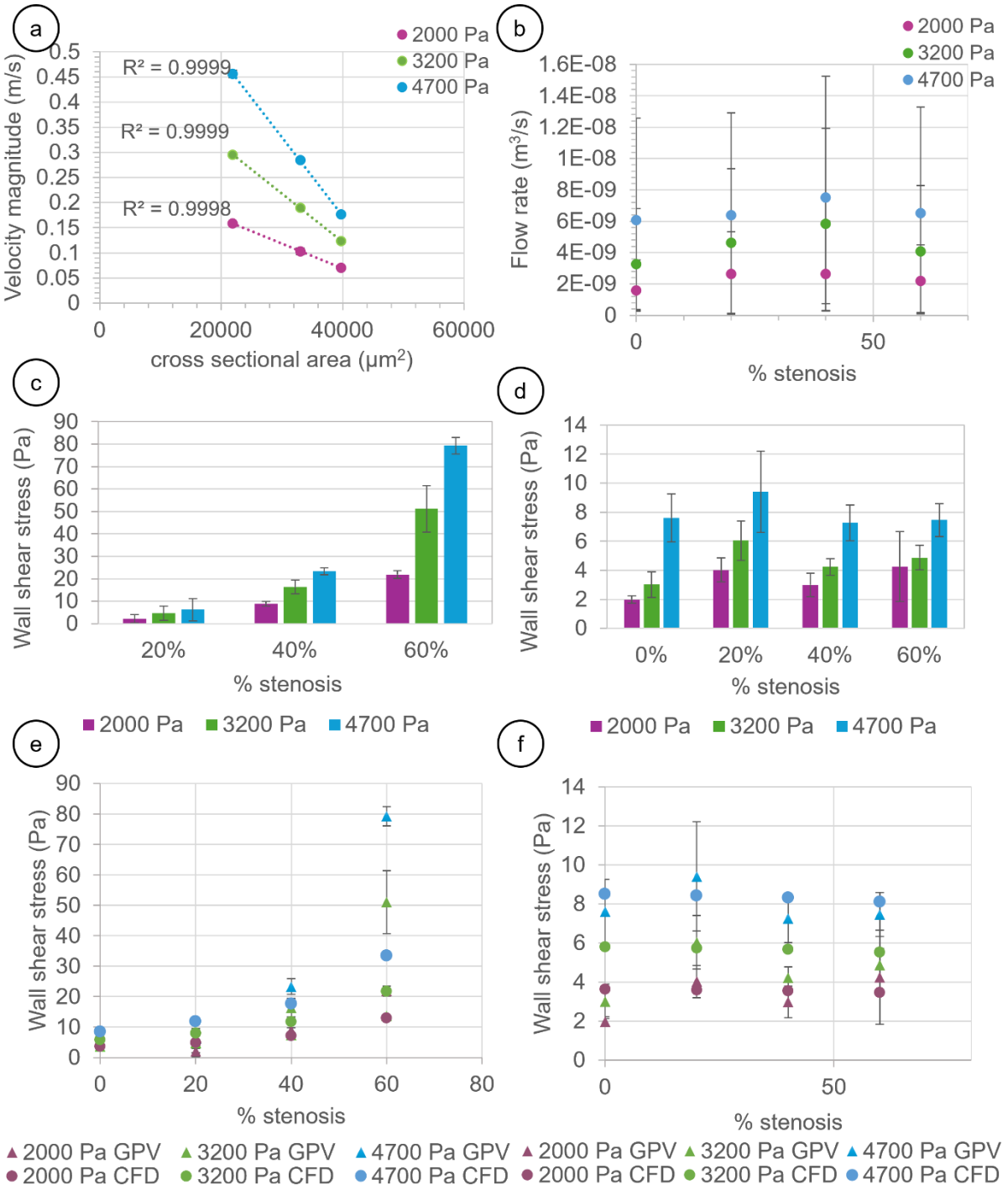

Figure 4.23: (a) The mean velocity magnitude of 400 µm devices with increasing cross-sectional area in the stenosed region with standard deviation, (b) The mean flow rate in the non-stenosed region of 400 µm devices with increasing stenosis with maxima and minima, (c) The wall shear stress in the stenosed region, (d) The wall shear stress in the non-stenosed region;(e) the wall shear stress in the stenosed region from GPV and CFD, (f) the wall shear stress in the non-stenosed region from GPV and CFD all at 20, 32 and 4700 Pa.

Figure 4.23a shows there is a linear decrease in average velocity magnitude with increasing cross-sectional area as expected with continuity. Figure 4.23b shows that the average flow rates were not significantly different according to standard deviations affected by the increase in the degree of stenosis, thus it can be concluded that the increased resistance caused by the stenosis in these cases is negligible. This suggests in practice in larger vessels, 400 x 126 μm in stenotic regions there needs to be greater than 60% stenosis to see a reduction in the bulk flow. *In vivo,* the flow rate decreasing as a result of increasing resistance is a key component of microvascular collapse and occurs in the early stages of acute compartment syndrome (222). *In vivo* there may be a point of stenosis there will be enough resistance to begin to see decreased blood flow and the beginning of capillary collapse which may pose an area for investigation for larger vessels.

Figure 4.23c shows with increasing stenosis there is a significant increase in the wall shear stress due to increased velocity gradient close to the wall in the stenotic region, which would have an impact on the endothelial cells lining a blood vessel should these phenomena be replicated *in vivo*.

Figure 4.23d shows in the non-stenotic region there are only very small changes in the wall shear stress values for the 20, 40 and 60% levels for all 2000, 3200 and 4700 Pa, as expected since the overall flow rate, and thus velocity gradient close to the wall, is unchanged, see Figure 4.23b. The small variations may be due to fluctuations in the channel width, thus affecting velocity, due to the fabrication method, for example, the 400 μm, 60% stenosis model had the largest variation in height down the geometry ranging from 115 to 139 μm.

Figure 4.23e shows the wall shear stress values from GPV as compared to CFD in the stenotic region. For the two lower applied pressures, at 20% stenosis, the CFD model gives very little change in values. At 2000 Pa the CFD model shear stress is slightly greater than the GPV, however, this could be due to the sampling range of GPV decreasing the flow rate measured, this is also the case for the 4700 Pa at 20%. At 40% stenosis, the CFD model accurately predicts the GPV at 2000 Pa. At 3200 and 4700 Pa, the CFD model underpredicts the values for shear stress at 40 and 60% stenosis. This may be due to the GPV algorithm overestimating the average velocity due to steep velocity gradients seen in papers by Hart *et al.* All CFD models were ensured to be mesh-independent with shear stress.

Figure 4.23f shows the CFD model has good agreement with the GPV in the non-stenosed region at 4700 Pa for all stenosis levels, at 3200 Pa for 20 and 60% stenosis and 2000 Pa for 20, 40 and 60% stenosis. This correlates to the lower shear stresses seen at 0 and 20% stenosis in Figure 4.23d at 2000 and 3200 Pa. At 40% stenosis 3200 Pa, it is seen that the experimental GPV wall shear stress is lower than the CFD, likely due to the same phenomena seen in Figure 4.23e.

Therefore, following the aforementioned decision tree, the wall shear stress in the stenotic area can be extracted from the CFD model for all 4700 Pa, 20 and 60% stenosis at 3200 Pa and 20-60% stenosis at 2000 Pa for all regions tested.

Such trends in behaviour are possible *in vivo,* i.e. the shear stress in larger channels may initially increase if a stenosis forms but then decrease as the flow rate becomes more restricted, however, this is not detectable in these 400 μm geometries up to 60% stenosis at 2000 - 4700 Pa. The shear stress values are for this specific model

and may be used to draw *in vitro-in vivo* correlations, however, data should be scaled accordingly when interpolating shear stress values *in vivo*. This can be done by the use of CFD models where geometries are not limited to the analysis method of experimental techniques. Dimensional analysis can be used for scaling, but there may be further phenomena that should be investigated experimentally where techniques allow such as elasticity of walls, blood rheology and a circular cross-sectional area. Correlations/ correction factors should be found from each of these variables to improve the model.

4.6 The effect of increasing stenosis on a ‘short stenosis’ 300 µm channel

Following the 400 µm geometries, four smaller 300 µm width devices with 0, 20, 40 and 60% stenosis were created with a reduced height of 142-150 µm and measured using GPV and modelled using CFD.

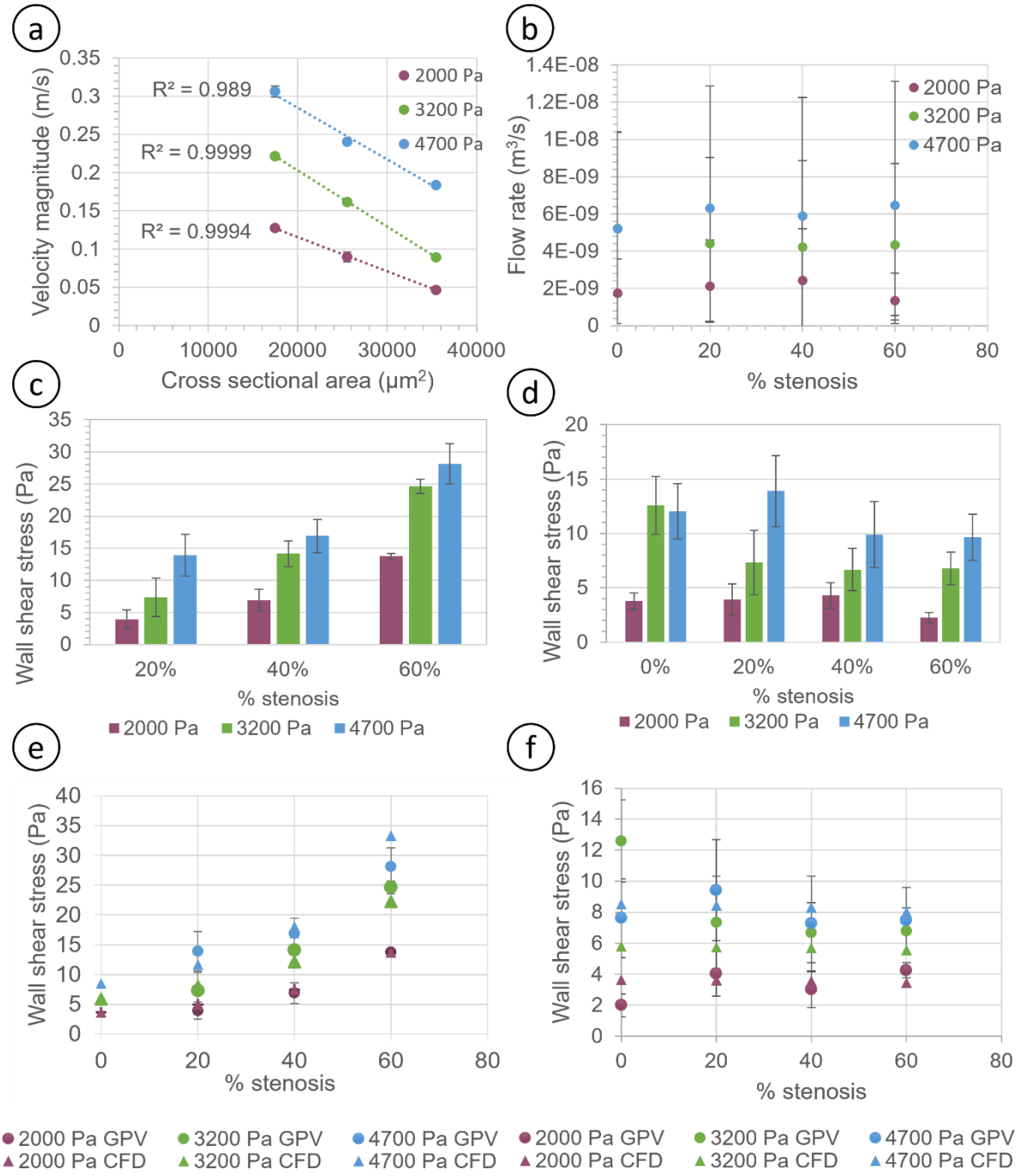

Figure 4.24 (a): The mean velocity magnitude of 300 μm devices with increasing cross-sectional area in the stenosed region and their standard deviations, (b) The mean flow of 300 μm devices with increasing stenosis in the non-stenosed region with their maxima and minima as calculated from the non-stenosed area (c), The wall shear stress in the stenosed region, (d) The wall shear stress in the non-stenosed region; all at 2000, 3200 and 4700 Pa, (e) The wall shear stress values as calculated from the 300 μm devices in the stenosed region from GPV and CFD, (f) The wall shear stress values from the non-stenosed region in the main channel

Figure 4.24a shows similarly to the 400 μm model, there is a linear decrease in velocity magnitude with increasing cross-sectional area as expected with continuity. Figure 4.24b shows that in the main channel, again, there was no significant change in flow rate with increasing stenosis, as for the previous case, indicating changes in flow resistance were again small.

Figure 4.24c shows that in the stenotic region, the wall shear stress significantly increased with increasing stenosis as seen with the 400 μm model. There is no significant difference between 3200 and 4700 Pa and 20% between 2000 and 3200 Pa. The range of wall shear stress here increases significantly with each pressure tested- this highlights the importance of considering blood pressure when taking shear stress measurements.

Figure 4.24d shows in the non-stenosed region of the channel the only significant difference measured with increasing stenosis was an increase in wall shear stress at 2000 Pa from the 40-60% stenosis.

Figure 4.24e shows the wall shear stress as estimated from GPV agreed with CFD for all models at 2000 Pa and 40 and 60% for 0 to 40%. For 60% at 3200 and 4700 Pa CFD estimated larger shear stress values, which could mean that the GPV value was underestimated due to the the inherent limitations of GPV.

Figure 4.24f shows the CFD model accurately predicts the wall shear stress at 0, 40 and 60% at 4700 Pa, 40% at 3200 Pa and 20 and 40% at 2000 Pa. Following the decision tree above, Figure 4.22, the wall shear stress in the stenotic region can be approximated using the CFD model for all regions.

Both of these models appropriately identified that increasing stenosis increases the wall shear stress in the stenotic region, however, due to the lack of additional resistance created by the stenosis in both the 300 and 400 μm models relative to the whole system; a smaller height 57 x 200 μm width geometry was tested.

4.7 The effect of increasing the degree of stenosis on the ‘short stenosis’ 200 μm channel

Following the 400 and 300 μm geometries, four smaller 200 μm width devices with 0, 20, 40 and 60% stenosis were created with a reduced height of 52-58 μm and measured using GPV and modelled using CFD.

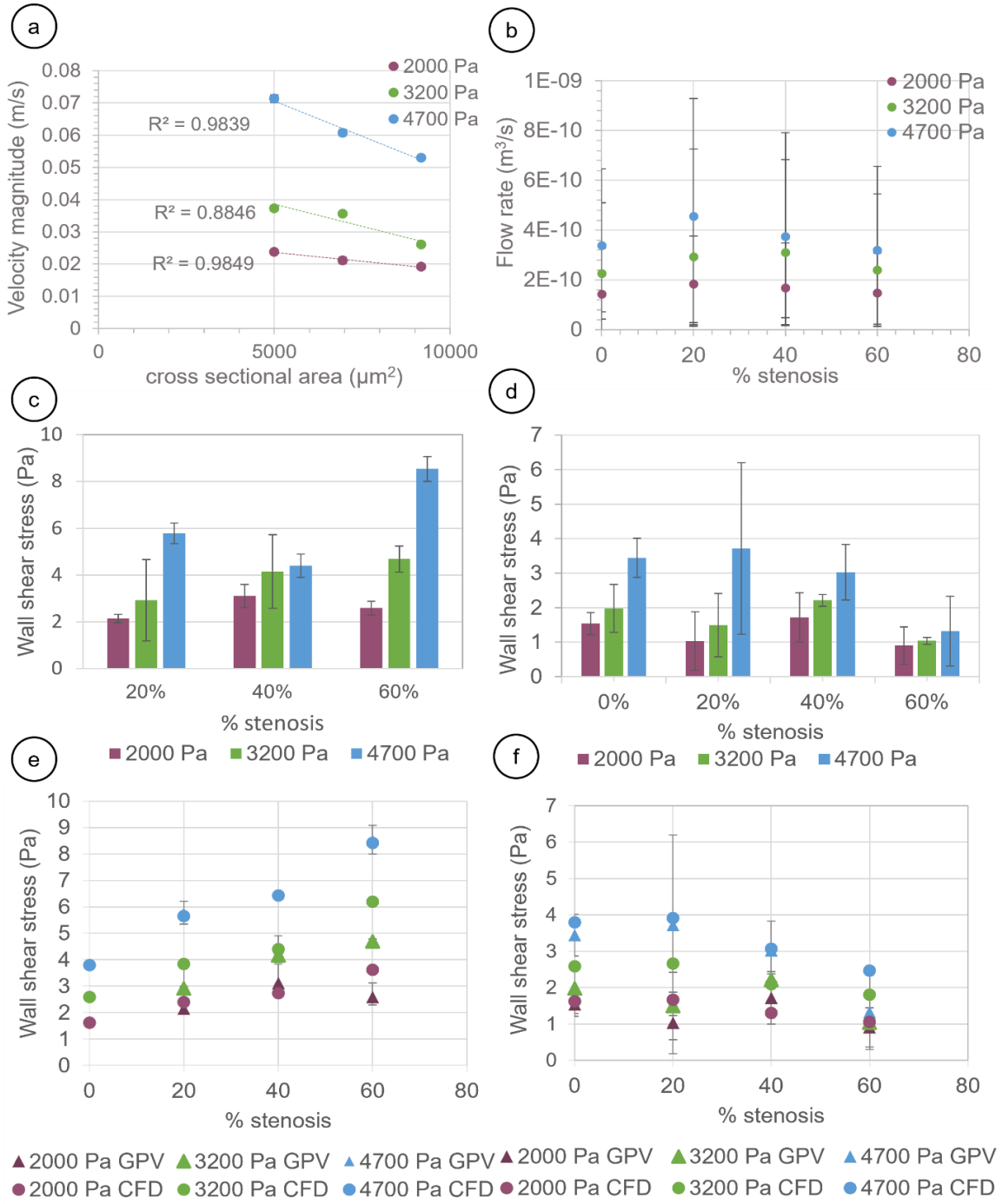

Figure 4.25 (a): The mean velocity magnitude of 200 μm devices with increasing cross-sectional area in the stenosed region and their standard deviations, (b) The mean flow rate of 200 μm devices with increasing stenosis in the non-stenosed region with their maxima and minima as calculated from the non-stenosed area (c), The wall shear stress in the stenosed region, (d) The wall shear stress in the non-stenosed region; all at 2000, 3200 and 4700 Pa, (e) The wall shear stress values as calculated from the 200 μm devices in the stenosed region from GPV and CFD, (f) The wall shear stress values from the non-stenosed region in the main channel

Figure 4.25b shows with increasing stenosis there is no significant change in flow rate when considering maximum and minimum values. This supports the trends seen in Figure 4.25a. However, at 4700 Pa there is a greater decrease which may be due to the increasing resistance as the stenosis increases. It should also be noted that the geometry of the 0% stenosis 200 μm channel was smaller with an average height of 52 μm as compared to 57, 58, and 63 μm on average with the 20, 40 and 60% channels, thus causing lower flow rates.

Figure 4.25c shows that there is a significant increase in wall shear stress at 2000 Pa from 20% to 40% then a decrease at 60%, this may be due to the high-velocity gradients and spatial velocity magnitude in the 60% stenosis. There is no significant difference at 3200 Pa with increasing stenosis. At 4700 Pa there is a significant decrease in the wall shear stress from 20 to 40% and an increase to 60% as seen in the 2000 Pa data which could also be explained by the increased resistance of the 60% model.

The wall shear stress in the non-stenosed region is shown in Figure 4.25d. There is no significant difference in the wall shear stress across the 2000 or 4700 Pa measurements. There is a significant decrease in the wall shear stress from 40-60% at the 3200 Pa level, which could be due to resolution. The insignificant difference in wall shear stress in the non-stenosed data is supported by the data in Figure 4.25b as there is no significant difference in flow rate and thus no significant difference in wall shear stress should be expected.

Figure 4.25e shows the wall shear stress in the stenosed region calculated from GPV and compared to that of the CFD model. There is good agreement between the wall

shear stress values at 3200 Pa at 20 and 40% and for 20 and 60% at 4700 Pa. The wall shear stress at 4700 Pa at 40% is lower than expected as seen in Figure 4.23c. At 2000 Pa there is good agreement between the 20 and 40% stenosis but the experimental shear stress value is lower than that of CFD. At 2000 Pa and 3200 Pa, the 60% GPV data is lower than the CFD model. This could be due to the sampling range of the GPV and also limitations based on resolution.

Figure 4.25f shows the wall shear stress values in the non-stenosed region mimic the errors seen in Figure 4.23e. The wall shear stress is accurately predicted for the 20% stenosis for all pressures tested. At 40% 4700 Pa, the GPV value is lower than expected and this is the same for the 2000 and 3200 Pa values at 60% stenosis. The flow rate between the non-stenosed region and the stenosed region of each device was checked to abide by continuity and thus rules out the possibility of the flow rate being the source of the difference with the CFD. This could be due to increased resistance in the experimental model that is not accounted for in the CFD model.

In the 200 μm geometry, the difference in wall shear stress values from all ranges tested is 8 Pa corresponding to 80 dyn/cm^2. This range falls within the range of shear stress experienced in the capillaries of 1-95 dyn/cm^2, which highlights the importance of taking the exact parameters for cell study and selecting a sensitive biomarker for analysis once an *in vitro-in vivo* correlation is fully formed (223). This also suggests that a 200 x 52 μm dimension device is appropriate for study with cells as the shear stress on the walls can mimic that of *in vivo* ranges and thus can be used further for cell study for shear stress measurements in a stenosed channel.

Despite the reduction in channel size in this case, the behaviour observed is consistent with the other short stenosis models, the effect of resistance is not seen to affect the flow rate to be able to detect a significant measurable decrease using GPV for all the pressures tested, only seeing some effect at 4700 Pa in the 200 μm at 40 to 60% stenosis. The head loss in the short stenosis models can be calculated using the contraction and expansion coefficients discussed previously in § 4.2.1.

4.8 The effect of increasing the degree of stenosis on the long stenosis channels

To better mimic microvascular collapse and create a greater resistance to see the effect of microvascular collapse a ‘long stenosis’ model was created according to § 3.4.3 of the methods chapter.

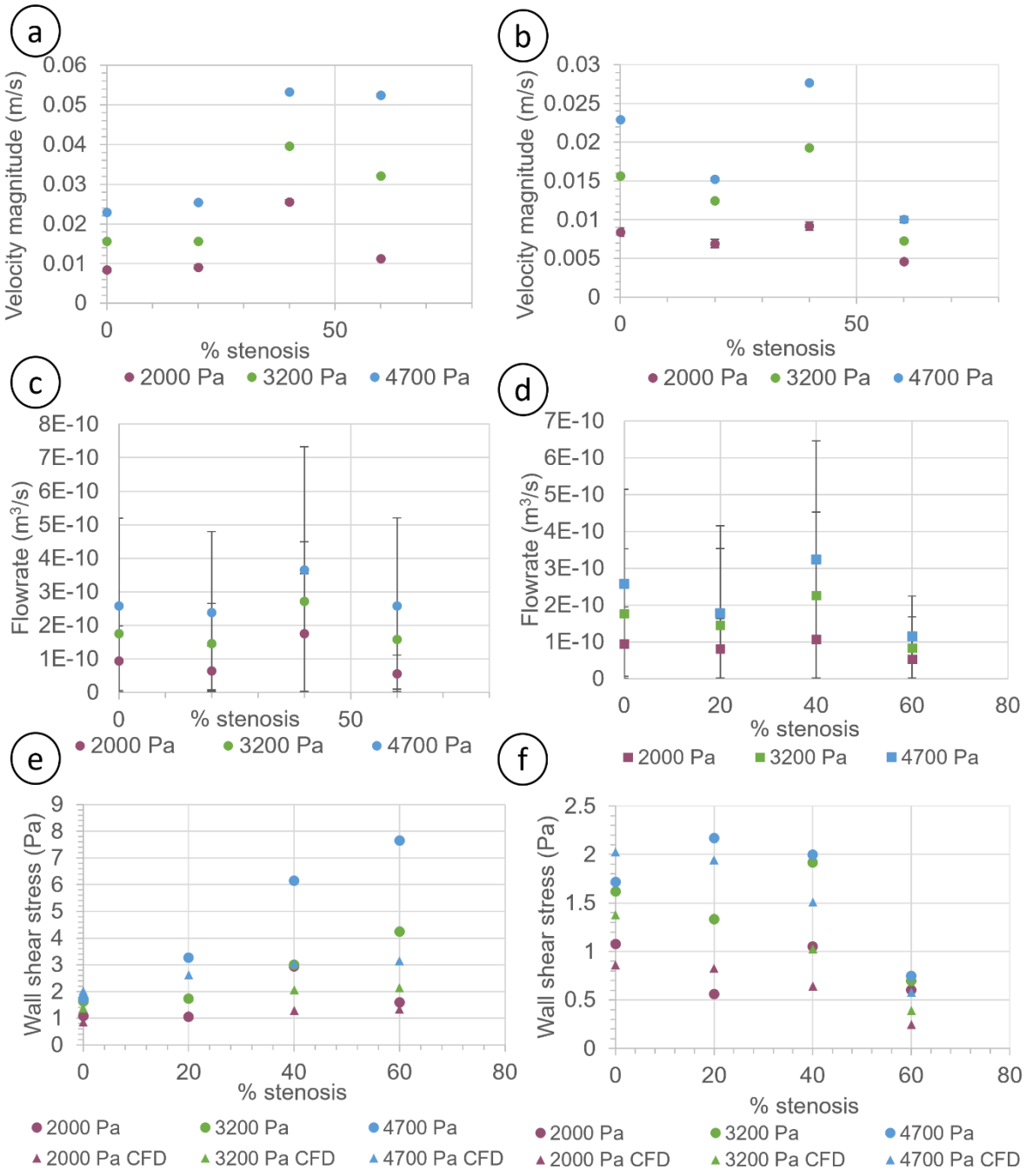

Figure 4.26 (a): The mean velocity magnitude of long 200 µm devices with increasing cross-sectional area in the stenosed region and their standard deviations, (b) The mean flow rate of long 200 µm devices with increasing stenosis in the non-stenosed region with their maxima and minima as calculated from the non-stenosed area (c), The wall shear stress in the stenosed region, (d) The wall shear stress in the non-stenosed region; all at 20, 32 and 4700 Pa, (e) The wall shear stress values as calculated from the long 200 µm *devices in the stenosed region from GPV and CFD, (f) The wall shear stress values from the non-stenosed region in the main channel, error bars covered by markers*

The effect of increasing the overall flow resistance is evident when a long stenosis is used. Figure 4.26a shows in the stenotic region there is an increasing average velocity magnitude with increasing stenosis up to 40% stenosis, after which it decreases, which corresponds with a reduction in velocity in the non-stenosed region in Figure 4.26b. This possibly suggests the reaching of the resolution limit of GPV, to check deviations in geometry did not cause this, the average flow rates are shown in Figures 4.26c and 4.26d. This suggests an increase in resistance seen by the decrease in flow rate between the 40 and 60% stenosis.

The model has a resistance range that increases over the total device resistance, 1.44 $x10^{13}$ $Pasm^{-3}$ with the stenotic region measurements.

These resistances are summarised in Table 4.10 and show the point at which there is a detectable increase in resistance detectable by GPV.

Table 4.10: Resistances of Long Stenosis

% stenosis	**Resistance of expansion + contraction Pa s m^{-3}**	**Resistance of non-stenotic region (Main channel measurements) Pa s m^{-3}**	**Resistance of stenotic region (Stenotic region measurements) Pa s m^{-3}**
0	0	1.44 x 10^{13}	0
20	68681	1.61 x 10^{13}	1.01 x 10^{13}
40	97614	1.71 x 10^{13}	1.86 x 10^{13}
60	53646	1.23 x 10^{13}	2.80 x 10^{13}

As there are large standard deviations in the measurements as seen in Figure 4.26c it cannot be statistically concluded from the experimental data alone there is a decrease of flow rate due to resistance, therefore the CFD models were created. Each model was checked to ensure the flow rate of the CFD model was within the

error range for the flow rate as shown in Figure 4.26. The CFD flow rates show that there is a decrease in the flow rate as the stenosis increases and this is likely due to the increase of resistance. Figure 4.26e shows the wall shear stress in the stenotic region was over-predicted by the GPV at the 40 and 60% stenosis, however at the 0 and 20% stenosis agreed with CFD values. At 2000 Pa of the 60% stenosis the value was an accurate prediction. In the non-stenotic region, the CFD model was a better model of wall shear stress, these differences are likely due to variation from an analytical solution as in experimental, and also *in vivo*, there will be other factors of influence.

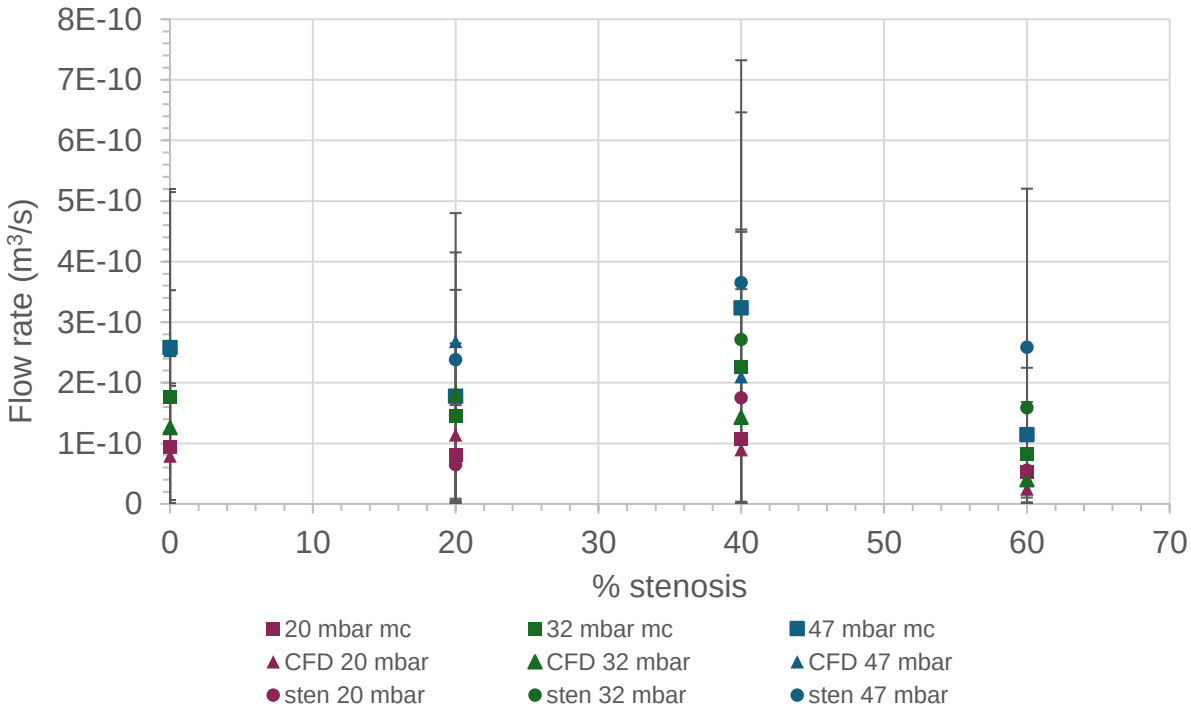

Figure 4.27: Flow rate agreement for the long stenotic model including in the main channel (mc), stenosis, (sten) and the CFD values

The sensitivity of biomarkers at the level of change of shear stress should be carefully considered. Correlations between *in vitro, in silico* and *in vivo* models should

be used when selecting shear stress ranges for selecting the correct biomarker for diagnosis based on the relative sensitivity. These models only consider straight channel geometries and should be developed further to include more geometric changes such as branching/ bifurcation as in Pan *et al.'s* investigation of wall shear stress on larger arteries (224).

4.9 Conclusions

The competition of 3D hydrodynamics such as continuity and resistance have a complicated dependence on wall shear stress as extracted from a 2D plane. A 200 x 57 μm model can accurately produce a range of wall shear stresses that mimic *in vivo* when tested at *in vivo* pressures and can be studied using optical techniques and ghost particle velocimetry. CFD models of flow behaviour can be produced and accurately predict wall shear stress values in both the non-stenotic and stenotic regions- allowing for comparisons where experimental technique, GPV is limited by resolution. However, these must be validated against measurements such as flow rate, of that of experimental data.

300 and 400 μm models allow insight into the changes in wall shear stress that are expected to be seen at larger geometries such as increased velocity magnitudes and large variability in flow rates due to the reduced resistance. These correlations could be used to predict changes in shear stress seen with changing geometries of vessels such as disease states. In the 200 μm short stenosis, the range of shear stress values mimics that of *in vivo* and therefore this device design is suitable for testing a range of *in vivo* conditions in a 3D model, however, this model only demonstrates the effects of continuity and not resistance.

The addition of a long stenosis model can be assumed when used in combination with a CFD model, to show the phenomena of resistance and thus mimics the start of microvascular collapse. *In vivo,* it is important to find sensitive biomarkers to small changes in shear stress and the area of which cell behaviour is to be measured as well as the relative blood pressure accounted for.

Chapter 5 The Influence of Increased Stenosis and Branching Geometry on Wall Shear Stress in *In Vitro* Models of Microvascular Collapse

Chapter 5: The Influence of Increased Stenosis and Branching Geometry on Wall Shear Stress in In Vitro Models of Microvascular Collapse

5.1 Introduction

The research presented in this chapter is concerned with how flow distribution, and consequently local values of wall shear stress, change in response to stenosis (and thus change in resistance to flow) in branched channels designed to mimic microvascular collapse in a network. Building on the 200 μm long stenosis model from Chapter 4, three types of channel designs were developed and investigated: a model branched according to Murray's law, an evenly branched model, and a model with a side branch. The shear stress was investigated in branched models to scope a diagnostic range of biomarkers for the diagnosis of ACS, and to increase physiological relevance.

In microfluidic research, different branching geometries of lab-on-a-chip models are investigated as discussed in §2.2.2, however, three different types of branching were investigated throughout this chapter (102)(104,225). It is well known that the flow in microfluidic devices is laminar, and the flow obeys the Poiseuille equation for laminar flow in a pipe, with the special case of the application to a rectangular cross-section as founded by Reynolds and Poiseuille (226).

In networks the hydrodynamics change due to the branching in the flow. Three types of branching were investigated, denoted: (i) side channels, (ii) even branching, and (iii) branching following Murray's law representing cases of Murray's law as described in §2.1.3 and other factors such as angiogenesis and growth around obstructions

(182,227). The branching is likely to affect the flow direction and resistance; depending on the relative geometries and angles, shear stress and thus biological response, therefore, it must be included in the design of PDMS microvasculature models. These models were selected to test a range of geometries and to investigate the effect of increasing resistance within a branched network. In Murray's Law models of biological systems, the shear stress remains constant down the bifurcation, however, this is not typical of side wall branching (108)(228)(229). The methods described above were used in developing devices to understand the features of ACS.

Some branched microfluidic models do so at right angles, however, this will not accurately model wall shear stress *in vivo* due to pressure losses at right angles being greater than the intentionally minimised pressure losses seen in biological systems. Other models investigate the degree at which the branch is from the main channel which varies depending on a number of factors (62)(230).

5.2 Experimental Parameters

The flow behaviour in the branched microfluidic models described in detail in materials and methods was investigated at 2000, 3200 and 4700 Pa using GPV according to Table 5.1. The frame rate used was 10000-20000 fps at 1024 (w) by 1024 (h) to 1024 (w) by 768 (h) pixel resolution respectively.

Table 5.1: Models investigated in this chapter as detailed in § 3.4.6-3.4.8.

	% stenosis			
	0	20	40	60
Even Branching	✓	✓	✓	✓
Murray's Branching	✓	✓	✓	✓
Side Branching	✓	✓	✓	✓

The velocity vectors in each model were calculated following the GPV procedure as described in §3.6. The velocity profiles were then extracted perpendicular to the channel walls according to Figure 5.1.

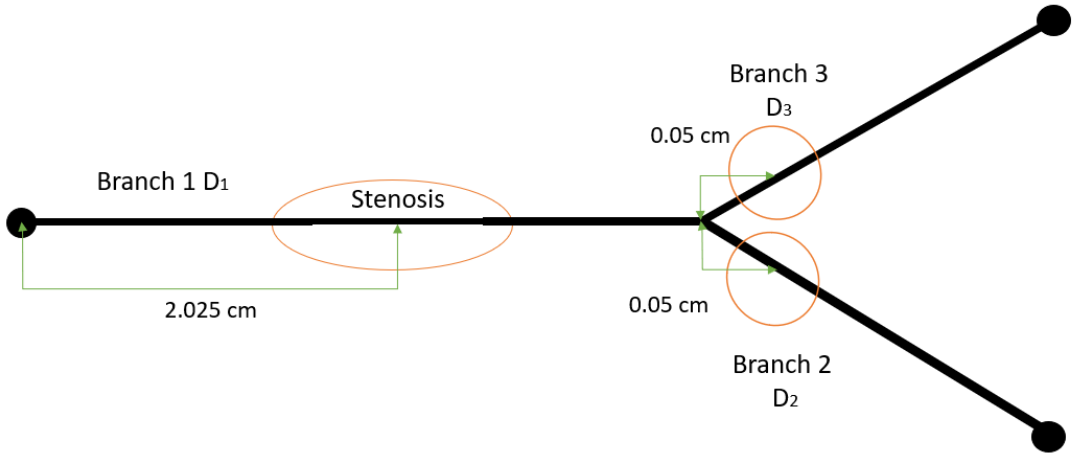

Figure 5.1: Branched model highlighting areas in which each reading is taken from

From these velocity vectors the flow rate and wall shear stress were determined as described in § 4.2.1.

The measured heights of each device were as measured in Table 5.2:

Table 5.2: Measured heights of each branched device, even branched, Murray's and side branched models

Height (μm)	Even Branching				Murray's Branching				Side Branching			
	0%	20%	40%	60%	0%	20%	40%	60%	0%	20%	40%	60%
Average	53.1	34.7	36.8	43.2	58.3	62.2	50.4	52.0	43.8	36.8	39.1	44.4
Max	79.5	37.0	43.7	46.4	60.6	71.0	59.5	57.6	47.5	42.1	45.6	48.5
Min	39.1	30.3	32.7	37.4	54.3	55.1	46.5	50.1	40.1	32.0	32.7	39.2

CFD models were created using the method described in §3.8. The model was created with the average height dimensions following the geometry and branching as described in § 3.4.6-3.4.8. Velocity profiles and wall shear stress values as calculated by ANSYS Fluent were extracted in the same location as shown in Figure 5.1 at h=H/2.

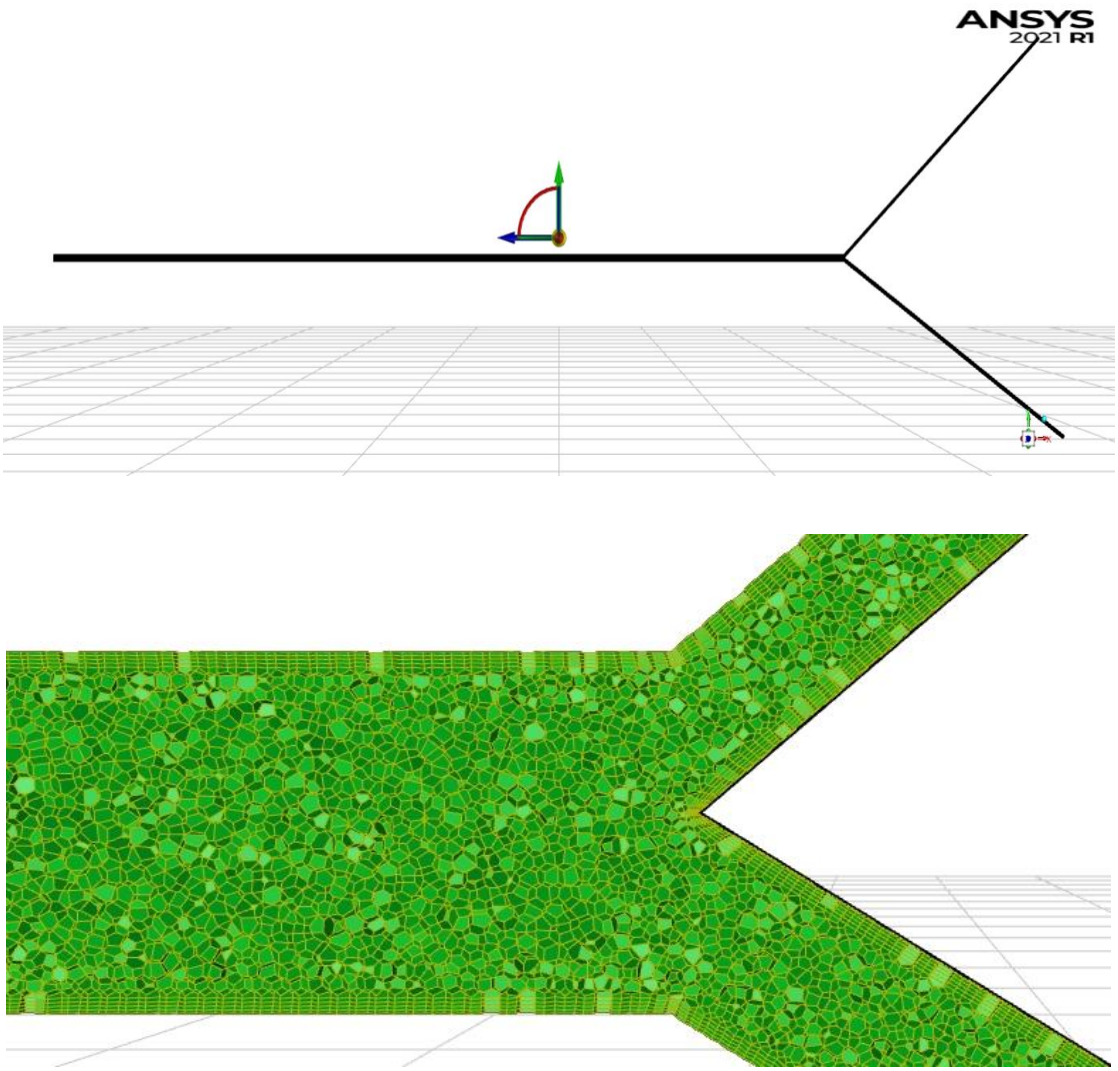

Figure 5.2 CFD mesh from Murray's law model 0% stenosis

5.3 Murray's Law

5.3.1 Geometric Murray's Law

To mimic *in vivo* networks, a microfluidic design of the microvasculature needs to consider the branching of capillary networks according to Murray's Law (55), which ultimately defines the branching geometry according to Equations 2.1, 2.2 and 2.3 and the geometry shown in Figure 5.3.

$$D_1^3 = D_2^3 + D_3^3 \tag{2.1}$$

Where (55):

$$\cos \alpha_1 = \frac{D_1^4 + D_2^4 - (D_1^3 - D_2^3)^{\frac{4}{3}}}{2D_1^2 D_2^2} \tag{2.2}$$

$$\cos \alpha_2 = \frac{D_2^4 + D_3^4 - (D_2^3 - D_3^3)^{\frac{4}{3}}}{2D_2^2 D_3^2} \tag{2.3}$$

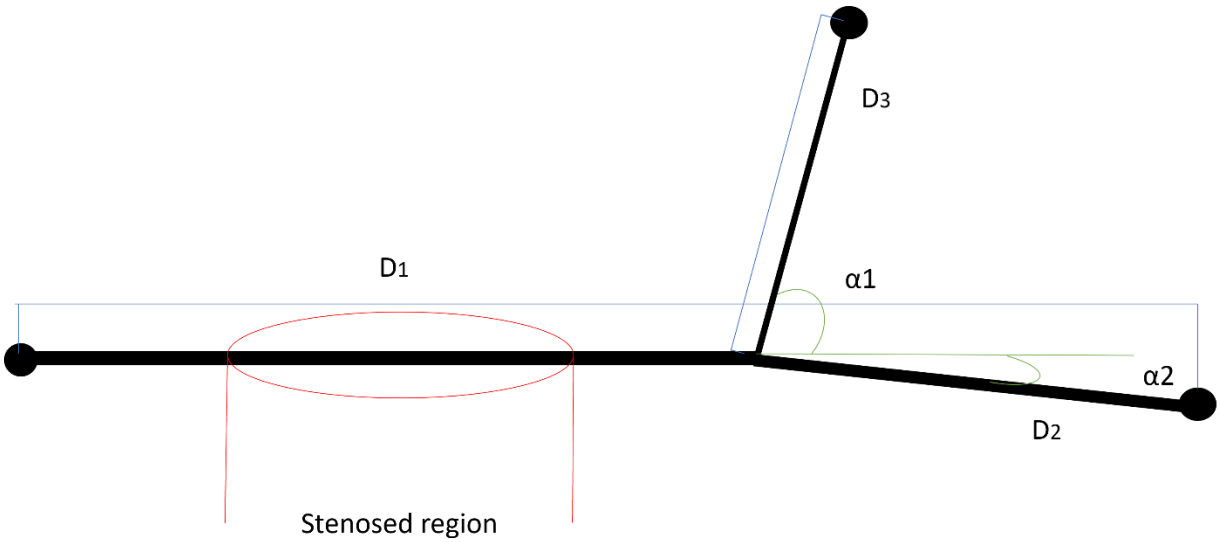

Figure 5.3: Murray's Law Device design

Table 5.3: Design parameters for a device following Murray's Law

Device	D_1 (μm)	D_2 (μm)	D_3 (μm)	α_1 (°)	α_2 (°)
A	200	75	100	25.4	42.2

5.3.2 Error Quantification

Murray's law is based on the derivation of the Hagen-Poiseuille Equation and the continuity equation from the Navier-Stokes Equation, with the assumptions of steady flow, incompressible fluid, fluid only flowing symmetrically in the x direction and fully developed flow as described in § 3.8.5. There are two competing factors, the energy required to overcome viscous drag (P_f) and energy required to maintain the volume of blood flow (P_m) which sum to the total power required (P_t) as shown in Equation 5.1 (54), where *m* is the metabolic coefficient.

$$P_t = P_f + P_m = \frac{8\pi}{\mu} Q^2 \frac{1}{(\frac{D}{2})^4} + m(\frac{D}{2})^2 l \tag{5.1}$$

Where μ is the dynamic viscosity, *Q* is the flow rate, *D* the diameter and *l* the length.

Using Poiseuille's law, this is then related to the conductance, *c*, the inverse of resistance.

$$Q = c\frac{dP}{dx} \tag{5.2}$$

Where:

$$c = \frac{\pi r^4}{8\mu l} \tag{5.3}$$

Where *r* is the radius, and *r=D/2*.

By calculating $\frac{d^2P}{dr^2}$ with the full derivation in Appendix 4, Murray derived:

$$Q = kr^3 \tag{5.4}$$

Where:

$$\sum Q = \sum kr^3 = k\sum r^3 \tag{5.5}$$

Thus, for branched cylindrical networks with 3 branches:

$$r_1^3 = r_2^3 + r_3^3 \tag{5.6}$$

Murray's derivation considers minimisation of energy loss within the branches and is designed to have the largest surface area, through microvascular branching to maximise the surface for transmural diffusion, which is often approximated by Fick's Law, Equation 5.7. However, this is only an approximation as this diffusion occurs in a non-Newtonian blood and Fick's law assumes the transfer takes place within a Newtonian fluid (54).

$$J = -D\frac{d\varphi}{dx} \tag{5.7}$$

Where J is the diffusion flux vector, *D* is the diffusion coefficient and $\frac{d\varphi}{dx}$ is the concentration gradient across the barrier (54). This is included in the Murray's law derivation through the metabolic constant.

These equations are based on channels with a circular cross-section, however, in microfluidics, channels have rectangular cross-sections as discussed in §3.5. As the height of the microfluidic geometry cannot easily be varied, a constant height of 50

μm was selected. Thus, to enable calculations following Murray's law dimensionally, the hydraulic diameter was used in calculations when designing channels as a fixed height could be used where:

$$\mathrm{D_{hyd}} = \frac{2\mathrm{wh}}{\mathrm{w} + \mathrm{h}} \tag{5.8}$$

Using the assumption of Newtonian laminar flow of water in a straight pipe with a no-slip boundary condition at the wall, the hydraulic diameter was calculated according to Equation 5.8. The height and width values for the microfluidic channels were measured, with the results are summarised in Table 5.4.

Table 5.4: Height, width and hydraulic diameter measurements of the Murray's law devices in each branch

Measurement (μm)		**% stenosis**			
		0	20	40	60
	av. height	58.3 (+/- 4)	62.2 (+/- 8)	52.0 (+/-6)	50.4 (+/-4)
Branch 1	av. width	211.3 (+/- 3)	207.0 (+/- 4)	215.4 (+/- 13)	208.5 (+/- 6)
	av. hyd. D	91.3	95.7	83.8	81.2
Branch 2	av. width	72.7 (+/-3)	76.3 (+/-4)	77.3 (+/-4)	74.0 (+/-3)
	av. hyd. D	64.7	68.6	62.2	60.0
Branch 3	av. width	99.6 (+/- 6)	103.7 (+/- 8)	101.7 (+/- 4)	102 (+/- 5)
	av. hyd. D	73.5	77.8	68.9	67.5

To see how closely the Murray's law geometric approximation applied to the channel once manufactured, the percentage difference between r_1^3 and $r_2^3 + r_3^3$ was calculated. Additionally, the values of hydraulic radius were compared for the special case of Hooper's law, Equation 5.9, typically applied to larger vessels such as arterial branching (54).

$$r_1^{2.98} = r_2^{2.98} + r_3^{2.98} \tag{5.9}$$

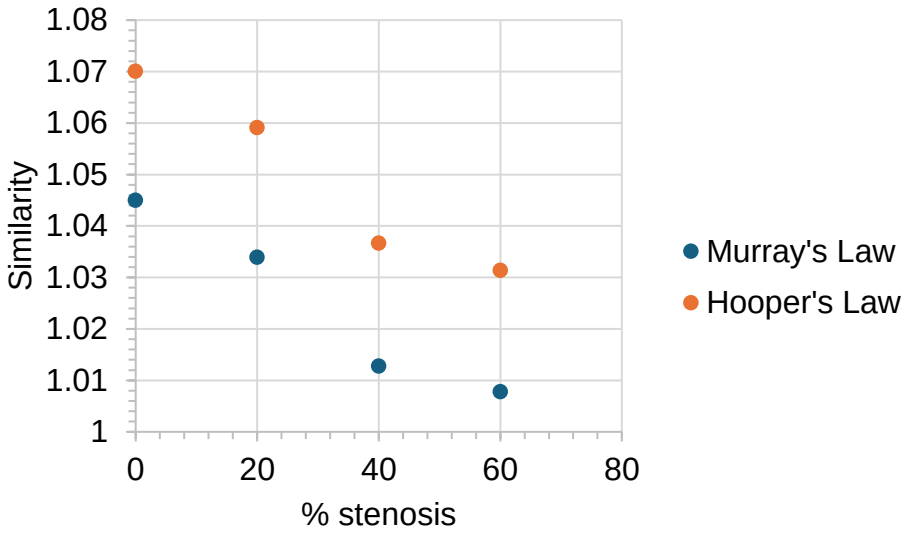

Figure 5.4: Similarity between hydraulic radius values when fabricated and their closeness to following Murray's and Hooper's Law

The similarity of the radius values from fabrication compared to that calculated using Murray's law and Hooper's law shows that the measured microfluidic geometry using the assumption of a hydraulic diameter there is up to 95.5% agreement with Murray's law and 93% agreement with Hooper's Law, showing how accurately microfluidic devices can be fabricated to the prescribed dimensions. The larger difference with Hooper's law may be seen as Hooper's law is considered for modes of arteries and thus channels with larger geometries (54). Thus, it can be said that using the hydraulic diameter, particularly in microfluidic models in which the height of the device cannot be changed per vessel, there is close dimensional agreement with Murray's Law once fabricated using the photolithography and soft lithography processes detailed in Chapter 3.

The shear stress in these models was extracted at h=H/2, however, there is a variation of shear stress across the cross-section as shown in Figure 5.5.

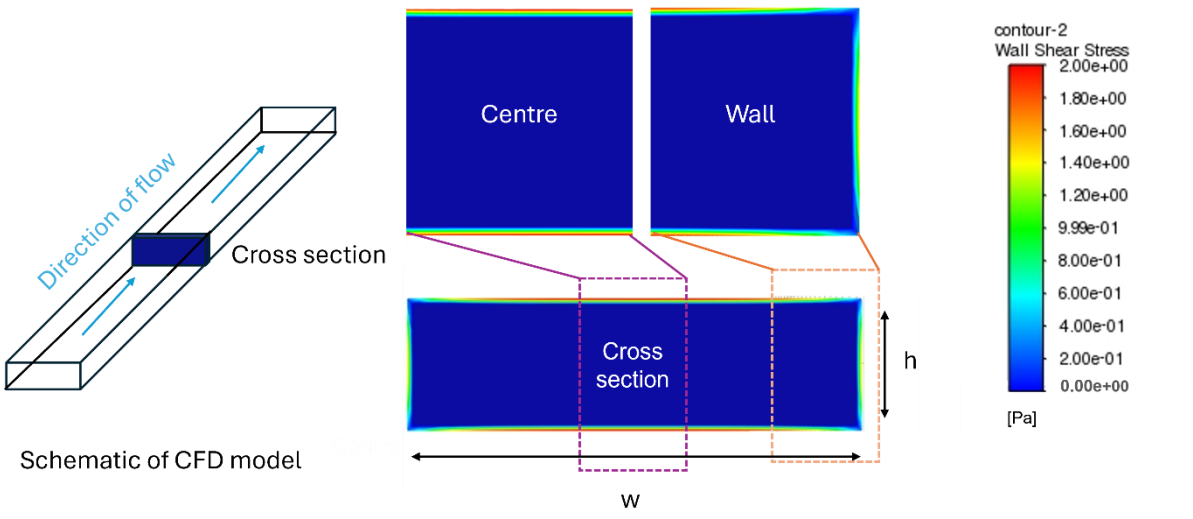

Figure 5.5: Wall shear stress distribution across the cross-section of Branch 1 on a 200 µm Murray's law device from CFD model 0% stenosis at 3200 Pa

Figure 5.5 shows the variation of shear stress across the cross-sectional area with the centre being 0 Pa and the walls having larger shear stresses up to 2 Pa. Figure 5.5 also shows that the walls at h=0 and h=H have a greater shear stress than the walls at w=0 and w=W. Therefore, compared to a circular cross-section where the wall shear stress is constant around the circumference, i.e. no azimuthal effect, for rectangular cross-sections, this is not the case, and the shear stress depends both on height and width. Throughout this chapter, all shear stress values are extracted at h=H/2, w=0 and w=W. This will not be the maximum wall shear stress in the geometry, and this should be considered when choosing where to grow cells in the device and the distribution of shear stress across the cross-section that the cells will be exposed to.

5.4 Bifurcation Design

Networks are characterised by the number of branches, N, at each node, k. Under the assumption that the flow is incompressible, there is no accumulation, and the mass is conserved; the flow in a branched capillary can be assumed to behave by the Hagen-Poiseuille equation as we have seen from the flow behaviour in Chapter 4. Where:

$$Q_{1,2} = \left(\frac{\pi}{128\mu}\right)\Delta P_{1,2} G_{1,2} \tag{5.10}$$

And G is a constant for cylindrical channels (135,231):

$$G_{1,2} = \frac{D_{1,2}^4}{l_{1,2}} \tag{5.11}$$

But, as seen in Chapter 4, for rectangular cross-sections;

$$R = \frac{1}{1-0.63\left(\frac{h}{w}\right)}\frac{12\mu L}{h^3 w} \tag{5.12}$$

$$Q_{1,2} = \frac{\Delta P_{1,2}}{\frac{1}{1-0.63\left(\frac{h}{w}\right)}\frac{12\mu L}{h^3 w}} \tag{5.13}$$

If the daughter vessels are equal in size, then the following can be derived for branched models with circular cross sections.

$$\beta_{dk} = \frac{D_k}{D_{k-1}} \tag{5.14}$$

Where β is the ratio of channel widths.

$$N_k \dot{V}_k = \frac{N_k \pi D^2 v_k}{4} = N_{k-1} \dot{V}_{k-1} = \frac{N_{k-1} \pi D^2{}_{k-1} v_{k-1}}{4} \quad (5.15)$$

Where *v* is the velocity, $\dot{V}$ is the volumetric flow rate, *D* the diameter, *N* the total number of branches and *k* the branching level (231). This equation shows the total volumetric flow rate at each branching level assuming the flow is incompressible is equal. For one channel branching into two, *k=1* and *n=2*.

Thus, it can be assumed that:

$$\beta^2{}_{dk} u_k n_k = \beta^2{}_{dk} u\, n = 1$$

Therefore, the pressure at the bifurcation can be assumed to follow:

$$\Delta P = R\dot{V}, \text{ where } \dot{V} = \frac{\pi d^2 v}{4} \text{ and } R = \frac{128v}{\pi v d^4}$$

In cases where this is not seen, such as when resistance increases or in the body where there is branching in which the daughter vessels are not of the same dimension, it has been suggested by Bengtsson and Eden that the requirement is for there to be a constant power asserted per unit area of the wall, characterised by a consistent wall shear stress (57). The branching behaviour can be modelled using Equation 5.16, where k is the level, N is the number of branches, d is the (231)

$$\frac{4N_k \Delta P Q_k}{N_k \pi d^2 l_x} = \frac{4N_{k-1} \Delta P Q_{k-1}}{N_k \pi d^2{}_{k-1} l_{x-1}} \quad (5.16)$$

And:

$$\frac{pu\beta_D^2}{\beta_D \gamma} = 1 \quad (5.17)$$

Where, β_d, γ and p are branching factors and *n* is the number of the daughter branch and u is the kinematic factor.

$$u^2 = \beta_D, u = n^{-\frac{1}{5}}, \beta_D = n^{-\frac{2}{5}}$$

So (231),

$$\frac{p}{\gamma} = n^{\frac{3}{5}} \tag{5.19}$$

5.5 Side Branching

Models of blood flow involving side branching also show a change in wall shear stress, with their inclusion in studies being deemed ‘crucial’ and without them models leading to overestimates of wall shear stress ranges (232)(233)(234). Although this side branching is often modelled for larger blood vessels such as arteries, it is important they are investigated for capillary networks also where side branches are seen as there may be similar phenomena that will influence decisions made when selecting shear stress ranges for biomarker testing.

5.6 Determination of Variables

The resistance of each device with no stenosis was estimated using the same method as Chapter 4. Table 5.5 shows the relative resistances.

Table 5.5: Resistance of each non-stenosed branched device

	Resistance (Pa s/m^3)			
Device	**Branch 1**	**Branch 2**	**Branch 3**	**Total**
Murrays	1.4 x 10^{13}	2.2 x 10^{12}	1.2 x 10^{13}	4.8 x 10^{13}
Even	1.2 x 10^{13}	4.0 x 10^{12}	4.0 x 10^{12}	1.9 x 10^{13}
Side	3.1 x 10^{13}	1.1 x 10^{13}	1.1 x 10^{13}	5.3 x 10^{13}

The flow rate of each device with no stenosis was also estimated using the same method as Chapter 4. Table 5.6 shows the relative flow rates.

Table 5.6: Flow rate of each non stenosed device

	Flow rate (m^3/s)		
Device	Q at 2000 Pa	Q at 3200 Pa	Q at 4700 Pa
Murray's	4.7×10^{-11}	6.7×10^{-11}	9.87×10^{-11}
Even	1.0×10^{-10}	1.6×10^{-10}	2.4×10^{-10}
Side	3.8×10^{-11}	6.0×10^{-11}	8.9×10^{-11}

5.6.1 Analytical vs Experimental Flow Rate

The flow rate both analytically and from GPV in each device was calculated according to § 4.2.2 and § 4.2.3 respectively.

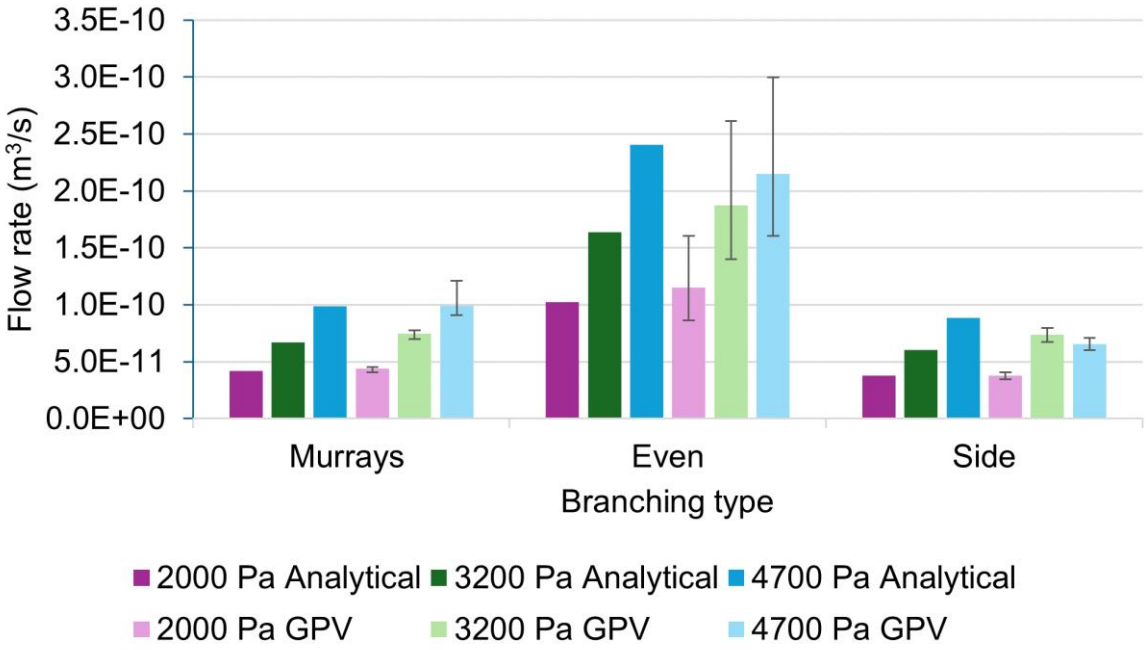

Figure 5.6: Flow rates as calculated using resistance calculations and as measured using GPV.

Figure 5.6 shows estimating the flow rate using the method of determining resistance detailed in Chapter 4 gave good accuracy for both the Murray's Law and the even branched model. For the side model, at 2000 Pa the analytical estimate was a good approximation, however, there were differences at 3200 and 4700 Pa. This may be due to the angle of the side branch influencing the resistance and pressure loss at the bifurcation, investigated through the use of CFD. The even branching model has the greatest variation of flow rate which was due to the greatest range of height +/- 20 μm down the length of the device. The even branched model also had the largest flow rates which was again due to its greater height and lower resistance as shown in Table 5.5.

The flow rates in the branched models are lower than those of the long stenosis model from Chapter 4 due to the increased resistance caused by the addition of the branches. Table 5.7 shows the Murray's Law device had a 2.08-2.46x lower flow rate than the long device from Chapter 4, compared to the even at 0.99-1.12x and the side branching at 2.5-3.16x. This is due to the dimensions of each channel and the addition of the extra branches. The addition of each branch should make the multiple up to 3x, however, there is a large variation with height, $1/h^3$, as seen in Equation 5.13 which when determining resistance will also provide a large influence. The resistance of the long stenosis model from experimental data was determined to be 2 $x10^{13}$ $Pasm^{-3}$ close to the 1.9 x 10^{13} $Pasm^{-3}$ for the even model from Table 5.5, which supports the similar flow rates seen in Table 5.7, thus showing the change of height of the channel has a comparable influence on the resistance as the addition of two 200 μm branches.

Table 5.7: Geometries and average flow rates for non-stenosed channels

	Flow rate (m^3/s)		
Pressure (Pa)	2000	3200	4700
Long	**1.0×10^{-10}**	**1.8×10^{-10}**	**2.1×10^{-10}**
Murray's	4.4×10^{-11}	7.5×10^{-11}	1.0×10^{-10}
Multiple vs long	2.29	2.46	2.08
Even	1.0×10^{-10}	1.6×10^{-10}	1.9×10^{-10}
Multiple vs long	0.99	1.12	1.10
Side	3.8×10^{-11}	7.4×10^{-11}	6.5×10^{-11}
Multiple vs long	2.66	2.50	3.16

5.7 Murray's Branching

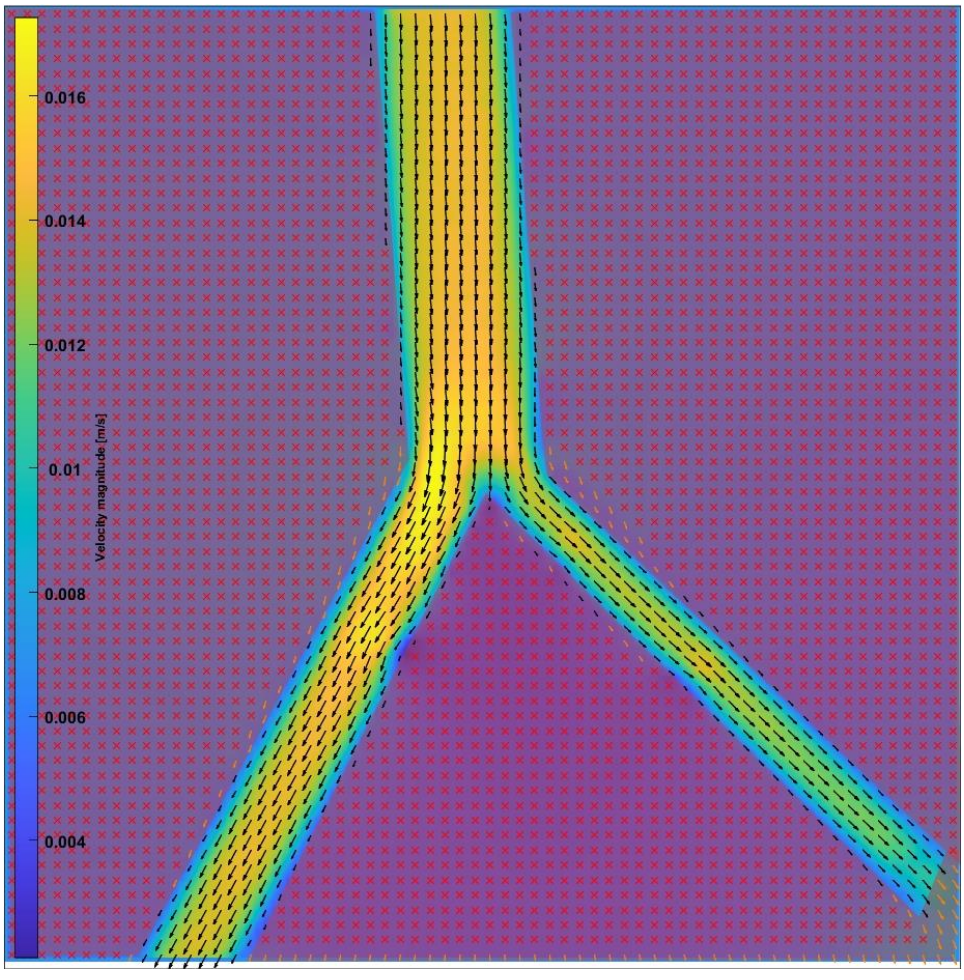

Figure 5.7: A Murray's branched device 0% stenosis at 3200 Pa

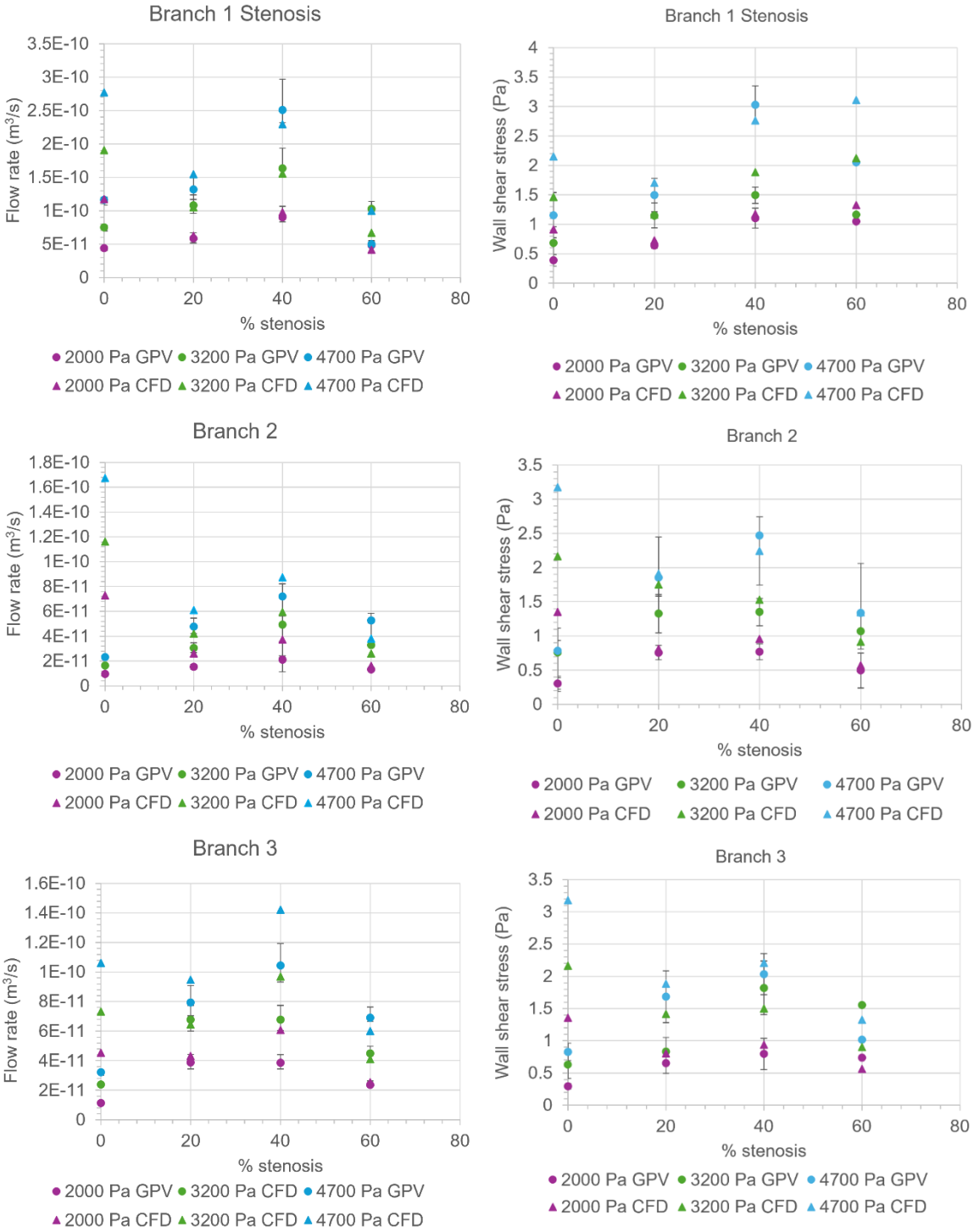

Figure 5.8: Flow rate and wall shear stress as measured by GPV and CFD in the Branch 1 Stenosis, Branch 2 and Branch 3 at 2000, 3200 and 4700 Pa, for the Murray's law model

In the device branching according to Murray's law, it was found that the average flow rate in the Branch 1 region increased up to the 40% stenosis for 2000, 3200, and 4700 Pa. There was a decrease for all pressures at 60% stenosis; this is due to the reduced flow rate caused by the increased resistance seen in the 60% stenosis model due to the reduced cross-sectional area as seen in Chapter 4. As stated previously in Table 5.7 the addition of branching from a non-branched long stenosis model decreases the flow rate by 2.08-2.46x, thus, increasing the stenosis in the branched case decreases the flow rate. The GPV and CFD average resistance was calculated using Equation 4.2 as shown in Figure 5.9, demonstrating the increase in resistance with increasing stenosis.

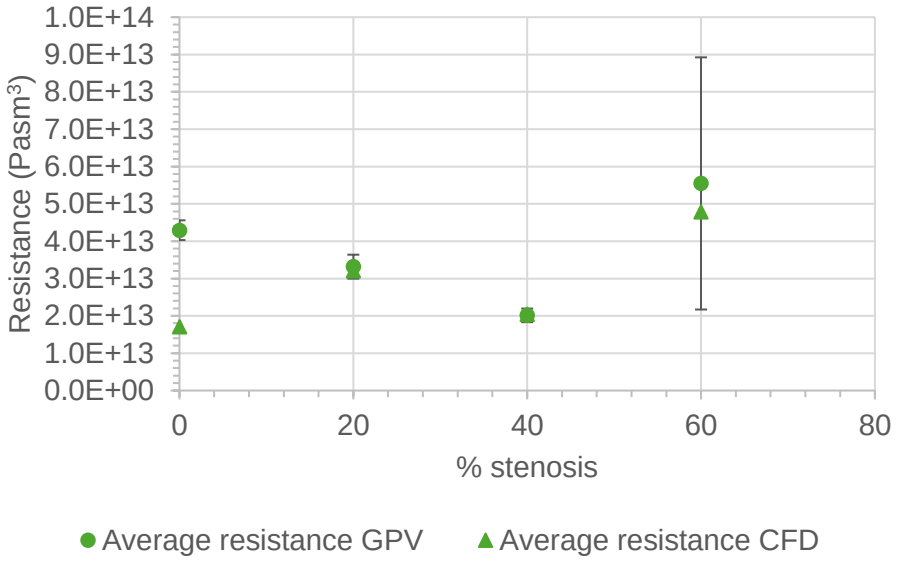

Figure 5.9 Resistance data for Branch 1 of the Murray's law models from GPV and CFD

The same trend is seen in Branch 2, although the average flow rate in Branch 2 is lower than in Branch 3 for all pressures and stenosis tested. This means that there is increased resistance in Branch 2 which would be expected due to the lower

dimensions 75 μm and 100 μm and a constant height. In both Branch 2 and Branch 3 the flow rate follows the same trend, with the flow rate in the Branch 3 channel being 75% of the Branch 2, which again is supported by the resistance through the dimensions of the device design.

Figure 5.8 shows the wall shear stress in the device increases with increasing stenosis up to 40% stenosis, which again is supported by the flow rate and resistance data. The resistance of the 60% stenosis model is enough to significantly decrease the flow rate and thus the wall shear stress decreases even though the stenotic region is decreasing in cross-sectional area. This is seen both in the Branch 2 and Branch 3 channels, highlighting the peak in shear stress. In the stenotic region, we see an increase in the wall shear stress with increasing stenosis, which increases significantly at 4700 Pa at 40% stenosis.

The total flow rate can be found from either inlet or outlet flows as shown:

$$Q_{in} = Q_{out} \text{ where } Q_{out} = Q_1 + Q_2 \tag{5.20}$$

As the cross-sectional area of the stenosis decreases, the velocity magnitude increases in a smaller cross-sectional area, due to continuity, thus shear stress in the stenosed region increases (provided increased resistance to flow does not dominate). This phenomenon is also described and seen in the fixed stenotic models in Chapter 4.

As described with Murray's law, the wall shear stress should be consistent throughout the device and into the smaller branches. In Figure 5.10, we can see that in almost all models this was the case, and therefore, despite the device being created with a rectangular cross-section, we see the same phenomena as expected with Murray's

branching law seen in circular cross channels. The branches are numbered according to Figure 5.3. The wall shear stresses go through a maxima as the increased resistance in the 60% case causes a decrease in the overall flow rate.

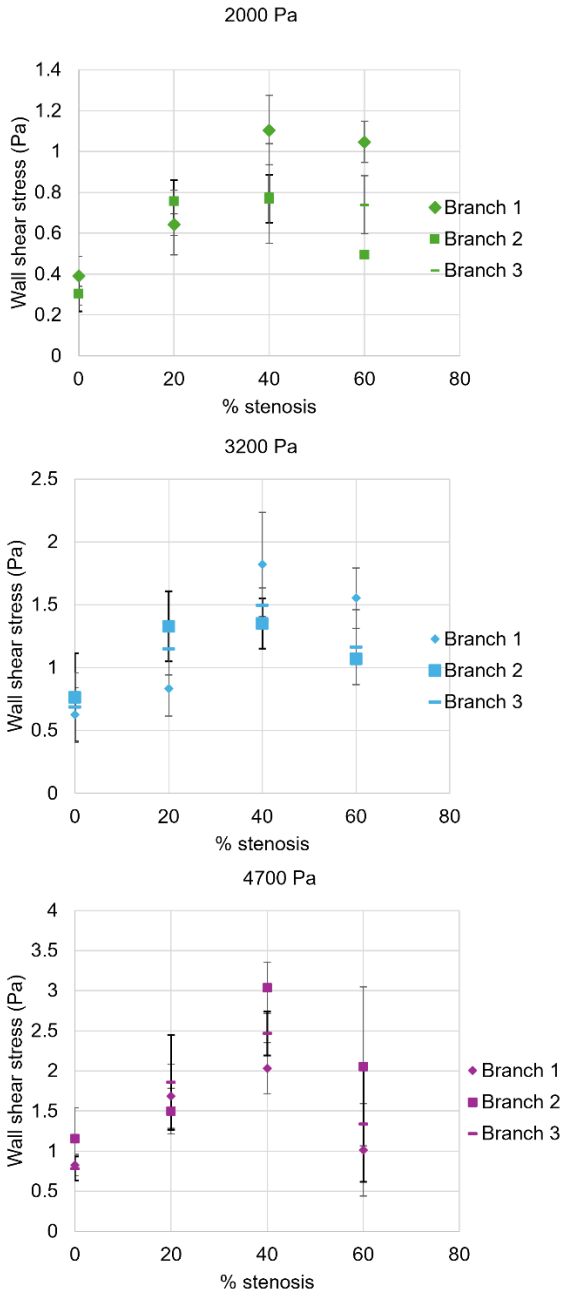

Figure 5.10: Wall shear stress in each branch at 2000 Pa, 3200 Pa and 4700 Pa

This is useful for microfluidic model development as this confirms that when developing devices for constant wall shear stress, with different flow rates, Murray's law can be applied with the hydraulic diameter assumption.

Figure 5.8 also shows the experimental data compared to the wall shear stress data collected from the CFD. The figure shows that in Branch 2 and 3, the wall shear stress is accurately modelled for the 20, 40 and 60% stenosis, however, there was variation on the 0% model. This is also the case for the Branch 1 stenosis data excluding the maximum pressure at maximum stenosis, which may be due to PIV errors described in Chapter 4. In the stenosed region, the CFD model was an accurate predictor of the wall shear stress at 20% stenosis and at 2000 and 4700 Pa for the 40% model. The results maintain the wall shear stress as the geometry changes and agree with the ratios of dimensions seen in Murray's law geometrically. Therefore, this model can be used to expose the cells to constant wall shear stress whilst the flow rate in each area changes. This design could be useful for lab-on-a-chip models in combination with CFD models where a certain flow rate is required for mass transfer under constant shear. Furthermore, this model can be used to measure a range of shear stresses from 0.2-3.4 Pa at 2000 to 4700 Pa modelling shear stress values and pressure values seen *in vivo* and thus would be suitable for cell behaviour investigation.

Although this model holds true geometrically, it is important to consider the effect of this geometry and the hydraulic diameter approximation on resistance as shown in Figure 5.11.

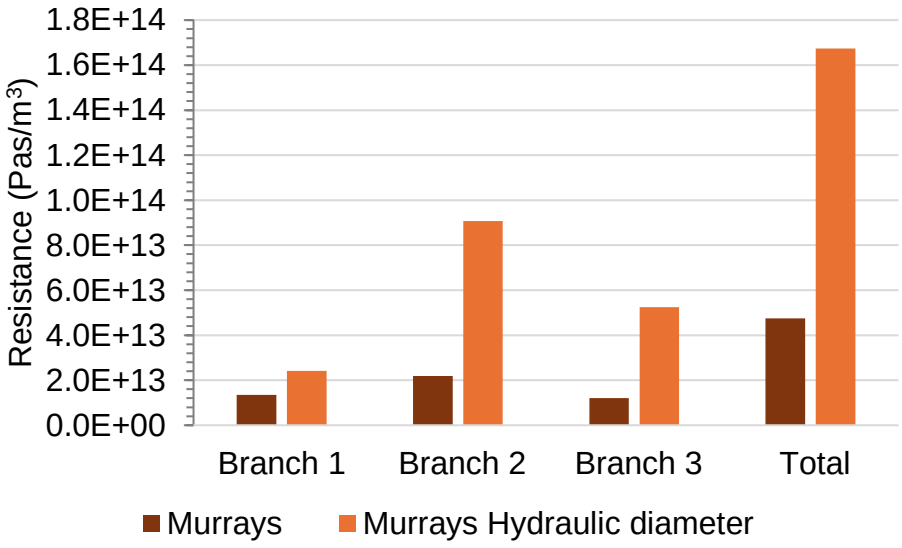

Figure 5.11: Estimation of resistance using Murray's law formula with resistances calculated using Equation 5.12 for rectangular cross sections and calculated using Poiseuille's law using a hydraulic diameter

Murray's law geometrically holds true using $r_1^3 = r_2^3 + r_3^3$, however, based on the design assuming hydraulic diameter, there is a larger error when calculating resistance for the rectangular channels using this approximation as shown in Figure 5.11. As shown in Figure 5.5 the shear stress around the cross-sectional area varies with width and height and therefore Murray's law may only be geometrically true when compared to systems with the same aspect ratios and extracting the wall shear at w=0 and w=W at H/2. This should be considered when designing devices and choosing where to construct hydrogels for cell growth. The resistance here may also not represent the case of the minimum resistance in a network system with the fewest energy losses in the fluid network as the derivation of Murray's law states.

5.8 Even Branching

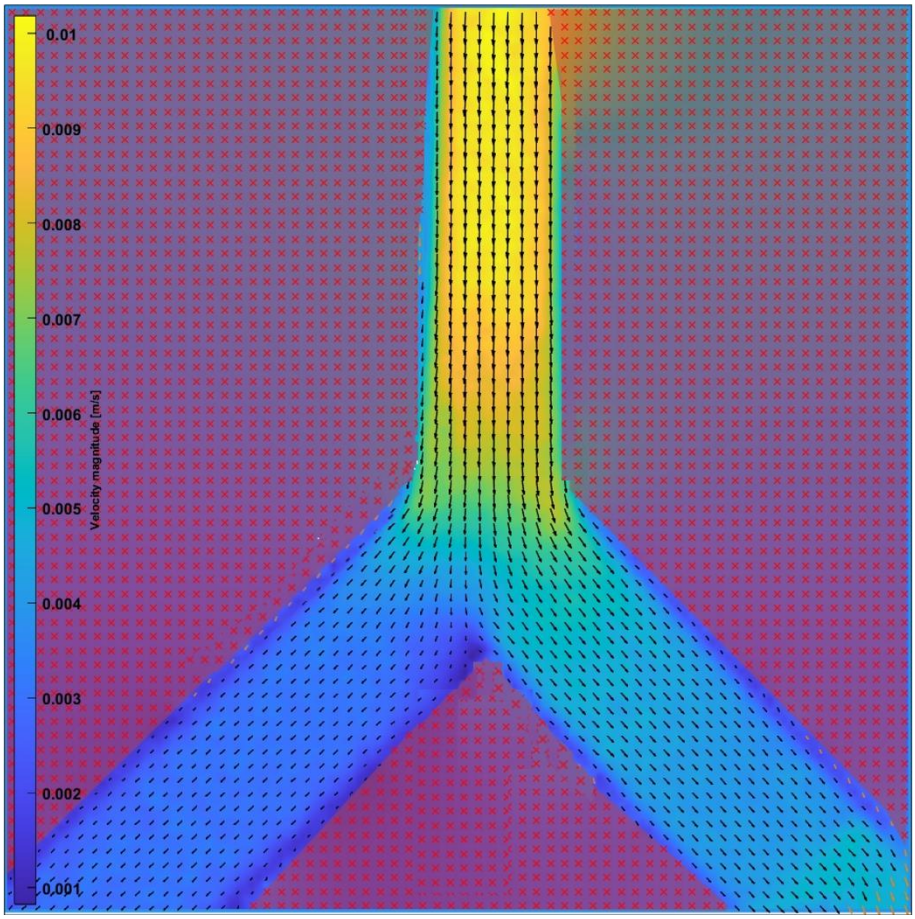

Figure 5.12: The velocity distribution map for an evenly branched 200 μm model with 20% stenosis at 3200 Pa

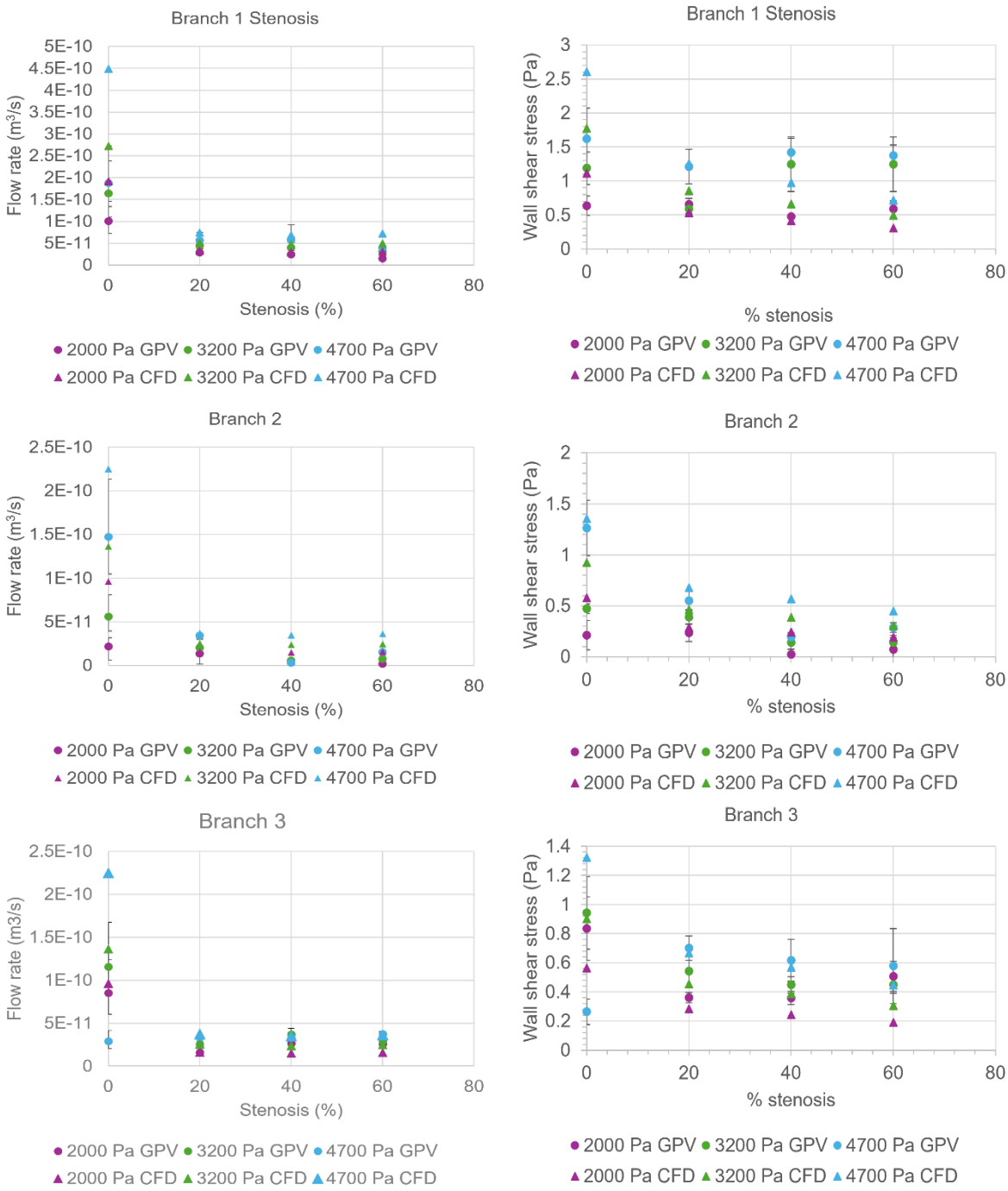

Figure 5.13: Flow rate and wall shear stress as measured by GPV and CFD in the Branch 1 Stenosis, Branch 2 and Branch 3 at 2000, 3200 and 4700 Pa, for the even branched model

Figure 5.13 shows in the even branched model there was a decrease of flow rate with increasing stenosis in all branches. This is expected due to the increasing resistance in the model as shown in Figure 5.14. This is also seen in the branches 2 and 3 as the resistance is summative.

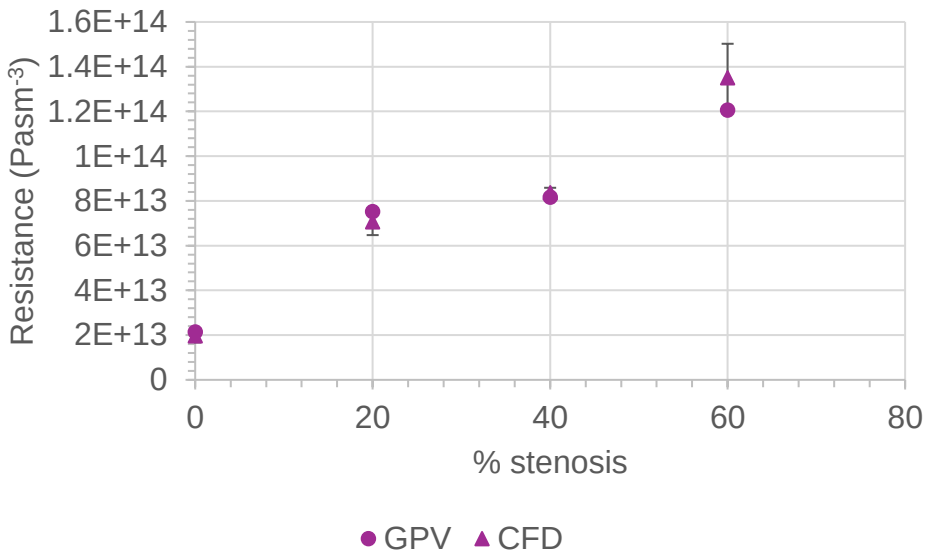

Figure 5.14: Resistance with increasing stenosis in evenly branched models from GPV and CFD

The flow rate in microvascular networks can change for various reasons, aside from the vessel diameter, the length of each vessel, and tapering of the vessel. Other factors *in vivo* such as the elasticity of the vessel wall and the rheology of blood can make further differences (103).

Figure 5.13 shows there was a stable wall shear stress as measured by GPV in the stenosed region of the device. This occurred with a variable flow rate therefore the width of the channel decreasing has a comparatively similar effect on the wall shear stress as the reduction in flow rate.

In Branch 2 there is a decrease in the wall shear stress with increasing stenosis, which is supported by the flow rate data. Figure 5.13 shows the CFD model was an accurate predictor of the 20% stenosis model in the Branch 2 channel. In the Branch 2 channel at 0% stenosis, the CFD model overpredicts the wall shear stress. This is also the case for 4700 Pa at 40 and 60% stenosis. In the stenosis, the CFD model underpredicts wall shear stress for 20-60% stenosis. This combines real world variation with the ideal case seen in CFD. In Branch 3 the wall shear stress decreases from 0 to 20% stenosis and then shows no significant difference as the stenosis increases further. The wall shear stress remains stable at all pressures as stenosis increases from 20-60%. The wall shear stress in Branch 2 remains higher than in the Branch 3 channel for almost all 20-60% stenosis. This may be due to a factor in Branch 3 increasing the resistance of the channel and thus decreasing the flow rate and wall shear stress, however, it can be seen from Figure 5.15 that the flow did not always prefer one branch over the other. In the 20% model, the flow was even between the two branches, however, in the 40% and 60% model the flow went preferentially to Branch 2.

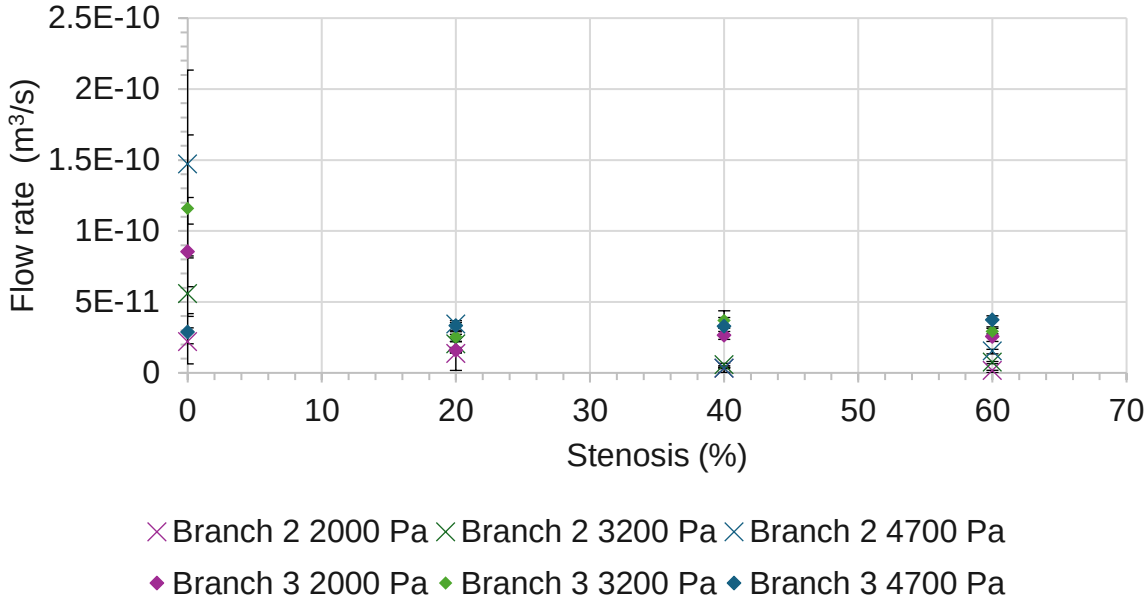

Figure 5.15: The flow rate in branch 2 vs branch 3 at all pressures in all stenosis even branched models

In Branch 2 and 3, the CFD model accurately predicts the wall shear stress in the 20% model for all pressures tested, at 60% stenosis the CFD model underpredicts the wall shear stress as measured by GPV. The CFD model assumes no preference of flow down either branch and thus the wall shear stress in both the Branch 2 and Branch 3 channels is the same, as would be expected given the governing physics of the flow. This does not account for the variation seen experimentally and *in vivo.* In the stenotic region, the CFD model predicts a consistent decrease in wall shear stress with increasing stenosis, which is due to the reduction in flow rate despite the decrease in the geometry. This shows the difference between ideal systems and experimental systems and emphasises the importance of combining *in vivo, in silico* and *in vitro* models when quantifying hydrodynamic ranges in biological systems. This might be due to some degree of blockage in the channels or small changes in the dimensions of each branch, so that they are not perfectly identical.

5.9 Side Branching

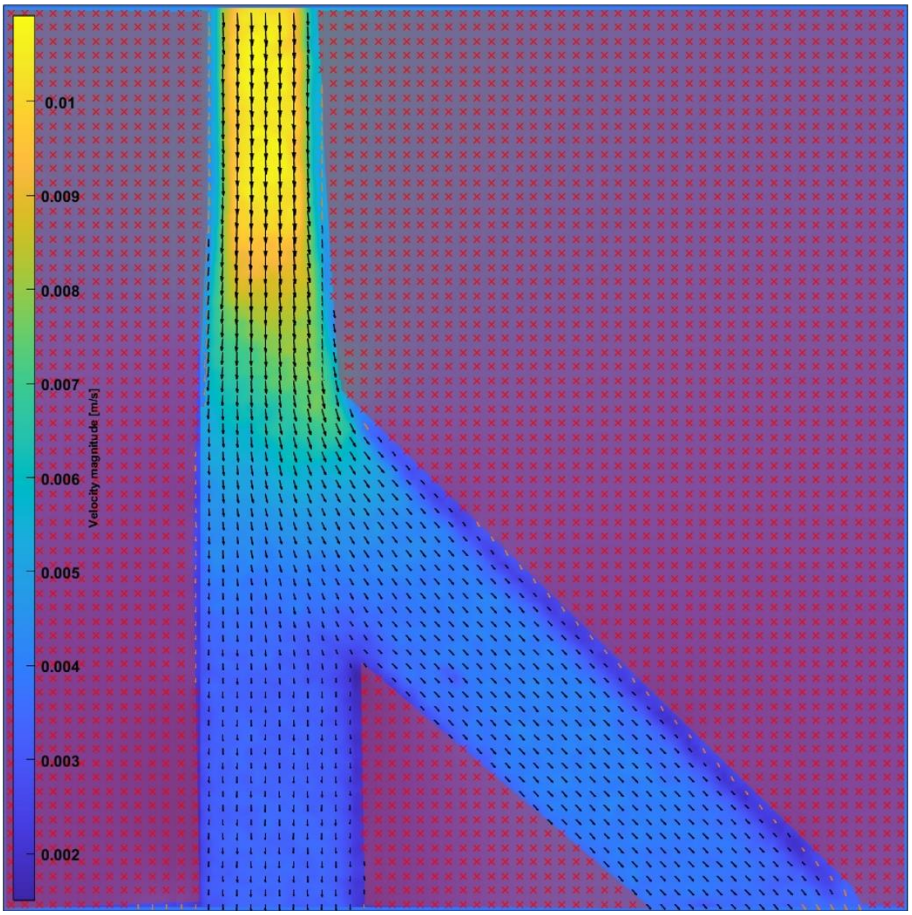

Figure 5.16: GPV spatial velocity distribution from the 20% stenosed side branch 200 µm channel at 3200 Pa

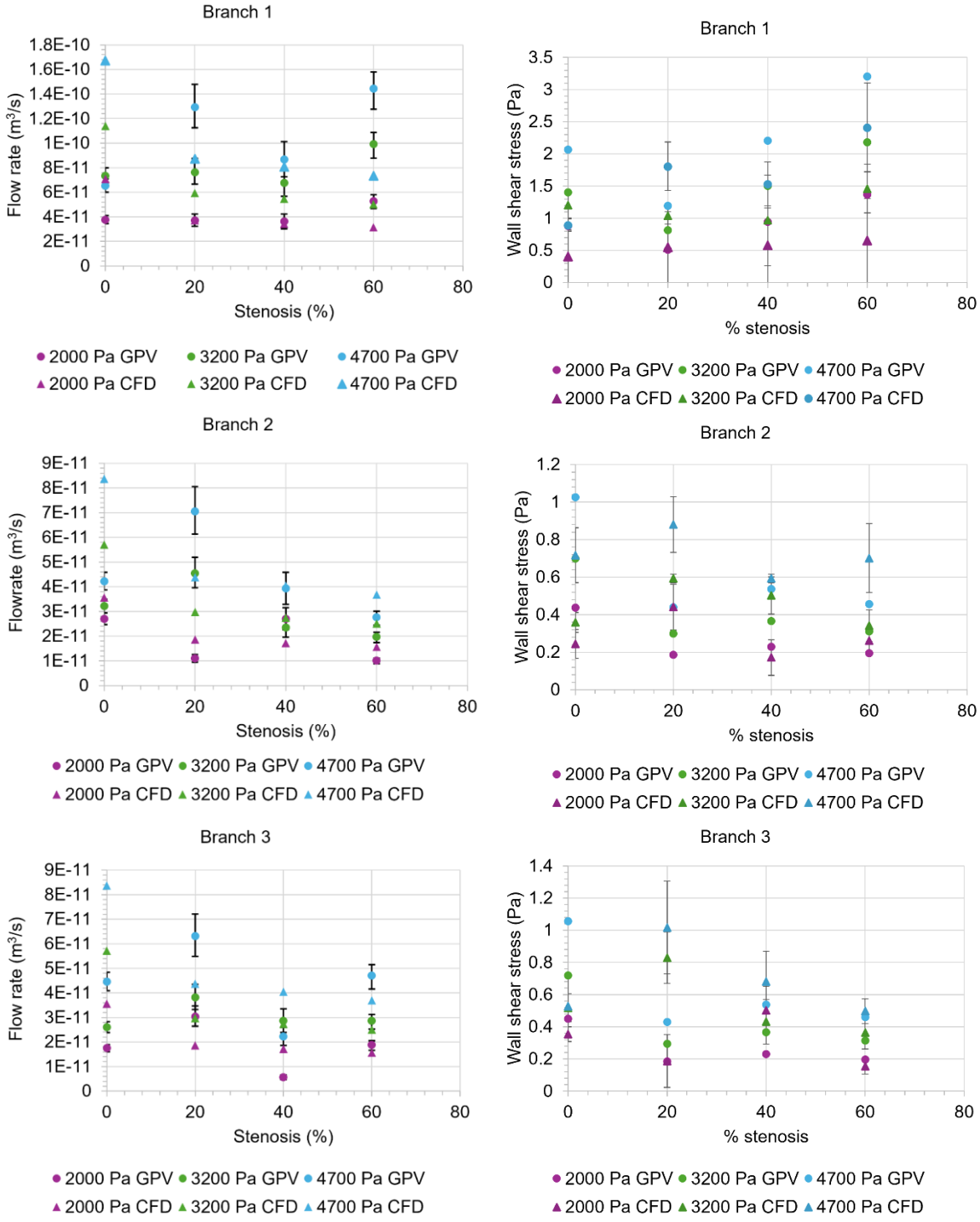

Figure 5.17: Flow rate and wall shear stress as measured by GPV and CFD in the Branch 1 Stenosis, Branch 2 and Branch 3 at 2000, 3200 and 4700 Pa, for the side branched model

In the device with the side branch in the stenotic region, there was a large variation in the flow rate. The resistance in the side channel model was the greatest as seen in Table 5.5. Figure 5.17 shows that in Branch 3, there was no stable trend across the measurements with increasing stenosis. This may be due to the fluctuation of flow due to resistance changes in the channel from fabrication and would reflect geometry changes *in vivo* due to variations in lumen diameter. This is also seen in the Branch 2 channel. The order of magnitude of the flow rates is the same, however, fluctuations in device height, agglomerations of nanoparticles and tubing fixtures can at the microscale influence the preference of flow to either side as seen in Figure 5.18. This shows for the majority of measures the flow rate was evenly dispersed between each branch, however, in some cases such as at 2000 Pa this was not the case. As there is no preferential side that this flow is directed to, the effect of the angle on the diversion of flow can be ruled out, suggesting this is more likely due to formation errors in the mould. Although every effort was made to maintain even resistance through experimental factors such as height and tubing at this resolution there is the diversion of flow down either branch cannot be prevented if there are deformations in the negative mould or unremovable impurities.

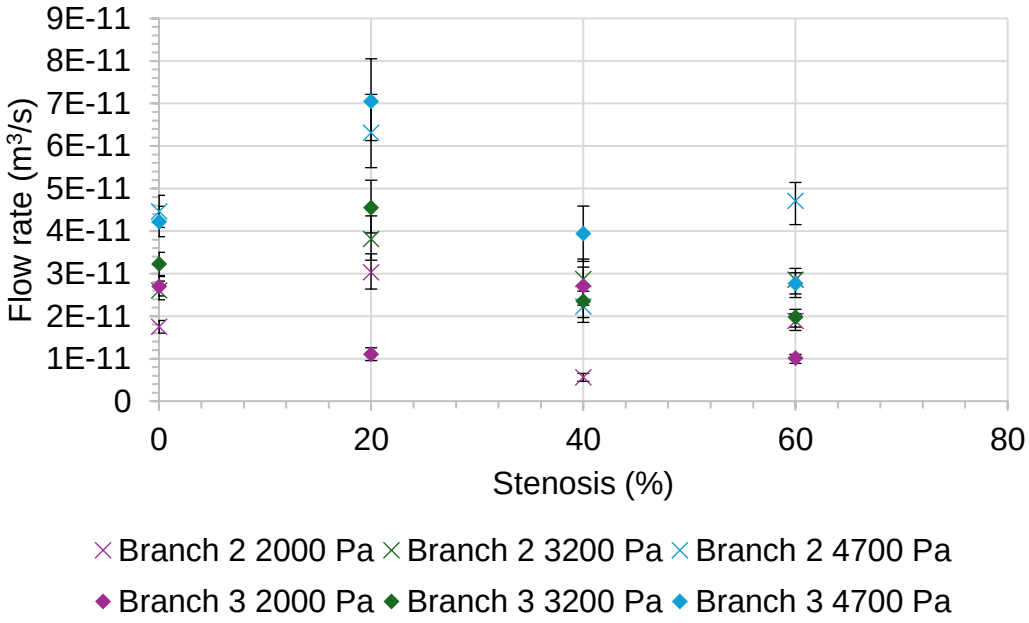

Figure 5.18 Flow rate in Branch 2 and 3 in each stenosis at 2000, 3200 and 4700 Pa in the side branch models.

The wall shear stress in the Branch 3 channel follows the same trend as the flow rate, with an increase from 0-20% then decreased and steadily increased again. In these measurements, there is no statistical difference in the wall shear stress between each pressure due to the overlap of standard deviation error bars. In Branch 2 there is lots of variation throughout the data and this is again could be due to the diversion of flows down either channel.

The wall shear stress in the Branch 2 channel also shows no significant difference between 20 and 40, then 40 to 60% stenosis. The wall shear stress in both channels is within the same range of 0.08-1.2 Pa in both channels and there is no significant difference between the two, without a significantly different flow rate. This will only occur when the flow is diverted. The wall shear stress in the stenosed region is

greater than that in the branches, which was not true of the branching in the Murray's law model. As the cross-section of each channel was equal, this show that a side branch at a 45° angle with the same dimensions will give no significant difference in wall shear stress without a diversion of flow. This is due to the cross-sectional area being the same and when there is no diversion of flow the velocity profile being the same.

Figure 5.17 also shows the CFD model data was less representative of the fluid dynamics measured using GPV than in the case of Murray's law. The CFD model overpredicted the wall shear stress at 4700 Pa excluding at 20%, this is likely due to the sampling technique of the GPV reducing the measurement. At 3200 Pa the CFD model was a good predictor of wall shear stress in the stenotic region and shows how sensitive the measurements of wall shear stress are at this scale. Figure 5.17 shows that the Branch 2 channel for the CFD model often overpredicted the wall shear stress, however, this is likely due to the higher flow rate in the Branch 2 channel in cases where the flow was diverted. This was also true for Branch 3. In the 20% stenosis model, we see this particularly clearly with most of the flow going to the Branch 3 channel at 2000 Pa. The CFD estimates the flow rate in the side branch to be the same as the flow in the main channel due to their equal dimensions and the law of continuity. In cases where the diversion of flow is not seen, i.e. 60% stenosis, the CFD model accurately predicts the wall shear stress in the lower-order branches. There is also agreement that the wall shear stress in the stenosed region will be higher than in the daughter vessels, which is to be expected due to the reduced cross-sectional area, as discussed in Chapter 4. The CFD model here provides the solution according to the governing equations of fluid motion, however, there are

large amounts of real-world variation that can influence the measurement. However, to validate the CFD models use, there needs to be a perfect system modelling ideal flow in the real world. At the microscale with the variation included from fabrication for some models this was not possible.

This data shows that the use of a side branch model can be effective at giving a more accurate representation of flow diversion that may be seen *in vivo* and also a greater range of wall shear stresses through the model, but also maintains equal wall shear stress in the daughter branches as is seen in Murray's law. Furthermore, this model also provides a range of shear stresses from 0-3.1 Pa for pressures of 2000-4700 Pa, falling inside the range of *in vivo* shear stresses in the capillaries at physiologically relevant pressures, providing another suitable design for the creation of a lab-on-a-chip device for investigation of biomarker response.

In these models, the wall shear stress is lower than in the models discussed in Chapter 4. This is due to the greater resistance imposed by the length of the device and branching- which would be seen *in vivo* with variation in capillary length. Additionally with increasing stenosis, the wall shear stress in any branched model does not increase past 3.5 Pa, an order of magnitude smaller than in the short, fixed stenosis models of Chapter 4. This means the model with branching is less representative of the whole range of shear stress conditions.

However, there is more variation across the devices so the designs would be useful for understanding the biomarkers in the effluent released from cells in a variety of environments, as a blood test would not be taken from one capillary and would be sampled as a total from a range of different environments. The ability to detect

certain proportions of biomarker changes in the range of environments would be better investigated under these conditions for sample collection but not for studying individual cell behaviour under a microscope and thus both types of models are needed.

The flow rates in these models are not always detected to abide by continuity with some diversions of flows totalling over 100%. This must be due to the GPV technique and its accuracy. Particularly as the aspect ratio changes such as in Murray's device. This is discussed in §4.3.1. As the model is at steady state and there is no accumulation as seen due to the measurement of a flow and the small standard deviation between measurements, thus the model can be assumed to behave at a steady state when the flow in is equal to the flow out in each run and model. The difference between each model, increasing stenosis, can be assumed to be the factor at play if fluctuations in geometry cannot be accounted for and experimentally it was determined that there were no leaks, losses, or air bubbles that restricted the flow.

5.10 Pressure loss

In models in which the branching follows a change in flow direction there will be pressure loss due to the bend. This pressure loss can be calculated using Equation 5.20.

$$Q_0 = Q_1 + Q_2 \tag{5.20}$$

Where:

$$Q = \frac{\Delta P}{R} \tag{4.2}$$

As seen in Chapter 4. This equation can also be calculated using the equation for flowrate in a rectangular channel in Chapter 4 and thus becomes (135):

$$R = \frac{12\mu L}{1 - 0.63\left(\frac{h}{w}\right)} \frac{1}{h^3 w} \tag{5.12}$$

Where the resistance in the system is as depicted in Figure 5.19.

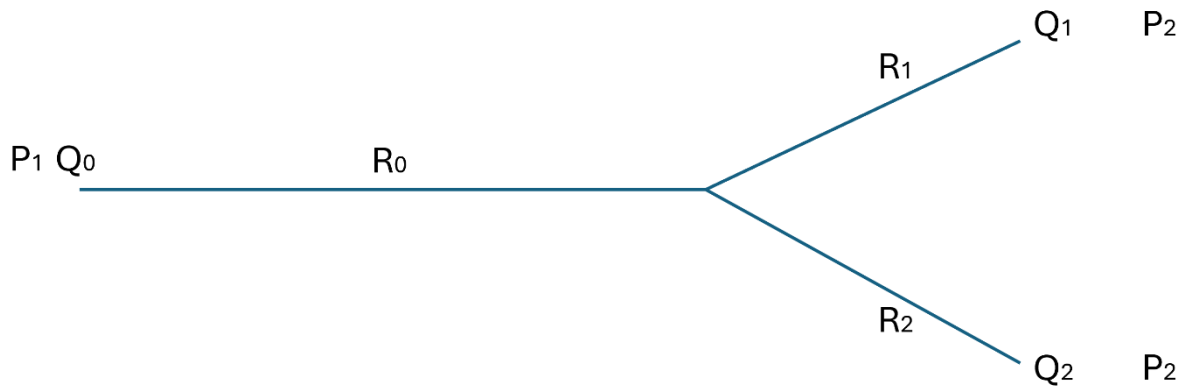

Figure 5.19: Pressure, resistance and flow rate in a branched system

This pressure loss cannot be determined experimentally due to the size of the pressure drop; however, the pressure can be extracted from the CFD simulations. Analytically, in models of bifurcations, pressure losses are often assumed to be due to their frictional losses and not as a result of directional changes (235).

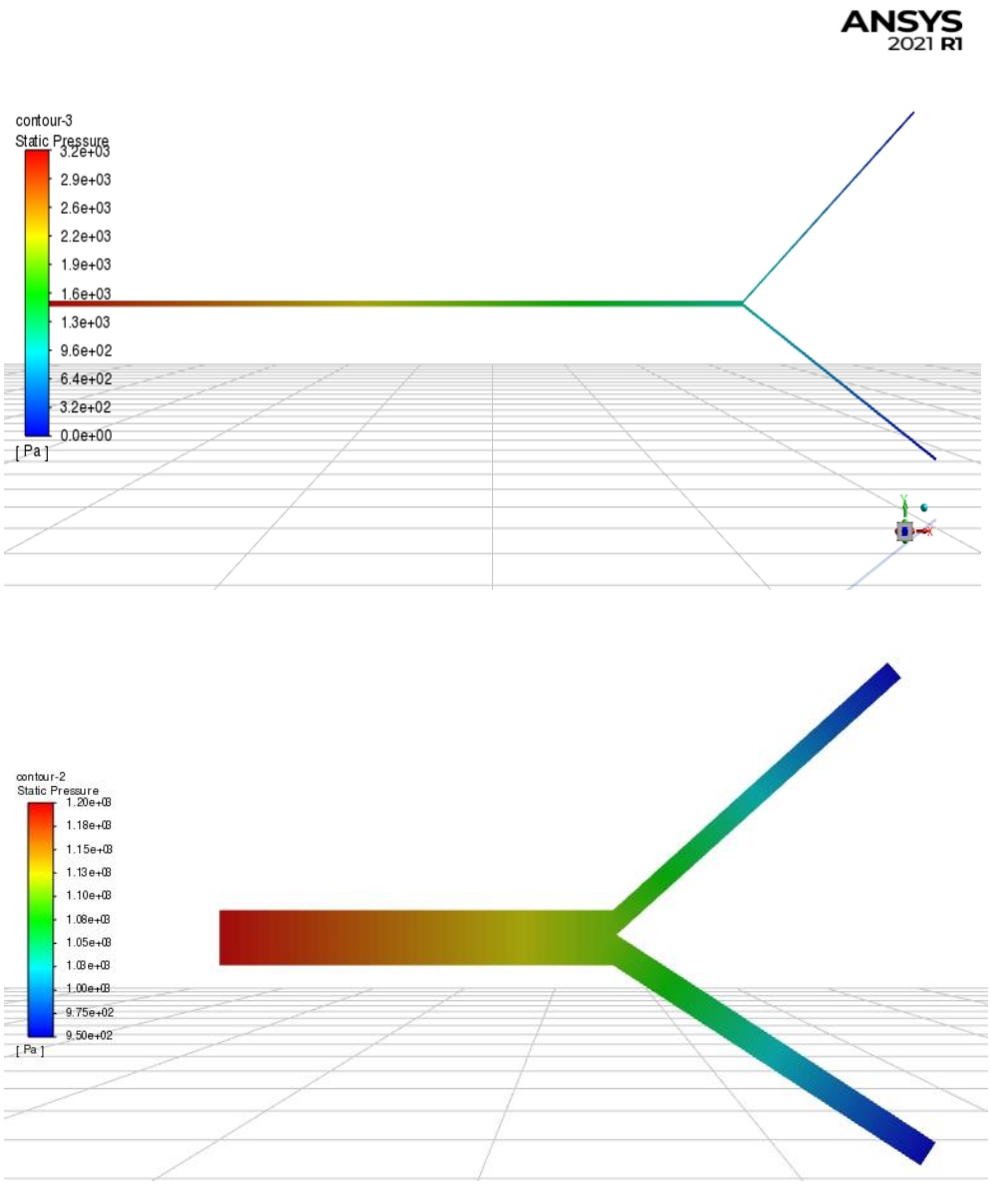

Figure 5.20: Pressure drop along a 200 μm non-stenosed model following Murray's law at 3200 Pa

Figure 5.20 shows the pressure is distributed evenly between channels at this scale and decreases down the length of the channel, there is no significant effect at the bifurcation as a result of the geometry and the change of direction of the fluid.

5.11 Branching

In numerical models of branching, there can be a kinematic factor, ω, to describe the relationship between the velocity in the main channel and the first daughter branch where k is the number of branches, for bifurcations, as here, this value is 2 (231).

$$\omega_k = \frac{v_k}{v_{k-1}} \tag{5.21}$$

This can also be used to describe the behaviour of pressure changes due to branching between the daughter branch and main channel (231).

$$p_k = \frac{\Delta P_k}{\Delta P_{k-1}} \tag{5.22}$$

However, these models are appropriate where the dimensions of the daughter branch are identical and thus would not prove true for cases such as Murray's branching- which is seen in capillary networks. These models are assumed for the isokinetic form- where there is no increasing resistance. This would not be true for the capillary networks in the case of microvascular dysfunction, as there is increasing resistance in the network and thus these assumptions cannot be made for this case. In further studies, it is important to consider the effect of increasing resistance whilst maintaining geometry and controlling experimental variables, such as by making a model that deforms.

5.12 Application of findings to *in vivo* studies

Historically, there is not a good agreement between *in vivo* data of flow behaviour in branched models and microfluidic devices owing to the limitations of cross-sectional

area, but also due to changes in branching due to obstructions *in vivo*, with systems more likely to grow and adapt to deliver the best hydrodynamic environment for the exchange of material such as diffusion in the alveoli (231). Matching this data to *in vivo* data would be difficult due to geometry and resolution limitations and thus this data may only be used for *in vitro/ in vivo* correlation. Other factors particular to blood such as rheology and hemocrit should be investigated. Although investigation of blood flow involving the rheological properties of blood is important for quantification of wall shear stress-it is beyond the scope of this work. There is some debate surrounding blood rheology and its *in vivo–in vitro* correlation. In 1930 the blood flow rheology changed based on geometry in a phenomenon known as the Fåhræus-Lindqvist effect, however, some *in vivo* experiments disagree (236). This effect should be investigated by using a blood or blood mimic in these models.

In vivo, branching may have a further effect on blood behaviour. With the haematocrit values changing there may also be aggregation as a result of this, therefore, rheology should be quantified in the dimension and at the bifurcated angle. Yang et al. 2016 (107) investigated the effects of bifurcation angle on blood flow in the microvasculature, including the effect of rheology and found that of the bifurcation angles tested at low Reynolds numbers, there was no effect, however, there was a pressure loss due to branching that was localised. A series of branched microfluidic devices could be used in series to investigate a full microvascular network, however, this would only become possible when the resolution of analysis techniques improves.

5.13 Conclusions

Branched microfluidic devices have been created and measurements of the flow have illustrated the ranges of wall shear stress obtainable through increased resistance and thus reduction of flow rate.

The wall shear stress inside branched and Murray's branching models remains equal down both branches despite their change in geometry however this cannot be concluded when there are unevenly distributed flows. Uneven distributions of flow were present in all models with some being explained due to increased resistance due to dimensional changes, and this is more likely to be seen *in vivo*. All models gave a range of shear stress values comparable to that seen *in vivo* whilst being measured at physiologically relevant pressures and thus makes them good for use for lab-on-a-chip models with cells. The effect of the increase of stenosis in these models was similar to Chapter 4 seen between the 40 and 60% stenosis on the overall flow rate and begins to show a model of microvascular collapse, despite being at lower flow rates than the models in Chapter 4 due to the greater resistance imposed by branching.

Chapter 6 The Effect of Increasing Resistance in a Novel Deformable Model of microvascular Collapse on Wall Shear Stress

Chapter 6: The Effect of Increasing Resistance in a Novel Deformable Model of Microvascular Collapse on Wall Shear Stress

6.1 Introduction

A deformable microfluidic device was created to increase the physiological relevance of the *in vitro* model by mimicking the response of a dynamically increasing stenosis and to specifically investigate shear stress and resistance changes in this system. 'Short' deformable models and 'long' deformable models, matching the dimensions of the fixed stenosis models described in Chapter 4 and geometrically detailed in Chapter 3 were fabricated and tested. A deformable model with even branches was tested to see the effect on downstream branching resembling the network behaviour described in Chapter 5. Fixed CFD models matching the geometries of the *in vitro* devices were developed to measure wall shear stress in the deformable region and to compare shear stress values from the deformable *in vitro* models with the steady-state fixed CFD models.

6.2 Material choice: PDMS composition and elasticity

The elasticity of the capillary wall is debated throughout the literature as discussed in § 2.1.3 but can be assumed to be roughly 1 kPa. Therefore, a range of PDMS base to curing agent ratios were tested to achieve the lowest Young's modulus and thus the highest deformability possible as seen in Weibel *et al.*, 2007 (117). The PDMS base to curing agent ratio was varied and the stress and strain were measured on the Zwick Roell tensile tester as discussed §3.3.

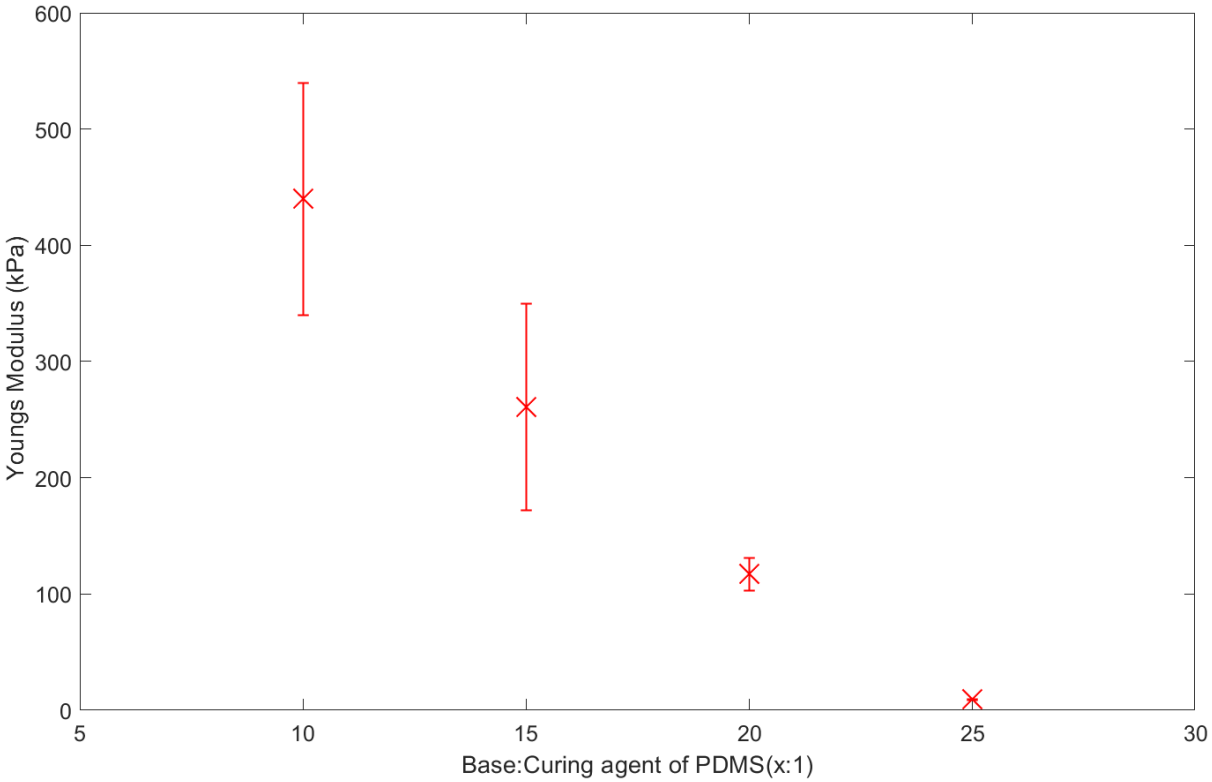

Figure 6.1: The Young's moduli of the PDMS as calculated from measurements of stress and strain by the Zwick Roell tensile tester with increasing base-to-curing agent ratio

The PDMS elastomer has a Si-O backbone and ($Si(CH_3)_2O$) branching. The CH_3 and Si-O bond together during the cross-linking stage and this determines its properties (237). The number and degree of these bonds determine the flexural properties, thus by increasing the ratio of base to curing agent from 10:1 to 25:1, fewer cross-links/ bonds are formed and the polymer is more flexible, decreasing its Young's modulus (238). Figure 5.1 showed that by increasing the base-to-curing agent ratio, the Young's modulus of the PDMS decreased from 440 kPa at 10:1 to 7 kPa at 25:1. There was also less variation in the 25:1 measurement and the elasticity was a closer mimic to that *in vivo*, of approximately 1 kPa suggesting there was a more even distribution of bonds and curing in the sample tested (239). Ratios beyond 25:1

were found to lose structural integrity and were unusable. Other factors such as time and curing temperature can affect the elastic properties of PDMS and thus these were ensured to be constant as discussed in Methods §3.2 (240). Due to this, values of Young's modulus values of PDMS quoted in the literature should not be used without careful consideration of the manufacturing parameters. This data set concludes PDMS in ratios from 10:1 to 25:1, cured at 70°C for 1.5 h, are suitable polymers for *in vitro* modelling due to their elasticity. This was a useful test for determining the best PDMS ratio to use, however, the achievable deformation in the set channel geometry at the microscale needed to be investigated.

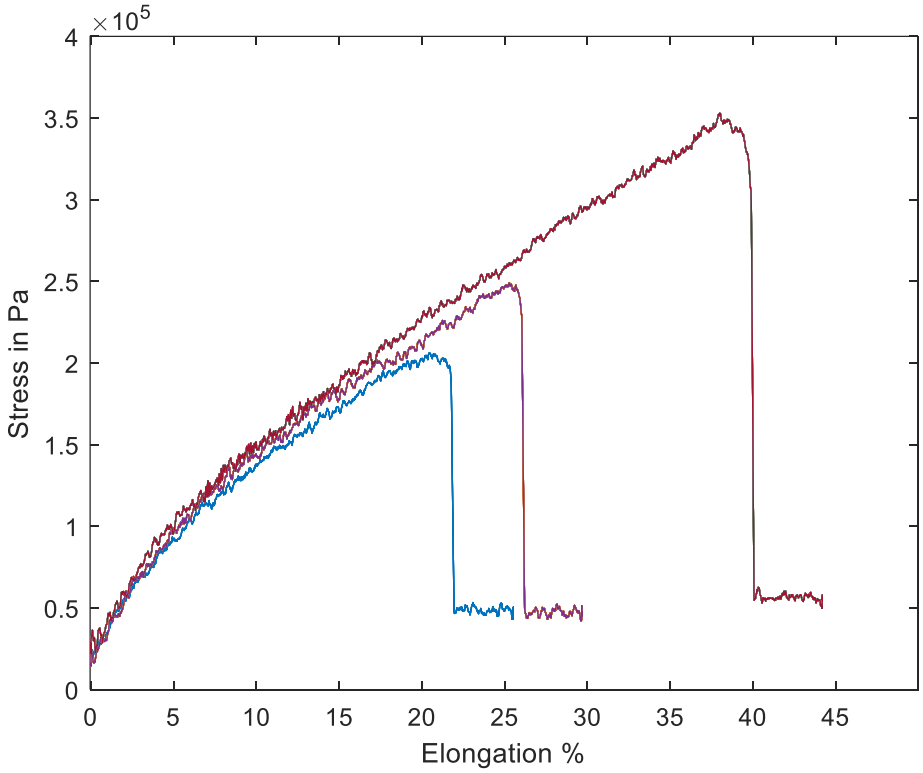

Figure 6.2 Stress-strain graph for the 25:1 PDMS with 3 repeats from the Zwick Roell

Figure 6.2 shows for the 25:1 PDMS there was initially a linear increase of stress with increasing strain, showing the material behaves according to Hooke's law, Equation 3.1. Hooke's law of linearly elastic solids also applies to the capillary, therefore, 25:1

PDMS is a suitable material for the deformable walls to mimic capillary behaviour (134). This study is conducted using the aforementioned dumbbell test and therefore the deformation whilst in the channel geometry must be studied.

$$E = \frac{\sigma}{\varepsilon} \tag{3.1}$$

6.3 Single Pump 'Short' Deformation

A single small pump 700 µm in length and 65 µm of wall thickness was used at 25:1 base to curing agent to see if full deformation was achievable for a short stenosis as shown in Figure 6.3. To ensure the experimental set-up was free from leaks through the micropumps, the pumps were filled with a solution of bromocresol purple (Sigma, U.K) and 0.1 M sodium hydroxide (Sigma, U.K.) to make a dark purple dye distinguishable from the microparticle dispersion in the channel on the greyscale microscope. Leaks could be detected when the internal fluid turned dark, the exit channel was purple and GPV results showed areas of anomalies.

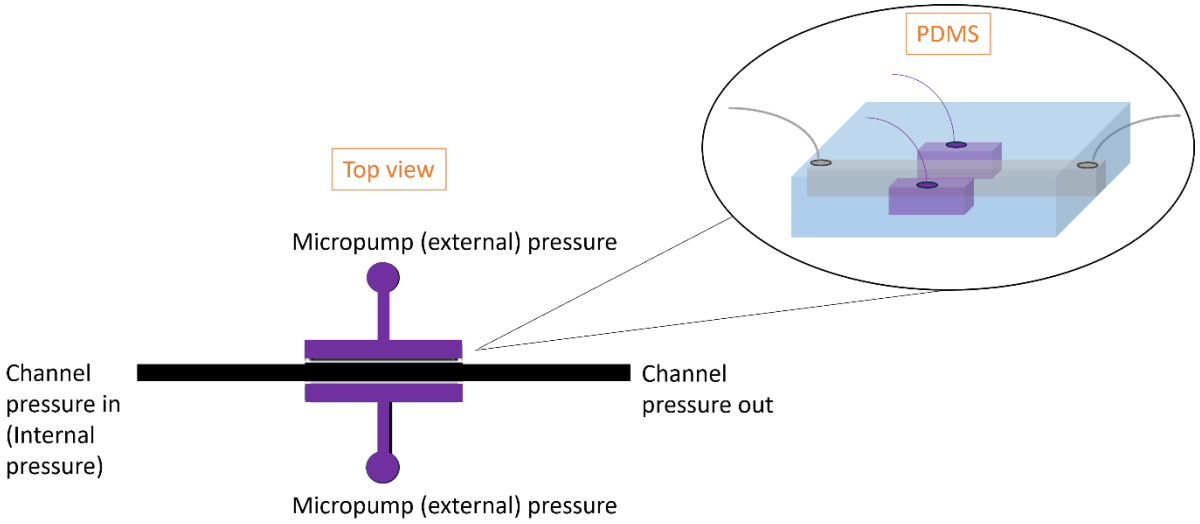

Figure 6.3: Schematic representation of the pressure supply to the micropump system and main channel with purple bromocresol dye

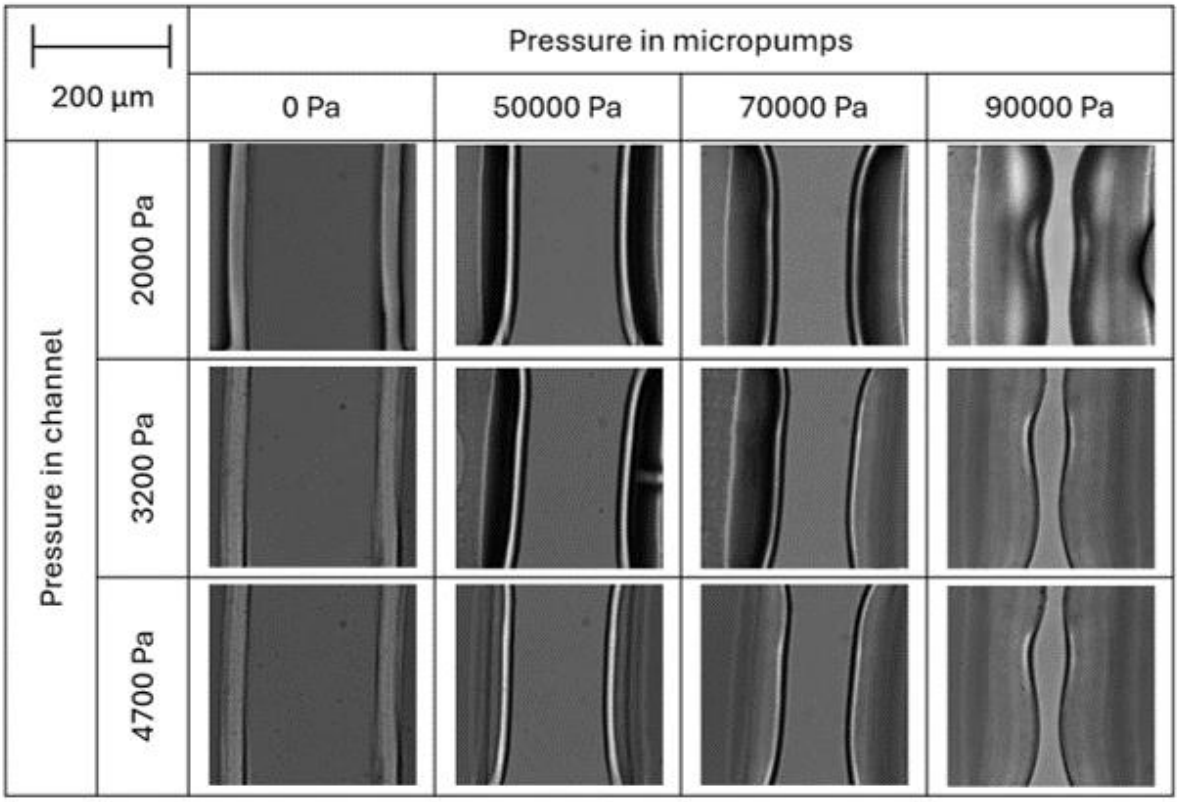

Figure 6.4: The deformation of a 25:1 channel with channel pressure at 2000-4700 Pa and pressure supplied to the micropumps from 0-900000 Pa for a single short deformable pump

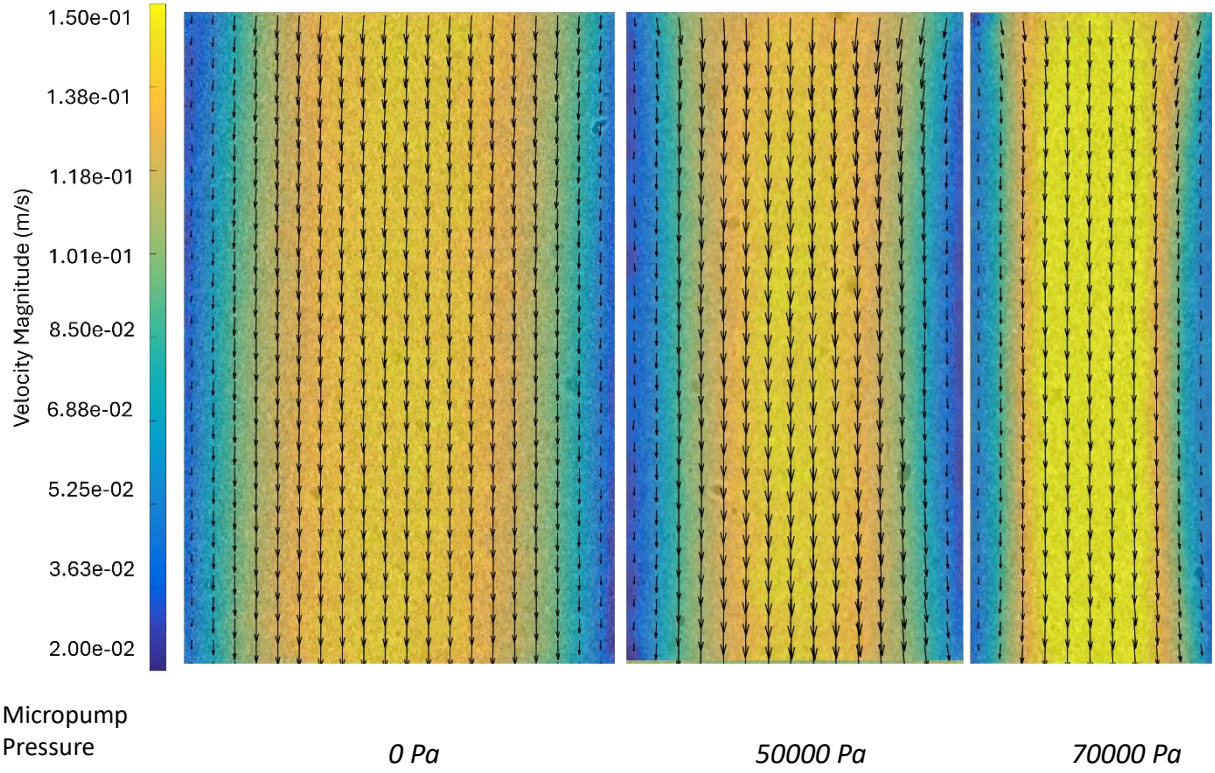

Figure 6.5: GPV velocity spatial distributions of a short deformable stenosis model at 3200 Pa at 30000 fps

Figure 6.4 proves that with a 25:1 ratio a single 700 µm length micropump could deform over 60% of the channel with a 25:1 base to curing agent ratio of PDMS. Furthermore, this initial test identified that at maximum deformation, GPV would not be possible due to the reduced width of the channel, resolution, and the ability to see a speckle pattern. The velocity profile experimentally would not be able to be measured at 300 µm channels greater than 80% stenosis due to the resolution limits of the PIV algorithm being reached as not enough interrogation areas could fit into the width of the stenosis to achieve accurate readings while capturing the displacement in the direction of the fluid movement as seen in Figure 6.6 and seen in the errors forming in Chapter 4.

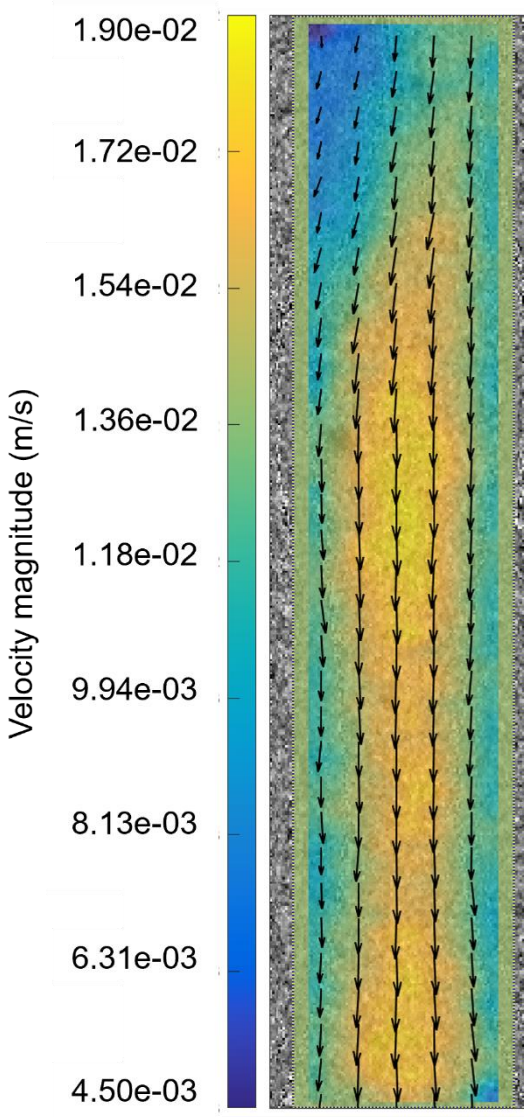

Figure 6.6: GPV taken at maximum stenosis at 3200 Pa internal pressure at 90000 Pa external pressure showing areas of errors in a short deformable model at 30000 fps

However, it can be verified that there is still flow from the velocity detected in the stenosis despite not being able to measure parabolic flow and from fluid exiting the microfluidic set-up. This is due to the shape of the deformation of the cross-sectional area thus, allowing some flow through the channel due to the rectangular geometry

as seen in Figure 6.7. In the deformable stenosis, the cross-section is hypothesised to deform as shown in Figure 6.7, which can be verified through microscopy.

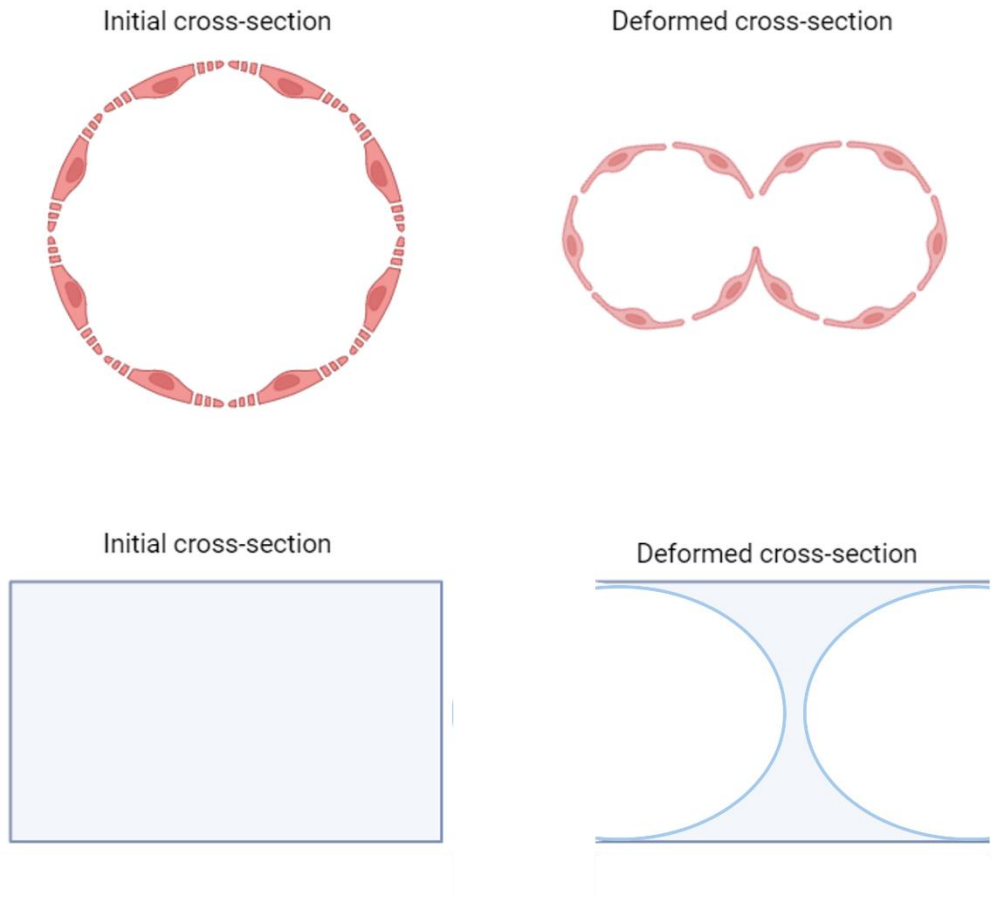

Figure 6.7: Cross-section of a capillary deformation and expected cross-sectional deformation of a microfluidic device created on Biorender.com

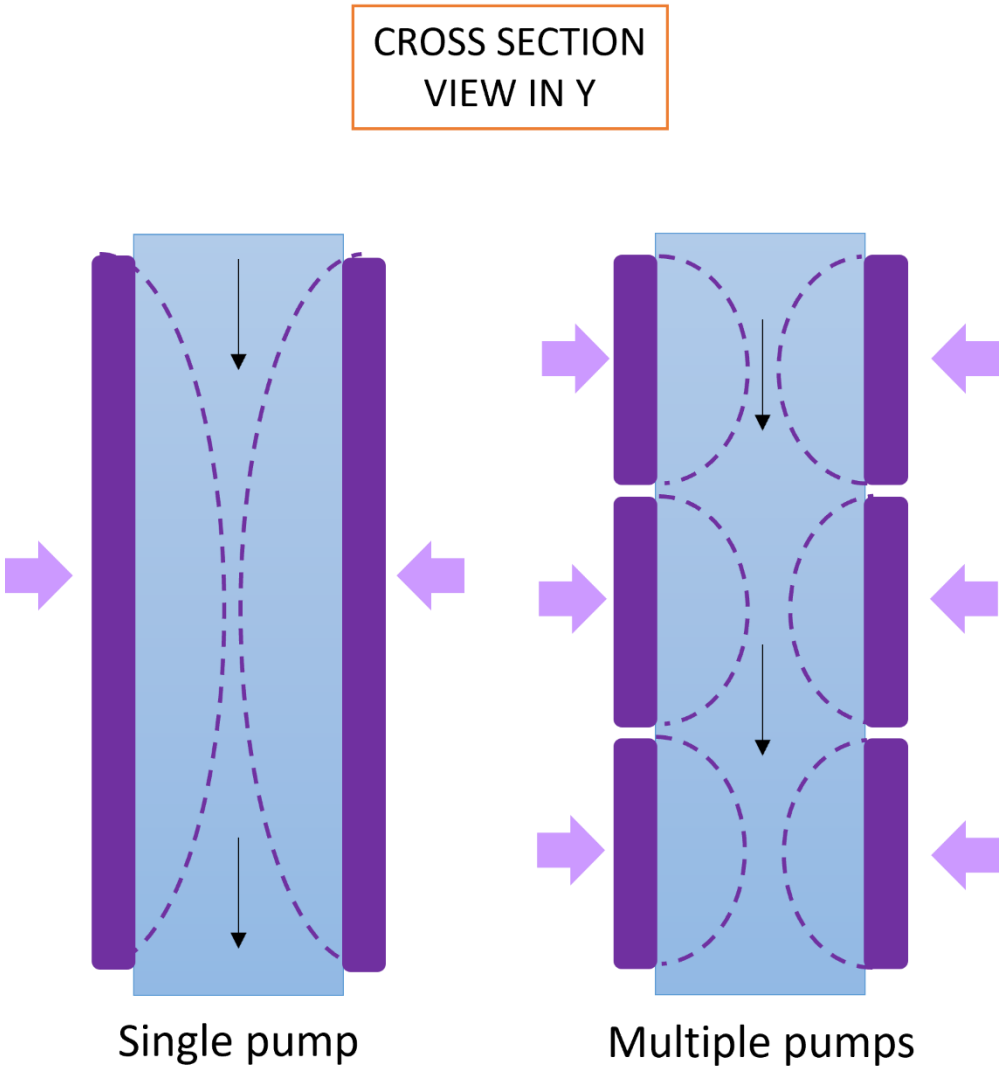

Figure 6.8 Cross-sectional view of channel deformation in the Y plane at y=Y/2

In vivo, it has been reported that the shape of the capillary change is buckling as shown in Figure 6.7 (125,133,215). This is not achievable through microfluidic models due to the manufacturing process but as with the design of the microfluidic device, both *in vitro* models and *in vivo* data, as stated in Ghazy *et al.* (121), show non-linearity in the deformation down the length of the channel as seen in Figure 6.8 (50). A correlation of cross-sectional area change should be used when applying this deformation model to models of cylindrical collapse. Additionally, when considering

blood flow properties this non-linearity in the geometry must be considered as it has been found to affect blood flow behaviour as seen in Ghazy *et al.* (121).

Thus, it cannot be determined that the microfluidic channel is 100% closed to flow from GPV alone, due to where the central plane is measured, H/2, and depending on the cross-section of the channel in the XY plane. The microscope must be used for the assessment of the full channel closer by adjusting the height. This means flow might not fully have stopped and depends on the resistance of the geometry, however, the deformation of a 25:1 PDMS channel may begin to increase resistance in the same manner seen in Chapters 4 and 5.

Furthermore, increasing the internal channel pressure from 2000 Pa to 4700 Pa had no significant effect on the width of the channel for the short stenosis. The interaction here can be determined to be one way applied from the micropump to the fluid in the channel. There was also no hysteresis observed at the low flow rates which supports both of the conclusions found by Katz *et al.* (114).

6.4 Long Deformable Stenosis

6.4.1 Maximum Deformation

Knowing that deformation can be achieved for the short stenosis, the long stenosis model was investigated to investigate the greater effect of resistance. Three different designs of pumps were investigated for their deformability for the base-to-curing agent ratios of PDMS of 10:1, 15:1, 20:1 and 25:1 as shown in Figure 6.9. The pumps were inflated until rupture through increasing the pressure at 10000 Pa intervals with the maximum deformation being measured through recording of frames

using PFV software and measured using ImageJ at the point of maximum deformation. This was repeated thrice on new PDMS models, and the mean average deformation was calculated as well as the range as shown in Figure 6.10.

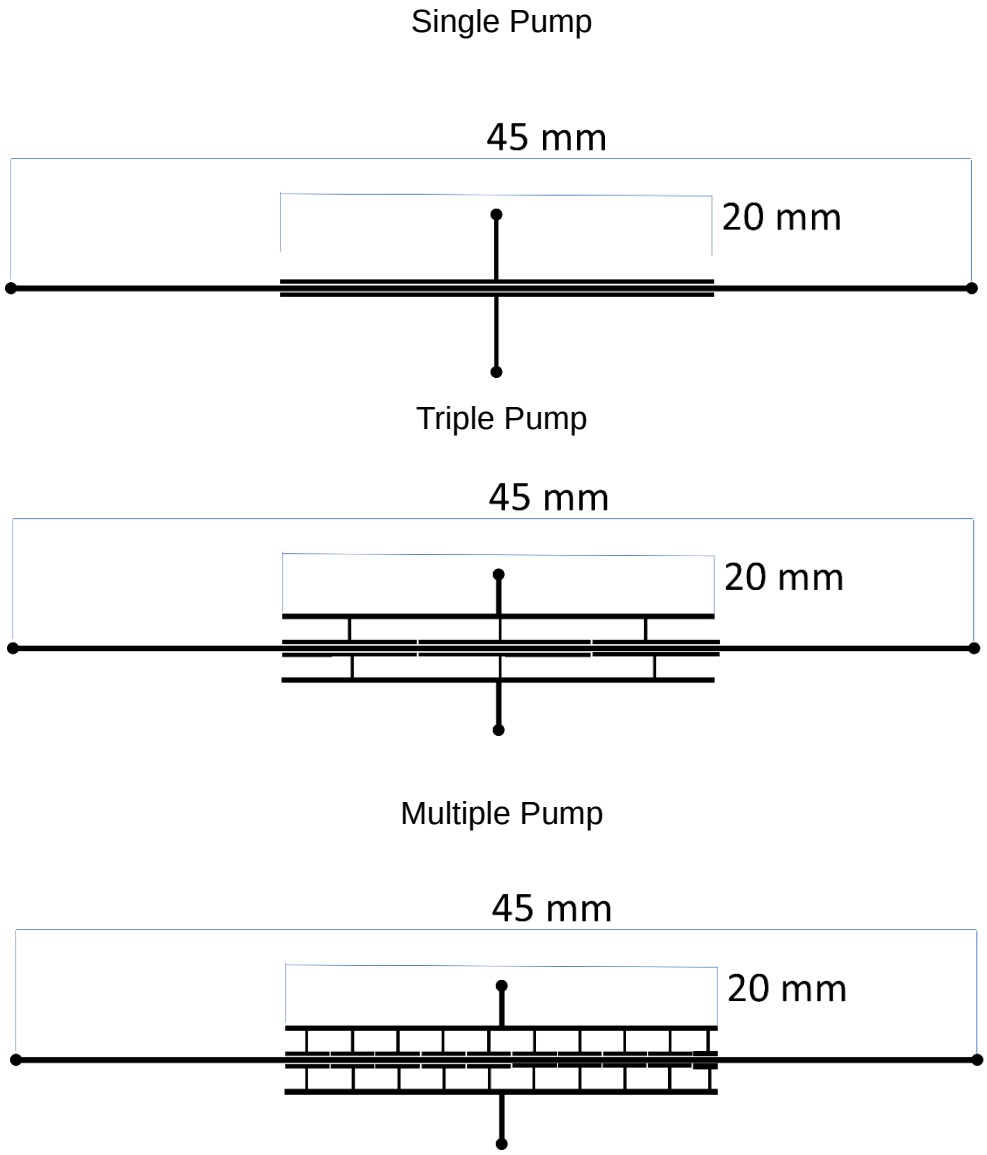

Figure 6.9: Different pump designs tested in varying ratios of PDMS as detailed in materials and methods §3.4.5.

Figure 6.10: The mean average (of three measurements) percentage of maximum deformation achieved in situ with each type of pump design of the long stenosis deformable models and the range of the pressure corresponds to Figure 6.11.

It was found that although the 20:1 ratio PDMS allowed for some deformation and less tearing, the greatest deformation was done by using a 25:1 ratio. As seen from Figure 6.1, this is when the Young's modulus of the device is the lowest as to be expected from an elastic material following Hooke's law. The pumps in series were seen to have the most deformation and have the least tearing when tested, however, in practice a maximum of 23% deformation could be achieved in the 25:1 long stenosis multi-pump model. Larger pumps such as the single and triple pump models in Figure 6.9 were found to rupture at lower pressures. As the PDMS composition, width between the main channel and the pump and the pressures involved are equal the result of this difference is because of the geometry and structural design of the pumps in this setting.

The modelling of the deformation achieved in the vessel is complicated. Most commonly pressure vessels are cylindrical, reducing stresses on corners which are more likely to rupture. However, given the soft lithography technique used in this model creating a cylindrical cross-section was not possible. Assuming a Young's modulus of 7 kPa, thin wall theory was applied to calculate the maximum amount of deformation on each wall. Assuming thin wall theory, Chapter 2, a pressure vessel with walls with a Young's modulus of 7 kPa should be able to deform across the width of the channel where the wall thickness, t, is less than the width, w with a Poisson's ratio for PDMS of 0.5 (241). Figure 6.10 proves that the thin wall approximation cannot be used in this case when modelling collapse in a microfluidic device. This is additionally due to the variation in wall thickness as the thinnest wall is between the channel and the pump reservoir, which means that the deformation would not be even on all sides as thin wall theory assumes.

Furthermore, there is no confirmed mechanism for how thick-walled vessels deform under pressure and most investigations are done based on computational simulations, specifically finite element analysis or experimental study, although there have been attempts to find a correlation with thin wall theory with correction factors (242). As stated in previous literature there is no commonly used 'thick wall theory' for rectangular vessels particularly that in which one wall is thinner than the other as in this case. Finite element models could be used in this case to estimate or a deformable CFD model with fluid structure interaction but would not account for external experimental difficulties such as the retention of tubing to the channel at high pressures, where the PDMS could not retain the tubing in the set up under pressure

and it was ejected, thus stressing the importance of combining CFD with experimental data.

Each device had maximum pressure limits when tested before the micropumps ruptured or the tubing was forced from the pressurised system. To prevent rapidly over-pressurising the device the pressure was raised by 10000 Pa every 50 s, the maximum limit of the pressure controller.

6.4.2 Maximum Pressure

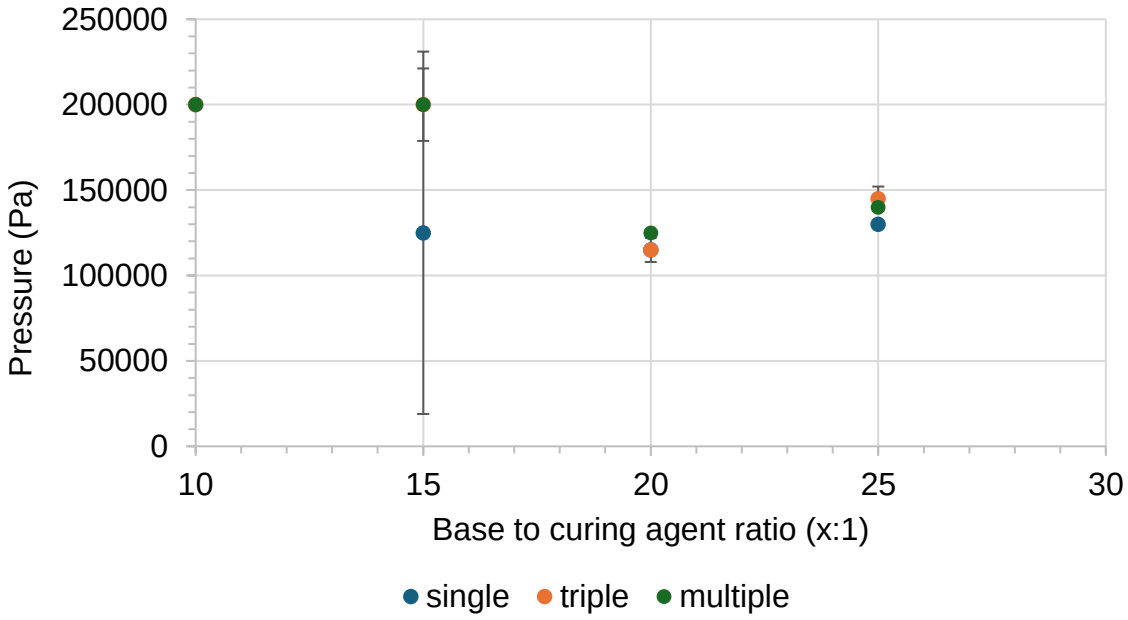

Figure 6.11: The maximum working pressure of the external micropumps before the device ruptured for all three deformable geometries, some points overlap

Experimentally, decreasing the Young's modulus by using 25:1 and using the multiple pump deformable design described in §3.4.9, it was found that up to 23% deformation could be achieved at 140000 Pa. The 25:1 ratio of PDMS could withstand a higher pressure than the 20:1 ratio of base to curing agent PDMS and

also could achieve more deformation as shown in Figure 6.10, therefore, this model was selected for use in the deformable experiments. According to Equation 6.1 with decreasing cross-sectional area, the force the material experiences increases at constant pressure. With greater force, there should be greater deformation as seen when combining Equations 3.1 and 6.1.

$$E = \frac{\sigma}{\varepsilon} \tag{3.1}$$

$$P = \frac{F}{A} \tag{6.1}$$

Increasing the pressure, P, in a fixed geometry increases the force, F, on the cross-sectional area, A. The deforming cross-sectional area is not different enough in each design at a 0.7% and 3% decrease of the total area for the triple and multiple pumps respectively to quantify a statistical difference, (>5%), in the maximum pressure the device can withstand using this method. However, the device was seen to withstand pressure for longer without tearing with the complex multiple pump design, with the PDMS between each pump acting as a support.

However, using the 25:1 ratio meant that with the more elastic properties of the PDMS, when the micropumps were placed under pressure the whole system was more likely to tear and the attachments to the microfluidic tubing were more likely to be ejected from the microfluidic device as the connection could not withstand the pressure. Therefore, the model was adapted with a 25:1 cured lower layer covering the geometry for 1.5 hours to give the Young's modulus found in Figure 6.1, but a layer of 10:1 PDMS was added after 0.5 hours and then the whole device was cured for an extra hour to provide support for the tubing as the 10:1 ratio was less elastic

and could withstand higher pressures without tearing, keeping the connected tubing in place at higher pressures. This is depicted in Figure 6.12.

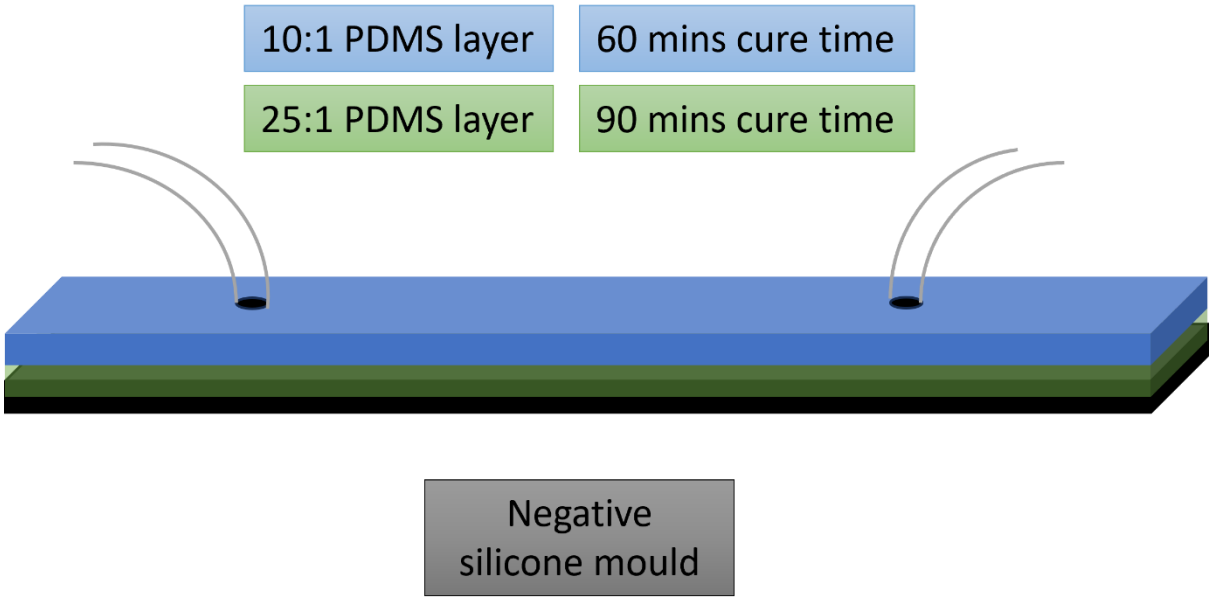

Figure 6.12: Image showing layers of PDMS and their total cure time

The 25:1 PDMS was cured for the first 0.5 hours using a hot plate thus the heat was supplied from the base, curing the mould faster than the top of the PDMS. This was done to allow a gradient of cured material and allow the 10:1 PDMS to be joined to the 25:1 PDMS, preventing the two layers from separating. This allowed for the creation of multipump devices that were up to but not consistently 100% deformable as seen in Figure 6.13 and overcame the issues of tearing the device and the retention of tubing. Both the long deformable and branched deformable models were then produced using this adapted methodology and could withstand pressures up to 140000 Pa. Increasing the pressure past this point the internal geometry ruptured as seen in Figure 6.13b.

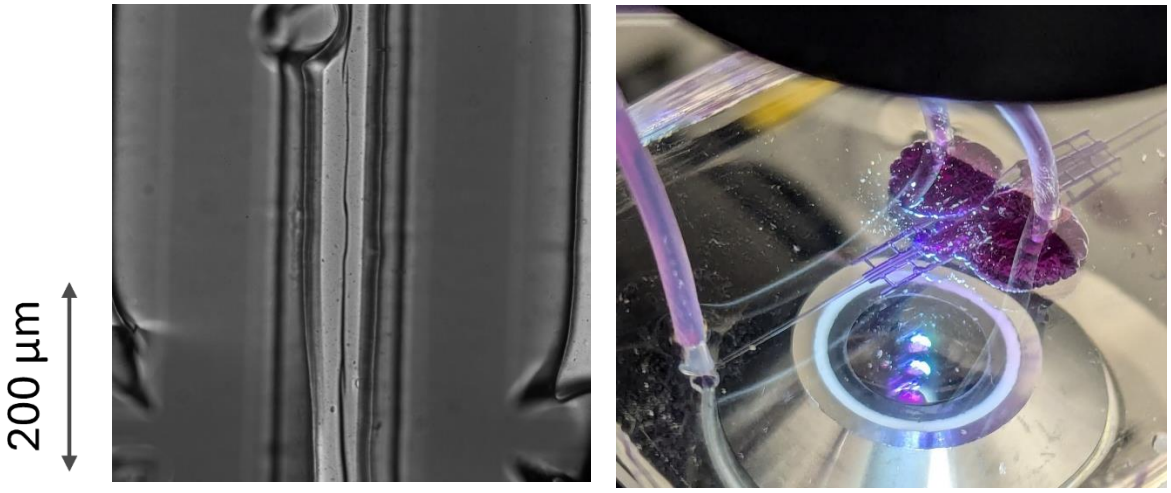

Figure 6.13: Closure of 25:1 and 10:1 combination of branched deformable device, 100% deformation at 150000 Pa, figure b rupture of internal geometry at 150000 Pa

6.5 Experimental Parameters

The GPV was run at 10000-20000 fps 1024 (w) x 1024, 768 (h) px resolution 1 px = 1 µm at 20x zoom. The height of the short deformable model was 126 µm (+/-9 µm), the height of the long deformable model was 37 µm (+/- 6 µm), the height of the branched deformable model was 44 µm (+/- 5 µm). The long deformable model had an initial width of 195 (+/- 5 µm) and the long branched deformable model had an initial width of 200 µm (+/- 6 µm).

The measurements were taken at the locations highlighted in yellow in Figure 6.14.

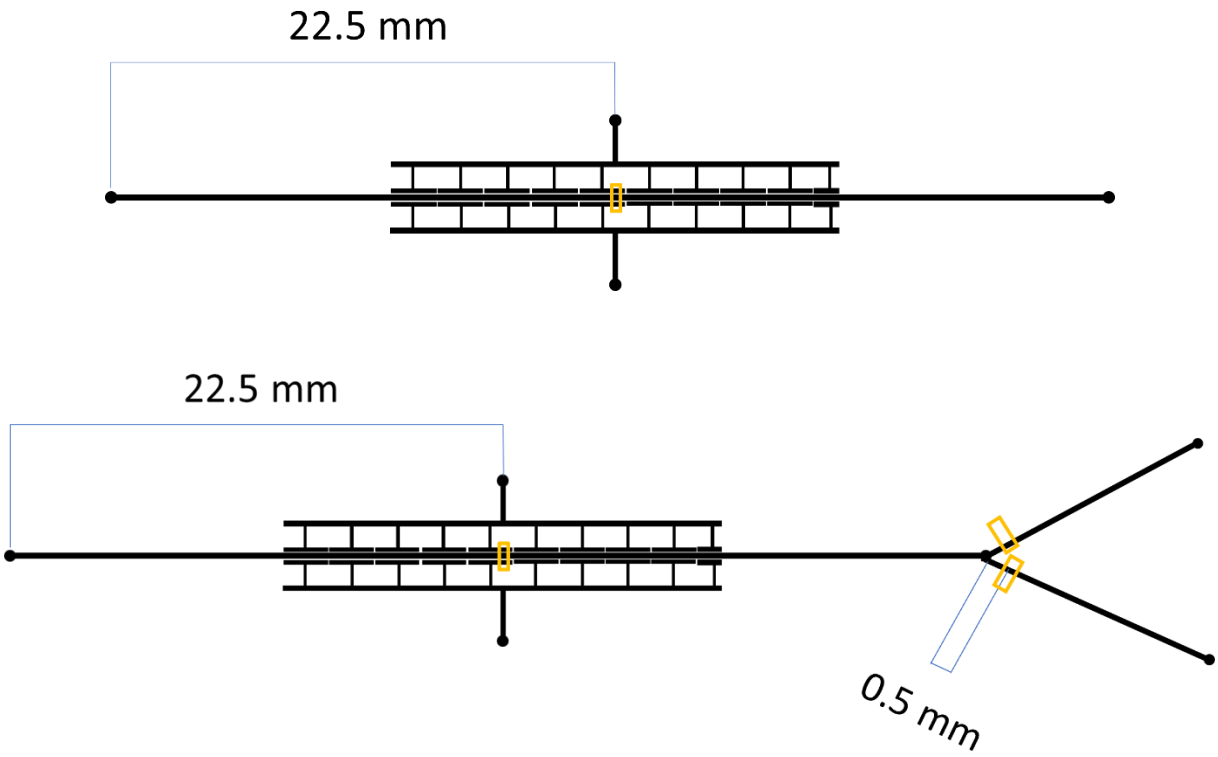

Figure 6.14: Location of GPV measurements in deformable models highlighted in yellow

6.6 GPV Deformable Model

The 25:1 and 10:1 combined deformable non-branched model deformed up to 4% stenosis and withstood pressures of up to 140000-180000 Pa.

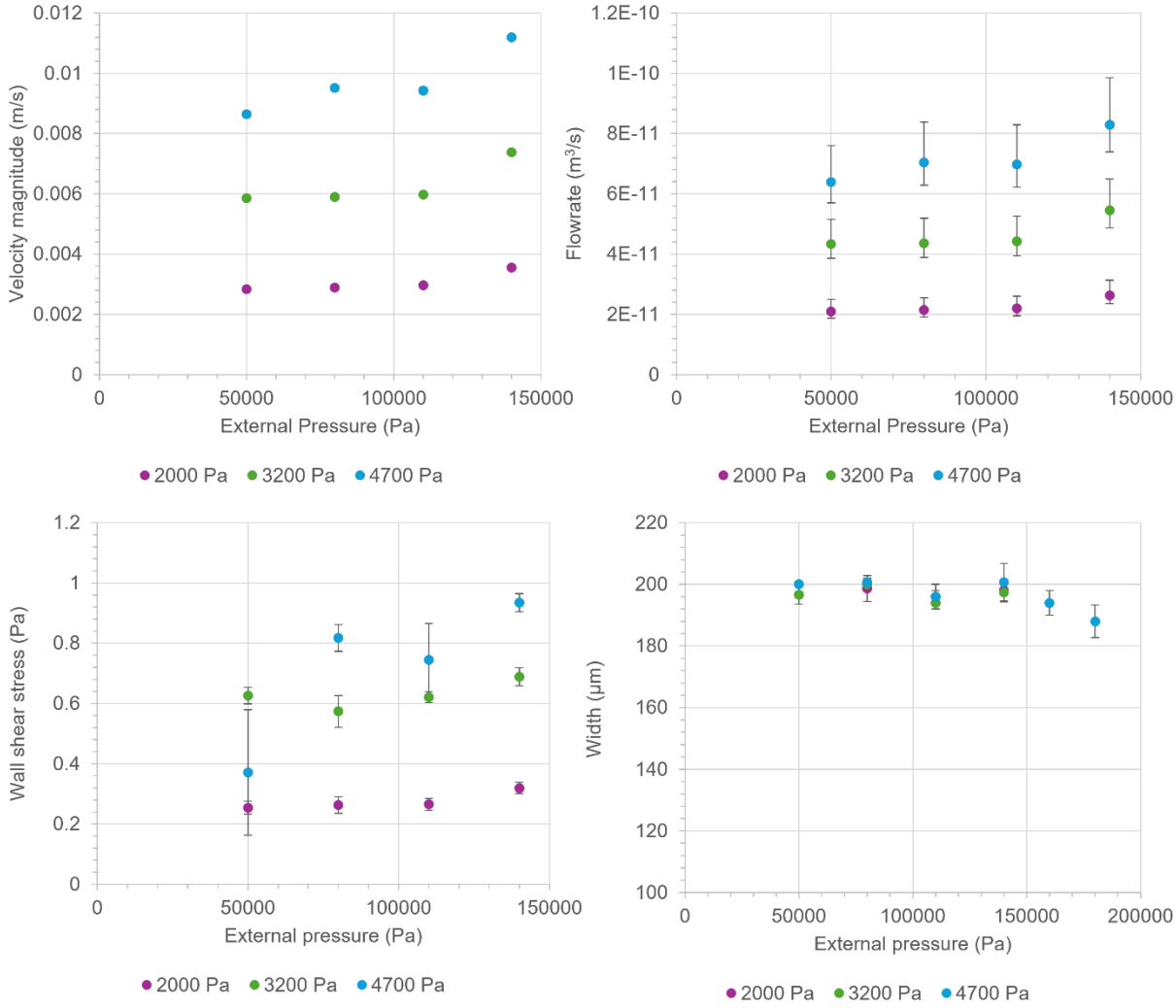

Figure 6.15: Data extracted from ghost particle velocimetry measurements in the deformable model with micropumps in series showing the velocity magnitude with standard deviation (too small to see), flow rate and range, wall shear stress and standard deviation and channel width with increasing pressure – Maximum 4% stenosis

Figure 6.15 shows that in the deformable model, there is a small increase in the velocity magnitude when the external pressure increases for all pressures. This is shown more predominantly when the external pressure exceeds 110000 Pa and there is greater deformation of the channel. This is due to the decreasing cross-

sectional area as shown in Figure 6.15b. With a decreased cross-sectional area, at constant pressure, there will be an increase in velocity due to continuity as seen in Chapter 4. However, there is no significant difference in the measurements of flow rate, which is likely due to the corresponding no significant difference in deformation at the lower external pressures tested. The deformable model was not able to deform past the point to decrease the overall flow rate as seen in Figure 6.15b. This would be the region in which resistance is increased and there is a decrease in flow rate as a result. However, with increasing external pressure applied to the side walls there is an increase in the wall shear stress. This suggests that when there is compression and deformation *in vivo*, also representing the 3D case, there would be an increase in the wall shear stress and thus cells would be under a different environment. As there is no distinguishable decrease in flow rate, it is likely that the deformation in this channel did not occur following the predicted cross-sectional area seen in Figure 6.7, and perhaps due to the elasticity of the PDMS there was some deformation in the z axis direction causing the channel to bulge upwards.

6.6.1 Resistance to flow

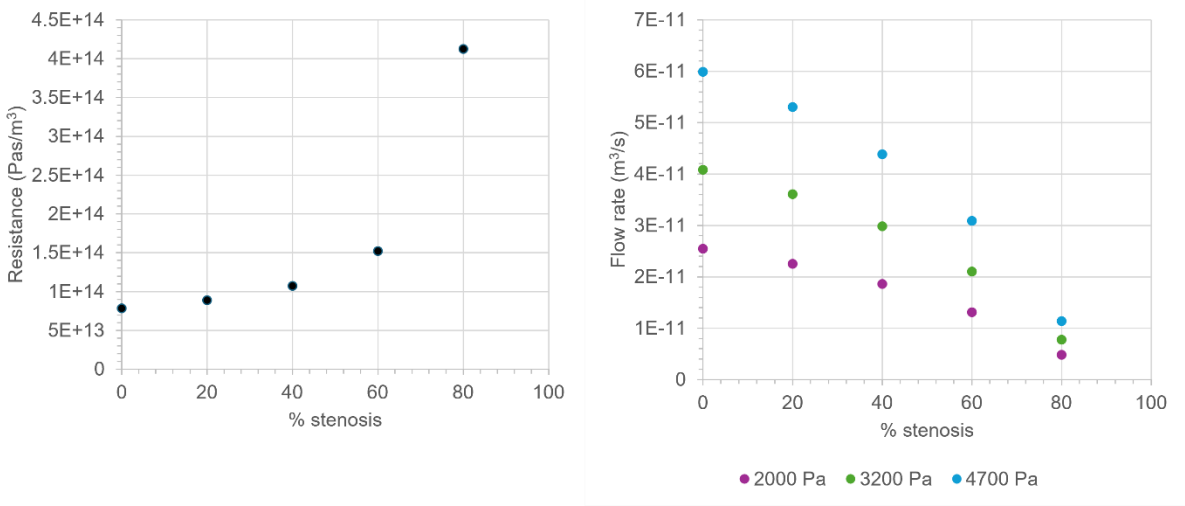

Figure 6.16 Analytical resistance calculations for resistance and flow rate of the deformable model

Figure 6.16 shows the resistance of the model exponentially increases with increasing stenosis as calculated using Equation 4.4 for resistance in a rectangular channel following the method described in §4.2.2. The device is separated into a static 0.025 m long channel and a region of decreased stenosis at 0.02 m and the resistance of each area is summed. Similarly to §4.3.1 with a pressure driven flow and no known resistance of fittings in a laminar system, without CFD the pressure drop due to the tapering into/ out of the stenosis cannot be calculated and may provide some error between measurements. Additionally, the shape of the cross section of the deformable region, as shown in Figure 6.7 will give rise to some error where the analytical resistance is overestimated. This is due to the estimate assuming a rectangular cross-section with the width of the maximum stenosis in this region.

As seen in Figure 6.16b the flow rate is also expected to decrease with increasing stenosis due to the exponential increase in resistance shown in Figure 6.16a. Table

6.1 provides analytical and experimental resistance values for non-deformed multipump deformable device.

Table 6.1: Analytical and experimental resistance values for non-deformed multipump deformable device

Method	**Flow rate (av) (m^3/s)**		
	Pressure (Pa)		
	2000 Pa	3200 Pa	4700 Pa
GPV	2.1×10^{-11}	4.3×10^{-11}	6.9×10^{-11}
Analytical	2.5×10^{-11}	4.1×10^{-11}	6.0×10^{-11}

As the GPV shows that where there was no change in width in Figure 6.15d at 50000 Pa externally the corresponding flow rate from Figure 6.15b was used as the non-deformed geometry. Due to the large standard deviation of experimental measurements due to the geometry and fabrication process used on the GPV data, there is agreement between the GPV and analytical data for the flow rate in a non-deformed deformable channel for all internal/channel pressures tested, however, there is no agreement when the external pressure is applied, likely due to the same reasons discussed in §6.6.

To improve upon the analytical prediction of the resistance in the deformable system using the method in §4.2.3 CFD techniques should be used, that can consider the change in cross sectional area in 3D and other pressure losses in the system, such as with a flexible wall, fluid structure interaction and fittings.

6.6.2 CFD

Fixed stenotic models were created following the dimensions of the deformable model at 0, 20, 40 and 60% stenosis following the method described in §3.8. The boundary conditions were 2000, 3200 and 4700 Pa at the inlet and 0 Pa at the outlet with no slip on the walls. A CFD model with a deformable wall was also attempted but numerical issues with these simulations could not be resolved. A summary informing future work is given in Appendix 5.

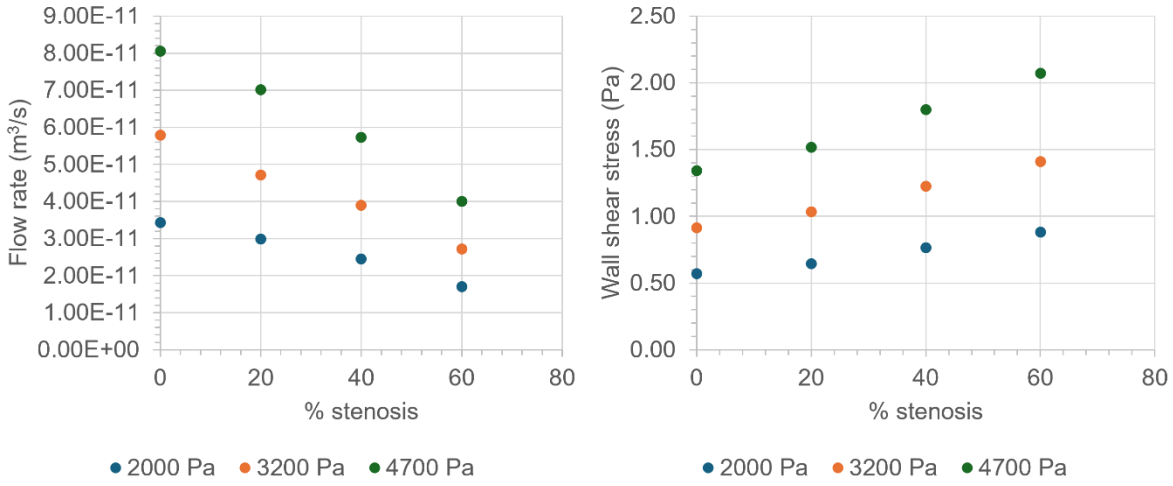

Figure 6.17 a,b: CFD values for the fixed stenotic models of the dimensions of the dynamic microfluidic model at 0, 20, 40, and 60% stenosis, tested at 2000, 3200, and 4700 Pa.

Figure 6.17 shows for the fixed CFD model with increasing stenosis there is decreasing flow rate, which is corroborated by the analytical prediction of flow rate in Figure 6.16. The trend in flow rate does not agree with experimental data in Figure 6.15, which is likely due to the errors discussed in §6.6. Figure 6.17b shows in the stenotic region there is an increase in wall shear stress with increasing stenosis,

following the trends seen in Chapter 4. The data set extends the range of deformation as the deformable microfluidic model could deform 4%, but the CFD model shows from 0 to 60% deformation.

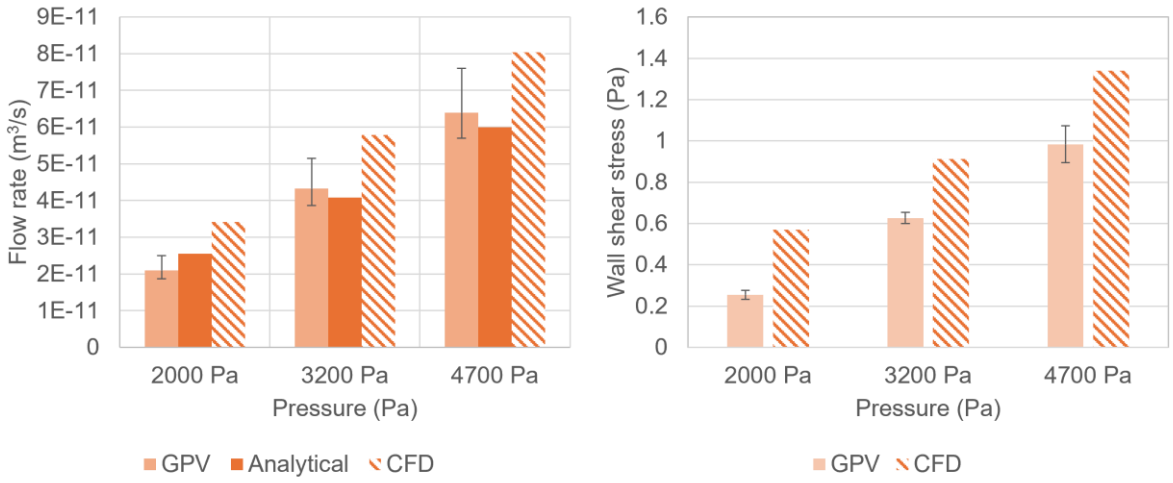

Figure 6.18: GPV, analytical, and CFD values for the fixed stenotic model at 0% stenosis, tested at 2000, 3200, and 4700 Pa.

Figure 6.18 shows the GPV results showed good agreement with the analytical method of calculating flow rate as described in §4.2.2. The CFD model predicted higher values than the GPV data which is likely due to the sampling range of the GPV data compared to the aspect ratio discussed §4.3.1, which can underpredict flow rate values as compared to CFD. The wall shear stress from the CFD model is seen to be higher than the GPV data, this is due to the resolution of the measurement with the CFD having a smaller cell size closer to the channel wall providing a more accurate estimate of wall shear stress. This is also coupled with the higher flow rate in the CFD model in Figure 6.18a.

6.7 GPV and CFD Deformable Branched Model

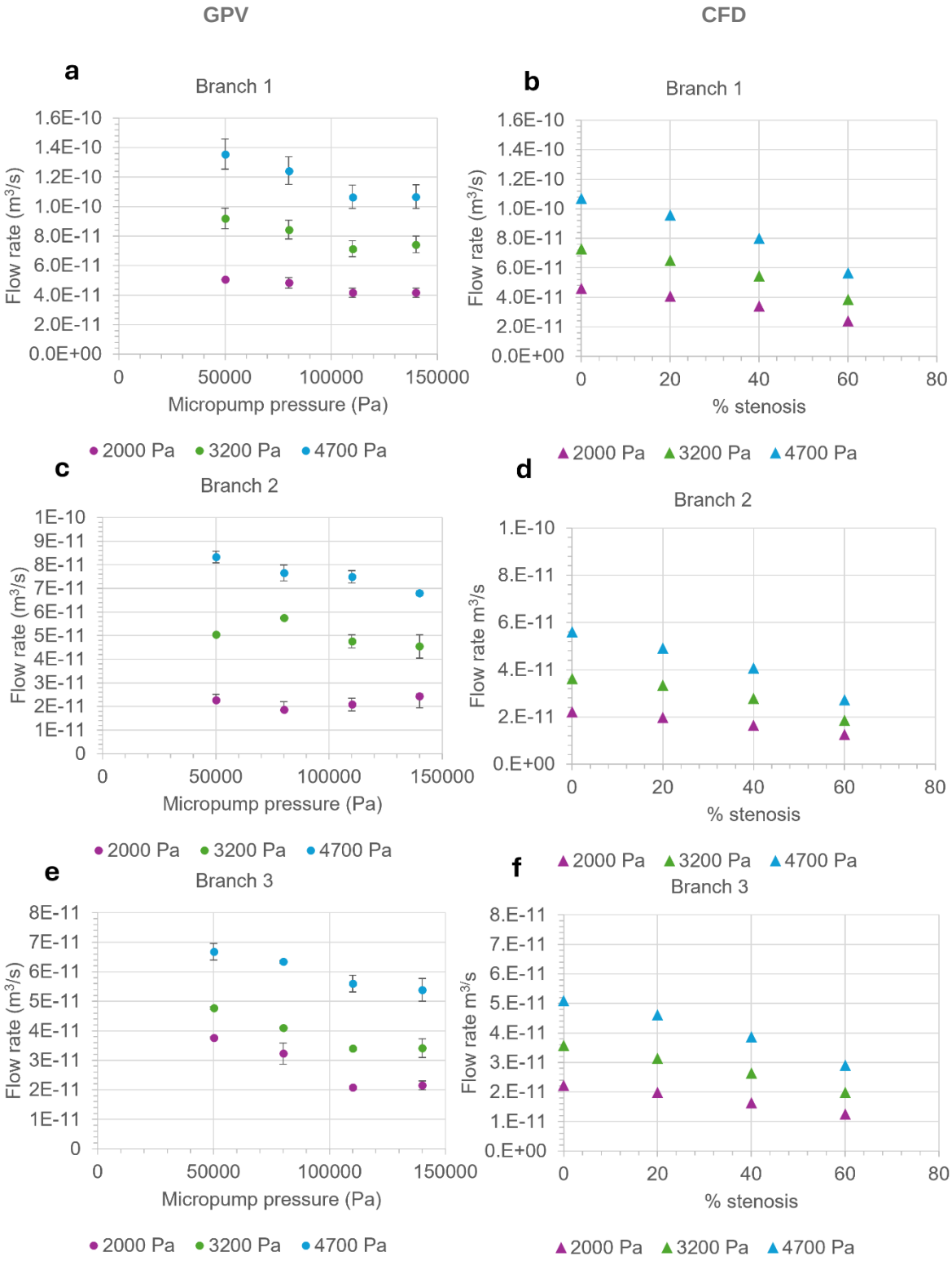

Figure 6.19: The flow rate in the branched deformable model in each branch from GPV and CFD at 2000 Pa, 3200 Pa, and 4700 Pa

Figure 6.19 shows that for all pressures the average flow rate in all branches decreased with increasing deformation, due to the increase of resistance in the channel due to the decrease in cross-sectional area as seen in Chapters 4 and 5. The width of the channel was measured as the external pressure was increased as in §6.4.1 and shows a non-linear decrease with external pressure as seen in Figure 6.20. This suggests the same trend could be seen *in vivo* and does not exactly follow Hooke's law of a linearly elastic solid but may deviate towards representing trends explored *in vivo* such as Fung's constitutive equation of hyperelasticity for non-linear models (121).

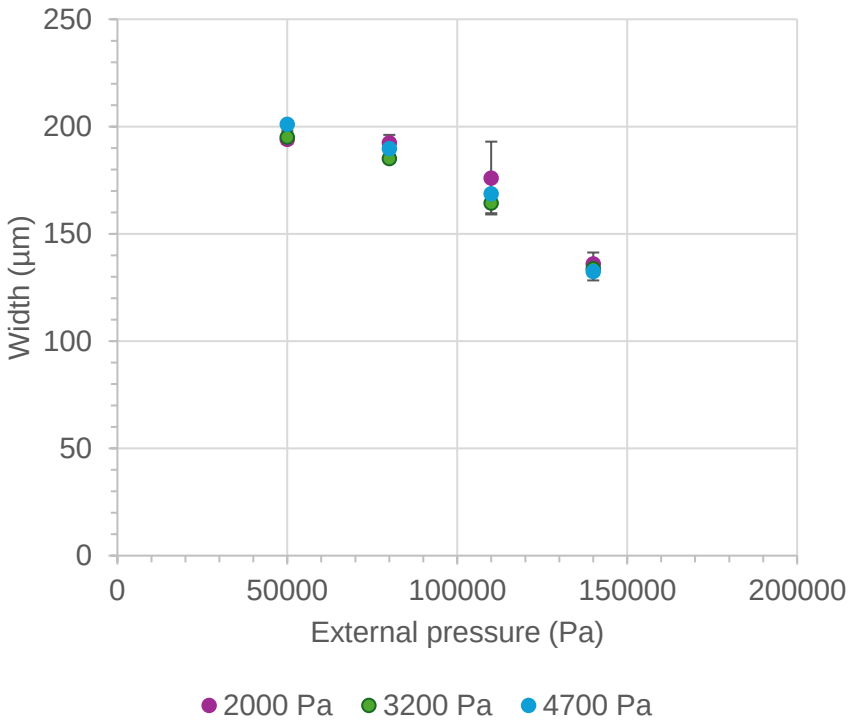

Figure 6.20: Deformation of the stenotic region in response to increasing external pressure in the long deformable branched model

As seen in Figure 6.19, the flow rate in Branch 3 at 2000 Pa initially begins higher than in Branch 2, however, as the external pressure increases past 110000 Pa the flow rate in the right branch becomes higher. This is not seen in the 3200 or 4700 Pa runs as the flow rate in Branch 2 remains higher for all pressures tested. This could be due to there being some dead volume whilst running at 2000 Pa. The flow is seen to be equal between the branches at 110000 Pa external pressure and also at 3200 Pa with 50000 Pa external pressure. This may be the point at which there is an even balance between external and internal forces. Furthermore, it could be due to asymmetric deformation due to the geometry and elasticity of the pumps which could be nonlinear and may be true of in vivo capillary surfaces in disease states.

Once the pressure is increased past this point there is an increased flow rate in Branch 2. This could be for many reasons but is likely due to a decreased resistance in Branch 2 due to geometry or defects in the model. To investigate this further the channel dimensions of the branches were measured and found to be 203 μm (+/-1) μm and 189 (+/-1) for Branch 2 and 3 respectively. This explains why there is a preference for flow toward Branch 2 as there is less resistance. As each branch was between 189-203 μm in width the GPV is at a high enough resolution to accurately measure the flow rate, however, this error increases with increasing stenosis as seen in Chapter 4. Here there is a measured effect of increasing resistance in the model on the flow rate, providing a good model for representing the increase of resistance during microvascular collapse.

When the pumps were inflated to their maximum, some asymmetry in the geometry was observed, as shown in Figure 6.8. This means that the flow may be diverted to the right side, however, this effect was found to be small and is likely that there are

undetectable fluctuations in the cross-section that cannot be measured due to the nature of taking these measurements whilst the device is inflated.

Figure 6.19 also shows the flow rate values from the CFD model. The CFD values are lower than the GPV values. This may be due to the GPV sampling technique or could be due to the difficulty of measuring height in the deformable model. Measuring height in the deformable model can be done following the method in §3.5, however, this was complex due to the delicacy of the fine complex geometry and often led to tearing. Therefore, this measurement was also checked using the microscope and this may introduce further errors. Assuming a larger height would give a closer estimate of resistance to the CFD and could support the argument in §6.8, that in the deformable models, there is some deformation in the z-axis. Figure 6.19 shows the trend in the flow rate follows the same decrease for both the CFD and experimental models suggesting it is a factor in the calculation that changes, most likely deformation in the z axis.

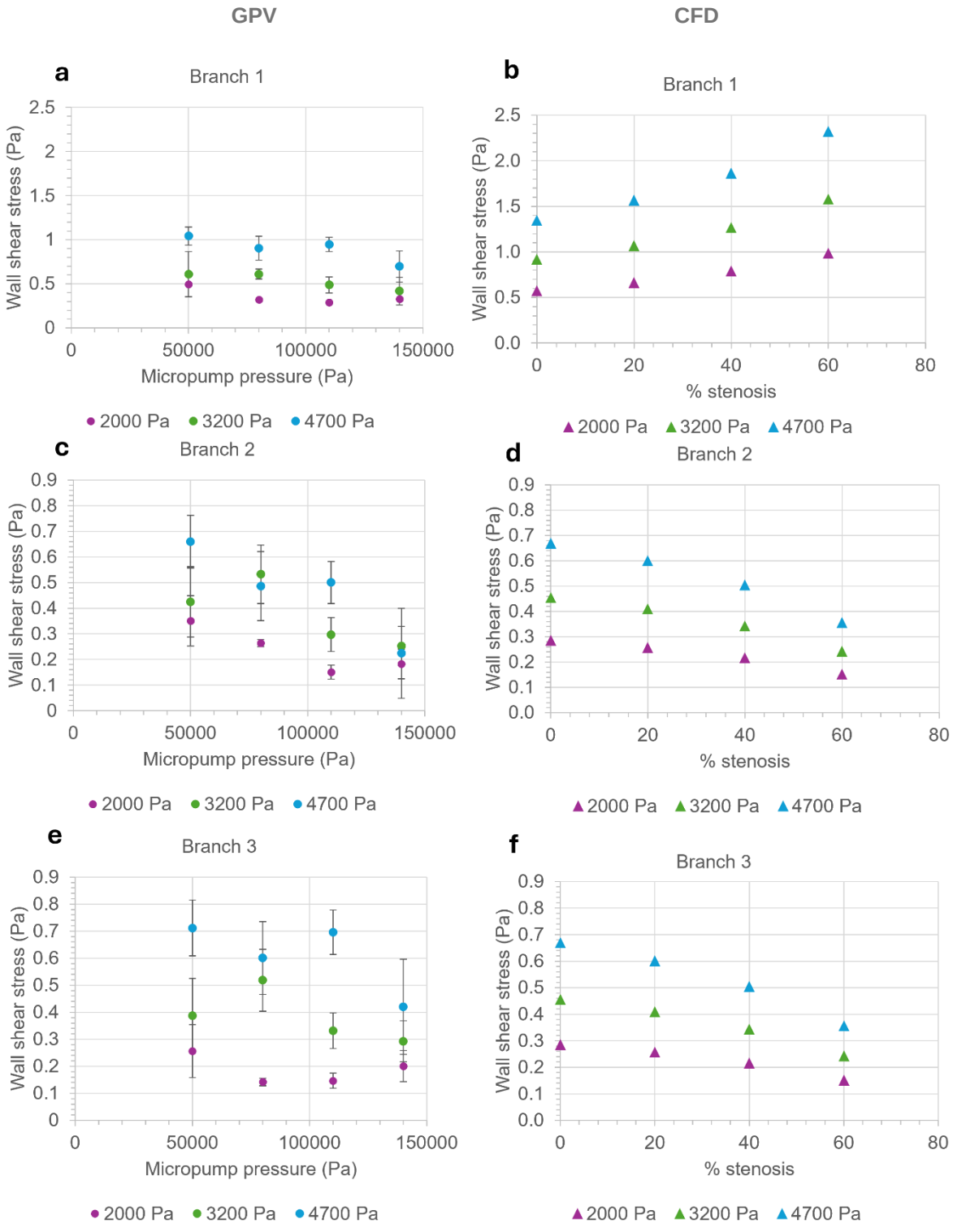

Figure 6.21 The wall shear stress in the branched deformable model in each branch from GPV and CFD at 2000 Pa, 3200 Pa, and 4700 Pa

Figure 6.21 shows the wall shear stress in Branch 1 had no significant decrease when measured using GPV. This may be due to the decrease in flow rate as seen in Figure 6.19 with a smaller decrease in cross width as seen in Figure 6.20. The CFD data for Branch 1 shows an increase in wall shear stress with increasing stenosis which suggests the method of deformation seen in the GPV model is not as expected and may deform in the z axis or non-linearly.

Figure 6.21 shows that for both branches 2 and 3, there is a decrease in the wall shear stress in the branches with increasing stenosis, which is to be expected with the decreasing flow rate as seen in Figure 6.19. There is good agreement between the wall shear stress values from GPV and the CFD model for the branched values at 0%. The GPV predicts a greater decrease in wall shear stress with increased deformation, however, this may be due to the resolution at which the GPV is measured, particularly after 110000 Pa where the deformation is 15% and above. This may be due to deformation seen in the channel or could be due to errors from GPV resolution.

6.8 Deformable Compared to Branched Deformable

The flow rate in the deformable model is lower than that in the branched deformable model. This is due to the reduced height of the deformable model at 37 μm compared to 44 μm. This is enough to significantly decrease the flow rate in the geometry compared to the branched model despite the increased resistance of extra branching in the model. The wall shear stress in the branched deformable model is higher than the non-branched model which is due to the higher flow rates also. This proves that height is an important factor when comparing devices and should be fixed where

possible also supporting the use and design of a fixed height deformable wall geometry.

6.9 Deformable Compared to Fixed

The flow rate in the deformable model is lower than that of the fixed model due to its higher resistance due to the smaller height of the deformable channel. The lower variation in height from the deformable channel means that there is a reduction in the standard deviation and error from model to model and thus the deformable model is better for identifying trends and removing fabrication errors limited by the manufacturing process. The wall shear stress is of the same range in both models 0-2 Pa respectively.

6.10 Conclusions

The deformable model was created to more closely mimic *in vivo* pathophysiology and identify trends in resistance not limited by changes in height caused by fabrication methods between different geometries. Despite the model showing variation in height down the length of the geometry, there are no large changes of variation between models, as only one mould was used, and thus this model identifies the increasing resistance at an earlier stage of stenosis, 20% compared to that of a fixed stenosis 60%. The shear stress ranges seen in the deformable model are of the order 0-2.5 Pa which again represents values of wall shear stress seen *in vivo*. Thus, another model capable of representing the shear stress environment whilst maintaining physiologically relevant pressures is created suitable for use for lab-on-a-chip models involving cell lines. All the models developed quantifiable

hydrodynamic behaviour useful for the development of an *in vitro* model of microvascular collapse and can be used to inform biological studies. CFD models can be used to extend the range of obtainable data when validated with experimental models, where experimental resolution is limited, however, experimental data can be used to highlight variation seen from non-ideal behaviour as would be seen *in vivo.*

Chapter 7: Conclusions and Future Work

7.1 Conclusions

In this research, novel *in vitro* models of microvascular collapse were created using a range of microfluidic and microfabrication techniques and the resistance and shear stress were analysed using Ghost Particle Velocimetry. CFD models were created to expand on data collected by experimental techniques when limited by resolution and validated against the experimental measurements.

The literature review carried out identified a need for combining computational methods with experimental methods to validate computational data for biological studies, which was often missing. Limitations often faced involved spatial analysis, the impact of non-ideal systems and the ability to determine specific variables such as wall shear stress at the microscale. The size constraints of experimental techniques and replication of *in vivo* geometries are limited, however, the potential of using soft-lithography and photolithography was exploited to create the microfluidic devices used in this thesis.

The key findings of this work are as follows:

GPV can be used to infer wall shear stress, through the estimation of dv/dx, in microfluidic devices at the scales fabricated in this research, which has not to the author's knowledge been done before. This provides an accessible technique with advantages over microPIV as previously discussed. GPV can be used for wall shear stress measurements in different aspect ratios and branching geometries as seen in Chapter 4 and 5.

Furthermore, Chapter 4 demonstrates that in the *in vitro* model of microvascular collapse the competition of 3D hydrodynamics such as continuity and resistance have a complicated dependence on wall shear stress as extracted from a 2D plane and this could be used to identify a peak in wall shear stress that can be used to inform biological studies to aid in the diagnosis of Acute Compartment Syndrome.

A 200 x 57 μm model can accurately produce a range of wall shear stresses that mimic *in vivo* ranges when tested at *in vivo* pressures and can be studied using optical techniques and ghost particle velocimetry. This creates the first device in this thesis that mimics wall shear stress values *in vivo* and provides a model that can be used for biological studies, however the long stenosis models both a suitable range of shear stress values and increasing resistance.

CFD models of flow behaviour can be produced and accurately predict wall shear stress values in both the non-stenotic and stenotic regions- allowing for comparisons where experimental technique, GPV is limited by resolution. This can be seen in Chapters 4 and 5. These models can be useful for extending the range of measurement, perhaps to greater stenosis values and ultimately a state of stopped-flow, additionally reducing the need for experimental data collection.

Using larger aspect ratio devices in Chapter 4, the 300 and 400 μm models allow insight into the changes in wall shear stress that are expected to be seen at larger geometries such as increased velocity magnitudes and flow rates due to the reduced resistance. This also identified there are less stable flow rates in this geometry and thus how behaviour may change *in vivo,* with less stability in larger geometries and higher wall shear stress.

Branched microfluidic models are useful in creating models with different flow rates in different areas and respond to increases in stenosis through change of wall shear stress through increased resistance and thus reduction of flow rate. This is good for controlled exposure of cell lines and should be used for biological investigation as different shear stresses can be tested under more controlled conditions. Additionally, as seen in Chapter 5, the wall shear stress inside branched and Murray's branching models remains equal down both branches despite their change in geometry however this cannot be concluded when there are unevenly distributed flows.

Chapter 6 identifies that deformable microfluidic models can be created using 25:1 and 10:1 PDMS in layers that can achieve in the branched model up to 23% stenosis. These models can be used to increase resistance in the channel, but their study is difficult due to the geometric deformation in all axis, which makes predictions both analytically and through CFD difficult as the cross-sectional area is unknown, however, this more closely mimics the *in vivo* case. Chapter 6 also concludes the increase of resistance in the deformable model is dependent on the shape of the cross-section.

A number of experimental difficulties and limitations were identified in this research which highlights the need for careful quantification in both the manufacture and measurements made on micro devices. These limitations were (i) the resolution limit of the GPV, (ii) local variations in channel cross-sectional area which are an artefact of the accuracy of the fabrication method and (iii) difficulties in making accurate measurements of the geometry. Combined use of experimental and in silico approaches helped overcome these, for example, data from the CFD can be used beneath the resolution limit of the GPV data when calculating wall shear stress.

Improvements in fabrication methods, for example, through making the deformable wall channel, were also made in this work.

7.2 Future Work

The purpose of this research was to aid towards a criterion for diagnosis of Acute Compartment Syndrome. These microfluidic models begin the development of an *in vitro* model of microvascular collapse to aid in diagnostic studies. However, it must noted that the range of shear stress difference between measurements is often small, sometimes with increments that are, when measured with GPV, statistically insignificant with an increase of 20% in stenosis as seen in the deformable model and supported by CFD measurements. The dependence of biomarkers to exhibit quantifiable change based on these small increments at pressures of 2000, 3200, and 4700 Pa should be investigated. Additionally, higher resolution flow measurement techniques should be used with a lower range of error in both the fabrication and analysis techniques when this becomes available.

Once the biological studies are conducted, the data should be combined with *in vivo* and *silico* data, patient data, and animal studies. The whole range of data can be cross-analysed by artificial intelligence and machine learning models to identify diagnostic ranges in human patients with ACS, decreasing the number of false diagnoses, and increasing positive patient outcomes.

Other specific recommendations for carrying forward experiments and modelling work are given in the below sections.

7.2.1 Experimental Studies

To develop the model to become suitable to characterise biomarkers used for the diagnosis of Acute Compartment Syndrome the experimental devices should be adapted to further mimic *in vivo*.

The fluid should be replaced with either an optically transparent shear-thinning blood mimic for the analysis of rheological behaviour using GPV, or with whole blood to investigate the effect of red blood cells which are seen to affect flow during branching. This change in rheology will affect the shear stress and must also be done at 37°C to mimic *in vivo* temperatures. This would be useful to understand the impact of the different rheology of the blood mimic on the flow compared with the simple Newtonian fluid used in this study.

When techniques allow, the creation of physiologically relevant circular cross sections should be formed in the microfluidic device with the deformable buckling shape achieved as well as studies into the distensibility and if possible, polymers that closer mimic the Young's modulus of the capillary wall. This could be investigated biologically using 3D bioprinting techniques. Furthermore, the cells should be sheared under these conditions, perhaps with the addition of a hydrogel matrix, however, the effect of this alone on the hydrodynamics should be quantified. The shearing of these cells can identify ranges of biomarkers released.

7.2.2 Computational Studies

The models created in this thesis could be modified to contain non-Newtonian fluids such as blood to investigate haemodynamics, this could be validated with microPIV

data which would not be affected by the loss of transparency of whole blood as GPV would.

Due to experimental limitations, such as a tearing before the point of maximum deformation, a CFD model which incorporates a deformable wall using a dynamic mesh should developed. This was attempted in this work but could not be completed due to difficulties with the numerics which could not be resolved. A summary of this work is given in Appendix 5 to inform future studies.

8. References

1. von Keudell AG, Weaver MJ, Appleton PT, Bae DS, Dyer GSM, Heng M, et al. Diagnosis and treatment of acute extremity compartment syndrome. Lancet [Internet]. 2015 Sep 26 [cited 2020 Nov 5];386(10000):1299–310. Available from: http://www.thelancet.com/article/S0140673615002779/fulltext

2. Halanski MA, Morris MR, Harper BL, Doro C. Intracompartmental pressure monitoring using a handheld pressure monitoring system. JBJS Essent Surg Tech. 2015;5(1):3–6.

3. Von Keudell AG, Weaver MJ, Appleton PT, Bae DS, Dyer GSM, Heng M, et al. Emergency surgery 3 Diagnosis and treatment of acute extremity compartment syndrome. Lancet [Internet]. 2015 [cited 2024 Mar 9];386:1299. Available from: www.thelancet.com

4. McQueen MM, Duckworth AD. The diagnosis of acute compartment syndrome: a review [Internet]. Vol. 40, European Journal of Trauma and Emergency Surgery. Urban und Vogel GmbH; 2014 [cited 2020 Nov 5]. p. 521–8. Available from: https://pubmed.ncbi.nlm.nih.gov/26814506/

5. Bathrinarayanan PV, Hallam SM, Grover LM, Vigolo D, Simmons MJH. Microfluidics as a Powerful Tool to Investigate Microvascular Dysfunction in Trauma Conditions: A Review of the State-of-the-Art. Adv Biol [Internet]. 2024 Jul 19;2400037:1–25. Available from: https://onlinelibrary.wiley.com/doi/10.1002/adbi.202400037

6. Tran AA, Lee D, Fassihi SC, Smith E, Lee R, Siram G. A systematic review of

the effect of regional anesthesia on diagnosis and management of acute compartment syndrome in long bone fractures [Internet]. Vol. 46, European Journal of Trauma and Emergency Surgery. Springer; 2020 [cited 2020 Dec 7]. p. 1281–90. Available from: https://doi.org/10.1007/s00068-020-01320-5

7. McQueen MM, Gaston P, Court-Brown CM. Acute compartment syndrome. J Bone Jt Surg - Ser B. 2000;82(2):200–3.

8. Taylor RM, Sullivan MP, Mehta S. Acute compartment syndrome: Obtaining diagnosis, providing treatment, and minimizing medicolegal risk. Curr Rev Musculoskelet Med [Internet]. 2012 Sep [cited 2020 Dec 11];5(3):206–13. Available from: https://pubmed.ncbi.nlm.nih.gov/22644598/

9. Quintens L, Herteleer M, Vancleef S, Carette Y, Duflou J, Nijs S, et al. Anatomical Variation of the Tibia – a Principal Component Analysis. Sci Rep [Internet]. 2019 May 21 [cited 2024 Jul 3];9(1):7649. Available from: https://doi.org/10.1038/s41598-019-44092-8

10. Stornelli N, Wydra FB, Mitchell JJ, Stahel PF, Fabbri S. The dangers of lithotomy positioning in the operating room: Case report of bilateral lower extremity compartment syndrome after a 90-minutes surgical procedure. Patient Saf Surg [Internet]. 2016 Jul 26 [cited 2021 Mar 29];10(1):18. Available from: http://pssjournal.biomedcentral.com/articles/10.1186/s13037-016-0106-9

11. Loloi J, Burton AT, Walsh LT, Sahu N, Jain R. Bilateral Compartment Syndrome in Intravenous Drug Abuse. Cureus [Internet]. 2018 Dec 4 [cited 2021 Mar 29];10(12). Available from: /pmc/articles/PMC6367106/

12. Tuna S, Duymus TM, Mutlu S, Ketenci IE, Ulusoy A. Upper extremity acute

compartment syndrome during tissue plasminogen activator therapy for pulmonary embolism in a morbidly obese patient. Int J Surg Case Rep. 2015 Jan 1;8:175–8.

13. Siau K. P0001 BILATERAL LOWER LIMB CHRONIC COMPARTMENT SYNDROME IN AN ELDERLY MALE: A CASE REPORT. Eur J Intern Med. 2009 May 1;20:S9.

14. McMillan TE, Gardner WT, Schmidt AH, Johnstone AJ. Diagnosing acute compartment syndrome—where have we got to? [Internet]. Vol. 43, International Orthopaedics. Springer Verlag; 2019 [cited 2020 Dec 11]. p. 2429–35. Available from: /pmc/articles/PMC6848051/?report=abstract

15. Bango J, Zhang E, Aaron DL, Diwan A. Two cases of acute anterolateral compartment syndrome following inversion ankle injuries. Trauma Case Reports [Internet]. 2020 Dec 1 [cited 2020 Dec 11];30:100371. Available from: /pmc/articles/PMC7649348/?report=abstract

16. Hartsock LA, O'Farrell D, Seaber A V., Urbaniak JR. Effect of increased compartment pressure on the microcirculation of skeletal muscle. Microsurgery [Internet]. 1998 Jan 1 [cited 2020 Dec 29];18(2):67–71. Available from: https://onlinelibrary.wiley.com/doi/10.1002/(SICI)1098-2752(1998)18:2%3C67::AID-MICR1%3E3.0.CO;2-R

17. Coulton S, Bourne S, Catliffe S, Brooks R, Jollow D. Acute compartment syndrome of the lower limb following childbirth: A case report. J Med Case Rep [Internet]. 2020 Sep 4 [cited 2020 Dec 29];14(1):140. Available from: https://jmedicalcasereports.biomedcentral.com/articles/10.1186/s13256-020-

02459-w

18. Smith RDJ, Rust-March H, Kluzek S. Acute compartment syndrome of the thigh in a rugby player. BMJ Case Rep [Internet]. 2015 Aug 6 [cited 2020 Dec 29];2015. Available from: /pmc/articles/PMC4533690/?report=abstract

19. Mustafa NM, Hyun A, Kumar JS, Yekkirala L. Gluteal compartment syndrome: A case report. Cases J [Internet]. 2009 Nov [cited 2020 Dec 29];2(11):190. Available from: /pmc/articles/PMC2783145/?report=abstract

20. Takeda S, Tatebe M, Sakai A, Hirata H. Two cases of unidentified acute compartment syndrome. BMJ Case Rep [Internet]. 2018 [cited 2020 Dec 29];2018. Available from: /pmc/articles/PMC5884265/?report=abstract

21. Mehta V, Chowdhary V, Lin C, Jbara M, Hanna S. Compartment syndrome of the hand: A case report and review of literature. Radiol Case Reports [Internet]. 2018 Feb 1 [cited 2020 Dec 29];13(1):212–5. Available from: /pmc/articles/PMC5826729/?report=abstract

22. Christoforidis C, Lepetsos P, Papadakis S, Gketsos A, Balfousias T, Macheras G. Journal of Research and Practice on the Musculoskeletal System Acute compartment syndrome of the foot after an ankle sprain: a case report. [cited 2020 Dec 29]; Available from: www.jrpms.eu

23. Long B, Koyfman A, Gottlieb M. Evaluation and Management of Acute Compartment Syndrome in the Emergency Department. J Emerg Med. 2019 Apr 1;56(4):386–97.

24. Broadhurst PK, Robinson LR. Compartment syndrome: Neuromuscular

complications and electrodiagnosis. Muscle Nerve [Internet]. 2020 Sep 22 [cited 2020 Dec 11];62(3):300–8. Available from: https://onlinelibrary.wiley.com/doi/abs/10.1002/mus.26807

25. Khan IA, Mahabadi N, D'Abarno A, Varacallo M. Anatomy, Bony Pelvis and Lower Limb: Leg Lateral Compartment [Internet]. StatPearls. Treasure Island (FL); 2024. Available from: http://www.ncbi.nlm.nih.gov/pubmed/15556329

26. Mehta V, Chowdhary V, Lin C, Jbara M, Hanna S. Compartment syndrome of the hand: A case report and review of literature. Radiol Case Reports. 2018 Feb 1;13(1):212–5.

27. Findlay S, Liu D, Rijhsinghani A. Acute Compartment Syndrome: Clinical Course and Laboratory Findings in Pregnant Patients with McArdle's Disease [Internet]. Vol. 15, Pain Medicine (United States). Blackwell Publishing Inc.; 2014 [cited 2021 Mar 30]. p. 481–2. Available from: https://academic.oup.com/painmedicine/article-lookup/doi/10.1111/pme.12279

28. Meshram P, Joseph J, Zhou Y, McFarland EG. Acute compartment syndrome caused by hematoma after shoulder surgery: a case series. J Shoulder Elb Surg [Internet]. 2021 Jun 3 [cited 2021 Mar 30];30(6):1362–8. Available from: https://linkinghub.elsevier.com/retrieve/pii/S1058274620306947

29. Bango J, Zhang E, Aaron DL, Diwan A. Two cases of acute anterolateral compartment syndrome following inversion ankle injuries. Trauma Case Reports. 2020 Dec 1;30:100371.

30. Epstein FH, Odeh M. The Role of Reperfusion-Induced Injury in the Pathogenesis of the Crush Syndrome. N Engl J Med [Internet]. 1991 May 16

[cited 2020 Dec 29];324(20):1417–22. Available from: https://www.nejm.org/doi/full/10.1056/NEJM199105163242007

31. Agius C, Cole E. Acute compartment syndrome (ACS) - a case of delayed diagnosis. Int J Orthop trauma Nurs [Internet]. 2021 Jul 1 [cited 2022 Apr 20];42. Available from: https://pubmed.ncbi.nlm.nih.gov/34010742/

32. Mullett H, Al-Abed K, Prasad CVR, O'Sullivan M. Outcome of compartment syndrome following intramedullary nailing of tibial diaphyseal fractures. Injury. 2001 Jun 1;32(5):411–3.

33. Broadhurst PK, Robinson LR. Compartment syndrome: Neuromuscular complications and electrodiagnosis. Muscle Nerve [Internet]. 2020 Sep 22 [cited 2021 Mar 30];62(3):300–8. Available from: https://onlinelibrary.wiley.com/doi/abs/10.1002/mus.26807

34. Merle G, Comeau-Gauthier M, Tayari V, Kezzo MN, Kasem C, Al-Kabraiti F, et al. Comparison of Three Devices to Measure Pressure for Acute Compartment Syndrome. In: Military Medicine [Internet]. Oxford University Press; 2020 [cited 2020 Dec 11]. p. 77–81. Available from: https://pubmed.ncbi.nlm.nih.gov/32074299/

35. Blaisdell FW. The pathophysiology of skeletal muscle ischemia and the reperfusion syndrome: a review [Internet]. Vol. 10, Cardiovascular Surgery. 2002 [cited 2021 Mar 30]. Available from: www.e1sevier.comllocatelcardiosur

36. Janzing HMJ, Broos PLO. Routine monitoring of compartment pressure in patients with tibial fractures: Beware of overtreatment! Injury [Internet]. 2001 [cited 2022 Apr 20];32(5):415–21. Available from:

https://pubmed.ncbi.nlm.nih.gov/11382429/

37. Cascio BM, Wilckens JH, Ain MC, Toulson C, Frassica FJ. Documentation of acute compartment syndrome at an academic health-care center [Internet]. Vol. 87, Journal of Bone and Joint Surgery - Series A. J Bone Joint Surg Am; 2005 [cited 2021 Mar 29]. p. 346–50. Available from: https://pubmed.ncbi.nlm.nih.gov/15687158/

38. O'Sullivan STFRCS, O'Donoghue J., McGuiness A, O'Shaughnessy M. Does patient controlled analgesia lead to delayed diagnosis of lower limb compartment syndrome? Plast Reconstr Surg [Internet]. 1996 [cited 2021 Mar 29];97(5):1087–9. Available from: https://journals.lww.com/plasreconsurg/Citation/1996/04010/DOES_PATIENT_CONTROLLED_ANALGESIA_LEAD_TO_DELAYED.53.aspx

39. Shakespeare DT, Henderson NJ, Clough G. The slit catheter: a comparison with the wick catheter in the measurement of compartment pressure. Injury. 1982;13(5):404–8.

40. Mancini DM, Bolinger L, Li H, Kendrick K, Chance B, Wilson JR. Validation of near-infrared spectroscopy in humans. J Appl Physiol [Internet]. 1994 [cited 2021 Mar 29];77(6):2740–7. Available from: https://journals.physiology.org/doi/abs/10.1152/jappl.1994.77.6.2740

41. Whitesides TE, Haney TC, Morimoto K, Harada H. Tissue pressure measurements as a determinant for the need of fasciotomy. Clin Orthop Relat Res [Internet]. 1975 [cited 2021 Apr 19];No.113(113):43–51. Available from: https://pubmed.ncbi.nlm.nih.gov/1192674/

42. Mcqueen MM, Court-Brown CM. COMPARTMENT MONITORING IN TIBIAL FRACTURES THE PRESSURE THRESHOLD FOR DECOMPRESSION. Vol. 78, J Bone Joint Surg [Br]. 1996.

43. Osborn CPM, Schmidt AH. Management of Acute Compartment Syndrome. J Am Acad Orthop Surg [Internet]. 2020 Feb 1 [cited 2020 Dec 7];28(3):e108–14. Available from: https://journals.lww.com/10.5435/JAAOS-D-19-00270

44. Bhattacharyya T, Vrahas M. The Medical-Legal Aspects of Compartment Syndrome : JBJS. J Bone Jt Surg [Internet]. 2004 [cited 2021 Mar 30];86(4):864–8. Available from: https://journals.lww.com/jbjsjournal/Fulltext/2004/04000/The_Medical_Legal_Aspects_of_Compartment_Syndrome.29.aspx

45. Osborn CPM, Schmidt AH. Management of Acute Compartment Syndrome. J Am Acad Orthop Surg [Internet]. 2020 Feb 1 [cited 2020 Dec 11];28(3):e108–14. Available from: https://journals.lww.com/10.5435/JAAOS-D-19-00270

46. Dong R, Liu S, Li Y, Gao F, Gao K, Chen C, et al. Revisiting hemodynamics and blood oxygenation in a microfluidic microvasculature replica. Microvasc Res [Internet]. 2024 Mar 1 [cited 2024 Mar 9];152:104640. Available from: https://linkinghub.elsevier.com/retrieve/pii/S0026286223001668

47. Müller B, Lang S, Dominietto M, Rudin M, Schulz G, Deyhle H, et al. High-resolution tomographic imaging of microvessels. In: Stock SR, editor. Proceedings of SPIE - The International Society for Optical Engineering 7078:70780B [Internet]. 2008 [cited 2022 Jul 6]. p. 70780B. Available from: https://www.researchgate.net/figure/The-typical-diameters-wall-thicknesses-of-

blood-vessel-for-humans-and-mice-are-given-in_fig5_224902259

48. Camasão DB, Mantovani D. The mechanical characterization of blood vessels and their substitutes in the continuous quest for physiological-relevant performances. A critical review. Mater Today Bio [Internet]. 2021 Mar;10(March):100106. Available from: https://linkinghub.elsevier.com/retrieve/pii/S2590006421000144

49. Muntner P, Shimbo D, Carey RM, Charleston JB, Gaillard T, Misra S, et al. Measurement of Blood Pressure in Humans: A Scientific Statement From the American Heart Association. Hypertension [Internet]. 2019 May;73(5):E35–66. Available from: https://www.ahajournals.org/doi/10.1161/HYP.0000000000000087

50. Chow KW, Mak CC. A simple model for the two dimensional blood flow in the collapse of veins. J Math Biol [Internet]. 2006 Jun 24;52(6):733–44. Available from: http://link.springer.com/10.1007/s00285-005-0351-5

51. Crnic A, Rohringer S, Tyschuk T, Holnthoner W. Engineering blood and lymphatic microvascular networks. Atherosclerosis [Internet]. 2024 Jan [cited 2024 Mar 9];117458. Available from: https://doi.org/10.1016/j.atherosclerosis.2024.117458

52. Cleaver O, Melton DA. Endothelial signaling during development. Nat Med [Internet]. 2003 Jun 1;9(6):661–8. Available from: https://www.nature.com/articles/nm0603-661

53. Santamaría R, González-Álvarez M, Delgado R, Esteban S, Arroyo AG. Remodeling of the Microvasculature: May the Blood Flow Be With You. Front

Physiol [Internet]. 2020 Oct 15 [cited 2022 Jul 6];11. Available from: /pmc/articles/PMC7593767/

54. Sherman TF. On connecting large vessels to small. The meaning of Murray's law. J Gen Physiol [Internet]. 1981 Oct 1;78(4):431–53. Available from: https://rupress.org/jgp/article/78/4/431/27121/On-connecting-large-vessels-to-small-The-meaning

55. Lee JY, Lee SJ. Murray's law and the bifurcation angle in the arterial micro-circulation system and their application to the design of microfluidics. Microfluid Nanofluidics [Internet]. 2010 Jan 16 [cited 2020 Nov 12];8(1):85–95. Available from: https://link.springer.com/article/10.1007/s10404-009-0454-1

56. Duchamp M, Bakht SM, Ju J, Yazdi IK, Zhang W, Zhang YS. Perforated and Endothelialized Elastomeric Tubes for Vascular Modeling. Adv Mater Technol [Internet]. 2019 Sep 4 [cited 2020 Nov 5];4(9):1800741. Available from: https://onlinelibrary.wiley.com/doi/abs/10.1002/admt.201800741

57. Painter PR, Edén P, Bengtsson HU. Pulsatile blood flow, shear force, energy dissipation and Murray's Law. Theor Biol Med Model. 2006;3.

58. Chen Y, Bai G-Q, Ren L, Bai Y, Sun M, Shang T, et al. Blood physiological and flow characteristics within coronary artery circulatory network for human heart based on vascular fractal theory. Adv Mech Eng [Internet]. 2020 Jul 1 [cited 2025 Jan 2];12(7). Available from: https://www.researchgate.net/publication/342662109_Blood_physiological_and_flow_characteristics_within_coronary_artery_circulatory_network_for_human_heart_based_on_vascular_fractal_theory

59. Bsat S, Halaoui A, Kobeissy F, Moussalem C, El Houshiemy MN, Kawtharani S, et al. Acute ischemic stroke biomarkers: a new era with diagnostic promise? Acute Med Surg [Internet]. 2021 Jan 28 [cited 2024 Jun 18];8(1). Available from: https://onlinelibrary.wiley.com/doi/10.1002/ams2.696

60. Papaioannou TG, Karatzis EN, Vavuranakis M, Lekakis JP, Stefanadis C. Assessment of vascular wall shear stress and implications for atherosclerotic disease. Int J Cardiol. 2006 Oct 26;113(1):12–8.

61. Chatterjee S. Endothelial Mechanotransduction, Redox Signaling and the Regulation of Vascular Inflammatory Pathways. Front Physiol [Internet]. 2018 Jun 7;9(JUN):1–16. Available from: https://www.frontiersin.org/article/10.3389/fphys.2018.00524/full

62. Duncker DJ, Bache RJ. Regulation of Coronary Blood Flow During Exercise. Physiol Rev [Internet]. 2008 Jul [cited 2024 Jul 2];88(3):1009–86. Available from: www.prv.org

63. WyssInstitute. Diagnostics [Internet]. 2024 [cited 2024 Jul 29]. Available from: https://wyss.harvard.edu/technologies/diagnostics/

64. Schofield Z, Baksamawi HA, Campos J, Alexiadis A, Nash GB, Brill A, et al. The role of valve stiffness in the insurgence of deep vein thrombosis. Commun Mater [Internet]. 2020 Sep 16;1(1):65. Available from: https://www.nature.com/articles/s43246-020-00066-2

65. Miao H, Hu Y-L, Shiu Y-T, Yuan S, Zhao Y, Kaunas R, et al. Effects of Flow Patterns on the Localization and Expression of VE-Cadherin at Vascular Endothelial Cell Junctions: In vivo and in vitro Investigations. J Vasc Res

[Internet]. 2005 [cited 2021 Jan 15];42(1):77–89. Available from: https://www.karger.com/Article/FullText/83094

66. Li W, Wang H-F, Li Z-Y, Wang T, Zhao C-X. Numerical investigation of drug transport from blood vessels to tumour tissue using a Tumour-Vasculature-on-a-Chip. Chem Eng Sci [Internet]. 2019 Nov [cited 2024 Mar 11];208:115155. Available from: https://doi.org/10.1016/j.ces.2019.115155

67. Jia Y, Jiang J, Ma X, Li Y, Huang H, Cai K, et al. PDMS microchannel fabrication technique based on microwire-molding. Sci Bull [Internet]. 2008 Dec 19 [cited 2024 Jul 15];53(24):3928–36. Available from: www.scichina.com%7Ccsb.scichina.com%7Cwww.springerlink.com

68. Priyadarshani J, Chakraborty S, Das S. Nature-Inspired Bio-Microfluidic Device by Soft Lithography Technique. In: Proceedings of IEEE Sensors. Institute of Electrical and Electronics Engineers Inc.; 2018.

69. McDonald JC, Whitesides GM. Poly(dimethylsiloxane) as a material for fabricating microfluidic devices. Acc Chem Res [Internet]. 2002 [cited 2020 Nov 3];35(7):491–9. Available from: https://pubs.acs.org/doi/abs/10.1021/ar010110q

70. Friend J, Yeo L. Fabrication of microfluidic devices using polydimethylsiloxane. Biomicrofluidics [Internet]. 2010 [cited 2020 Nov 3];4(2). Available from: /pmc/articles/PMC2917889/?report=abstract

71. Sia SK, Whitesides GM. Microfluidic devices fabricated in poly(dimethylsiloxane) for biological studies [Internet]. Vol. 24, Electrophoresis. John Wiley & Sons, Ltd; 2003 [cited 2020 Nov 3]. p. 3563–76. Available from:

https://onlinelibrary.wiley.com/doi/full/10.1002/elps.200305584

72. Kim M, Huang Y, Choi K, Hidrovo CH. The improved resistance of PDMS to pressure-induced deformation and chemical solvent swelling for microfluidic devices. Microelectron Eng. 2014 Jul 25;124:66–75.

73. Ren K, Zhou J, Wu H. Materials for microfluidic chip fabrication. Acc Chem Res [Internet]. 2013 Nov 19 [cited 2020 Nov 3];46(11):2396–406. Available from: https://pubs.acs.org/doi/abs/10.1021/ar300314s

74. Rao HX, Liu FN, Zhang ZY. Preparation and oxygen/nitrogen permeability of PDMS crosslinked membrane and PDMS/tetraethoxysilicone hybrid membrane. J Memb Sci. 2007 Oct 15;303(1–2):132–9.

75. McDonald JC, Duffy DC, Anderson JR, Chiu DT, Wu H, Schueller OJA, et al. Fabrication of microfluidic systems in poly(dimethylsiloxane) [Internet]. Vol. 21, Electrophoresis. Wiley-VCH Verlag; 2000 [cited 2020 Nov 3]. p. 27–40. Available from: https://onlinelibrary.wiley.com/doi/full/10.1002/%28SICI%291522-2683%2820000101%2921%3A1%3C27%3A%3AAID-ELPS27%3E3.0.CO%3B2-C

76. Priyadarshani J, Chakraborty S, Das S. Nature-Inspired Bio-Microfluidic Device by Soft Lithography Technique <tex>$\cdot$</tex>. In: 2018 IEEE SENSORS [Internet]. IEEE; 2018 [cited 2020 Nov 5]. p. 1–4. Available from: https://ieeexplore.ieee.org/document/8589750/

77. Barmaki S, Jokinen V, Obermaier D, Blokhina D, Korhonen M, Ras RHA, et al. A microfluidic oxygen sink to create a targeted cellular hypoxic

microenvironment under ambient atmospheric conditions. Acta Biomater. 2018 Jun 1;73:167–79.

78. Li Y, Lu Y, Chen Q, Kang Y, Yu L. Probing of peripheral blood mononuclear cells anchoring on TNF-alpha challenged-vascular endothelia in an in vitro model of the retinal microvascular. Biomed Microdevices [Internet]. 2017 Sep 1 [cited 2020 Oct 26];19(3):1–8. Available from: https://link.springer.com/article/10.1007/s10544-017-0194-z

79. Ryu H, Oh S, Lee HJ, Lee JY, Lee HK, Jeon NL. Engineering a Blood Vessel Network Module for Body-on-a-Chip Applications. SLAS Technol. 2015 Jun 1;20(3):296–301.

80. Orlova V V, Nahon DM, Cochrane A, Cao X, Freund C, van den Hil F, et al. Vascular defects associated with hereditary hemorrhagic telangiectasia revealed in patient-derived isogenic iPSCs in 3D vessels on chip. Stem Cell Reports [Internet]. 2022 Jul [cited 2024 Mar 11];17(7):1536–45. Available from: https://doi.org/10.1016/j.stemcr.2022.05.022

81. Vila Cuenca M, Cochrane A, van den Hil FE, de Vries AAF, Lesnik Oberstein SAJ, Mummery CL, et al. Engineered 3D vessel-on-chip using hiPSC-derived endothelial- and vascular smooth muscle cells. Stem Cell Reports [Internet]. 2021 Sep [cited 2024 Mar 11];16(9):2159–68. Available from: https://doi.org/10.1016/j.stemcr.2021.08.003

82. Brouns SLN, Provenzale I, Van Geffen JP, Van Der Meijden PEJ, Heemskerk JWM. Localized endothelial-based control of platelet aggregation and coagulation under flow: A proof-of-principle vessel-on-a-chip study. J Thromb

Haemost. 2020;18:931–41.

83. Huang J, Xu Z, Jiao J, Li Z, Li S, Liu Y, et al. Microfluidic intestinal organoid-on-a-chip uncovers therapeutic targets by recapitulating oxygen dynamics of intestinal IR injury. Bioact Mater [Internet]. 2023 [cited 2024 Mar 11];30:1–14. Available from: https://doi.org/10.1016/j.bioactmat.2023.07.001

84. Psevdos C, Giannokostas K, Moschopoulos P, Dimakopoulos Y, Tsamopoulos J. Incorporating the complex rheological behavior of blood in microvascular network simulations: Two-phase modeling and a model reduction approach. J Nonnewton Fluid Mech [Internet]. 2023 Dec;322(July):105134. Available from: https://doi.org/10.1016/j.jnnfm.2023.105134

85. Karst NJ, Geddes JB. Modeling transit time distributions in microvascular networks. J Theor Biol [Internet]. 2023 Sep;572(March):111584. Available from: https://doi.org/10.1016/j.jtbi.2023.111584

86. Uzu M, Takezawa T. Novel microvascular endothelial model utilizing a collagen vitrigel membrane and its advantages for predicting histamine-induced microvascular hyperpermeability. J Pharmacol Toxicol Methods [Internet]. 2020;106(May):106916. Available from: https://doi.org/10.1016/j.vascn.2020.106916

87. Miller SR, Jernigan SR, Abraham RJ, Buckner GD. Comparison of Bolus Versus Dual-Syringe Administration Systems on Glass Yttrium-90 Microsphere Deposition in an In Vitro Microvascular Hepatic Tumor Model. J Vasc Interv Radiol [Internet]. 2023 Jan [cited 2024 Mar 11];34(1):11–20. Available from: https://doi.org/10.1016/j.jvir.2022.07.032

88. Hodges NA, Barr RW, Murfee WL. The maintenance of adult peripheral adult nerve and microvascular networks in the rat mesentery culture model. J Neurosci Methods [Internet]. 2020 Dec [cited 2024 Mar 11];346:108923. Available from: https://doi.org/10.1016/j.jneumeth.2020.108923

89. Ferrari D, Sengupta A, Heo L, Pethö L, Michler J, Geiser T, et al. Effects of biomechanical and biochemical stimuli on angio- and vasculogenesis in a complex microvasculature-on-chip. iScience [Internet]. 2023 Mar [cited 2024 Mar 12];26(3):106198. Available from: https://doi.org/10.1016/j.isci.

90. Soon K, Li M, Wu R, Zhou A, Khosraviani N, Turner WD, et al. A human model of arteriovenous malformation (AVM)-on-a-chip reproduces key disease hallmarks and enables drug testing in perfused human vessel networks. Biomaterials [Internet]. 2022 Sep 1 [cited 2024 Mar 10];288:121729. Available from: https://linkinghub.elsevier.com/retrieve/pii/S0142961222003696

91. Pisano M, Triacca V, Barbee KA, Swartz MA. An in vitro model of the tumor-lymphatic microenvironment with simultaneous transendothelial and luminal flows reveals mechanisms of flow enhanced invasion †. Integr Biol [Internet]. 2015 [cited 2024 Mar 11];7:525. Available from: https://academic.oup.com/ib/article/7/5/525/5193018

92. Marsano A, Conficconi C, Lemme M, Occhetta P, Gaudiello E, Votta E, et al. Beating heart on a chip: a novel microfluidic platform to generate functional 3D cardiac microtissues. Lab Chip [Internet]. 2016 [cited 2024 Mar 11];16(3):599–610. Available from: www.rsc.org/loc

93. Akinbote A, Beltran-Sastre V, Cherubini M, Visone R, Hajal C, Cobanoglu D, et

al. Classical and Non-classical Fibrosis Phenotypes Are Revealed by Lung and Cardiac Like Microvascular Tissues On-Chip. Front Physiol. 2021;12(October):1–15.

94. Murrant CL, Fletcher NM. Capillary communication: the role of capillaries in sensing the tissue environment, coordinating the microvascular, and controlling blood flow. Am J Physiol Circ Physiol [Internet]. 2022 Nov 1 [cited 2024 Jul 3];323(5):H1019–36. Available from: www.ajpheart.org

95. Scott S, Ali Z. Fabrication Methods for Microfluidic Devices: An Overview. Micromachines [Internet]. 2021 Mar 18 [cited 2024 Mar 11];12(3):319. Available from: https://doi.org/10.3390/mi12030319

96. Fiddes LK, Raz N, Srigunapalan S, Tumarkan E, Simmons CA, Wheeler AR, et al. A circular cross-section PDMS microfluidics system for replication of cardiovascular flow conditions. Biomaterials [Internet]. 2010 May 1 [cited 2024 Jul 3];31(13):3459–64. Available from: https://linkinghub.elsevier.com/retrieve/pii/S0142961210001146

97. Tiwari SK, Bhat S, Dubey SP. Do it yourself- circular cross-section microfluidic channel. Cogent Eng [Internet]. 2024 Dec 31 [cited 2024 Jul 3];11(1). Available from: https://doi.org/10.1080/23311916.2023.2299039

98. Zhang X, Lorente S. The growth of capillary networks by branching for maximum fluid access. Sci Rep [Internet]. 2023 Jul 12 [cited 2024 Mar 15];13(1):11278. Available from: https://doi.org/10.1038/s41598-023-38381-6

99. Plyley MJ, Sutherland GJ, Groom AC. Geometry of the capillary network in skeletal muscle. Microvasc Res [Internet]. 1976 Mar;11(2):161–73. Available

from: https://linkinghub.elsevier.com/retrieve/pii/0026286276900480

100. Wang H, Fan L, Choy JS, Kassab GS, Lee LC. Simulation of coronary capillary transit time based on full vascular model of the heart. Comput Methods Programs Biomed [Internet]. 2024 Jan [cited 2024 Mar 15];243:107908. Available from: https://doi.org/10.1016/j.cmpb.2023.107908

101. Kovtanyuk A, Turova V, Sidorenko I, Chebotarev A, Lampe R. Modeling of the cerebral blood circulation in a capillary network accounting for the influence of the endothelial surface layer. Comput Methods Programs Biomed [Internet]. 2022 [cited 2024 Mar 15];224:107008. Available from: www.elsevier.com/locate/cmpb

102. Sherwood JM, Kaliviotis E, Dusting J, Balabani S. Hematocrit, viscosity and velocity distributions of aggregating and non-aggregating blood in a bifurcating microchannel. Biomech Model Mechanobiol [Internet]. 2014 Apr 1;13(2):259–73. Available from: http://link.springer.com/10.1007/s10237-012-0449-9

103. Popel AS. A Model of Pressure and Flow Distribution in Branching Networks. J Appl Mech [Internet]. 1980 [cited 2022 Apr 27];47(2):247. Available from: /pmc/articles/PMC5510952/

104. Abugattas C, Aguirre A, Castillo E, Cruchaga M. Numerical study of bifurcation blood flows using three different non-Newtonian constitutive models. Appl Math Model [Internet]. 2020 Dec 1 [cited 2024 Mar 15];88:529–49. Available from: https://linkinghub.elsevier.com/retrieve/pii/S0307904X20303425

105. Jiang J, Li C, Hu Y, Li C, He J, Leng X, et al. A novel CFD-based computed index of microcirculatory resistance (IMR) derived from coronary angiography

to assess coronary microcirculation. Comput Methods Programs Biomed [Internet]. 2022;221:106897. Available from: https://doi.org/10.1016/j.cmpb.2022.106897

106. Wain RAJ, Smith DJ, Hammond DR, Whitty JPM. Influence of microvascular sutures on shear strain rate in realistic pulsatile flow. Microvasc Res. 2018;118(February):69–81.

107. Yang J, Pak YE, Lee T-R. Predicting bifurcation angle effect on blood flow in the microvasculature. Microvasc Res [Internet]. 2016 Nov [cited 2024 Mar 15];108:22–8. Available from: http://dx.doi.org/10.1016/j.mvr.2016.07.001

108. Taylor DJ, Feher J, Halliday I, Hose DR, Gosling R, Aubiniere-Robb L, et al. Refining Our Understanding of the Flow Through Coronary Artery Branches; Revisiting Murray's Law in Human Epicardial Coronary Arteries. Front Physiol [Internet]. 2022 Apr 4;13. Available from: https://www.frontiersin.org/articles/10.3389/fphys.2022.871912/full

109. Zhang C, Xing D, Li Y. Micropumps, microvalves, and micromixers within PCR microfluidic chips: Advances and trends. Biotechnol Adv. 2007 Sep 1;25(5):483–514.

110. Trębacz H, Barzycka A. Mechanical Properties and Functions of Elastin: An Overview. Biomolecules [Internet]. 2023 Mar 22 [cited 2024 Jul 4];13(3):574. Available from: https://doi.org/10.3390/biom13030574

111. Ghazy M, Elgindi MB, Wei D. Analytical and numerical investigations of the collapse of blood vessels with nonlinear wall material embedded in nonlinear soft tissues. Alexandria Eng J. 2018 Dec 1;57(4):3437–50.

112. Haut RC, Little RW. A constitutive equation for collagen fibers. J Biomech [Internet]. 1972 Sep;5(5):423–30. Available from: https://linkinghub.elsevier.com/retrieve/pii/0021929072900012

113. Burton AC. On the Physical Equilibrium of Small Blood Vessels. Am J Physiol Content [Internet]. 1951 Jan 31 [cited 2024 Apr 12];164(2):319–29. Available from: https://www.physiology.org/doi/10.1152/ajplegacy.1951.164.2.319

114. Katz AI, Chen Y, Moreno AH. Flow through a Collapsible Tube. Biophys J [Internet]. 1969 Oct [cited 2024 Apr 12];9(10):1261–79. Available from: https://linkinghub.elsevier.com/retrieve/pii/S0006349569864519

115. HOLT JP. Flow of Liquids Through “Collapsible” Tubes. Circ Res [Internet]. 1959 May;7(3):342–53. Available from: https://www.ahajournals.org/doi/10.1161/01.RES.7.3.342

116. Knowlton FP, Starling EH. The influence of variations in temperature and blood-pressure on the performance of the isolated mammalian heart. J Physiol [Internet]. 1912 May 6 [cited 2024 May 8];44(3):206–19. Available from: https://www.ncbi.nlm.nih.gov/pmc/articles/PMC1512817/

117. Weibel DB, Siegel AC, Lee A, George AH, Whitesides GM. Pumping fluids in microfluidic systems using the elastic deformation of poly(dimethylsiloxane){. [cited 2021 Nov 30]; Available from: www.rsc.org/loc

118. Bashirzadeh Y, Qian S, Maruthamuthu V. Non-intrusive measurement of wall shear stress in flow channels. Sensors Actuators, A Phys [Internet]. 2018;271:118–23. Available from: http://dx.doi.org/10.1016/j.sna.2018.01.012

119. Riccomi M, Alberini F, Brunazzi E, Vigolo D. Ghost Particle Velocimetry as an alternative to μPIV for micro/milli-fluidic devices. Chem Eng Res Des. 2018 May 1;133:183–94.

120. Kiran RM, Chakraborty J, Dasgupta S, Chakraborty S. Flow-induced deformation in a microchannel with a non-Newtonian fluid. Available from: https://doi.org/10.1063/1.5036632

121. Ghazy M, Elgindi MB, Wei D. Analytical and numerical investigations of the collapse of blood vessels with nonlinear wall material embedded in nonlinear soft tissues. Alexandria Eng J. 2018 Dec 1;57(4):3437–50.

122. Rohan C.-Y, Badel P, Lun B, Rastel D, Avril S. Biomechanical response of varicose veins to elastic compression: A numerical study. J Biomech [Internet]. 2013 Feb 1 [cited 2024 May 8];46(3):599–603. Available from: https://linkinghub.elsevier.com/retrieve/pii/S0021929012006501

123. Olufsen MS, Ottesen JT, Tran HT, Ellwein LM, Lipsitz LA, Novak V. Blood pressure and blood flow variation during postural change from sitting to standing: model development and validation. J Appl Physiol [Internet]. 2005 [cited 2024 May 8];99:1523–37. Available from: http://www.jap.org

124. Tang C, Zhu L, Akingba G, Lu X-Y. Viscous flow past a collapsible channel as a model for self-excited oscillation of blood vessels. J Biomech [Internet]. 2015 Jul 16 [cited 2023 Apr 27];48(10):1922–9. Available from: https://linkinghub.elsevier.com/retrieve/pii/S0021929015002274

125. Mansilla Alvarez LA, Bulant CA, Ares GD, Feijóo RA, Blanco PJ. ScienceDirect A mid-fidelity numerical method for blood flow in deformable vessels. 2022

[cited 2024 May 8]; Available from: www.sciencedirect.comwww.elsevier.com/locate/cma

126. Yadav PK, Roshan M. Mathematical modeling of blood flow in an annulus porous region between two coaxial deformable tubes: An advancement to peristaltic endoscope. Chinese J Phys [Internet]. 2024 Apr [cited 2024 May 8];88:89–109. Available from: https://doi.org/10.1016/j.cjph.2024.01.017

127. Mirramezani M, Shadden SC. Distributed lumped parameter modeling of blood flow in compliant vessels. J Biomech. 2022 Jul 1;140:111161.

128. Lucca A, Busto S, Müller LO, Toro EF, Dumbser M. A semi-implicit finite volume scheme for blood flow in elastic and viscoelastic vessels. J Comput Phys [Internet]. 2023 Dec [cited 2024 May 8];495:112530. Available from: https://doi.org/10.1016/j.jcp.2023.112530

129. Nobile F. Coupling strategies for the numerical simulation of blood flow in deformable arteries by 3D and 1D models. Math Comput Model [Internet]. 2009;49(11–12):2152–60. Available from: http://dx.doi.org/10.1016/j.mcm.2008.07.019

130. Pedley TJ, Luo XY. Theoretical and Computational Fluid Dynamics Modelling Flow and Oscillations in Collapsible Tubes 1. Theor Comput Fluid Dyn. 1998;10:277–94.

131. Cai ZX, Luo XY. A fluid-beam model for flow in a collapsible channel. J Fluids Struct [Internet]. 2003 [cited 2024 May 8];17:125–46. Available from: www.elsevier.nl/locate/jnlabr/yjfls

132. Ariane M, Wen W, Vigolo D, Brill A, Nash FGB, Barigou M, et al. Modelling and simulation of flow and agglomeration in deep veins valves using discrete multi physics. Comput Biol Med [Internet]. 2017;89(May):96–103. Available from: http://dx.doi.org/10.1016/j.compbiomed.2017.07.020

133. Steinman DA, Ethier CR. The Effect of Wall Distensibility on Flow in a Two-Dimensional End-to-Side Anastomosis. J Biomech Eng [Internet]. 1994 Aug 1 [cited 2024 May 8];116(3):294–301. Available from: https://dx.doi.org/10.1115/1.2895733

134. Grotberg JB, Jensen OE. Biofluid mechanics in flexible tubes. Annu Rev Fluid Mech [Internet]. 2004 Jan 21 [cited 2024 May 8];36(Volume 36, 2004):121–47. Available from: https://www.annualreviews.org/content/journals/10.1146/annurev.fluid.36.050802.121918

135. Bruus H. Theoretical Microfluidics [Internet]. Oxford University PressOxford; 1997 [cited 2022 Jun 24]. Available from: https://academic.oup.com/book/54833

136. Chen Y zhou, He Q lin, Huang B, Shi X ding. Navier-Stokes/Allen-Cahn System with Generalized Navier Boundary Condition. Acta Math Appl Sin English Ser 2022 381 [Internet]. 2022 Feb 3 [cited 2022 Apr 27];38(1):98–115. Available from: https://link.springer.com/article/10.1007/s10255-022-1068-7

137. Tanyeri M, Ranka M, Sittipolkul N, Schroeder CM. A microfluidic-based hydrodynamic trap: design and implementation †. [cited 2022 Apr 21]; Available from: http://pubs.rsc.org

138. Incropera F, DeWitt D. Fundamentals of Heat and Mass Transfer [Internet]. 6th ed. Sons JW&, editor. New York; 2007 [cited 2019 Jan 30]. Available from: http://uotechnology.edu.iq/dep-materials/lecture/secondclass/HeatTransfer&FluidBOOKFrankPIncroperaFundamentalsofheatandmasstransfer2007.pdf

139. Alexiadis A. The discrete multi-hybrid system for the simulation of solid-liquid flows. PLoS One. 2015;10(5):1–26.

140. Ariane M, Vigolo D, Brill A, Nash FGB, Barigou M, Alexiadis A. Using Discrete Multi-Physics for studying the dynamics of emboli in flexible venous valves. Comput Fluids [Internet]. 2018;166:57–63. Available from: https://doi.org/10.1016/j.compfluid.2018.01.037

141. Gregorio S Di, Fedele M, Pontone G, Corno AF, Zunino P, Vergara C, et al. A computational model applied to myocardial perfusion in the human heart: From large coronaries to microvasculature. J Comput Phys [Internet]. 2021 [cited 2024 Apr 7];424:109836. Available from: www.elsevier.com/locate/jcp

142. Balogh P, Bagchi P. Three-dimensional distribution of wall shear stress and its gradient in red cell-resolved computational modeling of blood flow in in vivo-like microvascular networks. Physiol Rep [Internet]. 2019 May 6;7(9):e14067. Available from: https://onlinelibrary.wiley.com/doi/abs/10.14814/phy2.14067

143. Perinajová R, Juffermans JF, Westenberg JJM, van der Palen RLF, van den Boogaard PJ, Lamb HJ, et al. Geometrically induced wall shear stress variability in CFD-MRI coupled simulations of blood flow in the thoracic aortas. Comput Biol Med [Internet]. 2021 Jun [cited 2024 May 8];133:104385.

Available from: http://creativecommons.org/licenses/by/4.0/

144. Shi Y, Zheng J, Zhang Y, Sun Q, Shen J, Gao Y, et al. The influence of flow distribution strategy for the quantification of pressure- and wall shear stress-derived parameters in the coronary artery: A CTA-based computational fluid dynamics analysis. J Biomech [Internet]. 2023 Dec [cited 2024 May 8];161:111857. Available from: http://creativecommons.org/licenses/by/4.0/

145. Hamidah MA, Hossain SMC. Modeling analysis of pulsatile non-Newtonian blood flow in a renal bifurcated artery with stenosis. Int J Thermofluids [Internet]. 2024 May [cited 2024 May 8];22:100645. Available from: https://doi.org/10.1016/j.ijft.2024.100645

146. Whitesides GM. The origins and the future of microfluidics [Internet]. Vol. 442, Nature. Nature Publishing Group; 2006 [cited 2021 Mar 29]. p. 368–73. Available from: https://www.nature.com/articles/nature05058

147. Silva G, Leal N, Semiao V. Micro-PIV and CFD characterization of flows in a microchannel: Velocity profiles, surface roughness and Poiseuille numbers. Int J Heat Fluid Flow [Internet]. 2008 Aug 1 [cited 2024 Mar 14];29(4):1211–20. Available from: https://linkinghub.elsevier.com/retrieve/pii/S0142727X08000611

148. Bitsch L, Olesen LH, Westergaard CH, Bruus H, Klank H, Kutter JP. Micro PIV on blood flow in a microchannel. Proc 7th Int Conf Miniaturized Chem Biochem Anal Syst Oct 5-9, California, USA [Internet]. 2003;825–8. Available from: http://www.rsc.org/binaries/LOC/2003/Volume1/205-288.pdf

149. Hong H, Yeom E, Ji HS, Kim HD, Kim KC. Characteristics of pulsatile flows in

curved stenosed channels. Gurka R, editor. PLoS One [Internet]. 2017 Oct 19 [cited 2024 May 8];12(10):e0186300. Available from: https://doi.org/10.1371/journal.pone.0186300

150. Ha H, Nam K-H, Lee SJ. Hybrid PIV–PTV technique for measuring blood flow in rat mesenteric vessels. Microvasc Res [Internet]. 2012 Nov [cited 2024 May 8];84(3):242–8. Available from: https://linkinghub.elsevier.com/retrieve/pii/S0026286212001264

151. Lima R, Wada S, Takeda M, Tsubota K-I, Yamaguchi T. In vitro confocal micro-PIV measurements of blood flow in a square microchannel: The effect of the haematocrit on instantaneous velocity profiles. J Biomech [Internet]. 2007 [cited 2024 May 8];40:2752–7. Available from: www.elsevier.com/locate/jbiomech

152. Kähler CJ, Scholz U, Ortmanns J. Wall-shear-stress and near-wall turbulence measurements up to single pixel resolution by means of long-distance micro-PIV. Exp Fluids. 2006;41(2):327–41.

153. Frame M, Chapman G, Makino Y, Sarelius I. Shear stress gradient over endothelial cells in a curved microchannel system. Biorheology [Internet]. 1998 Jul;35(4–5):245–61. Available from: https://linkinghub.elsevier.com/retrieve/pii/S0006355X99800092

154. Buzzaccaro S, Secchi E, Piazza R. Ghost particle velocimetry: Accurate 3d flow visualization using standard lab equipment. Phys Rev Lett. 2013;111(4):1–5.

155. Kiratzis I, Kovalchuk NM, Simmons MJH, Vigolo D. Effect of surfactant addition

and viscosity of the continuous phase on flow fields and kinetics of drop formation in a flow-focusing microfluidic device. Chem Eng Sci [Internet]. 2022 Feb;248:117183. Available from: https://doi.org/10.1016/j.ces.2021.117183

156. Schofield Z. Experimental and Computational Investigation of The Mechanisms behind Deep Vein Thrombosis [Internet]. 2019. Available from: https://etheses.bham.ac.uk/id/eprint/10237/7/schofield2020PhD.pdf

157. MicroChem. SU-8 2000 Permanent Epoxy Negative Photoresist. 2019 [cited 2023 Oct 31]; Available from: www.atgc.co.jp

158. Sauzade M, Li L, Bakowski T, Strey HH, Brouzes E. Multi-layering of SU-8 exhibits distinct geometrical transitions from circular to planarized profiles. Biomicrofluidics [Internet]. 2020 Jan 1 [cited 2024 Jan 17];14(1):14116. Available from: https://doi.org/10.1063/1.5139031

159. Heidelberg. uMLA Technical Data [Internet]. 2024. Available from: https://heidelberg-instruments.com/product/μmla/

160. Alharbi A, Almutairi D, Hussain H, Alfihed S. Detailed Study of the Correlation between Cross-Linking of Thick SU-8 and UV–NIR Optical Transmission/Photoluminescence Spectroscopy. Polymers (Basel) [Internet]. 2023 Sep 23;15(19):3866. Available from: https://www.mdpi.com/2073-4360/15/19/3866

161. Ye S, Williams NX, Franklin AD. Aerosol Jet Printing of SU-8 as a Passivation Layer Against Ionic Solutions. J Electron Mater [Internet]. 2022 Apr 18 [cited 2024 Jan 4];51(4):1583–90. Available from: https://doi.org/10.1007/s11664-021-09396-4

162. Formlabs. Formlabs Stereolithography 3D Printers Tech Specs [Internet]. 2024. Available from: https://formlabs.com/uk/3d-printers/form-3/tech-specs/

163. Miranda I, Souza A, Sousa P, Ribeiro J, Castanheira EMS, Lima R, et al. Properties and applications of PDMS for biomedical engineering: A review. J Funct Biomater. 2022;13(1).

164. Vrhovec Hartman S, Božič B, Derganc J. Migration of blood cells and phospholipid vesicles induced by concentration gradients in microcavities. N Biotechnol [Internet]. 2018 Dec 25 [cited 2024 Jan 4];47:60–6. Available from: https://linkinghub.elsevier.com/retrieve/pii/S1871678417303734

165. Eckstein T, Vidal-Henriquez E, Bae A, Zykov V, Bodenschatz E, Gholami A. Influence of fast advective flows on pattern formation of Dictyostelium discoideum. PLoS One [Internet]. 2018 Mar 1 [cited 2024 Jan 4];13(3):e0194859. Available from: https://journals.plos.org/plosone/article?id=10.1371/journal.pone.0194859

166. Özbey A, Karimzadehkhouei M, Alijani H, Koşar A. Microparticle Inertial Focusing in an Asymmetric Curved Microchannel. Fluids 2018, Vol 3, Page 57 [Internet]. 2018 Aug 9 [cited 2024 Jan 4];3(3):57. Available from: https://www.mdpi.com/2311-5521/3/3/57/htm

167. Beh CW, Zhou W, Wang T-H. PDMS–glass bonding using grafted polymeric adhesive – alternative process flow for compatibility with patterned biological molecules. Lab Chip [Internet]. 2012 [cited 2024 Jan 4];12(20):4120. Available from: www.rsc.org/loc

168. Bhattacharya S, Datta A, Berg JM, Gangopadhyay S. Studies on surface

wettability of poly(dimethyl) siloxane (PDMS) and glass under oxygen-plasma treatment and correlation with bond strength. J Microelectromechanical Syst [Internet]. 2005 Jun [cited 2024 Jan 4];14(3):590–7. Available from: http://ieeexplore.ieee.org/document/1438429/

169. Jung K, Kim DG, Jung S-B. Adhesion of PDMS substrates assisted by Plasma Graft Polymerization. Surf Interface Anal [Internet]. 2016 Jul 10 [cited 2024 Jan 4];48(7):597–600. Available from: https://analyticalsciencejournals.onlinelibrary.wiley.com/doi/10.1002/sia.5985

170. Wang J, Wang S, Zhang P, Li Y. Easy-disassembly bonding of PDMS used for leak-tight encapsulation of microfluidic devices. 18th Int Conf Electron Packag Technol ICEPT 2017. 2017;(51205082):1051–5.

171. Yousuff C, Danish M, Ho E, Kamal Basha I, Hamid N. Study on the Optimum Cutting Parameters of an Aluminum Mold for Effective Bonding Strength of a PDMS Microfluidic Device. Micromachines [Internet]. 2017 Aug 22 [cited 2024 Jan 4];8(8):258. Available from: www.mdpi.com/journal/micromachines

172. Jiang X, Zheng H, Gourdin S, Hammond PT. Polymer-on-Polymer Stamping: Universal Approaches to Chemically Patterned Surfaces. Langmuir [Internet]. 2002 Apr 1 [cited 2024 Jan 4];18(7):2607–15. Available from: https://pubs.acs.org/sharingguidelines

173. Hennicker Plasma. Plasma Technology. 2023.

174. Shamsiah Mohamed N, Ching Theng K. Mechanical Properties of Graded Polydimethylsiloxane for Flexible Electronics. J Phys Conf Ser [Internet]. 2019 Jan;1150(1):012030. Available from:

https://iopscience.iop.org/article/10.1088/1742-6596/1150/1/012030

175. Sales FCP, Ariati RM, Noronha VT, Ribeiro JE. Mechanical Characterization of PDMS with Different Mixing Ratios. Procedia Struct Integr [Internet]. 2022 [cited 2024 Jan 4];37:383–8. Available from: www.sciencedirect.comwww.sciencedirect.com

176. Kim M, Moon BU, Hidrovo CH. Enhancement of the thermo-mechanical properties of PDMS molds for the hot embossing of PMMA microfluidic devices. J Micromechanics Microengineering. 2013;23(9).

177. Chambers J. Low “gradient”, low flow aortic stenosis. Heart. 2006;92(4):554–8.

178. Chiou CH, Yeh TY, Lin JL. Deformation analysis of a pneumatically-activated polydimethylsiloxane (PDMS) membrane and potential micro-pump applications. Micromachines. 2015;6(2):216–29.

179. Woodcock TE, Michel CC. Advances in the Starling Principle and Microvascular Fluid Exchange; Consequences and Implications for Fluid Therapy. Front Vet Sci [Internet]. 2021 Apr 6;8(April):1–11. Available from: https://www.frontiersin.org/articles/10.3389/fvets.2021.623671/full

180. Emerson DR, Cieślicki K, Gu X, Barber RW. Biomimetic design of microfluidic manifolds based on a generalised Murray’s law. Lab Chip [Internet]. 2006 Feb 24 [cited 2022 Jul 6];6(3):447–54. Available from: https://pubs.rsc.org/en/content/articlehtml/2006/lc/b516975e

181. Lee JY, Lee SJ. Murray’s law and the bifurcation angle in the arterial micro-circulation system and their application to the design of microfluidics. Microfluid

Nanofluidics. 2010;8(1):85–95.

182. Stephenson D, Lockerby AD. A generalized optimization principle for asymmetric branching in fluidic networks. Proc R Soc A Math Phys Eng Sci. 2016;472(2191).

183. Stephenson D, Patronis A, Holland DM, Lockerby DA. Generalizing Murray's law: An optimization principle for fluidic networks of arbitrary shape and scale. J Appl Phys [Internet]. 2015 Nov 6 [cited 2022 Jul 6];118(17):174302. Available from: https://aip.scitation.org/doi/abs/10.1063/1.4935288

184. Photron. Product Datasheet Nova S-16.

185. Photron. FastCam SA3 Datasheet. :2–3.

186. Photron. FastCam SA5 Datasheet.

187. Thielicke W, Sonntag R. Particle Image Velocimetry for MATLAB: Accuracy and enhanced algorithms in PIVlab. J Open Res Softw [Internet]. 2021 May 31 [cited 2022 Apr 27];9(1):1–14. Available from: http://openresearchsoftware.metajnl.com/articles/10.5334/jors.334/

188. Thielicke W, Stamhuis EJ. PIVlab – Towards User-friendly, Affordable and Accurate Digital Particle Image Velocimetry in MATLAB. J Open Res Softw [Internet]. 2014 Oct 16;2. Available from: http://openresearchsoftware.metajnl.com/articles/10.5334/jors.bl/

189. Naiim M, Boualem A, Ferre C, Jabloun M, Jalocha A, Ravier P. Multiangle dynamic light scattering for the improvement of multimodal particle size distribution measurements. Soft Matter. 2015;11(1):28–32.

190. MalvernPanalytical. Multi-angle dynamic light scattering (MADLS) [Internet]. 2024. Available from: https://www.malvernpanalytical.com/en/products/technology/light-scattering/multi-angle-dynamic-light-scattering

191. Huang G, Xu B, Qiu J, Peng L, Luo K, Liu D, et al. Symmetric electrophoretic light scattering for determination of the zeta potential of colloidal systems. Colloids Surfaces A Physicochem Eng Asp [Internet]. 2020 Feb;587(October 2019):124339. Available from: https://doi.org/10.1016/j.colsurfa.2019.124339

192. Hydrodynamics M, Zhang J, Chiu W, Hydrodynamics M, Cryo-microscopy E. Encyclopedia of Biophysics. Encyclopedia of Biophysics. 2013.

193. Jeong W, Seong J. Comparison of effects on technical variances of computational fluid dynamics (CFD) software based on finite element and finite volume methods. Int J Mech Sci [Internet]. 2014 Jan;78:19–26. Available from: http://dx.doi.org/10.1016/j.ijmecsci.2013.10.017

194. Nadeem S, Akhtar S, Saleem A, Akkurt N, Ali Ghazwani H, Eldin SM. Numerical computations of blood flow through stenosed arteries via CFD tool OpenFOAM. Alexandria Eng J [Internet]. 2023 Apr;69:613–37. Available from: https://doi.org/10.1016/j.aej.2023.02.005

195. Zhang H, Tang S, Yue H, Wu K, Zhu Y, Liu C, et al. Comparison of computational fluid dynamic simulation of a stirred tank with polyhedral and tetrahedral meshes. Iran J Chem Chem Eng. 2020;39(4):311–9.

196. Chen H, Zhou X, Feng Z, Cao SJ. Application of polyhedral meshing strategy in indoor environment simulation: Model accuracy and computing time. Indoor

Built Environ. 2022;31(3):719–31.

197. Anderson J. John Anderson. BMJ [Internet]. 2006 Jun 17;332(7555):1456.2. Available from: https://www.bmj.com/lookup/doi/10.1136/bmj.332.7555.1456-a

198. Galbraith CG, Skalak R, Chien S. Shear Stress Induces Spatial Reorganization of the Endothelial Cell Cytoskeleton. Cytoskeleton [Internet]. 1998 [cited 2024 Jan 16];40:317–30. Available from: https://onlinelibrary.wiley.com/doi/10.1002/

199. Via AG, Oliva F, Spoliti M, Maffulli N. . Muscles Ligaments Tendons J [Internet]. 2015 [cited 2020 Dec 27];5(1):18. Available from: /pmc/articles/PMC4396671/?report=abstract

200. Bidani A, Flumerfelt RW, Crandall ED. Analysis of the effects of pulsatile capillary blood flow and volume on gas exchange. Respir Physiol [Internet]. 1978 Oct;35(1):27–42. Available from: https://linkinghub.elsevier.com/retrieve/pii/0034568778900385

201. Chaudhry R, Miao J, Rehman A. Cardiovascular Physiology [Internet]. 2022. Available from: ncbi.nlm.nih.gov/books/NBK493197

202. Cottet J, Renaud P. Introduction to microfluidics. In: Drug Delivery Devices and Therapeutic Systems [Internet]. Elsevier; 2021. p. 3–17. Available from: http://dx.doi.org/10.1016/B978-0-12-819838-4.00014-6

203. Papautsky I, Ameel T, Frazier AB. A review of laminar single-phase flow in microchannels. ASME Int Mech Eng Congr Expo Proc. 2001;2(May):3067–75.

204. Perry RH, Green DW, Maloney JO. 7 Perry ’ s Chemical Engineers enginners handbook. Wiley Online Libr. 1997;43–4.

205. Ahmad NN, Ghazali NNN, Abdul Rani AT, Othman MH, Kee CC, Jiwanti PK, et al. Finger-Actuated Micropump of Constant Flow Rate without Backflow. Micromachines [Internet]. 2023 Apr 19;14(4):881. Available from: https://www.mdpi.com/2072-666X/14/4/881

206. McFarland M. Biosolids Engineering [Internet]. 1st ed. McGraw-Hill; 2001. Available from: https://www.accessengineeringlibrary.com/content/book/9780070471788

207. Rapp BE. Analytical solutions to Poiseuille flow problems in different geometries. In: Microfluidics [Internet]. Elsevier; 2023 [cited 2024 Mar 21]. p. 345–73. Available from: https://linkinghub.elsevier.com/retrieve/pii/B9780128240229000346

208. Tanyeri M, Ranka M, Sittipolkul N, Schroeder CM. A microfluidic-based hydrodynamic trap: Design and implementation †. 2011;

209. Cameron SM. Theoretical description of PIV measurement errors. Acta Geophys [Internet]. 2022 [cited 2024 Mar 12];70:2379–87. Available from: https://doi.org/10.1007/s11600-022-00901-9

210. Kähler CJ, Scharnowski S, Cierpka C. On the uncertainty of digital PIV and PTV near walls. Exp Fluids [Internet]. 2012 Jun 6 [cited 2024 Feb 23];52(6):1641–56. Available from: http://link.springer.com/10.1007/s00348-012-1307-3

211. Kefayati S, Milner JS, Holdsworth DW, Poepping TL. In vitro shear stress measurements using particle image velocimetry in a family of carotid artery models: Effect of stenosis severity, plaque eccentricity, and ulceration. PLoS

One. 2014;9(7).

212. Ameenuddin M, Anand M, Massoudi M. Effects of shear-dependent viscosity and hematocrit on blood flow. Appl Math Comput [Internet]. 2019 Sep 1 [cited 2024 Feb 23];356:299–311. Available from: https://linkinghub.elsevier.com/retrieve/pii/S0096300319302292

213. Sinha A, Shit GC, Kundu PK. Slip Effects on Pulsatile Flow of Blood through a Stenosed Arterial Segment under Periodic Body Acceleration. ISRN Biomed Eng [Internet]. 2013 Aug 18;2013:1–10. Available from: https://www.hindawi.com/journals/isrn/2013/925876/

214. Hudson SD. Poiseuille flow and drop circulation in microchannels. Rheol Acta [Internet]. 2010 Mar 21;49(3):237–43. Available from: http://link.springer.com/10.1007/s00397-009-0394-4

215. Bosman J, Tangelder GJ, Oude Egbrink MG, Reneman RS, Slaaf DW. Capillary diameter changes during low perfusion pressure and reactive hyperemia in rabbit skeletal muscle. Am J Physiol Circ Physiol [Internet]. 1995 Sep 1 [cited 2024 Mar 12];269(3):H1048–55. Available from: https://journals.physiology.org/doi/10.1152/ajpheart.1995.269.3.H1048

216. Späth M, Hohmann M, Rohde M, Lengenfelder B, Stelzle F, Klämpfl F. Determination of the diameter of simulated human capillaries using shifted position-diffuse reflectance imaging. J Biophotonics. 2021 Apr 1;14(4).

217. Hu D, Cai D, Rangan A V. Blood Vessel Adaptation with Fluctuations in Capillary Flow Distribution. Aegerter CM, editor. PLoS One [Internet]. 2012 Sep 27 [cited 2024 Mar 12];7(9):e45444. Available from: www.plosone.org

218. Howlett SE. Effects of Aging on the Cardiovascular System. In: Brocklehurst's Textbook of Geriatric Medicine and Gerontology [Internet]. Elsevier; 2010 [cited 2024 Jan 3]. p. 91–6. Available from: https://linkinghub.elsevier.com/retrieve/pii/B9781416062318100145

219. Casey DP, Curry TB, Joyner MJ. Measuring Muscle Blood Flow a Key Link Between Systemic and Regional Metabolism. Curr Opin Clin Nutr Metab Care. 2008;11(5):580–6.

220. Sree VD, Rausch MK, Tepole AB. Linking microvascular collapse to tissue hypoxia in a multiscale model of pressure ulcer initiation. Biomech Model Mechanobiol [Internet]. 2019 Dec;18(6):1947–64. Available from: http://www.ncbi.nlm.nih.gov/pubmed/31203488

221. Sree VD, Rausch MK, Tepole AB. Linking microvascular collapse to tissue hypoxia in a multiscale model of pressure ulcer initiation. Biomech Model Mechanobiol [Internet]. 2019 Dec 15;18(6):1947–64. Available from: https://doi.org/10.1007/s10237-019-01187-5

222. Cone J, Inaba K. Lower extremity compartment syndrome. Trauma Surg Acute Care Open [Internet]. 2017 Sep 14;2(1):e000094. Available from: https://tsaco.bmj.com/lookup/doi/10.1136/tsaco-2017-000094

223. Koutsiaris AG, Tachmitzi S V., Batis N. Wall shear stress quantification in the human conjunctival pre-capillary arterioles in vivo. Microvasc Res. 2013 Jan;85(1):34–9.

224. Pan F, Mori N, Mugikura S, Ohta M, Anzai H. The influence of blood velocity and vessel geometric parameters on wall shear stress. Med Eng Phys

[Internet]. 2024 Feb [cited 2024 Mar 12];124:104112. Available from: https://doi.org/10.1016/j.medengphy.2024.104112

225. A. S. Popel. A Model of Pressure and Flow Distribution in Branching Networks. J Appl Mech [Internet]. 1980 [cited 2024 Mar 15]; Available from: http://asmedigitalcollection.asme.org/appliedmechanics/article-pdf/47/2/247/5878432/247_1.pdf

226. Reynolds O. An experimental investigation of the circumstances which determine whether the motion of water in parallel channels shall be direct or sinuous and of the Society, The Royal Transactions, Philosophical Society, Royalaw of resistance in parallel channels. Soc R Trans Philos Soc R. 1883;174(1883):935–82.

227. Wang X, Sun Q, Pei J. Microfluidic-Based 3D Engineered Microvascular Networks and Their Applications in Vascularized Microtumor Models. Micromachines [Internet]. 2018 [cited 2022 Jul 6];9(10). Available from: /pmc/articles/PMC6215090/

228. Painter PR, Edén P, Bengtsson HU. Pulsatile blood flow, shear force, energy dissipation and Murray's Law. Theor Biol Med Model [Internet]. 2006 Aug 21 [cited 2024 Jul 18];3:31. Available from: /pmc/articles/PMC1590016/

229. Taylor DJ, Feher J, Halliday I, Hose DR, Gosling R, Aubiniere-Robb L, et al. Refining Our Understanding of the Flow Through Coronary Artery Branches; Revisiting Murray's Law in Human Epicardial Coronary Arteries. Front Mater [Internet]. 2022 Apr 4 [cited 2024 Jul 18];13:871912. Available from: /pmc/articles/PMC9119389/

230. Sayed Abu-Zaid T. Three-dimensional numerical study for determining the optimum diversion angle of bifurcating channels. Ain Shams Eng J [Internet]. 2023 Apr;14(4):101940. Available from: https://doi.org/10.1016/j.asej.2022.101940

231. Va'Clav T. Pressure Driven Microfluidics. 2007. 60–70 p.

232. Vardhan M, Gounley J, Chen SJ, Kahn AM, Leopold JA, Randles A. The importance of side branches in modeling 3D hemodynamics from angiograms for patients with coronary artery disease. Sci Rep [Internet]. 2019 Jun 20 [cited 2024 Jun 18];9(1):8854. Available from: www.nature.com/scientificreports

233. Gosling RC, Sturdy J, Morris PD, Fossan FE, Hellevik LR, Lawford P, et al. Effect of side branch flow upon physiological indices in coronary artery disease. J Biomech [Internet]. 2020;103:109698. Available from: https://doi.org/10.1016/j.jbiomech.2020.109698

234. Giannopoulos AA, Chatzizisis YS, Maurovich-Horvat P, Antoniadis AP, Hoffmann U, Steigner ML, et al. Quantifying the effect of side branches in endothelial shear stress estimates. Atherosclerosis [Internet]. 2016 Aug;251:213–8. Available from: http://dx.doi.org/10.1016/j.atherosclerosis.2016.06.038

235. Ř VT. Esda2004-58179 Pressure Driven Microfluidics. 2015;(August).

236. Fåhræus R, Lindqvist T. The viscosity of the blood in narrow capillary tubes. Am J Physicology. 1930;(8):562–8.

237. Ariati R, Sales F, Souza A, Lima RA, Ribeiro J. Polydimethylsiloxane

Composites Characterization and Its Applications: A Review. Polymers (Basel) [Internet]. 2021 Dec 5;13(23):4258. Available from: https://www.mdpi.com/2073-4360/13/23/4258

238. Sales FCP, Ariati RM, Noronha VT, Ribeiro JE. Mechanical Characterization of PDMS with Different Mixing Ratios. Procedia Struct Integr [Internet]. 2022;37(C):383–8. Available from: https://linkinghub.elsevier.com/retrieve/pii/S245232162200107X

239. Plyley MJ, Sutherland GJ, Groom AC. Geometry of the Capillary Network in Skeletal Muscle. Microvasc Res. 1976;11:161–73.

240. Wang Z, Volinsky AA, Gallant ND. Crosslinking effect on polydimethylsiloxane elastic modulus measured by custom-built compression instrument. J Appl Polym Sci [Internet]. 2014 Nov 15 [cited 2021 Nov 30];131(22):41050. Available from: https://onlinelibrary.wiley.com/doi/full/10.1002/app.41050

241. Mark JE. Polymer Data Handbook.

242. Kozlovsky P, Zaretsky U, Jaffa AJ, Elad D. General tube law for collapsible thin and thick-wall tubes. J Biomech. 2014 Jul 18;47(10):2378–84.

243. ANSYS. ANSYS Fluent 12.0 Theory Guide - 3.3.1 Dynamic Mesh Update Methods [Internet]. [cited 2024 Aug 27]. Available from: https://www.afs.enea.it/project/neptunius/docs/fluent/html/th/node40.htm#spring

244. Kowalczuk Z, Tatara MS. Analytical ‘steady-state’-based derivation and clarification of the courant-friedrichs-lewy condition for pipe flow. J Nat Gas Sci

Eng [Internet]. 2021 Jul;91(March):103953. Available from: https://linkinghub.elsevier.com/retrieve/pii/S1875510021001608

245. Courant R, Friedrichs K, Lewy H. On the Partial Difference Equations of Mathematical Physics. IBM J Res Dev [Internet]. 1967 Mar [cited 2024 Aug 5];11(2):215–34. Available from: http://ieeexplore.ieee.org/document/5391985/

Appendices

Appendix 1. ImageJ Macro for image processing.

```
#@ File (label = "Input directory", style = "directory") input
#@ File (label = "Output directory", style = "directory") output
setBatchMode(true);
run("Close All");
processFolder(input);

// function to scan folders/subfolders/files to find files with correct suffix
function processFolder(input) {
	list = getFileList(input);
	list = Array.sort(list);
	for (i = 0; i < list.length; i++) {
		if(File.isDirectory(input + File.separator + list[i]))
			processFolder(input + File.separator + list[i]);
		if(endsWith(list[i], ".tif") && startsWith(list[i], "result_") == false)
			processFile(input, output, list[i]);
	}
}
function processFile(input, output, file) {
	print("Processing: " + input + File.separator + file);
	open(input + File.separator + file);
	rename("stack");
	// Perform Z projection
	run("Z Project...", "projection=Median");
	rename("projection");
	// subtract projection for stack 32 bit
	imageCalculator("Subtract create 32-bit stack", "stack", "projection");
	rename("stack_minus_projection");
	selectWindow("stack_minus_projection");
```

```
        //
        run("Enhance Contrast", "saturated=0.35");
        //run("Apply LUT", "stack");
        run("8-bit");
        fileName = File.getNameWithoutExtension(file);
        resultFilePath = output + File.separator + "result_" + fileName + ".tif";
        print("Saving to: " + output);
        // Save the image as TIFF
        saveAs("Tiff", resultFilePath);
        run("Close All");
}
```

Appendix 2.

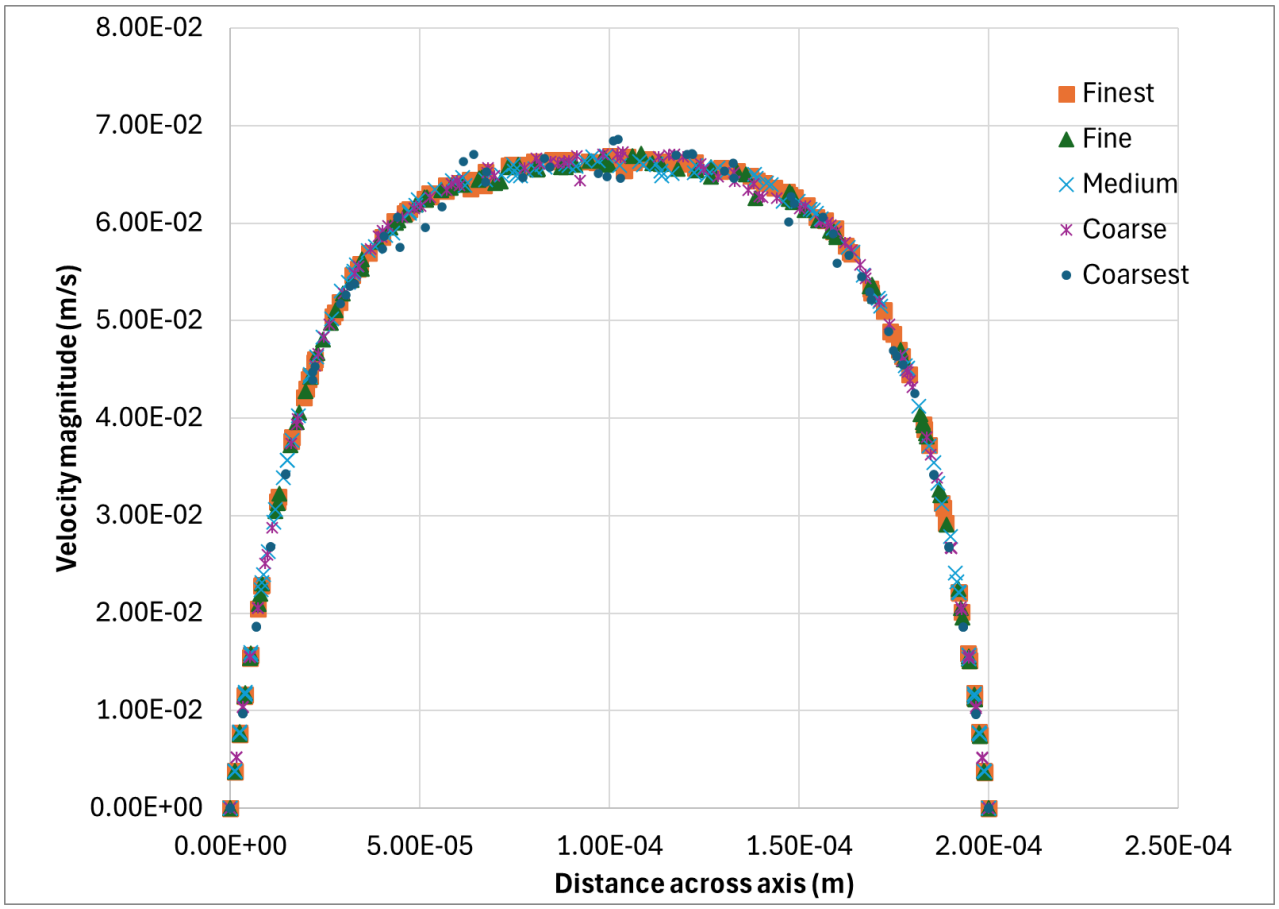

Figure 7.3. Velocity profiles from CFD 200 micron model at 3200 Pa, for cell sizes in table 7.1

Table 7.1 Cell sizes for CFD model where the cell size would be comparable with interrogation area in GPV measurements

Cell size (μm)	**finest**	**fine**	**medium**	**coarse**	**coarsest**
min	1.00	4.00	6.00	8.00	16.00
max	10.00	40.00	60.00	80.00	160.00

Appendix 3.

Calculation of shear stress

The values of the velocity profile were extracted across a line from the GPV data from PIVLab as detailed in section 3.6.5. The data was then extracted into excel and the shear stress calculated following this method:

X coordinate	Velocity (m/s)
J	A
K	B
L	C
M	D
N	E

At wall x=0 calculated x3, 1 per repeat

$$\boldsymbol{Shear\ stress = dynamic\ viscosity\ (Pa.s) * (B - A)/(K - J)}$$

At wall x=X calculated x3, 1 per repeat

$$\boldsymbol{Shear\ stress = dynamic\ viscosity\ (Pa.s) * (D - E)/(N - M)}$$

These 6 values were then averaged as one data set.

Appendix 4. Murray's Law derivation.

$$P_t = P_f + P_m = \frac{8\pi}{\mu} Q^2 \frac{1}{r^4} + mr^2 l$$

Using Poiseuille's law, this is then related to the conductance, c, the inverse of resistance.

$$Q = c\Delta P$$

$$Q = c\frac{dP_t}{dx}$$

Where:

$$c = \frac{\pi r^4}{8\eta l}$$

$$Q = kr^3$$

Power term,

$$\frac{Q8\eta}{\pi} = pr^4\, dP$$

$$p = \frac{Q8\eta}{\pi r^4}$$

Power required to maintain flow:

$$P_f = pQ = \frac{Q^2 8\eta}{\pi r^4}$$

And maintenance power, including metablic coefficient, m.

$$P_m = \pi m r^2$$

Thus:

$$P_t = P_f + P_m = \frac{Q^2 8\eta}{\pi r^4} + \pi m r^2$$

$$\frac{dP_t}{dr} = \frac{d(aQ^2 r^{-4} + br^2)}{dr} = -4aQ^2 r^{-5} + 2br$$

$$\frac{d^2\,P_t}{dr^2} = \frac{d(-4aQ^2 r^{-5} + 2br)}{dr} = 20af^2 r^{-6} + 2b$$

dP/dr=0 as a minimum

Where:

$$a = \frac{8\eta}{\pi} \text{ and } b = \pi m$$

$$Q^2 = \frac{b}{2a} r^6$$

$$k = \frac{b}{2a}$$

Thus:

$$\sum Q = \sum kr^3 = k \sum r^3$$

Thus, for branched cylindrical networks with 3 branches:

$$r_1^3 = r_2^3 + r_3^3$$

Appendix 5. CFD Model with Deformable Wall.

The CFD model was created using ANSYS Fluent with a deformable wall applied to a 2 mm rectangular section of the walls and refined at the walls using 4 boundary layers as described in Chapter 3. The mesh was separated into two regions a solid exterior with a coarser mesh and a fluid region with a finer mesh and refinement at the solid/fluid boundary to extract an accurate shear stress at the channel walls as seen in Figure 7.1.

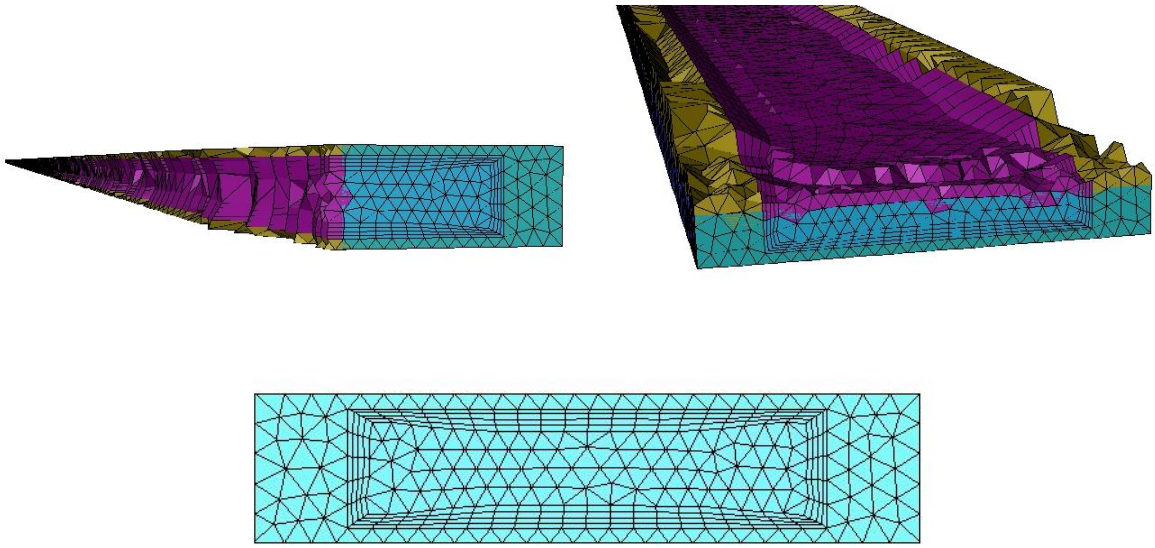

Figure 7.1: Mesh showing solid and fluid regions of the deformable wall CFD model with solid regions yellow and fluid regions pink

A polyhexacore mesh was initially tested to match the mesh used in Chapter 4, however, when the large deformation was applied, this created negative cell volumes due to the movement of the central node passed the edge of the cell. Thus, a tetrahedral mesh and smoothing techniques were used to overcome this error.

The dynamic mesh was coded for using the ‘user defined function’, UDF, Appendix 3, in Fluent. The define_grid_motion function was used with each deformable wall specified in separate UDF files as the two walls move in opposite directions and thus the velocity must be coded for separately.

The time step was specified, and the time taken to reach full deformation was calculated using Equation 7.1.

$$V = \frac{\Delta X}{2t} \tag{7.1}$$

Where v is the velocity, Δx is the distance and t is the time taken for the wall to reach the centre of the channel. This was decided to be a nominal 1 second to allow for a shorter simulation time as there is no value in literature for the speed at which one capillary collapses, although it is assumed to be instantaneous. The simulation ends when the walls have reached the central plane.

Adaptive meshing and smoothing were used. For tetrahedral dynamic meshing, the spring-based smoothing is most used to allow for change of mesh during deformation. The springs are set to be between the edges of the nodes and abide by Hooke’s law, as is seen in linearly elastic solids and models of deformable blood vessel walls. However, this is applicable to how the cells move together during the deformation and not forces applied to the simulation (243).

$$\vec{F}_i = \sum_{j}^{n_i} k_{i,j}\left(\Delta\vec{\mathrm{x}}_j - \Delta\vec{\mathrm{x}}_i\right) \tag{7.2}$$

Where k is the spring constant and $\Delta\vec{\mathrm{x}}_j$ is the displacement node of node j. A spring/Laplace/boundary layer smoothing was applied with a spring constant factor of

1 to allow for maximum damping in the springs during the dynamic movement of the mesh. This value is at a maximum to allow for large movement 50% of the geometry and lower values gave negative cell volume errors.

Laplacian smoothing moves the central vertex of the node to move to the centre of the neighbouring cells at a computational expense. This was also applied to prevent the negative cell volume error as remeshing should be applied as this was a large deformation, over 50% of the geometry width (243).

Boundary layer smoothing was also applied, which maintained the height of the refined cells at the edge of the boundary layers that were applied to the initial mesh. This allows for the wall shear stress to still be extracted accurately when the outer mesh deforms. This smoothing was applied with a convergence tolerance of 0.0001 and a maximum number of iterations of 100. The node relaxation was also set to 1 and the verbosity to 0.

Also to prevent the negative cell volume error, local cell, local face and region face remeshing was applied with a minimum length scale of 0.0001 m, maximum of 0.001m and maximum cell skewness of 0.9 and maximum face skewness of 0.7, every interval (243). This remeshed multiple faces and allowed the mesh to dynamically move across the 50% deformation mark.

The time step of transient simulations was determined by calculating the Courant number, C (244)(245).

$$C = \frac{V\Delta t}{\Delta h} \tag{7.3}$$

Where V is the average fluid velocity, Δt is the timestep and Δh is a characteristic cell size. The Courant-Friedrichs-Lewy (CFL) based condition was applied to solve the semi-implicit scheme (245), where 20 iterations per timestep was selected:

$$C = \frac{V\Delta t}{\Delta h} \leq C_{max} \tag{7.4}$$

The model was run on a high-performance computer, Bluebear, University of Birmingham, with 4 nodes and 100 cores.

As can be seen from Chapter 4, there is a large range of velocities across the geometry from the slower velocity magnitudes at the wall to the faster central velocities as well as a range of cell sizes with smaller cells at the wall with the addition of boundary layers as seen in Figure 6.16.

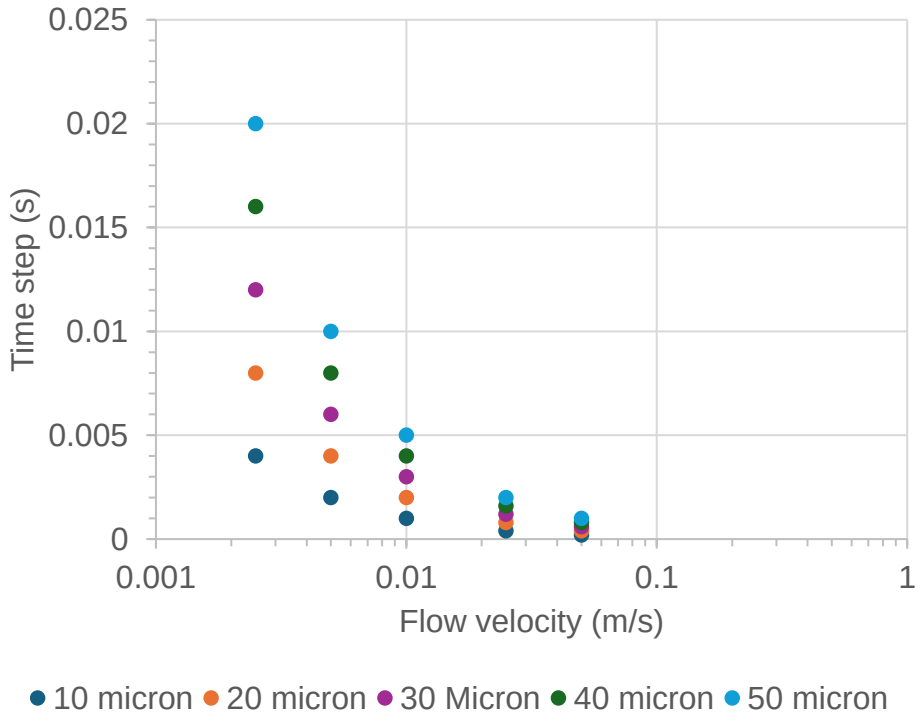

Figure 7.2: Timestep values for a Courant number of 1 for different flow velocities and different characteristic cell sizes

Figure 7.2 shows the timestep values for different flow velocities and average cell sizes to achieve a Courant number of 1. For an average cell size of 25 μm and a flow velocity of 0.25 m/s, the timestep should be 0.001 for a Courant number of 1 to allow for the model to accurately transfer data from each cell (245). For a timestep of 0.01, the simulation did not reach a steady state, therefore the timestep was reduced to 0.001 and the adaptive CFL model was applied.

The CFD simulation ran to 14 iterations, and then floating point errors occurred.